

Exploration targeting for gold deposits using spatial data analytics,  
machine learning and deep transfer learning in the Swayze and  
Matheson greenstone belts, Ontario, Canada

By

Mothepana Francisca Maepa

A thesis submitted in partial fulfillment

Of the requirement for the degree of

Doctor of Philosophy (PhD)

in Mineral Deposits and Precambrian Geology

The Faculty of Graduate Studies

Laurentian University

Sudbury, Ontario, Canada

© Francisca Maepa, 2021

**THESIS DEFENCE COMMITTEE/COMITÉ DE SOUTENANCE DE THÈSE**  
**Laurentian University/Université Laurentienne**  
Faculty of Graduate Studies/Faculté des études supérieures

Title of Thesis Titre de la thèse	Exploration targeting for gold deposits using spatial data analytics, machine learning and deep transfer learning in the Swayze and Matheson greenstone belts, Ontario, Canada	
Name of Candidate Nom du candidat	Maepa, Mothepana Francisca	
Degree Diplôme	Doctor of Philosophy	
Department/Program Département/Programme	Mineral Deposits and Precambrian Geology	Date of Defence Date de la soutenance May 19, 2021

**APPROVED/APPROUVÉ**

Thesis Examiners/Examineurs de thèse:

Dr. Richard Smith  
(Supervisor/Directeur(trice) de thèse)

Dr. Stephane Perrouty  
(Committee member/Membre du comité)

Dr. Daniel Kontak  
(Committee member/Membre du comité)

Dr. Michael Dentith  
(External Examiner/Examineur externe)

Dr. Kalpdrum Passi  
(Internal Examiner/Examineur interne)

Approved for the Office of Graduate Studies  
Approuvé pour le Bureau des études supérieures  
Tammy Eger, PhD  
Vice-President Research (Graduate Studies)  
Vice-rectrice à la recherche (Études supérieures)  
Laurentian University / Université Laurentienne

**ACCESSIBILITY CLAUSE AND PERMISSION TO USE**

I, **Mothepana Francisca Maepa**, hereby grant to Laurentian University and/or its agents the non-exclusive license to archive and make accessible my thesis, dissertation, or project report in whole or in part in all forms of media, now or for the duration of my copyright ownership. I retain all other ownership rights to the copyright of the thesis, dissertation or project report. I also reserve the right to use in future works (such as articles or books) all or part of this thesis, dissertation, or project report. I further agree that permission for copying of this thesis in any manner, in whole or in part, for scholarly purposes may be granted by the professor or professors who supervised my thesis work or, in their absence, by the Head of the Department in which my thesis work was done. It is understood that any copying or publication or use of this thesis or parts thereof for financial gain shall not be allowed without my written permission. It is also understood that this copy is being made available in this form by the authority of the copyright owner solely for the purpose of private study and research and may not be copied or reproduced except as permitted by the copyright laws without written authority from the copyright owner.

## Abstract

The rate of mineral deposit discovery has declined in the past decade despite increasing efforts from mining and government. The low rate of deposit discovery and the massive historical data available from brownfield exploration sites has prompted geoscientists to apply scale-integrated, empirical, and conceptual targeting approaches to exploration targeting. Applications of the mineral systems approach as a conceptual targeting method together with mineral prospectivity mapping has become the focus of predictive modelling for mineral exploration targeting.

Evaluating the essential ingredients that make up a mineral system at various scales with data science machine learning tools could potentially help improve exploration discovery. This study was aimed at mineral exploration targeting gold deposits in the Abitibi greenstone belt using various spatial analysis, machine learning, and transfer learning methods. The multi-scale spatial analysis of gold prospects in the Swayze greenstone belt revealed orogenic mineral systems display fractal characteristics at regional and deposit scales, that gold prospects are clustered within 2 -4 km distances, and that clustering within camps can be attributed to the occurrences of lower-order fault densities or intrusive source rocks. Analyzing spatial correlations between prospect distributions and geological features was instrumental in identifying the physical controlling parameters at various scales, which were primarily D<sub>2</sub> structures at regional scales and 2<sup>nd</sup> and 3<sup>rd</sup> order structures and competency contrast at prospect scales. Furthermore, the mineral prospectivity maps generated from the various machine learning methods such as support vector machines, random forest, radial basis function neural networks, and deep neural networks were not only beneficial in predicting prospective regions with > 80% accuracies but were essential for emphasizing important geoscience predictor layers that correlate well with mineral prospects. Deep transfer learning attempted for exploration targeting aimed at training a

deep neural network model on the Swayze greenstone belt and using the learnt knowledge to make predictions of prospectivity on the Matheson region resulted in over 70% prediction accuracies. Deep transfer learning was valuable in showing that pre-trained models can be used to generate prospectivity predictions in relatively greenfield exploration site where the distributions of prospects are unknown. Overall, this study demonstrates that data integration and applications of data science tools is effective for exploration targeting today.

Keywords: Mineral systems analysis, mineral prospectivity mapping, data integration, machine learning, cross-validation, feature importance, transfer learning

## Co-authorship Statement

This manuscript is composed of five chapters, of which three are research papers. Chapter 2 has been published in *Ore Geology Reviews*. Chapter 3 has been published with *Ore Geology Reviews*. Chapter 4 is currently under peer-review in *Ore Geology Reviews Journal*.

I am the first author for all papers, but the first paper (Chapter 2) is co-authored by Dr. Richard S. Smith, the second paper (Chapter 3) is co-authored by Dr. Richard S. Smith and Dr. Tessema Abera, and the third paper (Chapter 4) is co-authored with Dr. Richard S. Smith. All the geoscience data used in this study were obtained from the Ontario Geological Survey and the Geological Survey of Canada.

## Acknowledgements

I would like to thank my thesis supervisor, professor Richard S. Smith for his invaluable advice and guidance throughout my studies. I have been fortunate to have an advisor who is patient and kind. I would also like to thank my supervisory committee members, specifically Professor's Dan Kontak, Stephane Perrouty and Leonardo Feltrin for their advice and help in my research journey.

My sincerest gratitude goes to professor Abera Tessema for his mentorship and co-authorship in my research studies. I am grateful to Ivanhoe Mines, Queen Elizabeth Jubilee Diamond Scholarship and the International Development Research Center for sponsoring my studies

Thank you to the staff at the Goodman School of mines; specifically, Mojgan Adibpour for making sure that I was well taken care of throughout my studies in Canada. I am thankful for all the wonderful friendships I have fostered within the Harquail School of Earth Sciences department and the community of Sudbury.

I am grateful to my mother Mary Maepa and my siblings (Cleo, Puse and Pabi) for their love and support throughout my studies. Lastly, thank you to my husband CJ Spath for his continuous love and support.

# Table of Contents

## Contents

<b>Abstract</b> .....	<b>iii</b>
<b>Co-authorship Statement</b> .....	<b>v</b>
<b>Acknowledgements</b> .....	<b>vi</b>
<b>Table of Contents</b> .....	<b>vii</b>
<b>List of Figures</b> .....	<b>xi</b>
<b>List of Tables</b> .....	<b>xx</b>
<b>List of Appendices</b> .....	<b>xxii</b>
<b>Chapter 1: Introduction to thesis</b> .....	<b>1</b>
1.1 Research problem/ Research Motivation .....	1
1.2 Objectives of the thesis .....	2
1.3 Background .....	3
1.4 Structure of thesis .....	4
1.5 Innovative nature of the thesis (statement of original contributions).....	6
1.6 References .....	10
<b>Chapter 2: Examining the controls on gold deposit distribution in the Swayze greenstone belt, Ontario, Canada, using multi-scale methods of spatial data analysis.</b> .....	<b>14</b>
2.1 Abstract .....	14
2.1 Introduction.....	15
2.2 Geology, deformation, and gold mineralization .....	18
2.2.1 Geological setting .....	18
2.2.2 Exploration history in the Swayze greenstone belt .....	21
2.2.3 Deformation history .....	25
2.2.4 Characteristics of the gold deposits .....	27
2.3 Data .....	35
2.4 Methodology: Spatial analysis applied to mineral prospects .....	39
2.4.1 Fry Analysis .....	39
2.4.2 Fractal Analysis .....	40
2.4.3 Point-Pattern Analysis (Ripley’s K-Function analysis) .....	43
2.4.4 Evaluating spatial correlations of mineral prospects and geological features using distance distribution method .....	46

2.5. Results.....	48
2.5.1 The distribution of gold prospects by spatial autocorrelation techniques .....	48
2.5.2 Fractal dimensions of gold results .....	56
2.5.3 Point pattern analysis results .....	60
2.5.5 Analysis of the distance distribution of prospects and structures .....	63
2.6 Discussion .....	70
2.7 Conclusions.....	73
2.8 Acknowledgements .....	74
2.9 References.....	75
<b>Chapter 3: Support Vector Machine and Artificial Neural Network Modelling of Orogenic Gold Prospectivity Mapping in the Swayze greenstone belt, Ontario, Canada.....</b>	<b>88</b>
3.1 Abstract.....	88
3.2 Introduction.....	89
3.2.1 Mineral Prospectivity Mapping .....	89
3.2.2 The geology and stratigraphy of the Swayze greenstone belt.....	91
3.2.1 Deformational history of the Swayze greenstone belt .....	97
3.2.2 Mineral Deposit types in the Swayze greenstone belt.....	98
3.2.3 Mineral systems analysis of orogenic gold occurrences in the Swayze greenstone belt .....	100
3.3 Methodology .....	112
3.3.1 Weights of evidence.....	112
3.3.2 Artificial neural networks (Radial Basis function Neural Networks).....	115
3.3.3 Support Vector Machines (SVM) .....	118
3.3.4 Model cross validation .....	120
3.4 Datasets used and their significance in the Swayze greenstone belt mineral system.....	122
3.4.1 Data sources .....	122
3.4.2 The distribution of mineral deposit locations and non-deposit data selection .....	123
3.5 Predictor maps and their spatial association with gold based on weights of evidence statistical results and mineral-systems expressions.....	128
3.5.1 Proximity to permissive lithologies .....	128
3.5.1.2 Proximity to lithological contacts .....	131
3.5.3 Structures .....	131
3.5.4 Geophysics.....	137
3.5.5 Geochemistry .....	145
3.6 Results.....	153

3.6.1	Prospectivity modeling using prospect classification type 1 .....	153
3.6.2	Prospectivity modelling using prospect classification type 2 .....	164
3.6.3	Comparison of prospectivity models from prospect classification type 1 and type 2.....	164
3.7	Discussions .....	172
3.7.1	Mineral prospectivity mapping overview .....	172
3.7.3	Implications for exploration and target delineations.....	173
3.7.4	Comparison with previous study by Harris et al., (2001) .....	176
3.8	Conclusions.....	179
3.9	Acknowledgements .....	181
3.10	References.....	181
<b>Chapter 4: Investigating the applications of Deep Neural Networks, Random Forest, and Transfer Learning for exploration targeting in the Abitibi greenstone belt, Canada. ....</b>		<b>196</b>
4.1	Abstract.....	196
4.2	Introduction.....	197
4.2.1	Local geology of the Swayze greenstone belt.....	203
4.2.2	Local geology of the Matheson greenstone belt .....	206
4.3	Available data .....	209
4.3.1	Available data in the Swayze greenstone belt.....	209
4.3.2	Available data in the Matheson greenstone belt .....	211
4.4	Methodology.....	218
4.4.1	Fry analysis .....	218
4.4.2	Selection of training data for machine learning (deposit versus non-deposit point).....	219
4.4.3	Preprocessing steps in GIS.....	223
4.4.4	Data preprocessing steps in python.....	224
4.4.5	Deep neural networks.....	225
4.4.6	Loss functions and weight optimization .....	227
4.4.7	Model cross validation .....	229
4.4.8	Transfer learning: The definitions of transfer learning for mineral exploration .....	230
4.4.9	Random Forest classifier.....	232
4.4.10	Deriving feature importance in the deep neural network model.....	233
4.5	Results.....	233
4.5.1	Deep learning and random forest prospectivity analysis over the Swayze greenstone belt.....	234
4.5.2	Feature importance estimates from deep neural networks and random forest in the Swayze greenstone belt .....	237

4.5.3 Transfer learning between the north and south of the Swayze greenstone belt .....	243
4.5.4 Transfer learning between entire Swayze and Matheson greenstone belts .....	246
4.6 Discussions .....	252
4.7 Conclusions.....	256
4.8 Acknowledgements .....	257
4.9 References .....	258
<b>Chapter 5: Concluding statements .....</b>	<b>266</b>
5.1 Summary and conclusions .....	266
5.2 Implications for mineral exploration.....	270
5.3 Applications of the thesis workflow in greenfield exploration programs and suggestions for future work.....	272
<b>Appendices.....</b>	<b>275</b>

## List of Figures

Fig. 2- 1 Regional geological map of the Abitibi greenstone belt after Ayer et al (2002, 2005) showing the location of the Abitibi greenstone belt within the Superior Province, Canada, and the narrow septum of Archean volcanic intrusive rocks connecting the Swayze to the Abitibi greenstone belt. ....	23
Fig. 2- 2: Geological map of the Swayze greenstone belt showing felsic to ultramafic intrusive rocks and clastic metasedimentary rocks (Ayer and Trowell, 2002). The locations of orogenic gold deposit are displayed in red circles and an overlying standard deviation ellipse shows the orientation of the mineral deposits.....	24
Fig. 2- 3: Structural features covering the Swayze greenstone belt with overlying red circular points representing past producing mines, gold deposits, showings, and gold occurrences. ....	34
Fig. 2- 4: Grade vs tonnage plot for deposits and prospects in the Abitibi and Swayze greenstone belts. The plot is modified from Mathieu (2021). ....	37
Fig. 2- 5: Fry analysis translations from the autocorrelation of orogenic gold prospects with grade values < 5 g/t Au (A) and rose diagram showing primary orientations of prospects (B)...	49
Fig. 2- 6: Fry analysis translations from the autocorrelation of orogenic gold prospects with grade values > 5 g/t Au (A) and rose diagram showing primary orientations (B).....	50
Fig. 2- 7: Rose diagrams showing the Fry analysis translations of orogenic gold prospect distribution at local scales (< 2 km), district scales (2 – 10 km) and regional scales (> 10 km). Panels (A), (C) and (E) are low-grade prospects; (B), (D) and (E) are high-grade prospects.	52
Fig. 2- 8: Comparison of the spatial orientation of orogenic gold prospects to each other and point patterns representing the beginning and end of each fault feature mapped in the Swayze greenstone belt. The Fry analysis rose diagrams shows orogenic gold prospects orientations (A,	

B, and C) and fault point pattern orientations (D, E, and F) within the entire Swayze greenstone belt, in the north, and in the south respectively. See Table 2-5 for a comparison of spatial correlations between prospects and faults..... 55

Fig. 2- 9: Log-log plots defining the fractal properties of gold prospects in the Swayze greenstone belt. The plot shows that low-grade ranges < 5 g/t Au prospects (A) and high grade > 5g/t Au gold prospects (B) are bifractal in the Swayze greenstone belt. .... 59

Fig. 2- 10: Multi-distance cluster analysis (Ripley’s K-function) results showing the observed and expected spatial pattern for prospect distributions as a function of distance within permissive lithologies: mafic to intermediate metavolcanics rocks (A), and felsic to intermediate intrusive rocks (B). The observed spatial pattern (red) and the expected spatial pattern (black) curves are used to signify distance based spatial correlations. .... 62

Fig. 2- 11: Cumulative relative frequency curves showing distances of all gold prospects from faults ( $D(M)$ ), relative distances of non-prospects from faults ( $D(N)$ ), the upper statistical bound of non-prospect locations ( $Upper\_D(N)$ ) and the difference ( $D$ ) between prospects and non-prospect density distributions [(A) and (C)]. Graph of  $\beta$  -statistics of differences ( $D$ ) between the cumulative relative frequency of all prospects and non-prospects for distances from faults. The graph shows  $\beta$  -values as well as the intersection of the  $\chi^2$  significance level ( $\alpha=0.01$ ) [(B) and (D)]...... 64

Fig. 2- 12: Cumulative relative frequency curves showing relative distances of all gold prospects from  $D_1$  high strain zones ( $D(M)$ ), relative distances of non-prospects from  $D_1$  high strain zones ( $D(N)$ ), the upper statistical bound of non-prospect locations ( $Upper\_D(N)$ ) and the difference ( $D$ ) between prospects and non-prospect density distributions (A). Graph of  $\beta$  -statistics of differences ( $D$ ) between the cumulative relative frequency of all gold prospects and non-

prospects for distances from D<sub>1</sub> high strain zones. The graph shows  $\beta$  values as well as the intersection of the  $\chi^2$  at various significance levels ( $\alpha=0.10$  and  $0.9$ ) (B). ..... 67

Fig. 2- 13A: Cumulative relative frequency curves showing relative distances of all gold prospects from D<sub>2</sub> high strain zones ( $D(M)$ ), relative distances of non-prospects from D<sub>2</sub> high strain zones ( $D(N)$ ), the upper statistical bound of non-prospect locations ( $Upper\_D(N)$ ) and the difference ( $D$ ) between prospects and non-prospect density distributions (A). Graph of  $\beta$  - statistics of differences ( $D$ ) between the cumulative relative frequency of all gold prospects and non-prospects for distances from D<sub>2</sub> high strain zones. The graph shows  $\beta$  values as well as the intersection of the  $\chi^2$  at various significance levels ( $\alpha=0.01$ ) (B). ..... 68

Fig. 2- 14: Cumulative relative frequency curves showing relative distances of all gold prospects from D<sub>3</sub> high strain zones ( $D(M)$ ), relative distances of non-prospects from D<sub>3</sub> high strain zones ( $D(N)$ ), the upper statistical bound of non-prospect locations ( $Upper\_D(N)$ ) and the difference ( $D$ ) between prospects and non-prospect density distributions (A). Graph of  $\beta$  - statistics of differences ( $D$ ) between the cumulative relative frequency of all gold prospects and non-prospects for distances from D<sub>3</sub> high strain zones. The graph shows  $\beta$  values as well as the intersection of the  $\chi^2$  at various significance levels ( $\alpha=0.01, 0.05$  and  $0.95$ ) (B). ..... 69

Fig. 3- 1: A simplified regional geological map of the Archean Abitibi greenstone belt found within the Superior Province. The map shows the connection of the Swayze region to the Abitibi greenstone belt by a septum of mafic to ultramafic intrusive rocks (after Ayer et al., 2002, 2005). The thin black line is the outline of the Swayze greenstone belt. .... 95

Fig. 3- 2: A) Geological map of the Swayze greenstone belt (after Ayer and Trowel, 2002) showing D<sub>2</sub> and D<sub>3</sub> high strain zones, and locations of gold deposits. The corresponding stratigraphic section is shown on Appendix A. .... 96

Fig. 3- 3: Fry analysis of all orogenic gold prospects showing a general ESE -WNW and ENE-WSW trend of gold prospect orientations at various scales and grades after Maepa and Smith (2020).....	109
Fig. 3- 4: A) Simplified illustration of the architecture of radial basis function link nets (after Looney, 2002); B) Support vector machine architecture showing the optimum hyperplane for a two-class problem (after Zue and Carranza, 2011); C) Illustration of K-fold cross validation technique whereby k=5 subsets of training and validation data (Kubat, 2017).....	117
Fig. 3- 5: Proximity to permissive lithologies. ....	129
Fig. 3- 6: Proximity to lithological contacts .....	130
Fig. 3- 7: Proximity to D <sub>2</sub> and D <sub>3</sub> high strain zones. ....	134
Fig. 3- 8: Proximity to D <sub>2</sub> folds .....	135
Fig. 3- 9: Proximity to faults.....	136
Fig. 3- 10: The first vertical derivative of the 2 km upward continued RTP total magnetic intensity.....	139
Fig. 3- 11: Magnetic worms overlying the 2 km upward continued map.....	140
Fig. 3- 12: Proximity to magnetic worms. ....	141
Fig. 3- 13: Electromagnetic decay apparent conductivity map.....	143
Fig. 3- 14: Proximity to electromagnetic decay high apparent conductivities. ....	144
Fig. 3- 15: The bi-plots of the first and second principal component (A), first and third principal component (B) and a scree plot (C) for the logratio centered Swayze greenstone belt major oxide data.....	149
Fig. 3- 16: The first principal component PC1 of major oxide geochemistry. The geochemical data point locations are shown on Appendix D, E, and F.....	151

Fig. 3- 17: Spitz-Darling alteration index map. ....	152
Fig. 3- 18: Mineral prospectivity map derived from radial basis function neural networks learning with geochemistry predictor layers included. This prospectivity model was created using the prospect classification type 1. ....	156
Fig. 3- 19: Mineral prospectivity map derived from support vector machine with geochemistry predictor layers excluded. This prospectivity model was created using the prospect classification type 1. ....	157
Fig. 3- 20: Mineral prospectivity map derived from radial basis function neural network machine learning with geochemistry predictor layers included. This prospectivity model was created using the prospect classification type 1. ....	158
Fig. 3- 21: Mineral prospectivity map derived from support vector machines machine learning with geochemistry predictor layers excluded. This prospectivity model was created using the prospect classification type 1. ....	159
Fig. 3- 22: Training and validation plots from the radial basis function neural network models showing the mean training and validation accuracies, losses, and the standard deviation for RBFNN model with geochemistry (A and B) and RBFNN model without geochemistry (C and D). ....	160
Fig. 3- 23: The mean area under receiver operator curves for RBFNN models (A) and SVM models (C). and Feature importance scores derived from RBFNN (D) and SVM (D) models..	161
Fig. 3- 24: Comparison of the RBFNN and SVM prospective sites. The black boxed area shows predictions from both SVM and RBFNN and geological processes that may have contributed to the predictions. ....	162

Fig. 3- 25: The RBFNN mineral prospectivity map and predictor features; high strain zones, EM conductivities, magnetic worms and faults are shown on (A) and (B). The locations of new prospective regions (Target #1, Target #2 and Target #3) and existing mines and prospects (Joburke, Rundle, Jerome and Halcrow) are also overlain. .... 163

Fig. 3- 26: Mineral prospectivity map derived from the radial basis function neural network model with geochemistry predictor layers included. The prospectivity map indicates three potential targets in the area. This prospectivity model was created using the prospect classification type 2..... 166

Fig. 3- 27: Mineral prospectivity map derived from the support vector machines model with geochemistry predictor layers included. This prospectivity model was created using the prospect classification type 2..... 167

Fig. 3- 28: The mean area under receiver operator curves for RBFNN models and SVM models after k=10 subsets after training with prospect classification type 2..... 168

Fig. 3- 29: Feature importance estimations derived from the RBFNN and the SVM prospectivity models after training with prospect classification type 2..... 169

Fig. 3- 30: The RBFNN model showing prospectivity predictions overlain by faults and magnetic worms. The past producing Jorbuke mine and Kenty prospects are shown ..... 170

Fig. 3- 31: The high RBFNN model predictions are shown overlying the geological map of the Swayze with faults, EM conductivities, anomalous PC1 samples, and magnetic worms. The past producing Jorbuke mine and Kenty prospect are shown. .... 171

Fig. 3- 32: Comparison of current prospectivity maps with the weights of evidence prospectivity mapping results from Harris (2001). The mineral prospectivity maps of the southern Swayze

greenstone belt are shown side by side indicating prospectivity scores from weights of evidence (Harris et al., 2001) and the current radial basis function neural network study (right)..... 178

Fig. 4- 1 : Regional geological map of the Abitibi greenstone belt after Ayer et al (2002, 2005) showing the location of the Abitibi greenstone belt within the Superior Province, Canada. On the map, the locations of the Swayze greenstone belt and the Matheson greenstone belt are shown in a black and red outline, respectively. The E-W trending D<sub>2</sub> high strain zones are shown cutting across the Abitibi greenstone belt. .... 202

Fig. 4- 2: Geological map of the Swayze greenstone belt showing felsic to ultramafic intrusions and clastic metasedimentary rocks after Ayer and Trowell, (2002). The distributions of mineral deposits and mapped faults are overlain as points and polylines..... 205

Fig. 4- 3 : Geological map of the Matheson greenstone belt showing bedrock lithologies with felsic to ultramafic intrusions from a compilation of the Abitibi greenstone geology by Ayer et al. (1999). The map is overlain by mapped faults and mineral deposit distributions. .... 208

Fig. 4- 4 : Swayze region predictor maps derived from lithogeochemistry overlain by gold prospect locations. The maps show the distributions of principal component anomaly points overlain on the Swayze geological map (A), a proximity from PC1 anomalies map (B), a proximity from PC2 anomalies map(C), and a proximity from PC3 anomalies map (D). .... 214

Fig. 4- 5: The bi-plots of the first and second principal component (A), first and third principal component (B) and a scree plot (C) for the logratio centered Swayze greenstone belt major oxide data..... 215

Fig. 4- 6 : Swayze region predictor maps of distances from faults (A), a reduced-to-pole total magnetic intensity map (B), a reduced to pole total magnetic intensity map that has been upward continued to 2 km overlain by the derived magnetic worms (C), proximity to magnetic worms

(D), distances from high electromagnetic conductivity map (E), electromagnetic conductivity map (F), proximity to intrusive suites map (G), and the apparent magnetic susceptibility map (H). ..... 216

Fig. 4- 7 : Matheson region predictor layers showing the reduced-to-pole total magnetic intensity map (A), a 2 km upward continued reduced to pole total magnetic intensity map overlain by the derived magnetic worms (B), distances from faults (C), distances from magnetic worms (D), the apparent magnetic susceptibility map (E), and proximity to lithological contacts (F)..... 217

Fig. 4- 8 : Regional scale Fry analysis of gold deposit point distributions indicated using Fry translations and corresponding rose diagrams for the Swayze greenstone belt (A and B) and the Matheson greenstone belt (C and D). ..... 222

Fig. 4- 9 : Mineral prospectivity map created using a deep neural network with data from the entire Swayze region as defined on Table 4-4. .... 238

Fig. 4- 10 : Mineral prospectivity map created using the random forest algorithm with data from the entire Swayze regions defined on Table 4-4. .... 239

Fig. 4- 11: Deep neural network model performance metrics showing the training and validation accuracy plots (A) and the training and validation loss plot (B) for a model trained on the entire Swayze region with predictor layers shown on Table 4-4. .... 240

Fig. 4- 12 : A) Receiver operator curves derived from deep neural networks and random forest in the Swayze region. The curves with greater area under the curves indicate that the model’s predictive performance is greater. B) The feature importance plot estimations derived from deep neural networks and random forest graph shows how much each predictor variables contributed towards making prospectivity predictions for each machine learning method..... 242

Fig. 4- 13 : Deep neural network model performance metrics showing the training and validation accuracy plots (A) and the training and validation loss plot (B) for a model trained on the southern Swayze region generated for transfer learning from the south to the north Swayze regions with predictor layers shown on Table 4-4..... 244

Fig. 4- 14 : Mineral prospectivity map created using deep transfer learning from the southern to the northern Swayze regions. The southern prospectivity predictions is the colour image shown inside the dashed rectangle. The transfer learning prospectivity predictions in the northern Swayze region is shown in a solid rectangle. The area where the rectangles overlap (i.e., central Swayze region) is from the northern Swayze region transfer learning prediction results. .... 245

Fig. 4- 15 : Deep neural network model scores showing the training and validation accuracy plots (A) and the training and validation loss plot (B) for a model trained on the entire Swayze region for transfer learning from the Swayze region to the Matheson region with evidential layers defined on Table 4-4. .... 248

Fig. 4- 16 : The receiver operator curve metrics from a model pre-trained on the Swayze region for transfer learning shows an area under the receiver operator curve of 80%. .... 249

Fig. 4- 17 : The prospectivity predictions in the Matheson region obtained from the pre-trained (i.e., deep transfer learning) model in the Swayze region. .... 250

Fig. 4- 18 : The feature importance estimations derived from the deep transfer learning model and random forest on the pre-trained Swayze region. The plot shows how much each predictor variables contributed towards making prospectivity predictions for transfer learning from the Swayze to the Matheson region. .... 251

## List of Tables

Table 2- 1: A summary of the deformational events and associated structures in the Swayze greenstone belt. ....	26
Table 2- 2: Summary of the main gold deposits in the Swayze greenstone belt. ....	31
Table 2- 3 : Summary of the datasets used in the study and corresponding sources. ....	37
Table 2- 4: Results of spatial autocorrelation (Fry analysis) of gold deposits at varying gold grades (above and below the mean grade, 5 g/t Au) and varying scales of geological processes. ....	53
Table 2- 5: Comparison of Fry analysis spatial autocorrelations of gold deposit points and fault point orientations. The table show the primary orientations of gold deposits and mapped faults in the entire Swayze greenstone belt, the north, and south of the Swayze greenstone belt. The north and south of the Swayze greenstone belt are separated at 48° N. ....	56
Table 3 - 1 Key datasets used and corresponding description of types, formats and sources. ..	125
Table 3 - 2: List of evidential datasets and corresponding weight statistics from the weights of evidence model. ....	126
Table 3 - 3: Principal components of normalized lithogeochemical major oxide data from the Swayze greenston belt.....	148
Table 4- 1: A summary of the data used in the study from the Swayze greenstone belt and the Matheson greenstone belt. ....	213
Table 4- 2: The mineral exploration workflow that was followed in the study from data preprocessing to building deep learning models.....	220
Table 4- 3: Principal components of normalized lithogeochemical major oxide data from the Swayze greenstone belt. Shaded blocks show anomalous correlations between major oxide data and principal components. The corresponding principal component analysis data showing the	

amount of variance associated with each principal component of the major oxide datasets (results from Maepa et al., 2020)..... 235

Table 4- 4: A summary of evidential layers used for machine learning and transfer learning and the respective model performance accuracies of each analysis..... 236

## List of Appendices

Appendix A: A schematic stratigraphic section for the Swayze greenstone belt obtained from Breemen et al., 2006. The stratigraphic section was derived after Heather (2001) showing the U-Pb zircon ages for the northern, southern and central regions of the Swayze greenstone belt... 275	275
Appendix B: A Detailed description of the mineral deposit index files from the OGS 2019 file showing each prospect used in the Swayze greenstone belt study data..... 276	276
Appendix C: Tonnage and grade data for magmatic-hydrothermal gold deposits and prospects from the Abitibi and Swayze greenstone belt modified from Mathieu (2021)..... 288	288
Appendix D: Geological map of the Swayze greenstone belt overlain by geochemical sampling distribution. .... 291	291
Appendix E: A simplified architecture of a deep neural network ..... 292	292
Appendix F: A simplified architecture of transfer learning in mineral exploration targeting ... 293	293

# Chapter 1: Introduction to thesis

## 1.1 Research problem/ Research Motivation

The mineral exploration industry, academic institutions and government geological surveys collect massive amounts of data annually to help geoscientists better understand the geological controls of deposits and to find new targets. Studies of global exploration trends indicate that mineral exploration discovery rates have reduced dramatically despite increasing exploration spending (Schodde, 2004, 2017). This decrease can be attributed to most shallow targets having already been discovered, resulting in exploration being focused towards greater depths (McCuaig and Sherlock, 2017; Davies et al., 2020). Thus, studies that focus on understanding mineralization processes responsible for distributing deposits in the subsurface have become a key focus of mineral exploration targeting.

A scale-integrated mineral system approach that examines all geological processes responsible for distributing mineral deposits and associating these with their mappable expressions at surface is a crucial tool for exploration (McCuaig and Hronsky, 2014; Wyman et al., 2016; Groves et al., 2020). With increasing data collections and decreased deposit discoveries, geoscientists aspire to apply modern data science, spatial and statistical analysis techniques to assess this data and recognize trends in the data that are related to mineralization processes.

There is a need for more practical examples that apply the mineral systems concept as a conceptual modeling tool in conjunction with mineral prospectivity mapping to assist in finding new exploration targets. Mineral prospectivity mapping has been applied in the past to predict for new deposit targets using various machine learning tools (Agterberg, 1990; Bonham-Carter, 1994; Harris, 2002; Carranza, 2009; Rodriguez-Guliano et al., 2014). However, one of the drawbacks of

traditional machine learning approaches is that there is a requirement for adequate data for training machine learning algorithms into making data predictions. Consequently, mineral prospectivity mapping using machine learning is mostly applied in brownfield exploration environments that have adequate data for training and classification.

For mineral prospectivity mapping to be possible in greenfield environments, new methods such as transfer learning need to be considered. Transfer learning involves utilizing knowledge and parameters acquired from solving a prospectivity mapping problem in a well-understood brownfield environment and applying the pre-trained model knowledge to a new but related region (i.e., a greenfield site). This study aims to address the main research problems outlined by employing a mineral systems approach, scale – integrated spatial analysis methods, and mineral prospectivity mapping to ascertain the key geological controls of gold mineralization in the Swayze greenstone belt and to predict new exploration targets. Once this capability is established, this study further examines if deep neural networks and deep transfer learning can be applied in mineral exploration, whereby pre-trained deep learning models built from well understood geological settings can be used to make predictions in completely new regions with limited training data.

## 1.2 Objectives of the thesis

The objectives of this study are to use spatial statistical techniques to review the controls of gold mineral systems and to investigate machine learning approaches that could be helpful in recognizing magmatic-hydrothermal deposit targets in the Archean-age Abitibi greenstone belt, specifically two sub-belts known as the Swayze region and Matheson region. The main objectives of this study are:

- 1) To examine the controls of gold prospect distributions in the Swayze greenstone belt, Ontario, Canada, using multi-scale methods of spatial analysis.
- 2) To apply mineral prospectivity mapping in a manner consistent with the mineral systems approach for gold exploration targeting in the Swayze greenstone belt, using two machine learning methods (radial basis function neural networks and support vector machines).
- 3) To built deep learning models and apply deep transfer learning for exploration targeting in the Abitibi greenstone belt, specifically by learning mineralisation parameters in the Swayze area and using the learnt weight parameters to make predictions in an underexplored area, the Matheson region. The Matheson region is not sensu stricto a greenfield area, but it was treated as such in this study for the purpose of assessing how well a deep learning model previously trained on the Swayze region was capable of making new mineral prospectivity predictions in the Matheson region without prior knowledge of the distribution of deposits, prospects, and showings in the Matheson region.

### 1.3 Background

The study is conducted within the southern Abitibi greenstone belt in Ontario and Quebec, eastern Canada. The Abitibi greenstone belt is the largest Neoarchean greenstone belt in the world consisting of E-W trending, folded volcanic and sedimentary rocks units with intervening intrusive rocks (Thurston et al., 2008; Monecke et al., 2017). The lithological units in the Abitibi greenstone belt consist of east-trending ultramafic to felsic rocks that are interbedded with sedimentary rock of ages ranging between 2795 – 2695 Ma (Dubé et al., 2017; Monecke et al., 2017).

The belt hosts a wide range of commodities associated with volcanogenic massive sulfide deposits and orogenic gold deposits (Monecke et al., 2017). The structures within the Abitibi greenstone belt are dominated by brittle-ductile fault zones or high strain zones that trend in an E-W fashion, including the Porcupine-Destor and Cadillac-Larder fault zones which are north or south dipping and almost subvertical at the surface (Poulsen, 2017; Monecke et al., 2017). These high-strain zones and associated second- and third-order faults have been recognized to host major orogenic gold deposits in the Abitibi greenstone belt (Dubé et al., 2017).

The orogenic gold deposits in the Abitibi greenstone belt are also spatially associated with highly deformed rocks that have been metamorphosed to greenschist facies (Dubé et al., 2017). The current study mainly focuses on the Swayze region (also referred to as the Swayze greenstone belt) and the Matheson region found within the Abitibi greenstone belt. The Swayze region is the southwestern extension of the Abitibi greenstone belt about 70 km southwest of the city of Timmins, Ontario with the Matheson region a comparable distance to the east of Timmins (Ayer, 1995; Heather, 2001; Ayer and Trowell, 2002; Breemen et al., 2006).

Details of the geology and mineral deposits, prospects, and showings in the Swayze and Matheson regions in the Abitibi greenstone belt are discussed in Chapters 2, 3, and 4.

#### 1.4 Structure of thesis

This thesis is presented in a manuscript style with five chapters, three of which represent research articles that have been published and/or are currently under review in international peer-reviewed journals. Chapters 2, 3, and 4 were written as stand-alone manuscripts for publication in

scientific research journals, and therefore, the geological background presented in these chapters is repetitive.

The first chapter, Chapter 1, is this introductory chapter that outlines the overall research problem, the objectives and structure of the thesis.

Chapter 2 is written as a manuscript entitled “**Examining the controls on gold deposit distribution in the Swayze greenstone belt, Ontario, Canada, using multi-scale methods of spatial data analysis**” and has been published in *Ore Geology Reviews* (accepted 6 July 2020, *Ore Geology Reviews*, 125, <https://doi.org/10.1016/j.oregeorev.2020.103671>). This chapter evaluates the spatial controls of orogenic gold prospects found in the Swayze greenstone belt at various scales using spatial data analysis techniques such as Fry, fractal, and distance-based Ripley’s K-Function analysis. The distribution on gold prospects and their spatial alignment are evaluated to infer the fractal nature of mineral prospects, the geological features that correlate with and controlled mineral prospect alignments at regional, district to local scales. The chapter further evaluates the degree of cluster of prospects within mineralization camps. Understanding the major mineralization controls and the scales at which they operate is instrumental for the objective selection of predictor layers to use in exploration targeting and mineral prospectivity mapping.

Chapter 3 is written as a manuscript entitled “**Support Vector Machine and Artificial Neural Network Modelling of Orogenic Gold Prospectivity Mapping in the Swayze greenstone belt, Ontario, Canada**” and has been published in *Ore Geology Reviews*, 130, <https://doi.org/10.1016/j.oregeorev.2020.103968>. This chapter reviews magmatic-hydrothermal mineral systems and their involvement in gold distributions and endowment in the Swayze greenstone belt. The chapter also outlines how ore forming processes that make up a mineral system can be translated into mappable expressions in geoscience data which can later be used for

mineral prospectivity mapping. In this chapter, a spatial statistical probabilistic approach- weights of evidence and two machine learning techniques (support vector machines and radial basis function neural networks) are employed to help generate mineral prospectivity maps. The weights of evidence method were used to determine spatial correlations between gold prospects and input predictor maps and to objectively select suitable predictor maps for mineral prospectivity mapping. This aids an exploration geoscientist to understand which data are most important predictors of gold prospects.

Chapter 4 is written as a manuscript entitled “**Investigating the applications of Deep Neural Networks, Random Forest, and Transfer Learning in the Abitibi greenstone belt, Canada**” and is currently under review with the journal *Ore Geology Reviews* (submitted March 2021). This chapter evaluates deep neural networks as a potential tool for exploration targeting and compares the results obtained from deep neural networks with the random forest classifier. Furthermore, this chapter applies the concept of transfer learning to exploration targeting and outlines the procedure of training a deep learning model on the Swayze region and using the acquired knowledge from the Swayze regions (source domain) to make predictions for gold prospectivity in the Matheson region (target domain) without prior knowledge of prospect distributions in the Matheson region. Using a variance-based feature importance function the most influential layers used by the machine learning algorithms were also derived.

Each chapter has its own set of conclusions, but Chapter 5 brings these together and summarizes the main research conclusions.

#### 1.5 Innovative nature of the thesis (statement of original contributions)

Chapter 2 is a spatial data analysis study evaluating how the distribution of mineral prospects can provide critical information of metallogenic processes at multiple scales and the

results helps to validate common assumptions about controls of gold prospects. Although similar spatial analytical studies have been done elsewhere (Blenkinsop, 1995; Vearncombe and Vearncombe, 1999; Kreuzer et al., 2007; Mamuse et al., 2010; Lisitsin, 2015), this chapter applies the methods over the Swayze region with the goal of exploring the assumptions made by previous workers (Heather, 2001; Breemen et al., 2006) about the significance of structures in the Swayze region.

This chapter also examines the fractal nature of gold prospect distributions and how the fractal behaviour can be used to illustrate the factors that control gold mineralization in the Swayze region at regional to local scales. The study uses spatial autocorrelation techniques (Fry analysis) to help statistically estimate the primary distribution of mineral-prospects by grade values and their spatial correlations with faults at local to regional scales. Modelling mineral deposit distributions and fault correlations statistically helps to confirm and build upon previous work by statistically emphasizing the impacts of structures and lithological features on the distribution of gold showings in the Swayze region. The results from spatial analysis techniques such as Fry analysis and directional distribution were subsequently used for prospectivity analysis studies in chapter 3 and 4. Chapter 2 helped to delineate prominent fault orientations that are spatially and statistically associated with gold mineralization.

Chapter 3 discusses orogenic mineral systems in conjunction with mineral prospectivity mapping for mineral exploration targeting. Although mineral prospectivity mapping has been done in the past over the Swayze region by Harris et al (2001), the current study builds on Harris et al., (2001) work by 1) applying the mineral systems approach and demonstrating their expressions from historical geoscience work, 2) using robust machine learning models, support vector machines and artificial neural networks that have never been applied in the Swayze region, 3)

using python programming-language-based machine-learning algorithms which allowed the authors to use the latest data science techniques (such as stratified K-Fold cross validation, feature importance estimations, and data balancing procedures) to help reduce uncertainty and bias in the prospectivity modelling procedures.

Feature importance estimations have never been done when artificial neural network models are used to derive mineral prospectivity maps. However, De Sar (2019) has recently developed an algorithm that allows for determination of important features from artificial neural networks predictions. The variance-based feature-importance algorithm for artificial neural networks was applied to mineral exploration targeting to demonstrate the influence of each predictor layer. These results were impactful in helping to reduce the black-box nature of machine learning algorithms. Both the ANN and SVM prospectivity models predicted new targets and the feature importance estimates helped to rank the influence of predictor layers used by the machine learning models.

Chapter 4 explores building deep neural network and transfer learning models for mineral exploration targeting. Traditionally, machine learning requires that the locations of already known prospects used for the training data lie within the same regional area as the predictor maps. This is hard to do when dealing with greenfield environments that do not have enough training data to build machine learning classifiers. This chapter resolves this machine learning problem by developing a deep transfer learning model that was first trained on mineral deposits, prospects and showings in the Swayze region (as a source domain), the learned weights and parameters are saved and later used to make predictions on a completely new region, the Matheson area (target domain). Deep transfer learning is an original research project and is a fairly new concept that has no known published applications in mineral exploration targeting. In Chapter 4, the authors outlined the steps

for preparing the data and also discuss the limitations faced when deriving transfer-learned prospectivity maps.

An anonymous reviewer gave the following review on the third chapter of the thesis: *“The manuscript ‘‘Investigating the applications of Deep Neural Networks, Random Forest, and Transfer Learning for exploration targeting in the Abitibi greenstone belt, Canada’’ addresses the very important issue of transfer learning in machine learning applied to mineral potential mapping. This reviewer has been involved in several mineral potential evaluation studies over the last 15 years. The issue of applying machine learning done in one area to another similar area (i.e., transfer learning) is one of the most commonly asked questions by exploration geologists involved in mineral potential evaluation projects. Another commonly asked question is the importance of individual evidential layers in the final mineral potential model. In many machine learning algorithms, it is difficult to know which inputs are the most responsible for the results. This important issue is investigated by the authors, very successfully. As such, the paper would be a worthwhile contribution to these important issues.’’*

All three chapters in this thesis work together to tell a story of how historical geoscience data can be used to decipher new information that could potentially help in making future exploration decisions. The models derived in this study are based on current understanding and classifications of mineral deposits. The Swayze region contains more prospects and showings than actual deposits, some deposits are still currently being studied, and hence some gold deposit classification types may change as new research is being conducted and the current mineral prospectivity maps would then need to be refined to fit the new deposit models.

## 1.6 References

Agterberg, F.P., Bonham-Carter, G.F., Wright, D.F., 1990. Statistical pattern integration of mineral exploration. In Computer Applications in Resource Estimation Prediction and Assessment for Metals and Petroleum, Gaal, G., Merriam, D.F., eds., Pergamon Press, Oxford, 1 - 21.  
<https://doi.org/10.1016/B978-0-08-037245-7.50006-8>

Ayer, J., 1995. Precambrian geology northern Swayze greenstone belt. Ontario Geological Survey, Open File Report 297, 1- 57. Available from:

<http://www.geologyontario.mndmf.gov.on.ca/mndmfiles/pub/data/imaging/R297//r297.pdf>

[Accessed: 14 April 2020]

Ayer J.A., Trowel N.F., 2002. Geological compilation of the Swayze area, Abitibi greenstone belt; Ontario Geological Survey, Preliminary Map P.3511, scale 1:100 000. Available from:

<http://www.geologyontario.mndm.gov.on.ca/mndmfiles/pub/data/records/P3511.html>[Accessed:

14 April 2020].

Bonham-Carter, G.F., 1994. Geographic Information Systems for Geoscientists: Modelling with GIS. Computer and Geosciences. Pergamon, New York, 416 p. ISBN: 9780080418674

Breemen., O.V., Heather., K.B., Ayer., J.A., 2006. U-Pb geochronology of the Neoproterozoic Swayze sector of the southern Abitibi greenstone belt. Geological Survey of Canada, 1 -32.

<https://doi.org/10.4095/223016>

Blenkinsop, T. G., 1994. The fractal distribution of gold deposits: two examples from the Zimbabwe Archean craton. In: Kruhl J.H (eds) Fractals and Dynamic Systems in Geosciences.

Springer, Berlin, Heidelberg, 247 – 258. [http://dx.doi.org/10.1007/978-3-662-07304-9\\_19](http://dx.doi.org/10.1007/978-3-662-07304-9_19)

Carranza, E.J.M., 2009. *Geochemical Anomaly and Mineral Prospectivity Mapping*, 1st Edition. ed. Elsevier Science, Amsterdam, 368 p.

Davies, R.S., Groves, D.I., Trench, A., Dentith, M., 2020. Towards producing mineral resource-potential maps within a mineral systems framework, with emphasis on Australian orogenic gold systems. *Ore Geology Reviews*, 119, 103 – 369.

<https://doi.org/10.1016/j.oregeorev.2020.103369>

De Sá, C.R., 2019, Variance -based feature importance in neural networks, in Novak, P.K., Šmuc, T., DŽeroski, S., eds, *Discover Science 2019: Switzerland*, Springer Nature, 306 – 315.

<https://doi.org/10.1007/978-3-030-33778-0>

Dubé, B., Mercier-Langevin, P., Ayer, J., Atkinson, B., Monecke, T., 2017. Orogenic greenstone-hosted quartz-carbonate gold deposits of the Timmins-Porcupine camp. In: Monecke, T., Mercier-Langevin, P., Dube, B. (eds.), *Archean base and precious metal deposits, southern Abitibi greenstone belt, Canada*. Society of Economic Geologists, *Reviews in Economic Geology* 19, 51 - 79

Groves, D.I., Santosh, M., Zhang, L., 2020. A scale-integrated exploration model for orogenic gold deposits based on a mineral systems approach. *Geoscience Frontier*, 11, 719 – 738.

<https://doi.org/10.1016/j.gsf.2019.12.007>

Harris, J.R., 2002, *Processing and integration of geochemical data for mineral exploration: application of statistics, geostatistics and GIS technology*, PhD Thesis, University of Ottawa.

Heather, K., 2001. *The geological evolution of the Archean Swayze greenstone belt, Superior Province, Canada*. PhD Thesis. Keele University.

Kreuzer, O.P., Blenkinsop, T.G., Morrison, R.J., Peters, S.G., 2007. Ore controls in the Charters Towers goldfield, NE Australia: Constraints from geological, geophysical, and numerical analysis. *Ore Geol. Rev.* 32, 37 – 80.

Lisitsin, V., 2015. Spatial data analysis of mineral deposit point patterns: applications to exploration targeting. *Ore Geol. Rev.* 71, 861 – 881.

<https://doi.org/10.1016/j.oregeorev.2015.05.019>

Mamuse, A., Porwal, A., Kreuzer, O., and Beresford, S., 2010. Spatial statistical analysis of the distribution of komatiite-hosted nickel sulfide deposits in the Kalgoorlie terrane, Western Australia: clustered or not?. *Econ. Geol.* 105, 229 -242.

<https://doi.org/10.2113/gsecongeo.105.1.229>

McCuaig, T.C., and Hronsky, J.M.A., 2014, The mineral system concept: the key to exploration targeting., in Karen, D.K., Kelley, H.C.G., ed., *Building Exploration Capability for the 21<sup>st</sup> Century*, Society of Economic Geologists, Special publication 18, 153–175.

<https://doi.org/10.5382/SP.18.08>

McCuaig, T.C., Sherlock, R.L., 2017. Exploration Targeting. In Tschirhart, V., Thomas, M.D., ed., *Proceedings of Exploration 17: Sixth Decennial International Conference on Mineral Exploration*, 75 – 82.

Monecke, T., Mercier-Langevin, P., Dube, B., Frieman, B, 2017b. Geology of the Abitibi greenstone belt. In: Monecke, T., Mercier-Langevin, P., Dube, B. ed., *Archean base and precious metal deposits, southern Abitibi greenstone belt, Canada*. Society of Economic Geologists, *Reviews in Economic Geology*, 19, 7–49.

Poulsen, K.H., 2017, The Larder Lake-Cadillac Break and its gold districts: *Reviews in Economic Geology*, 19, 133–167.

Rodriguez-Guliano, V.F., Chica-Olma, M., and Chica-Rivas, M., 2014. Predictive modelling of gold potential with the integration of multisource information based on random forest: a case study on the Rodalquilar area, Southern Spain: *International Journal of Geographical Information Science*, 28, 1336 – 1354.

Schodde, R. C., 2004. Discovery performances of the western world gold industry over the period 1985–2003. PACRIM 2004 Proceedings, Melbourne.

Schodde, R., 2017. Long term trends in global exploration-Are we finding enough metals? In: 8th Fennoscandian Exploration and Mining Conference. Levi, Finland. 1–66.

Wyman, D.A., Cassidy, K.F., Hollings, P., 2016. Orogenic gold and the mineral systems approach: resolving fact, fiction, and fantasy. *Ore Geology Reviews*, 78, 322–335.

## Chapter 2: Examining the controls on gold deposit distribution in the Swayze greenstone belt, Ontario, Canada, using multi-scale methods of spatial data analysis.

### 2.1 Abstract

Understanding the spatial controls on mineral deposit and prospects is crucial in mineral exploration targeting. This paper uses a combination of spatial data analysis techniques, such as the distance distribution method, Fry, nearest neighbor index, Ripley's K-function multi-distance, and fractals to better define controls on the distribution of gold prospects in the Swayze greenstone belt, Ontario, Canada. According to results obtained with the distance distribution method, D<sub>2</sub> deformational zones were critical in controlling the spatial distribution of the gold mineralization, with 97% of the orogenic gold deposits occurring within 7 km distances from deformational zones (and 65% within 4 km). Fry analysis confirmed this spatial relationship with a close agreement between the orientations of the D<sub>2</sub> structures and gold deposit alignment. The outcome of Ripley's K-function cluster analysis suggests that gold deposits occur within 4 km distances of other gold deposits. These findings are consistent with the results from the fractal analysis, showing that gold deposit distribution is bifractal and that different geological features occurred at local (< 8 km) versus regional (> 8 km) scales. We conclude that higher-order D<sub>2</sub> structures and lower-order faults connected to the D<sub>2</sub> -related structures acted as pathways to focus gold-bearing hydrothermal

fluids, thus leading to the observed concentration and distribution of orogenic gold deposits at the regional to local scales.

Keywords: Fractals, Fry Analysis, Distance Distribution, Swayze Greenstone Belt, Gold.

## 2.1 Introduction

Understanding the spatial controls of mineral systems is an essential aspect of mineral exploration targeting. In well-mineralized and explored brownfields areas where the distribution of mineral deposits is relatively well known, spatial statistical tests can help develop a better understanding of the underlying metallogenic processes and their potential role in controlling the distribution of these deposits at various scales. Spatial statistical techniques that have been applied to the study of mineral deposit location point pattern data include: i) point pattern analysis (Getis and Boots, 1978; Ord and Getis, 1992; Diggle, 2003), ii) distance distribution analysis (Berman, 1977), iii) Ripley's K-function analysis (Ripley, 1977, 1981; Mamuse et al., 2010; Agterberg, 2013; Dixon, 2002), iv) fractal analysis (Blenkinsop and Sanderson, 1999; Mandelbrot, 1983; Carlson, 1991; Raines, 2008), and v) Fry analysis (Fry, 1979; Hanna and Fry, 1979; Vearncombe, 1999, Carranza, 2009).

Spatial statistical techniques such as Fry analysis have been instrumental in helping exploration geologists better define the spatial distribution of mineral deposits and reveal spatial

trends of critical metallogenic processes, thereby providing valuable tools for exploration targeting (Vearncombe and Vearncombe, 1999, 2002; Kreuzer, 2007; Carranza, 2009; Lisitsin, 2015).

Mineral deposits are small-scale expressions of much larger, non-random, crustal-scale geological processes that, as a whole are often referred to as a mineral system (Knox-Robinson and Wyborn, 1994; Wyman et al., 2016). According to the mineral systems approach (Wyborn et al., 1994), certain geological processes collectively act at various spatial scales to extract metals from large-scale source regions and concentrate them in favorable lithological and structural traps to form mineral deposits (Wyborn et al., 1994; McCuaig et al., 2010). Whilst the critical and constituent processes of the mineral system cannot be mapped, the associated geological expressions, commonly referred to as targeting elements and mappable proxies, can be identified and conveyed using available geoscience data (Wyborn et al., 1994).

Mineral deposits are also said to display fractal properties making them scale invariant (Blenkinsop and Sanderson, 1999). Fractals were first introduced by Mandelbrot (1983) to evaluate the ability of point patterns to exhibit scale invariance, complexity, and self-similarity (Cheng et al., 1996; Cheng, 1997). Prominent examples of fractal analyses designed to evaluate the spatial controls on mineral deposits include the studies by Turcotte (1986), Carlson (1991), Blenkinsop and Tromp (1995), Blenkinsop (2004), Raines (2008), Cheng (2008), Carranza, (2009) and Agterberg (2013).

Assessments of hydrothermal mineral systems and associated mineral deposit distributions indicate that mineral deposits display fractal, bifractal and/or multifractal characteristics linked to the geological processes that collectively occur to concentrate them to favorable locations (Cheng,

2008; Agterberg, 2013; Ord et al., 2016; Lester et al., 2012). The spatial analysis techniques discussed above are now widely accepted and play an important role in furthering our understanding of the spatial distribution of deposits and underlying geological controls (Raines, 2008; Mamuse et al., 2010; Agterberg, 2013). Point patterns can display three major characteristics: complete spatial randomness, clustering, and regular patterns (Diggle 1983; Getis and Boots, 1978).

Ore-forming processes tend to result in a clustering of deposits (Goldfarb et al., 2001) and the degree of clustering and dispersity of mineral deposits can reveal important information about possible underlying geological controls involved (Singer and Menzie, 2008; Mamuse et al., 2010). For example, Mamuse et al. (2010) assessed the geological controls on nickel sulfide deposits using nearest neighbor and K-function analysis, the results revealed that komatiite bodies containing nickel deposits displayed clustering behavior while the nickel deposits themselves displayed random distributions within their komatiitic host lithologies.

Assessing the clustering behavior of gold deposits within specific host lithologies is vital in distinguishing the geological controls on gold mineralization. The objectives of this study, which set out to use spatial statistical methods to examine the controls on gold deposit distribution in the Swayze greenstone belt, were to i) evaluate the controls on the spatial distribution of the orogenic gold deposits in this belt at various scales, using Fry analysis, ii) determine the fractal properties of the orogenic gold deposits to better understand the underlying geological processes, iii) determine the relationships between gold deposit point patterns and their structural and lithological controls using K-function and nearest-neighbor analyses, and iv) determine the density

distribution of mineral deposits along structures and high-strain zones (HSZ) using the distance distribution method.

## 2.2 Geology, deformation, and gold mineralization

### 2.2.1 Geological setting

The Swayze greenstone belt is located in the south-central portion of the Superior Province of Ontario, Canada (Fig. 2-1). The historic classification of the Swayze greenstone belt as a discrete lithostructural entity that is separate from the adjacent Abitibi greenstone belt is no longer tenable (Breemen et al., 2006) given the commonalities among depositional ages and rock assemblages in both belts (Ayer et al., 2002). Instead, the Swayze greenstone belt is now widely regarded as the southwestern extension of the gold endowed Abitibi greenstone belt (Heather, 2001; Ayer et al., 2002; Breemen et al., 2006; Thurston, 2008).

The Swayze greenstone belt, can be divided into a northern (above 48°N) and southern (below 48°N) segment, which is bounded by the Nat River granitoid complex in the north, the Ramsey-Algoma granitoid complex in the south, the Kenogamissi granitoid complex to the east and the Kapuskasing structural zone to the west (Heather 2001; Breemen et al., 2006). The northern Swayze greenstone belt is connected to the southwestern Abitibi greenstone belt by a narrow septum of volcano-sedimentary rocks associated with the Slate Rock HSZ (Breemen et al., 2006).

Geological mapping and geochronological work by Heather (2001) and Ayer et al (2002) demonstrate that the Swayze greenstone belt has a regular upward facing autochthonous regional

stratigraphy (Breemen et al., 2006). Six stratigraphic groups (Appendix A) were recognized by Heather (2001). From oldest to youngest, these are the Chester, Marion, Biscotasing, Trailbreaker, Swayze, and Ridout group. There also exists synvolcanic, syntectonic and post-tectonic intrusions with ages spanning from  $2739 \pm 2$  Ma to  $2568 \pm 4$  Ma that are discussed in detail by Breemen et al., (2006).

The oldest rocks are found in the Chester group which is dated at  $2739 \pm 1$  Ma and consists of mafic volcanics rocks overlain by sedimentary rocks and iron formations that have been disrupted by younger diorite and tonalite intrusions from the Kenogamissi granitoid complex (Breemen, 2006). The Chester intrusive complex hosts the low-grade high tonnage Côté Au(-Cu) deposit found in the southeastern regions of the Swayze greenstone belt (Kontak et al., 2013; Katz, 2016, Smith, 2016).

The overlying Marion group has U-Pb dates ranging from 2754 to 2724 Ma and is composed of mafic to intermediate volcanic rocks in the Strata Lake and Woman River formation capped by oxide-facies ironstone rocks (Heather 2001; Breemen et al., 2006). The volcanic rocks in the upper portions of the Woman River formation are variably chloritized and sulphidized in crackle breccia zones, interpreted pathways for paleo-hydrothermal fluids that precipitated in the overlying ironstones (Breemen et al., 2006). In the overlying Biscotasing group, with ages at  $2715 \pm 2$  Ma, there exists highly strained and amphibolite facies metamorphosed mafic to felsic metavolcanics rocks, chert-magnetite iron formation and clastic metasedimentary rocks (Breemen et al., 2006).

The overlying Trailbreaker group consists of mafic to intermediate volcanic rocks that are dated at  $2705 \pm 2$  Ma while the overlying Swayze group is dated at 2695 to 2703 Ma with rock assemblages consisting of mafic to ultramafic volcanic flows and sills as well as volcanoclastic and clastic sedimentary rocks. In the central portion of the Swayze greenstone belt, there is a notable depositional gap between the Marion Group and the overlying Trailbreaker group (Heather, 2001; Breemen et al., 2006).

At the top of the Swayze stratigraphic succession lies the Ridout group consisting of younger sedimentary and volcanic rocks aged at 2742 – 2670 Ma spatially associated with D<sub>2</sub> and D<sub>3</sub> high strain zones (Breemen et al, 2006), discussed below. The Chester, Marion, Biscotasing, Trailbreaker, Swayze group and Ridout groups have been correlated with coeval assemblages across the southern Abitibi such as the Pacaud, Deloro, Kidd-Munro, Tisdale, Blake River and the Timiskaming assemblages respectively by Ayer et al (2002). A detailed explanation of each lithostratigraphic groups and intrusive events is discussed in Breemen et al. (2006).

The 2690 to 2680 Ma period is regarded as the most tectonically active with demonstrated regional scale deformation and changes in sedimentation. The rocks of the Ridout Group were confined and restricted to the linear basins defined by E-ESE striking D<sub>2</sub> high strain zones and F<sub>2</sub> synclinal fold axes (Heather, 2001). Heather (2001) suggests that deformation in this period is characterized by orogen-wide shortening.

### 2.2.2 Exploration history in the Swayze greenstone belt

The Swayze greenstone belt (Fig. 2-2) comprises a range of intrusive and extrusive rock types, including felsic to ultramafic volcanic, and chemical and clastic sedimentary rocks with depositional ages ranging from 2740 to 2695 Ma (Heather, 2001; Breemen et al., 2006). Unlike the Abitibi greenstone belt (*sensu strictu*), which is richly endowed with respect to orogenic gold deposits, base metal (i.e., Cu, Pb, Zn), Ni, and Fe deposits, and industrial minerals (such as asbestos, talc and silica), the Swayze greenstone belt is regarded as poorly endowed (Ayer, 1995; Heather, 2001; Breemen et al., 2006). This perception has resulted in relatively low levels of exploration investment in the Swayze greenstone belt compared to the Abitibi greenstone belt (Hastie, 2017). However, the recent discovery of the world-class, high tonnage, low-grade Côté Au(-Cu) deposit with total measured and indicated resources (inclusive of reserves) of 6.5 million ounces and grades of 0.98 g/t Au suggests that the Swayze greenstone belt may be more prospective than previously assumed (Kontak et al., 2013; Katz et al., 2015; Katz, 2016; Smith, 2016; Katz et al., 2017; Hastie, 2017; Hastie et al., 2020; IAMGold Corporation, 2021).

The geological work undertaken in the Swayze greenstone belt includes: i) detailed mapping of the entire Swayze greenstone belt carried out by Heather (2001) as part of an academic study, ii) mapping and data compilations by Ayer (1995) and Ayer et al. (2002), and iii) a previous mineral prospectivity map of the Swayze greenstone belt generated by Harris et al. (2002) using geological and geochemical data; iv) there is currently a new remapping project as part of a PhD study by Gemmel and some field results are published in Huagaard et al. (2017); v) there is an ongoing PhD research study by Hastie on the Kenty, Namex, Jerome and Rundle deposits and

work by Hastie et al (2020) gives evidence of gold remobilization in the Kenty and Jerome deposits. There are also recent and ongoing geophysical work involving reflection seismic and magnetotelluric surveys currently being done over the Swayze greenstone belt by the Metal Earth project (Cheraghi et al., 2020; Gill et al., 2021).

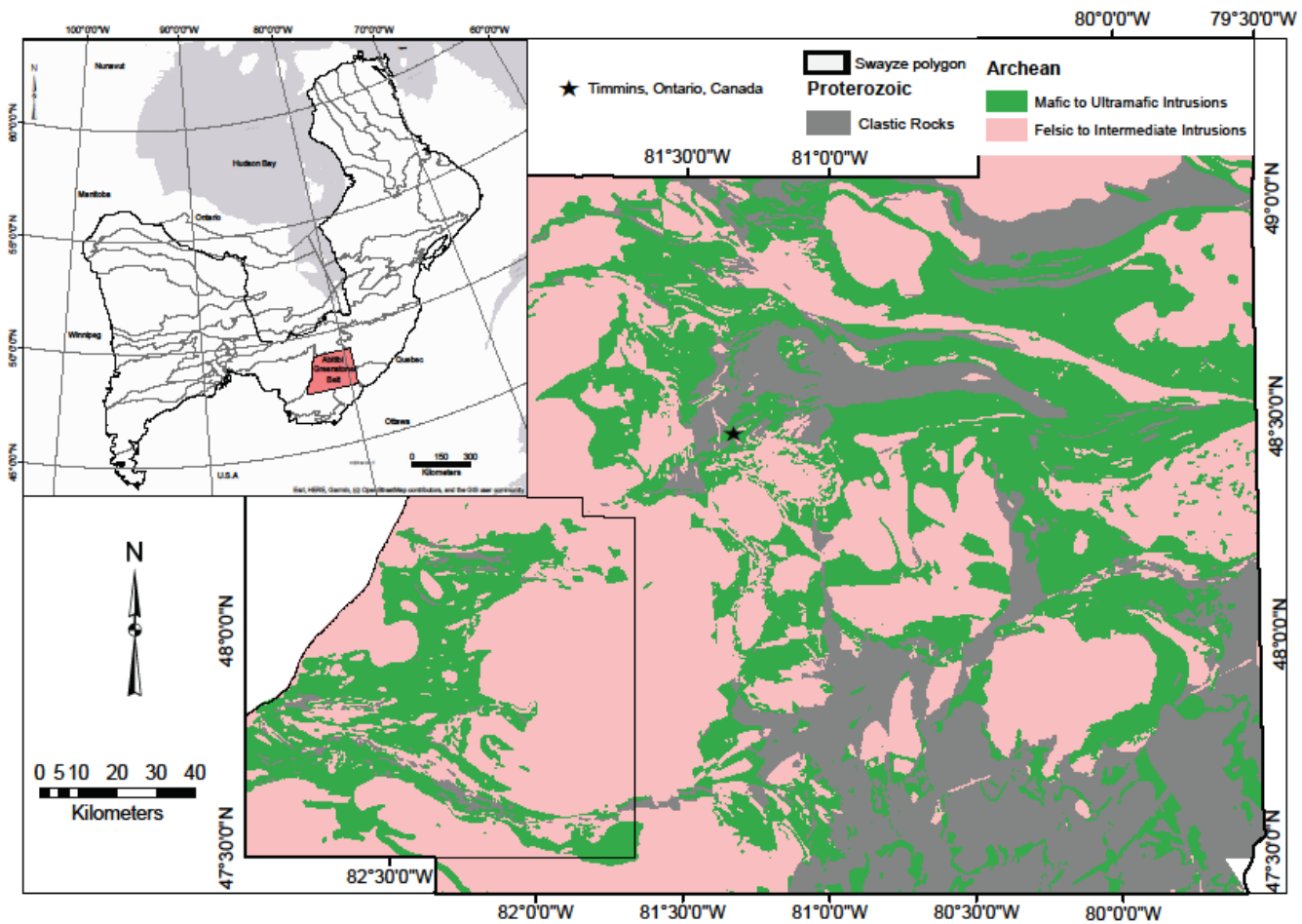


Fig. 2- 1 Regional geological map of the Abitibi greenstone belt after Ayer et al (2002, 2005) showing the location of the Abitibi greenstone belt within the Superior Province, Canada, and the narrow septum of Archean volcanic intrusive rocks connecting the Swayze to the Abitibi greenstone belt.

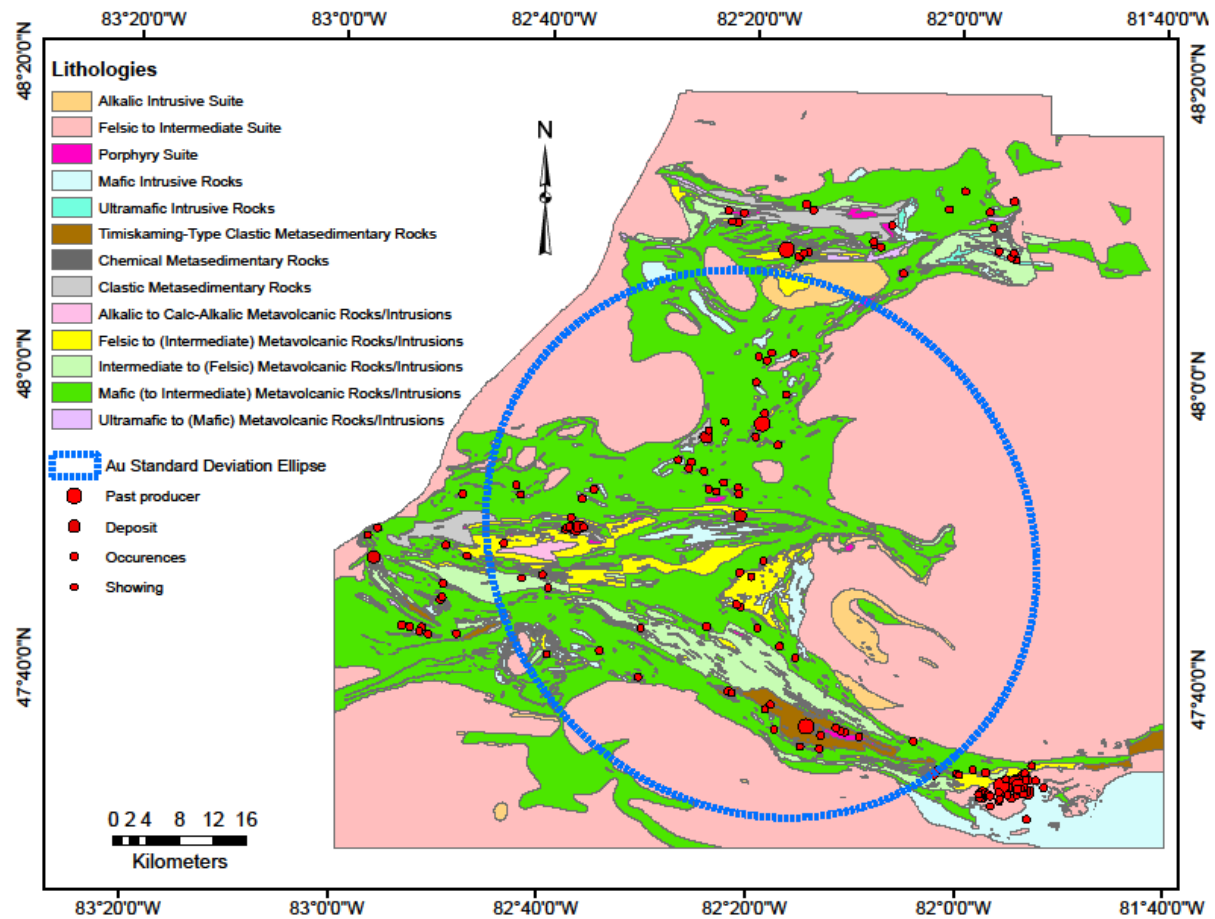


Fig. 2- 2: Geological map of the Swayze greenstone belt showing felsic to ultramafic intrusive rocks and clastic metasedimentary rocks (Ayer and Trowell, 2002). The locations of orogenic gold deposit are displayed in red circles and an overlying standard deviation ellipse shows the orientation of the mineral deposits.

### 2.2.3 Deformation history

The Swayze greenstone belt underwent several deformational events and recorded a complex structural history as attested by multiple generations of foliations, faults, and folds of different orientations. Heather (2001) identified multiple fabric elements such as foliations and cleavages, illustrating multiple crosscutting overprinting relationships and suggesting a range of relative ages from synvolcanic to syntectonic to late tectonic.

Heather (2001) also recognized > 60 high-strain zones ranging from < 1 m to > 10 m in width. The multiple deformational events recognized in the Swayze greenstone belt range in age from 2740 to 2660 Ma. The deformational events resulted in folding, foliation, regional shearing, and brittle faulting (Heather, 2001). The high-strain zones are dominantly E- to ESE-striking but N- to NE-striking high-strain zones also exist. The Swayze greenstone belt deformational events and associated structural features are summarized in Table 2-1 (Fig. 2-3). Milne (1972) suggested that the E- to ESE-striking (90 - 112.5 degrees) Porcupine-Destor fault zone, known to host gold within or in its vicinity, extends from the Abitibi into the northern Swayze greenstone belt where it is known as the Slate Rock HSZ (Bleeker et al., 2014).

The southern Swayze greenstone belt is cut by the D<sub>2</sub> Ridout HSZ which Heather (2001) believed to be an extension of the Cadillac-Larder fault zone found to host numerous deposits in the Abitibi greenstone belt to the east (Atkinson, 2013). This paper will mostly focus on the early 2700 – 2680 D<sub>2</sub> and 2680 -2670 D<sub>3</sub> deformational events because the timing of these deformations is thought to have been synchronous with orogenic gold mineralization (Heather, 2001).

Table 2- 1: A summary of the deformational events and associated structures in the Swayze greenstone belt.

Deformational event	Igneous events	Timing [Ma]	Associated structures	Principal orientations
D <sub>1</sub> Event	Chester Group		McOwen high strain zone	N-S striking (000 - 180 degrees)
	Marion Group	2750 – 2700	Fawn high strain zone	NE-striking (45 degrees)
	Biscotasing Group Synvolcanic intrusions Trailbreaker Group		F1 folds	E - ESE plunging (90 - 112.5 degrees)
D <sub>2</sub> Event	Swayze Group	2700 – 2680	Slate Rock high strain zone	ENE -WSW (067.5 - 247.5 degrees)
	Syntectonic intrusions		Ridout high strain zone	ESE – WNW (112.5 - 292.5 degrees)
	Ridout Group		Brett lake high strain zone	ESE – WNW (112.5-292.5 degrees)
			Swayze lake high strain zone	ESE – WNW (112.5 -292.5 degrees)
			Rollo high strain zone	ENE -WSW (067.5 - 247.5 degrees)
			Biscotasing high strain zone	ESE -striking (112.5 - 292.5 degrees)
			Rundle high strain zone	ESE – WNW (112.5 - 292.5 degrees)
			F2 folds Brittle fractures	E – ESE plunging (90 - 112.5 degrees) ESE -striking (112.5 degrees)
D <sub>3</sub> Event	Syntectonic intrusions	2680 -2670	Wakami high strain zone	NE-striking (45 degrees)
	Post-tectonic intrusions		Newtown high strain zone	NE-striking (45 degrees)
	Ridout Group		Hardiman high strain zone	NE-striking (45 degrees)
			Brittle fractures	ENE striking (067.5 - degrees)

## 2.2.4 Characteristics of the gold deposits

### 2.2.4.1 Gold deposits of the SGB

The Swayze greenstone belt hosts a variety of gold deposit types whose genesis is poorly understood. The gold deposits in the Swayze greenstone belt have been subdivided into five categories: i) Intrusion-related deposits, such as the Côte Au(-Cu) deposit which is hosted within a multi-phase, subvolcanic intrusive complex (Kontak et al., 2013; Rodgers et al., 2013; Katz, 2016; Smith, 2016; Katz et al., 2017) ; ii) current ongoing research by Kontak and Hastie suggests the Rundle, Jerome and Namex are possibly intrusion-related (instead of the previous “mesothermal gold” classification by the 2019 mineral deposit index and the Fumerton and Houle, (1995)); iii) greenstone hosted deposits, such as the Kenty, that are typically hosted in tholeiitic iron-rich basalts (Hastie, 2017); iv) Banded iron formation (BIF) hosted deposits, such as the 4K deposit (Fumerton and Houle, 1995); and v) auriferous VMS deposits such as the Shunsby (Heather, 1998; Ayer et al., 2005).

The current gold deposit, prospect, and showings classifications in the Swayze greenstone belt are subject to change because there is still detailed deposit-scale analyses that need to be done, similar to what is taking place at the Côte Au(-Cu) deposit. Although prospects and showings in the southeastern Swayze greenstone belt and in the vicinity of the Côte Au(-Cu) deposit were said to display orogenic-style mineralization (Rodgers et al., 2013), structural geology work by Smith (2016) indicates that auriferous veins found within the Chester intrusive complex in the

southeastern Swayze greenstone belt are genetically related to the intrusion-related Côté Au(-Cu) deposits.

Furthermore, detailed structural mapping by Smith (2016) indicates that the auriferous veins pre-dated the 2700 Ma regional deformational structures associated with the D<sub>2</sub> Ridout high-strain zones. Work by Katz et al., (2020) suggests that the gold prospects in the southeastern Swayze greenstone belt represent porphyry-type gold deposits. The prospects in the southeastern Swayze greenstone belt are found within quartz veins and the tonalite-diorite units of the 2740 Ma Chester intrusive complex (Katz, 2016; Smith, 2016). Table 2-2 and appendix B provides a summary of the known orogenic and intrusion-related gold deposits in the Swayze greenstone belt.

#### 2.2.4.2 Orogenic and intrusion-related gold deposits

Several magmatic-hydrothermal gold systems exist in the Swayze greenstone belt, specifically orogenic and intrusion-related gold deposit style of mineralization. Intrusion-related gold deposits are a group of deposits primarily hosted within or nearby intrusions and represent a distinct group of magmatic-hydrothermal systems (Sillitoe et al., 1988; Sillitoe, 1991; Thompson et al., 1999; Lang and Baker, 2001). Several features commonly seen in intrusion-related gold deposits are that they occur in metaluminous, subalkalic intrusions of intermediate to felsic compositions that lie near the boundary between ilmenite and magnetite series (Sillitoe, 1991; Hollister, 1992; Baker, 2001).

Intrusion-related gold deposits are associated with carbonic hydrothermal fluids; metal assemblages comprise of Au±Bi±W±Te±As±Mo and/or Sb as well as low concentrations of base metals; and the general inferred tectonic setting is convergent plate boundaries such as in back-arc, collisional, post-collisional and magmatic arc environments (Sillitoe, 1991; Hollister, 1992; Lang et al., 1997; Thompson et al, 1999; Baker, 2001; Lang and Baker, 2001). The intrusion-related gold deposits genetic model includes a multiphase igneous complex comprising of batholiths, plutons, domes and/or dikes and sills that were rapidly emplaced (Lang and Baker, 2001).

The igneous intrusions are subalkalic, metaluminous I-type intrusions that contain significant ilmenite and minor magnetite and have a reduced oxidation state (Lang and Baker, 2001). The intrusion-related gold systems are CO<sub>2</sub> rich and deposits show pervasive sericite, feldspathic, greisen, silicic, calc-silicate and argillic alteration signatures (Touret, 19992; Lang and Baker, 2001). The deposits are also characterized by patterns of zonation that Hart et al (2000) placed into three categories based on spatial relationship to intrusions, namely: the intrusion-hosted deposit zone, proximal deposit zone and the distal deposit zone (Lang and Baker, 2001).

According to Lang and Baker (2001), some intrusion-hosted deposits show strong structural influence. Early regional-scale structures are seen to have controlled emplacement of magmas while the CO<sub>2</sub> magmatic-fluid contents are said to account for the brittle-ductile strain at district scales (Lang and Baker, 2001).

Orogenic gold deposits (Groves et al., 1998, 2003) represent a diverse group of deposits widely considered to form in accretionary or, less commonly, collisional tectonic environments at

depths of > 4 km, typically late in the structural history of the host terrane with gold mineralization characteristically linked to compressive deformation and regional greenschist to amphibolite facies metamorphic conditions (Calvert and Ludden, 1999; Groves et al., 1998, 2020; Gaboury, 2019).

The known examples of orogenic gold deposits formed during Archean to Phanerozoic times and have a diverse metal association characterized by Au ± Ag, As, Bi, Sb, W, and Te with low-levels of Pb, Zn (Groves et al., 2020; Pitcairn et al., 2006). Proposed sources of gold and hydrothermal fluids include metamorphic devolatilization of a subducted oceanic slab that overlies a sulfide-rich sedimentary package (Groves et al., 2020). The hydrothermal fluid is low-salinity, CO<sub>2</sub>-H<sub>2</sub>O (+CH<sub>4</sub>, N<sub>2</sub>) and aqueous-carbonic fluid that carries gold

Structures in orogenic mineral systems are critical because they act as conduits for fluid migration from metamorphic dehydration zones in the lower crust to metal precipitation zones in the upper crust (Gaboury, 2019). Studies of Archean orogenic gold deposits (Groves et al., 1998, 2003; Goldfarb et al., 2001; Pirajno, 2009) similar to those in the Swayze greenstone belt show that orogenic gold can be hosted in a variety of rock types, mainly in ultramafic, mafic, and felsic igneous rocks as well as banded iron formation and other sedimentary rocks.

According to Table 2-2, and apart from intrusion related gold and gold-rich VMS deposits, the gold deposits in the Swayze greenstone belt are characteristic of orogenic gold deposits hosted in a variety of sedimentary, volcanic, and intrusive rocks that have been metamorphosed to greenschist and amphibolite facies with the gold deposits commonly found in spatial proximity to brecciated, sheared and highly strained deformational zones (Fumerton and Houle, 1991; Hastie et al., 2015, 2016).

Table 2- 2: Summary of the main gold deposits in the Swayze greenstone belt.

Deposit	Classification	Host rocks	Structural features	Metamorphism	Alteration and mineralogy	Other details	Literature
Jerome	Orogenic	Hosted along sheared contact between altered monzonitic rocks (feldspar porphyry rocks) and the intruded polymictic conglomerates.	Within the D <sub>2</sub> Ridout HSZ. Mineralization is within the contacts, sheared and brecciated rocks.	Regional, greenschist metamorphism	Carbonate, silicification, biotitic, hematitic, and chloritic alterations.	Au occurs in quartz-carbonate veins, it also lies within shear zones and fracture-controlled pyrite veins that are folded.	Fumerton and Houle (1991,1995); Hastie et al., (2015, 2017); Hastie et al., (2020)
Kenty	Orogenic	Deposit is within quartz veins and in pillowed, iron-rich tholeiitic basaltic rocks	Mineralization is emplaced along a system of fractures, joints and breccias.	Regional, Greenschist	Quartz-feldspar veins are associated with alteration halos ankerite-albite-sericite-pyrite-chlorite.	Au is associated with carbonate alteration, disseminated pyrite and quartz veins.	Fumerton and Houle (1995, page 224); Hastie et al., (2020)
Namex	Intrusion-related Au	Feldspar porphyry unit and altered polymictic conglomerate.	Within the D <sub>2</sub> Ridout high strain zone.	Regional, greenschist metamorphism	Extensional veins consist of quartz-ankerite-tetrahedrite	Low grade gold: in disseminated pyrite within feldspar porphyry. Higher grade Au (0.2ppm) associated with tetrahedrite and telluride veins.	Fumerton and Houle (1991,1995); Hastie et al (2017); Hastie et al., (2020)
Côté Au-(Cu)	Intrusion related Au	Au is disseminated in low Al-tonalite, diorite and quartz diorite intrusions plus magmatic and hydrothermal breccia bodies.	There are small (< 3 m) E-W trending deformational zones associated with the Ridout high strain zone that occurs 3 km north of the deposit.	Regional greenschist facies metamorphism	Extensive biotite alteration along Au-Cu hydrothermal breccia bodies is partially overprinted by fracture-controlled muscovite alteration.	The deposit is low-grade and high tonnage with inferred resource of 6.5 million ounces of Au	Kontak et al., (2013); Rodgers, (2013); Smith, (2016); Katz et al. (2017)

Rundle	Intrusion related Au	Quartz veins, feldspar Porphyry stock (diorite) and SE trending sheared ultramafic to mafic metavolcanics.	Tight to isoclinal and west plunging F1 folds overprint the feldspar porphyry dikes.	Regional, greenschist, post mineralization	Silicification. sericite, chlorite, and feldspar alterations are found along mafic metavolcanics and metasedimentary rocks.	Au is associated with early fracture-controlled pyrite veins.	Love and Roberts (1991); Fumerton and Houle (1991, 1995); Hastie (2017); Hastie et al., (2020)
Joburke	Orogenic	Quartz-carbonate veins, metavolcanics (basalt), and near quartz feldspar porphyry and quartz-albite-carbonate vein.	Joburke deformational zone and the Slate Rock high strain zone, and along the McKeith lake fault.	Regional greenschist metamorphism	Dominantly Fe-carbonate and weak chlorite alterations	The quartz carbonate veins are associated with disseminated iron sulfides.	Fumerton and Houle (1991, 1995); Hastie et al., (2015, 2016).
Orofino	Orogenic	Quartz veins and replacement ore deposits whereby diorite is strongly sheared, altered, and contains 5 to 25% sulfides	Deposit located in the nose of a regional fold anticline that plunges to the west.	Regional greenschist metamorphism	Carbonatization and chlorite alterations	Associated minerals: Pyrite, chalcopyrite, galena, sphalerite	Fumerton and Houle (1991, 1995)
Chester 2 Zone	Possibly Intrusion-related	Hosted in deformed quartz-sulfide veins and granodiorite felsic intrusive rocks.	Deposit hosted within a NE- trending shear zone.	Regional greenschist metamorphism	Chloritic, biotitic, carbonatization, pyritic and supergene malachite and azurite alterations	Associated minerals: chalcopyrite, molybdenite, gold, telluride, bornite, covellite, pyrrhotite	Fumerton and Houle (1991, 1995)

#### 2.2.4.3 Scale-integrated spatial analysis

There are multiple factors that introduce variations in gold deposits at prospect to deposit-scales which has led various authors (Groves et al., 2003; McCuaig and Hronsky, 2014; Wyman et al., 2016; Groves et al., 2020) to suggest a scale-integrated approach in mineral exploration that considers common regional to district-scale controls as essential to the distribution of gold deposits. Researchers agree that the most critical elements of a mineral system are geodynamic setting, fertility, crustal architecture, and preservation factors (Groves et al., 2020; McCuaig and Hronsky, 2014). To best understand the primary controls on mineralization, it is important that mineral systems be considered at all scales, from their broad geodynamic setting to the scale of individual deposits (Groves et al., 2020).

At the province scale, features such as first-order lithospheric-scale faults reflect the geodynamic setting of the region and act as fluid pathways (Groves et al., 2020). According to Groves et al (2020), second-order faults are found proximal to lithospheric-scale pathways, along zones of weaknesses such as lithological contacts where they act as the main fluid focusing mechanisms towards district scales. At deposit scales, third-order structures further focus mineralization fluids to their depositional sites where rheological contrast between fluid and lithologies help to facilitate metal precipitation (Groves et al., 2020). When incorporating a mineral-system approach to deposit distributions, it is important to recognize that fertile tectonic settings have the potential for multiple mineral systems types to form in these settings (e.g., intrusion-related and orogenic gold deposits such as is the case in the Swayze greenstone belt).

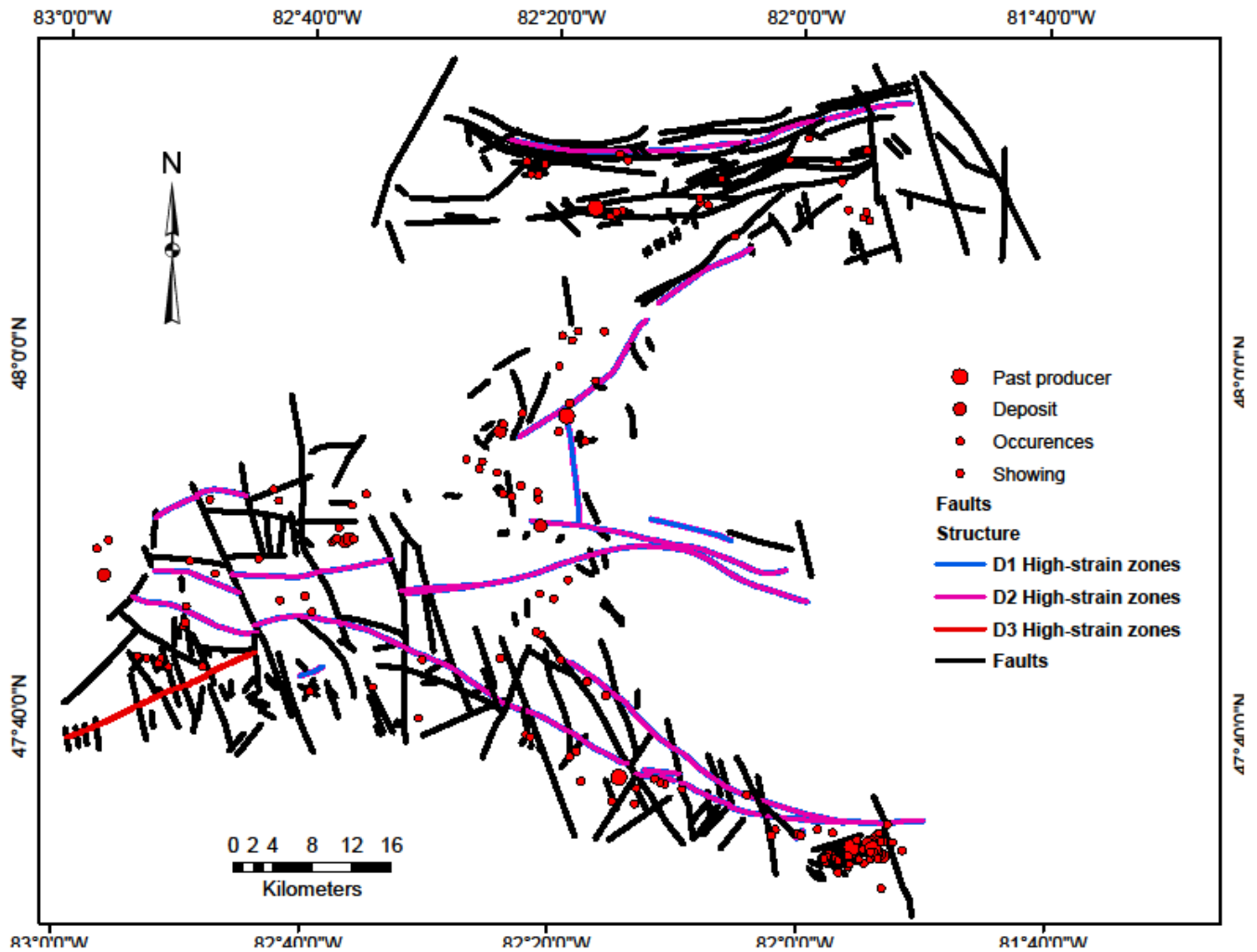


Fig. 2- 3: Structural features covering the Swayze greenstone belt with overlying red circular points representing past producing mines, gold deposits, showings, and gold occurrences.

### 2.3 Data

This study used publicly available mineral occurrence, structural, geological, and geophysical data provided by the Ontario Geological Survey (OGS) and Geological Survey of Canada (GSC) summarized on Table 2-3. A mineral deposit index (Appendix B) containing descriptions and locations of mineral deposits, prospects, and showings in the Swayze greenstone belt (Fumerton and Houle, 1995) was used to show locations of gold deposits in this study. According to the definitions of Fumerton and Houle (1999b): i) “showings” represent traces of mineralization observed in core or outcrop, ii) “prospects” represent ores that were mined on a trial basis, and iii) “deposits” represent gold accumulations for which a reserve has been calculated.

To remove the bias caused by having a single ore body represented more than once in the mineral deposit inventory, the point data were thinned so that no two points can be found less than 500 meters from each other (Lisitsin, 2015); this resulted in the deposit point data used being reduced from 124 to 108. Analysis for district (> 2 km) to regional-scale (> 10 km) geological controls was done on this thinned dataset. However, the analysis was replicated on the original data (124 points) since this was expected to provide more detailed information at scales < 500 m.

The geographic coordinates of prospects, occurrences, showings, and mines are shown as a single point representing the midpoint of the mineralization projected to surface rather than the area (i.e., polygon) it encompasses. The gold grades are reported in grams per ton with all 124 gold deposits, prospects and showings containing grades ranging between 0.02 to 43 g/t of gold (Fumerton and Houle, 1995). Overall, the gold deposits, prospects and showings have an average

grade of 5.5 g/t, which was used as a marker for distinguishing between high and low gold grade gold mineralization.

A grade vs tonnage plot for the Abitibi and Swayze greenstone belts modified from Mathieu (2021) with the Joburke, Rundle, and Orofino prospects added is shown on Fig. 2-4. The plot highlights the low-grade and high tonnage Côte Au-(Cu) and Malartic deposits as well as the high-grade Kirkland Lake deposits found in the Swayze and Abitibi greenstone belts. According to the grade vs tonnage plots, the deposits and prospects from the Swayze and Abitibi greenstone belt show average grades ranging between 5 and 8g/t Au. The details of the deposits and prospects shown on Fig. 2-4 are shown on Appendix C.

To avoid confusion, the term “prospect” is used collectively in this study to refer to all classifications from showing to mine.

The mineral deposit index files used in this study are publically available data obtained from the Ontario geological survey. The data representing a deposit, prospect and showing of gold has been populated by the OGS following decades of field work and exploration by workers in the Swayze greenstone belt. A summary of the deposits, prospects and showings of gold in Appendix C shows the classifications of each prospect based on field evidence, assay results and field relationships.

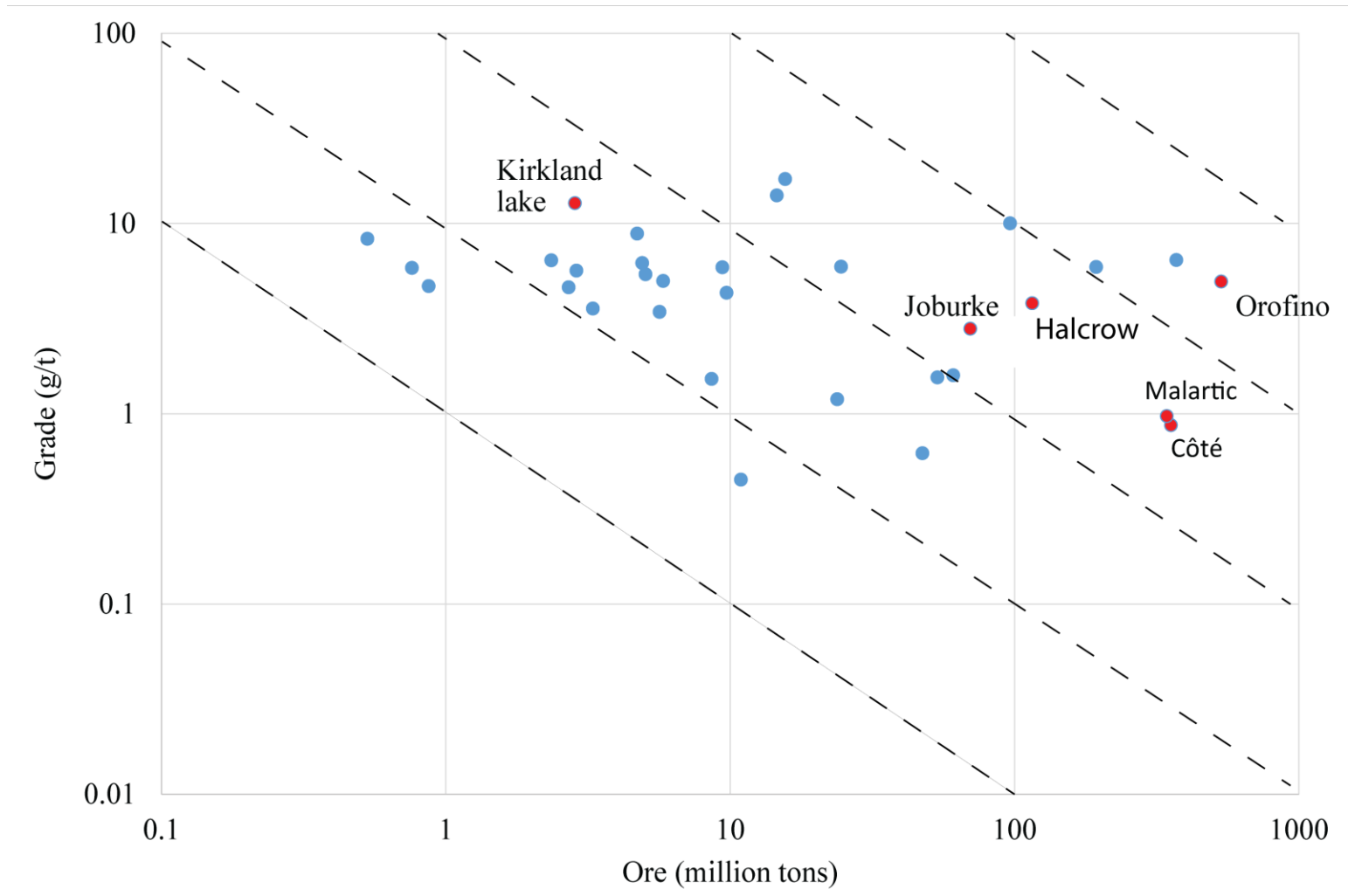


Fig. 2- 4: Grade vs tonnage plot for deposits and prospects in the Abitibi and Swayze greenstone belts. The plot is modified from Mathieu (2021).

Table 2- 3 : Summary of the datasets used in the study and corresponding sources.

Dataset	Type	Format	Source	Data description
Mineral prospects	Gold deposits, mines, prospects, and occurrences	GIS vector (points)	Ontario Geological Survey	A mineral deposit inventory data compiled by Fumerton and Houle (1995, 2010) and updated yearly by the Ontario Geological Survey
Geology	Bedrock geology mapped at 1:100 000 scale	GIS vector (polygons)	Ontario Geological Survey	Geological mapping by Heather (2001); compilation map by Ayer et al (2002) and Breemen et al., (2006)
Geophysics	Magnetic (1st and second order derivative maps, and analytical signal map)	Grid	Geological Survey of Canada grid	200 m line-spacing total intensity map
Structures	High strain zones, faults, and shears	GIS vectors (polylines)	Ontario Geological Survey	Structural data covering the Swayze greenstone belt mapped in the field and interpreted using aeromagnetic data

## 2.4 Methodology: Spatial analysis applied to mineral prospects

It is crucial that the relationship between the distribution of known mineral deposits and structures be analyzed to shed more light on which structures may have acted as conduits for hydrothermal fluid flow and help better define areas that may be prospective. Four methods were applied in this study to help evaluate the spatial patterns of known orogenic gold occurrences and their spatial associations with faults and deformational zones: Fry analysis, fractal analysis, point pattern analysis and the distance distribution method. The spatial distribution of gold prospects was assessed in this study based on the scale of geological processes for gold prospect (i.e., local, camp and district to regional-scales), and the grade of gold prospects, whereby controls of low grade ( $< 5.5\text{g/t Au}$ ) and high grade ( $> 5.5\text{g/t Au}$ ) gold prospect distributions are assessed separately.

### 2.4.1 Fry Analysis

Fry analysis (Fry, 1979), originally designed to evaluate the strain directions in rocks, can also be used to analyze the spatial autocorrelation of point patterns whereby  $n$  data points will result in  $n^2 - n$  translations (Hanna and Fry, 1979). An especially useful application of Fry analysis in exploration targeting is its ability to help determine the spatial relationships of known mineral prospects and structures (faults and shears) for gold prospects that are structurally controlled.

Fry analysis has been applied at regional scales to infer large-scale metallogenic controls (Kreuzer et al., 2007; Austin and Blenkinsop, 2009; Lisitsin, 2015); however, applications also include determining the orientations of ore controls, and the spacing and grade distributions at deposit scales (Vearncombe and Vearncombe, 1999; Carranza, 2009; Lisitsin, 2015).

Fry analysis can be done using specialized point distribution software or manually by drawing points on paper and overlying it with tracing paper and using the tracing paper to mark each point as an origin for translations. All the points on the first sheet of paper will serve as one of multiple origins on the tracing paper and the positions of the remaining points are recorded with respect to each of these origins. For  $n$  points, there are  $n^2-n$  translations created and the point translations are referred to as 'Fry plots' (Vearncombe and Vearncombe, 1999; Carranza, 2009).

The Fry analysis undertaken in this study was done using the SpaDIS (developed by Julian Vearncombe) and DotProc (developed by Aleksey Kuskov) software packages. The spatial autocorrelations of point patterns representing mineral prospects and their corresponding rose diagrams are generated to show the principal orientations of mineral prospects at various scales and ore grade values.

#### 2.4.2 Fractal Analysis

Fractals were first introduced by Mandelbrot (1983) with fractal analysis used to evaluate a point distributions ability to exhibit scale invariance. This is done by checking if the patterns

look the same at different cell sizes (i.e., scales). Objects that display fractal characteristics are said to have the same geometric structures at various spatial scales hence, the fractal dimension ( $D_f$ ), fractals in nature can display monofractal, bifractal or multifractal characteristics (Ord et al., 2016). Monofractals display a single value of  $D_f$ , bifractal objects are characterized by having two fractal dimensions while multifractals have more than two  $D_f$  values (Carlson, 1991; Cheng and Agterberg, 1995; Blenkinsop and Sanderson, 1999; Agterberg, 2013).

The two commonly used fractal modelling methods are the cluster density fractal analysis model and the box-counting method. In the density cluster technique (Feder, 1988), circles of different radius  $r$  are drawn around all points in the study area and the number of point patterns that lie within these circles is counted and then averaged for each different value of  $r$  (Feder, 1988; Carlson, 1991; Agterberg, 2013). The resulting average value  $N(r)$  is assumed to be in the form:

$$N(r) = C r^{Dc}, \quad (1)$$

proportional to  $r^{Dc}$  where  $Dc$  is the cluster fractal dimension and  $C$  is a constant of proportionality (Carlson, 1991; Blenkinsop, 1994; Blenkinsop and Tromp, 1995; Agterberg, 2013). The second most used fractal analysis method is the box-counting method made popular by Mandelbrot (1985) and first applied by Carlson (1991) to evaluate the spatial distribution of precious metal ore deposits in the western United States. The box-counting method divides the area of a point pattern dataset up into small cells and considers a larger box with a variable side-length  $r$  and the number of cells  $N(r)$ , containing one or more points are counted and averaged for all positions. If the point distribution is scale invariant (i.e., fractal), the relationship is checked to see if it obeys a power-law function equation (Feder, 1988; Mandelbrot, 1983; Blenkinsop, 1995) of the form:

$$N(r) = C r^{-D_f} \quad (2)$$

where  $C$  is a constant of proportionality and the power  $D_f$  is the fractal dimension, which varies between 0 and 2, whereby 2 represents no clustering (or dispersity) and progressively lower values approaching 0 represent increasing clustering (Blenkinsop, 2004). This paper uses the box-counting method to determine fractal nature of mineral-prospect distributions in the Swayze greenstone belt. The power-law relationship can be represented on a log-log graph with the equation:

$$\log nN(r) = \log C - D_f \log r \quad (3)$$

If the distribution of a point pattern is fractal, the  $N(r)$  versus  $r$  plot on a log-log scale will show a straight line with a slope of  $-D_f$ . If the slope of the line is kinked, the point where the kink in the graph appears represents a box size,  $r$ , where one geological process overtakes another in determining the fractal nature of the point-pattern distribution. Fractal dimensions can be used in mineral exploration to determine the scales of geological processes that impacted the distributions of mineral deposits (Carranza, 2009).

Fractal analysis of point pattern distributions plotted on a log-log plot are subjected to a roll-off or censoring whereby the point distribution shows a low number of features at lower size ranges making it hard to fit the straight line (Blenkinsop and Sanderson, 1999; Vearncombe, 1999, 2000) while features at higher size ranges are subject to truncation (Vearncombe, 1999, 2000, 2001). Blenkinsop (1994, 2004) suggests that roll-off is caused by the lack of information and data

regarding smaller prospects or mines, and on the history of deposit discovery (where exploration is usually concentrated around known deposits).

The roll-off effect can be modelled with a larger sample size using a continuous curve; however, roll-off on a smaller sample size may give false bifractal results (Raines, 2008; Agterberg, 2013). Because roll-off and truncation effects are commonly seen on log-log fractal plots, Vearncombe (1999, 2000, 2001) suggested that fractal dimensions should be determined at the central portions of the data range where a good linear slope can be extracted. The degree of fit of the straight line is quantified by the  $R^2$  values and generally, the higher the coefficient of determination ( $R^2$ ) the better the model fits the data. However, since  $R^2$  does not determine if the regression model is accurate, a standard error (SE) of the regression slope is also calculated. The standard error determines the average distance that the observed values deviate from the regression line. It is assumed in this paper that a high  $R^2$  and low  $SE$  means a higher accuracy in the fitted regression that represents fractal behavior.

#### 2.4.3 Point-Pattern Analysis (Ripley's K-Function analysis)

The locations of mineral deposits are regarded as expressions of stochastic geological processes and as such, point pattern analysis can be used to determine their distributions and relationships with each other (Porwal, 2006; Singer and Menzie, 2008; Mamuse et al., 2010; Lisitsin, 2015). Patterns of point distributions are often tested for complete spatial randomness using a variety of distribution methods (Ripley, 1977). Point patterns can be evaluated using density-based methods such as kernel density smoothing (Silverman, 1986) and high/low

clustering methods (Ord and Getis, 1992) as well as distance-based methods that include nearest neighbor analysis (Ebdon, 1988) and multi-distance K-function analysis (Ripley, 1977, 1981).

Distance-based analysis of point patterns such as K-function and kernel density estimations are especially useful in mineral exploration because they evaluate point data characteristics at various scales and densities (Mamuse et al., 2010) and give a good direct description of second-order properties of a point pattern (O'Sullivan and Unwin 2003). In exploration targeting, point patterns representing the locations of mineral deposits are examined to check for: i) Clustered point patterns of mineral deposits that may reveal a relationship to related geological features or processes that concentrate mineralization fluids towards the same locations, ii) a random point pattern representing deposits that resulted from independent unrelated processes occurring by chance and iii) a dispersed (non-random) point pattern of mineral prospects that reveal processes involving the circulation of metallogenic fluids towards favorable but related locations (Diggle, 1983; Getis and Boots, 1978; Carranza, 2009). The point patterns representing mineral prospects in the Swayze greenstone belt were analyzed using i) the multi-distance spatial cluster analysis (Ripley K- Function analysis) to evaluate point pattern characteristics at various scales.

#### 2.4.3.1 Multi-distance spatial cluster analysis (Ripley' K- function analysis)

Ripley's K-function analysis is a distance-based method that analyzes cumulative distances of point patterns at a specified radius and compares the point pattern distribution with a theoretically defined randomly distributed point pattern that displays complete spatial randomness (Ripley, 1977; Zuo et al., 2009; Mamuse et al., 2010). The multi-distance spatial cluster analysis found in

ArcGIS is based on the Ripley's K-function analysis of evaluating the point patterns distribution by summarizing whether point patterns are clustered, dispersed or randomly distributed within a user-defined distance range (Bailey and Gatrell, 1995; Getis, 1984; Mitchel, 2005). The multi-distance Ripley's K-function in GIS is calculated at multiple distances to show how the distributions of points can vary within various scales, the Ripley's K-function ( $L(d)$ ) and expressed as:

$$L(d) = \sqrt{\frac{A \sum_{i=1}^n \sum_{j=1, j \neq i}^n k_{i,j}}{\pi n(n-1)}}, \quad (4)$$

where  $d$  is the distance,  $A$  is the total study area containing the  $n$  features being evaluated and the weight ( $k_{(i,j)}$ ) (Bailey and Gatrell, 1995). The output analysis from the  $L(d)$  method is a plot showing the relationship between the observed curve for the point pattern and the expected curve for complete spatial randomness at various distances. The Ripley's K-function analysis has been used in mineral exploration to evaluate the distribution of known mineral-prospect locations, to assess whether prospect locations display clustering or dispersed characteristics at various scales and within various host lithologies (Mamuse et al., 2010; Agterberg, 2013). Furthermore, analysis of point pattern distribution with respect to host lithologies can shed light on the geological controls of mineralization (Mamuse et al., 2010). This study seeks to analyze the spatial distributions of mineral prospects with respect to host lithologies in the Swayze greenstone belt.

#### 2.4.4 Evaluating spatial correlations of mineral prospects and geological features using distance distribution method

A conceptual modelling technique for deriving optimal distances for a set of mineral deposits, prospects, and occurrences to occur from certain geological features was evaluated for data covering the Swayze greenstone belt. The distance distribution analysis methodology described by Carranza (2009) is used to assess different geological features (lithologies and faults) and their spatial association with the occurrences of orogenic gold prospects using buffer (or proximity) analysis methods commonly found in GIS (Bonham-Carter, 1985; Berman, 1986; Carranza, 2009).

Various geological features were evaluated for spatial proximity with gold by creating multiple buffer zones of varying cumulative distances from the geological feature to a set of mineral-prospect locations (represented as  $D(M)$ ) and cumulative distances from a set of features to a random set of point locations (represented as  $D(N)$ ), representing non-prospects (Carranza, 2009). A randomly generated set of points was used to test the null hypothesis, the random set of points were created using a GIS tool. This tests the assumption that mineral prospects occur due to non-random geological processes that have acted dependently resulting in mineral deposition. For example, for an orogenic gold prospect to exist, there has to be a specific (non-random) source of heat, hydrothermal fluid circulation, deformational zones and faults to act as fluid pathways, and a disturbance in the metal ligand complexes to facilitate the deposition of gold. A graph of  $D(M)$  and  $D(N)$  are compared using Kolmogorov-Smirnov statistics to test the null hypothesis that

there is no spatial association between the distance from a set of mineral prospect points and geological features (Berman,1986; Carranza, 2009), where:

$$D = D(M)-D(N) \quad (6)$$

If the graph of  $D(M)$  is greater than or plots above the graph of  $D(N)$ , then  $D$  becomes positive (i.e.,  $> 0$ ), which means distances between mineral prospect locations and a set of geological features are spatially correlated. Conversely, if the graph of  $D(N)$  plots above  $D(M)$ , the value of  $D$  will be negative (i.e.,  $< 0$ ) indicating that there is no spatial association. An upper confidence band for the graph of  $D(N)$  is computed to determine statistically that  $D(M)$  is significantly greater than  $D(N)$ , the upper confidence band is calculated using (Berman, 1977; Berman, 1986; Carranza, 2009):

$$Upper\_D(N) = D(N) + \sqrt{9.21 (N + M)/4NM}, \quad (7)$$

where the numbers  $N$  and  $M$  represent the non-prospect and the prospect locations respectively and 9.21 is the  $\chi^2$  value for a significance level of  $\alpha = 0.01$  or 99% confidence for two degrees of freedom (Carranza, 2009). It is also important to define the optimal distance from geological features where mineral prospects have a high likelihood of occurrence. The optimal distance representing high spatial correlations between mineral prospect distribution and geological features can be determined through a test of the significance of positive spatial association after Carranza (2009). The test of significance is done by calculating the beta ( $\beta$ ) statistics using a  $\chi^2$  value distributed at two degrees of freedom and the values of  $D$  defined in equation 10 (Berman, 1986; Carranza, 2009):

$$\beta = 4D^2NM/(N+M) \quad . \quad (8)$$

In this study,  $M = 124$  and  $N = 126$ . The non-prospect locations were created using an ArcMap tool for creating a random number of points within the study area extent.

## 2.5. Results

### 2.5.1 The distribution of gold prospects by spatial autocorrelation techniques

#### 2.5.1.1 Fry analysis of low-grade and high-grade prospects

Evaluation of spatial distribution of gold prospects, prospects and occurrences by grade are shown on Fig. 2-5 and Fig. 2-6. The results for gold-prospect Fry translations for points with  $< 5$  g/t Au values are shown on Fig. 2-5A and their corresponding rose-diagram orientations on Fig. 2-5B indicates that mineralization has strong ESE - WNW (112.5 - 292.5 degrees) and NE - SW (45 - 225 degrees) orientations.

Higher-grade prospects ( $> 5$  g/t Au), translations and corresponding rose diagram orientations show prominent NW - SE (315 - 135 degrees) oriented directions and minor ENE - WSW (067.5 - 247.5 degrees) orientations (Fig. 2-6A and Fig. 2-6B).

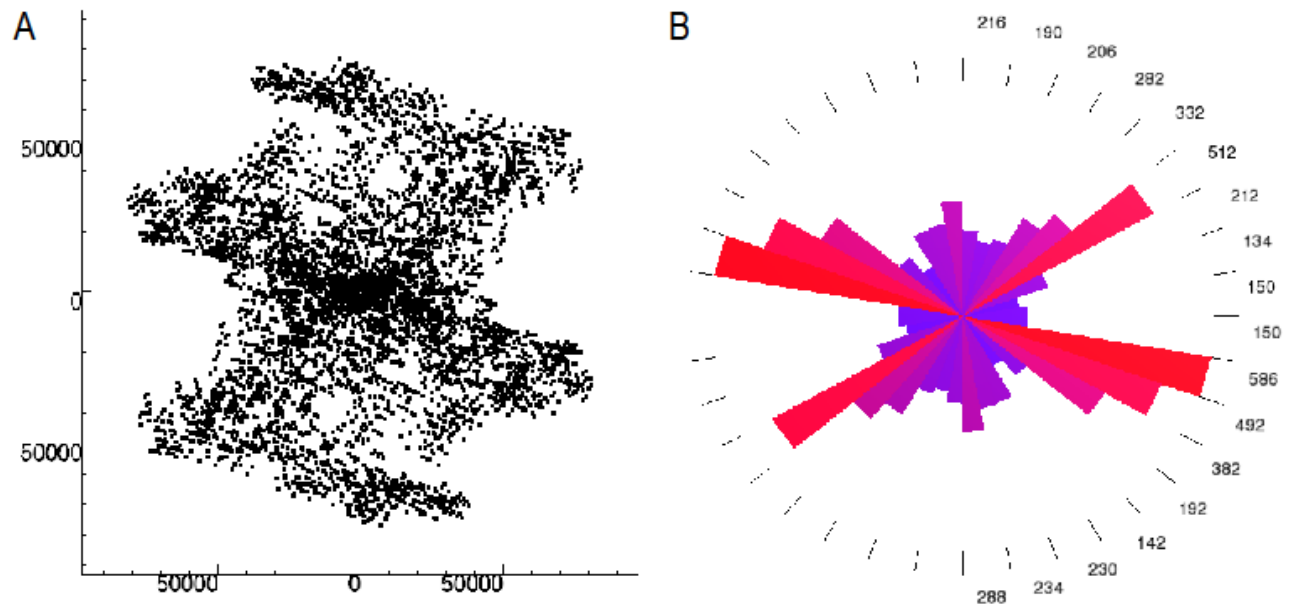


Fig. 2- 5: Fry analysis translations from the autocorrelation of orogenic gold prospects with grade values < 5 g/t Au (A) and rose diagram showing primary orientations of prospects (B).

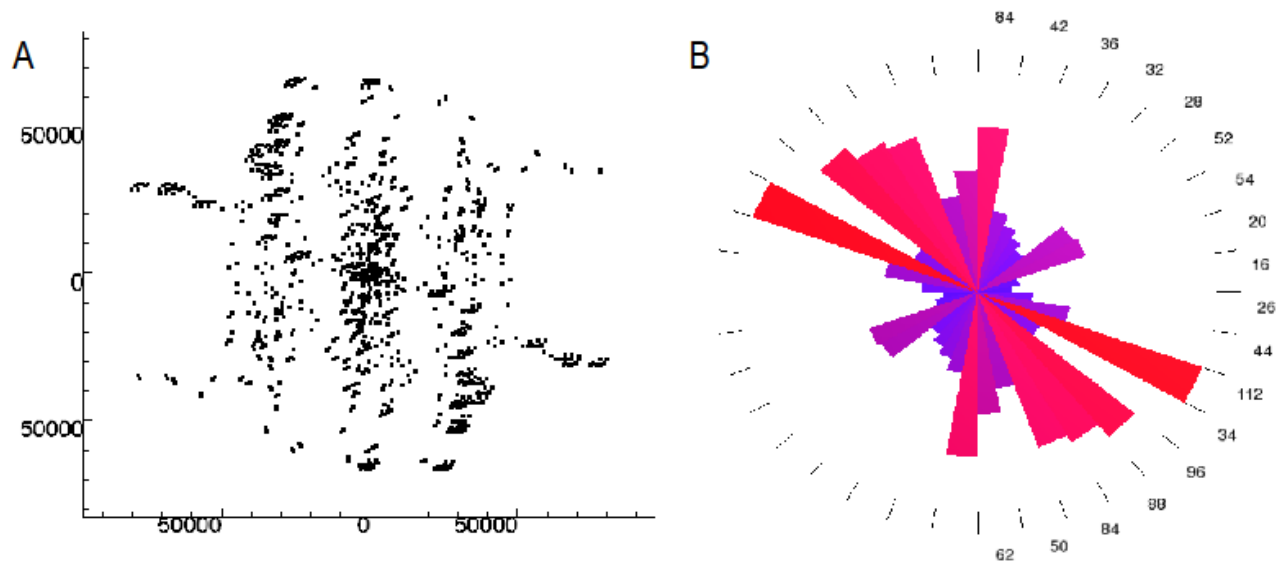


Fig. 2- 6: Fry analysis translations from the autocorrelation of orogenic gold prospects with grade values > 5 g/t Au (A) and rose diagram showing primary orientations (B).

The results for a scale-integrated spatial correlation analysis for determining spatial orientations of point data representing mineral deposits, prospect, and showing point distributions at local, district and regional scales are summarized on Fig. 2-7 and Table 2-4. Although point patterns were thinned to remove the bias due to high sampling densities near deposit camps (Singer

and Menzie, 2008; Lisitsin, 2015), the thinning removes spatial relationships at scales less than 500 m. Thus, only the local-scale mineralization controls were analyzed using the original (i.e., not thinned) point pattern data to determine the spatial distributions at < 2 km scale.

At local scales (< 2 km) of observation, mineral deposit, prospect and occurrence distributions with grades < 5 g/t Au (Fig. 2-7A) show ESE – WNW (112.5 - 292.5 degrees) and NE-SW (45 - 225 degrees) orientations while higher-grade prospects > 5 g/t Au show controls with dominant ENE - WSW (067.5 - 247.5 degrees) and NW -SE (315 – 135 degrees) orientations (Fig. 2-7B).

District scale (2 -10 km) geological controls reveal that low-grade gold deposits, prospects, and occurrences (< 5 g/t Au) show prominent ESE-WNW (112.5 - 292.5 degrees) and minor NE -SW directions (Fig. 2-7C). For prospects with higher grades, the geological controls show strong orientations in the N-S (000 - 180 degrees) directions and ENE-WSW (067.5 - 247.5 degrees) on Fig. 2-7D.

At regional scales (> 10 km), gold prospects with < 5 g/t Au have major NE – SW (45 – 225 degrees) directions and minor ESE - WNW (112.5 - 292.5 degrees) directions (Fig. 2-7E) while prospects with > 5 g/t Au show prominent NW - SE (315 – 135 degrees) and minor N - S (000 - 180 degrees) orientations (Fig. 2-7F).

The Fry analysis results indicate that the distribution of mineral deposit, prospects, and showings vary with the scale of observations, which implies that different geological processes may have acted at various crustal scales to distribute low- and high-grade orogenic gold prospects.

It is also noticeable from the results that the ENE -WSW (067.5 - 247.5 degrees), ESE – WNW (112.5 - 292.5 degrees) and NE – SW (45 - 225 degrees) directions appear to be the most common spatial orientations present at all scales.

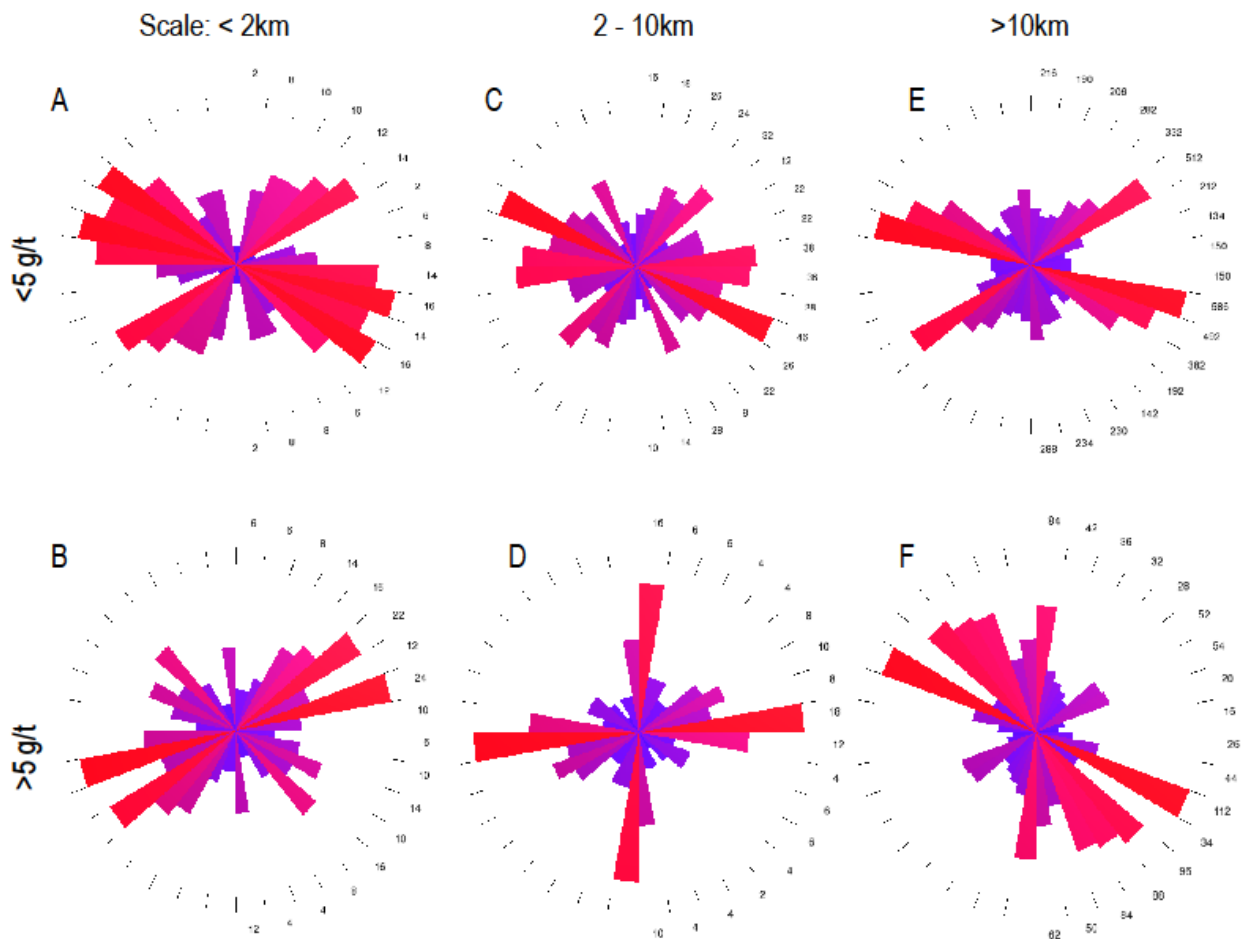


Fig. 2- 7: Rose diagrams showing the Fry analysis translations of orogenic gold prospect distribution at local scales (<math>< 2\text{ km}</math>), district scales (<math>2 - 10\text{ km}</math>) and regional scales (<math>> 10\text{ km}</math>).

Panels (A), (C) and (E) are low-grade prospects; (B), (D) and (E) are high-grade prospects. See Table 2-4 for a summary of the comparison of spatial correlations and prospect orientations at varying grades and scales.

Table 2- 4: Results of spatial autocorrelation (Fry analysis) of gold prospects at varying gold grades (above and below the mean grade, 5 g/t Au) and varying scales of geological processes.

Grade (g/t)	Scale of observations (km)		
	Local (< 2 km)	District (2 - 10 km)	Regional (> 10 km)
< 5 g/t Au	<b>ESE - WNW</b> and NE - SW	<b>ESE - WNW</b> and NE - SW	<b>NE - SW</b> and <b>ESE - WNW</b>
> 5 g/t Au	<b>ENE - WSW</b> and NE - SW	<b>ENE - WSW</b> and N - S	<b>NW - SE, N - S,</b> and <b>ENE - WSW</b>

The major orientation directions are shown in bold letters and minor orientations are in standard letters.

#### 2.5.1.2 Fry analysis of gold prospects in the north and south (implications for correlations with high strain zones)

Fry analysis was also applied to point pattern data representing locations of gold prospect as well as on point patterns representing the beginning and end of each mapped fault zone in the Swayze greenstone belt. The spatial autocorrelation analysis (summarized on Fig. 2-8 and Table 2-5) were performed on data points covering the total study area as well as for points in the northern and the southern Swayze greenstone belt separately, whereby the north and south of the Swayze greenstone belt was demarcated at latitude 48° 00' N (Fig. 2-2). The rose diagram plots on Fig. 2-

8A, Fig. 2-8B, and Fig. 2-8C, show the spatial autocorrelations for gold prospects in the entire Swayze greenstone belt, the northern Swayze greenstone belt, and the southern Swayze greenstone belt, respectively. Similarly, Fig. 2-8D, Fig. 2-8E, and Fig. 2-8F show rose diagrams for spatial correlations of faults in the entire Swayze greenstone belt, northern Swayze greenstone belt, and southern Swayze greenstone belt, respectively.

A comparison between all gold prospect points (Fig. 2-8A) and all fault points (Fig. 2-8D) shows that there are similarities in feature orientations in the ESE-WNW (112.5 - 292.5 degrees), N-S (000 - 180 degrees), and NE-SW (45 - 225 degrees) directions. The ESE - WNW (112.5 - 292.5 degrees) directions have been correlated with the 2700 - 2680 Ma D<sub>2</sub> Ridout, Rundle, Brett and Swayze Lake D<sub>2</sub> high strain zones in the southern Swayze greenstone belt while the NE-striking directions are associated with the 2680 – 2760 Ma D<sub>3</sub> Wakami, Newtown, and Hardiman high strain zones. The NE-striking directions are also associated with fractures associated with late brittle faulting (Heather, 2001).

A comparison of prospect (Fig. 2-8B) and fault point patterns in the north of the Swayze greenstone belt (Fig. 2-8E) shows that there are similarities in spatial orientations towards the ENE-WSW (067.5 - 247.5 degrees) which can be attributed to the Slate rock high strain zones. Mineral prospects in the north also shows NE-SW (45 - 225 degrees) striking directions (Fig. 2-8B) which are not seen in Fig. 2-8E. Fry translations from the southern Swayze greenstone belt prospect (Fig. 8C) and fault (Fig. 2-8F) rose diagrams both show similar orientations towards the ESE WNW (112.5 - 292.5 degrees) directions. Comparison of the spatial autocorrelations of

prospect point patterns and faults indicates a clear spatial alignment and possible control by the early D<sub>2</sub> and some D<sub>3</sub> high strain zones at large crustal scales. The spatial autocorrelation results support the assumption by Heather (2001) that D<sub>2</sub> high strain zones were synchronous with gold mineralization.

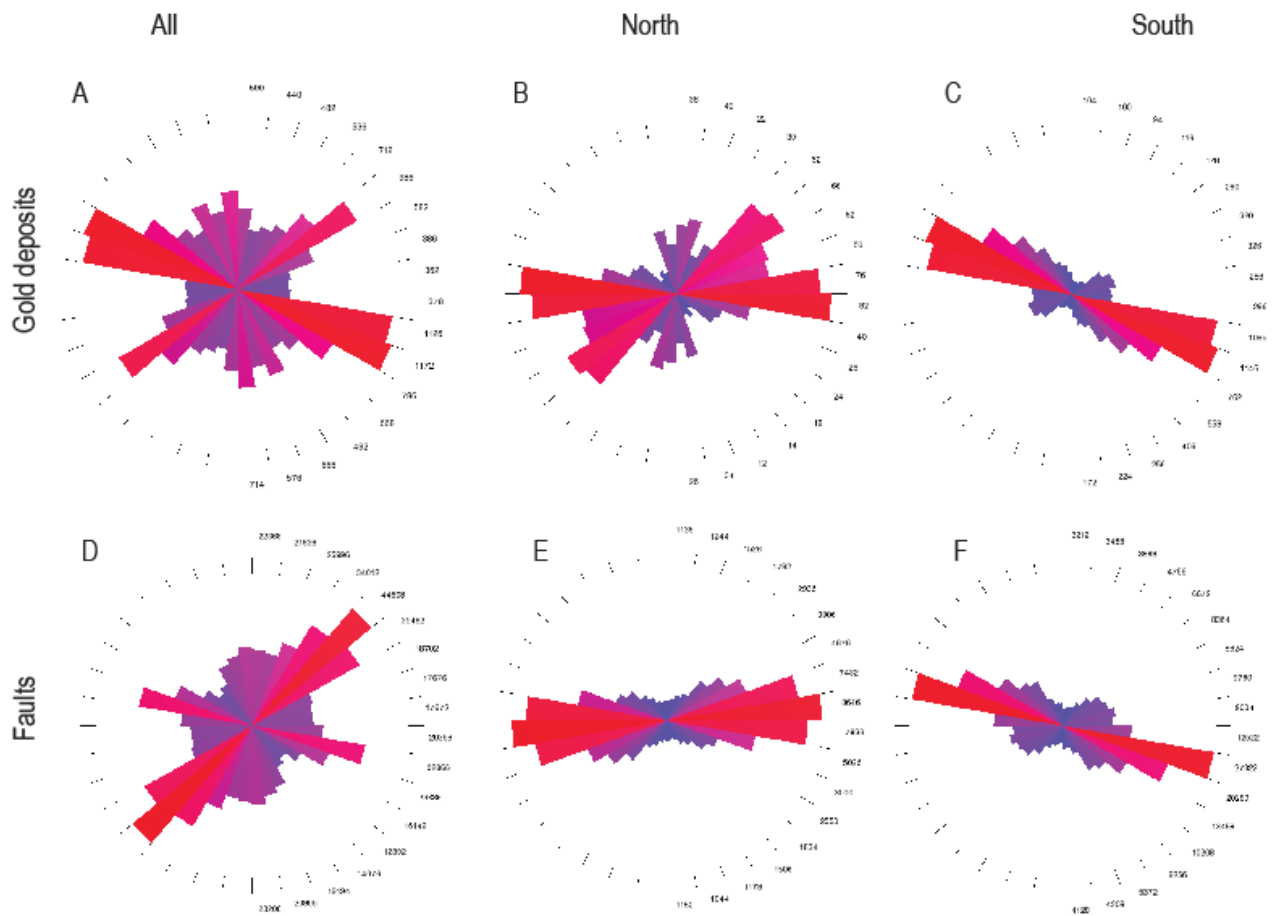


Fig. 2- 8: Comparison of the spatial orientation of orogenic gold prospects to each other and point patterns representing the beginning and end of each fault feature mapped in the Swayze

greenstone belt. The Fry analysis rose diagrams shows orogenic gold prospects orientations (A, B, and C) and fault point pattern orientations (D, E, and F) within the entire Swayze greenstone belt, in the north, and in the south respectively. See Table 2-5 for a comparison of spatial correlations between prospects and faults.

Table 2- 5: Comparison of Fry analysis spatial autocorrelations of gold prospect points and fault point orientations. The table show the primary orientations of gold prospects and mapped faults in the entire Swayze greenstone belt, the north, and south of the Swayze greenstone belt. The north and south of the Swayze greenstone belt are separated at 48° N.

	Entire Swayze greenstone belt	North Swayze greenstone belt	South Swayze greenstone belt
Orientations of prospects	<b>ESE - WNW, NE - SW,</b> and N-S	<b>ENE- WSW, ESE - WNW,</b> and N - S	<b>ESE – WNW</b>
Orientations of faults	<b>NE - SW, ESE - WNW,</b> and N – S	<b>ENE - WSW</b>	<b>ESE – WNW</b>

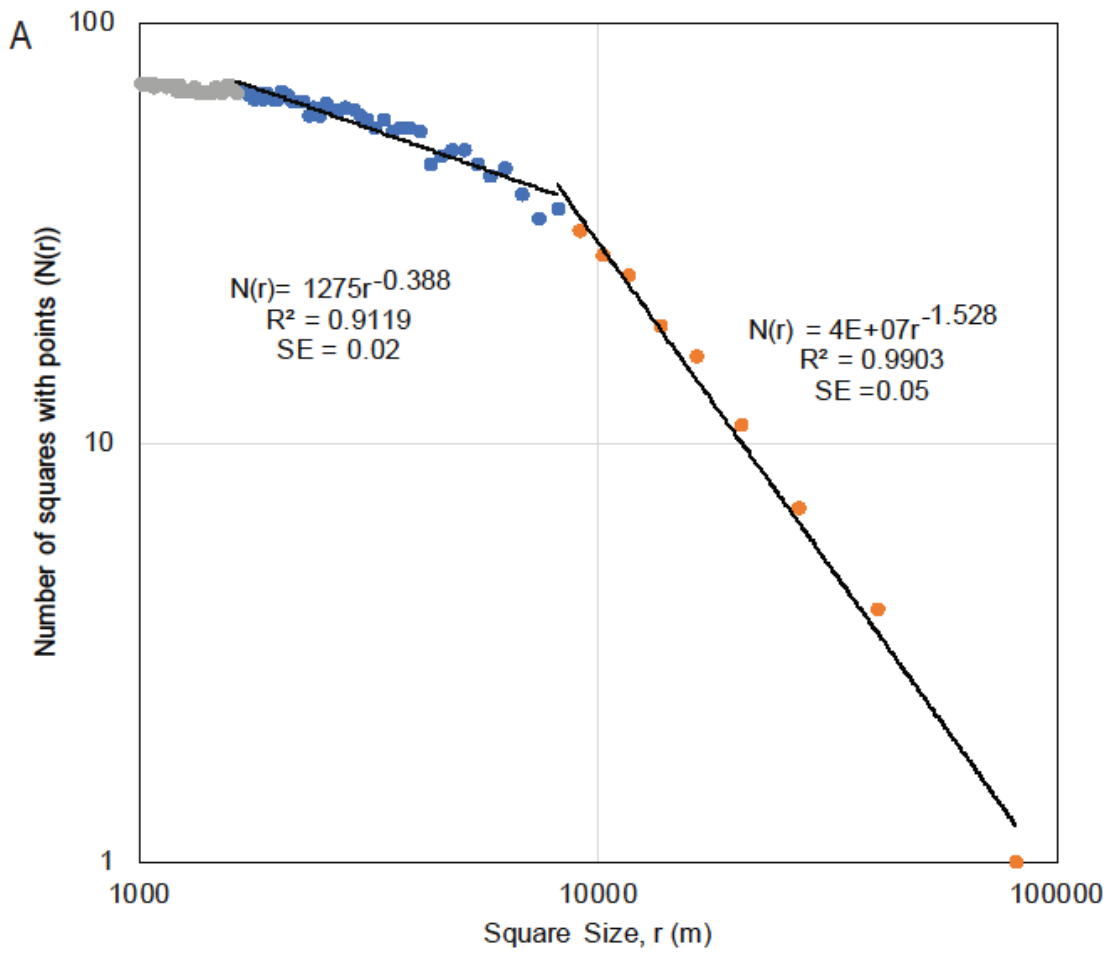
The major orientation directions are shown in bold letters and minor orientations are in standard letters

### 2.5.2 Fractal dimensions of gold results

Hydrothermal systems and their related geological processes can be observed at a range of spatial scales from lithospheric scales of 10s of km to micrometer scales and hence are multifractal in nature. Evaluation of the fractal nature of gold points in the Swayze greenstone belt for various prospect grades indicate prospect grades of < 5g/t show two fractal dimensions defined by a slope

$-D_f$  on a log-log plot (Fig 2-9A), satisfying a power-law relationship defined in Eq. (2). The first fractal dimension occurs at smaller scales,  $< 8$  km, where there is a linear power law relationship with a slope  $D_f=0.39$ , with  $R^2 = 0.91$  and  $SE = 0.02$ ; while larger scales,  $> 8$  km, display a fractal dimension with  $D_f= 1.53$ ,  $R^2 = 0.99$  and  $SE = 0.05$ .

The points shown in grey on Fig. 2-9A represent the roll-off effect described by Blenkinsop and Sanderson (1999), a consequence of under sampling at small scales. For grades  $> 5$  g/t Au, the log-log plot (Fig. 2-9B) also shows a bifractal relationships, whereby between  $1 \text{ km} < r < 8 \text{ km}$ , the fractal dimension  $D_f=0.32$ , with  $R^2 = 0.91$  and  $SE = 0.10$  and at scales  $> 8 \text{ km}$ ,  $D_f= 1.15$ ,  $R^2 = 0.93$  and the  $SE = 0.02$ . For both low- and high-grade prospects, the shallow slopes can be interpreted as greater clustering at scales  $< 8 \text{ km}$  and hence a different geological process occurring.



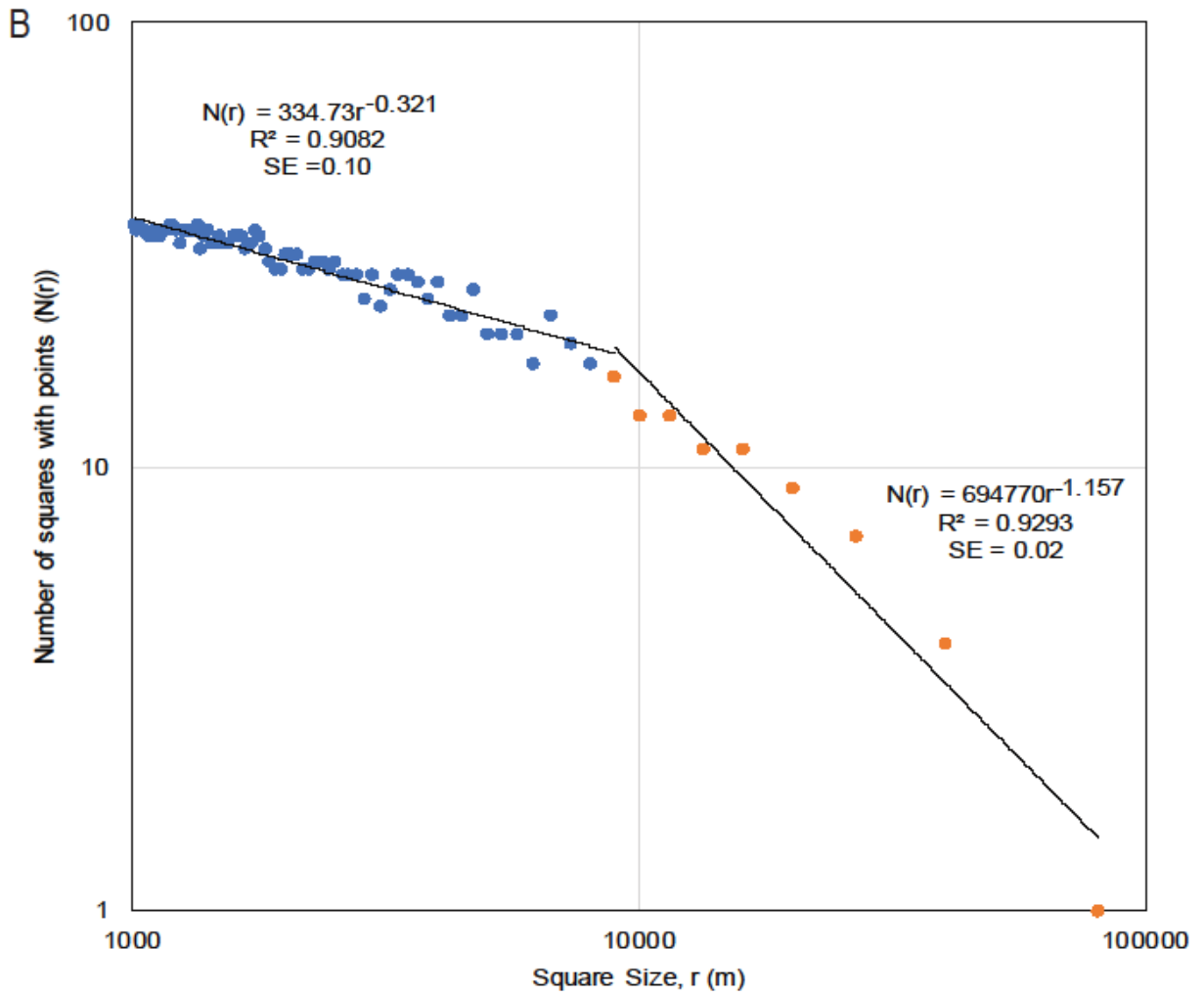


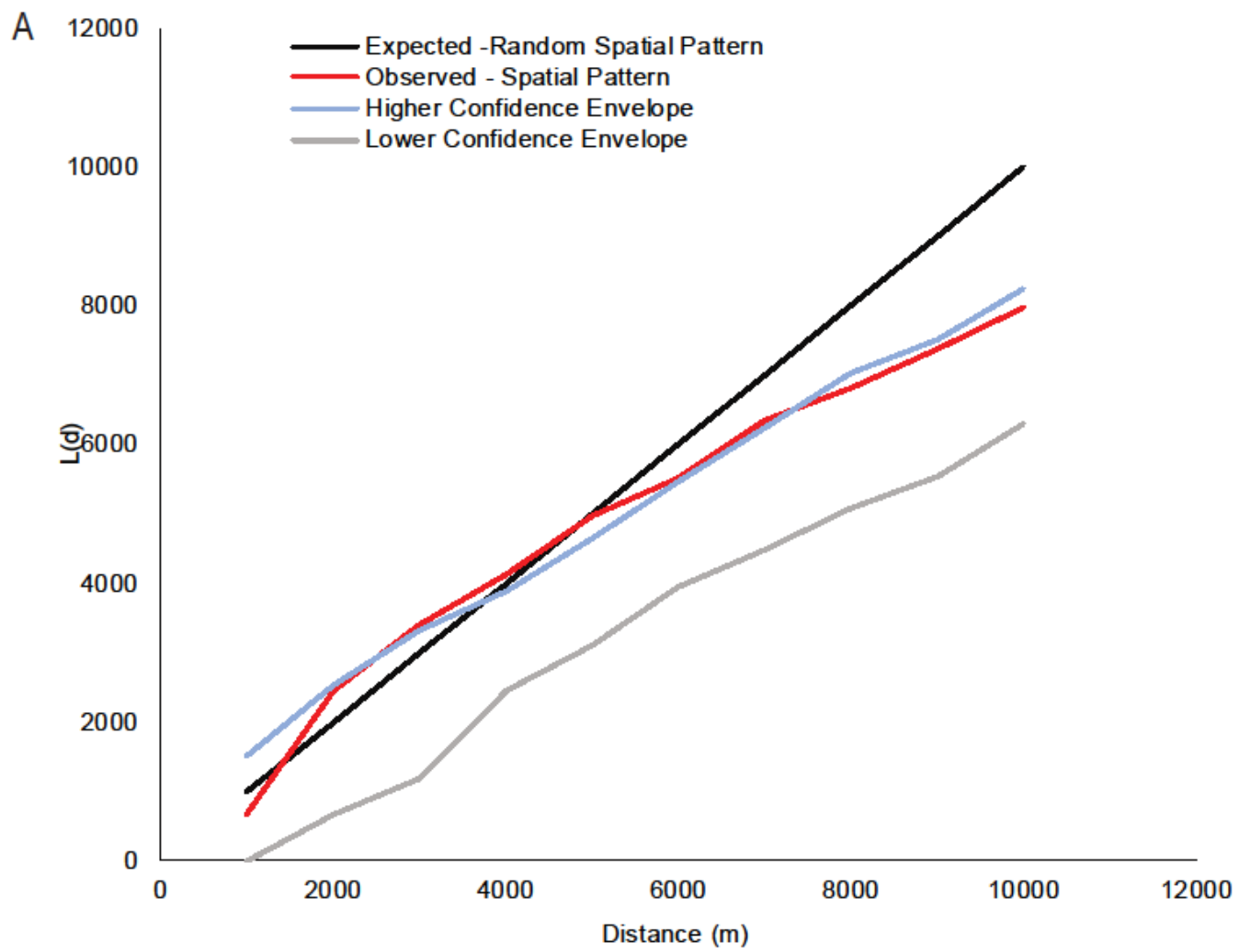
Fig. 2- 9: Log-log plots defining the fractal properties of gold prospects in the Swayze greenstone belt. The plot shows that low-grade ranges  $< 5$  g/t Au prospects (A) and high grade  $> 5$ g/t Au gold prospects (B) are bifractal in the Swayze greenstone belt.

### 2.5.3 Point pattern analysis results

The multi-distance spatial cluster analysis (Ripley's K-Function) was used to determine distance-based spatial correlations of points within permissive tracts for lithologies containing more than 9 prospect points. The results for analyzing the spatial point pattern distribution of orogenic gold prospects in the Swayze greenstone belt with respect to two host lithologies are shown on Fig. 2-10A and Fig. 2-10B, respectively.

The mafic to intermediate metavolcanic and intrusive rocks cover most of the Swayze greenstone belt, with a combined area of 1990 km<sup>2</sup> (Fig. 2-2) and contain 53 of the 'thinned' gold prospects in the study area. The  $L(d)$  plot for this lithology class shown on Fig. 2-10A shows a weak clustering of prospect points at < 4 km while distances > 4 km indicate dispersion in point patterns. The clustering is considered insignificant or weak because although the observed pattern plots above the expected distribution for points with complete spatial randomness (i.e., the expected random spatial pattern), the observed pattern lies along the lower confidence threshold curve at distances < 4 km.

The intermediate to felsic intrusive class of rocks analyzed in this study cover an area of 9 km<sup>2</sup> and contain 11 of the gold prospects points. The K-function's  $L(d)$  plot (Fig. 2-10B) shows statistically significant clustering of gold prospects hosted by felsic to intermediate intrusive rocks at distances between 2 – 4 km and significant prospect point dispersion at distances > 4 km.



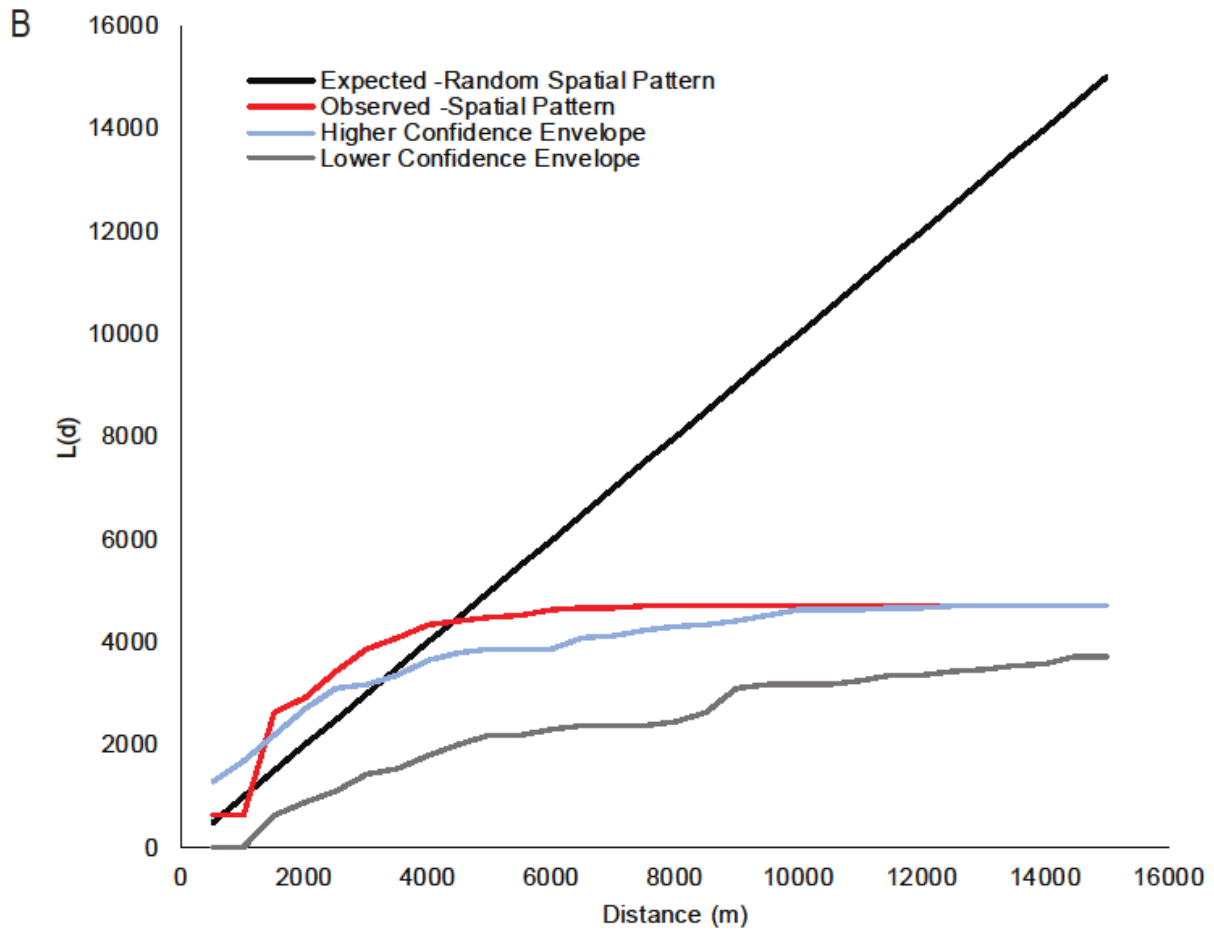


Fig. 2- 10: Multi-distance cluster analysis (Ripley's K-function) results showing the observed and expected spatial pattern for prospect distributions as a function of distance within permissive lithologies: mafic to intermediate metavolcanics rocks (A), and felsic to intermediate intrusive rocks (B). The observed spatial pattern (red) and the expected spatial pattern (black) curves are used to signify distance based spatial correlations.

### 2.5.5 Analysis of the distance distribution of prospects and structures

Faults are said to be the principal conduits for transporting orogenic gold mineralizing fluids to their known depositional sites. However, intrusion-related gold prospects and prospects of the Chester intrusive complex predated the regional structures of the 2700 Ma D<sub>2</sub> Ridout HSZ (Smith, 2013). The distance distribution analysis was therefore used to infer the statistical relationship between faults and orogenic gold prospects only, with implications for determining the optimal distances of gold mineralization from faulting.

The results (Fig. 2-11A and Fig. 2-11B) show that *all* gold prospects in the Swayze greenstone belt have statistically significant spatial correlation with faults (i.e., the graph of  $D$  is positive and the  $\chi^2$  significance level of 9.21 for two degrees of freedom is  $\alpha = 0.01$  or 99% confidence level). Furthermore, according to the curve of  $D$ , 85% and 97% of gold prospects occur within 2 and 4 km distances from faulting, respectively. Correlations between orogenic gold prospects and faulting (Fig. 2-11C and Fig. 2-11D) shows that there is a positive spatial association between orogenic gold and faulting, which corroborates what is seen already in the field (Heather, 2001; Breemen et al., 2006). According to the curve of  $D$ , at least 96% of gold occurrences can be found < 3 km from faulting.

Distance distribution diagrams illustrating the relationship between all gold prospects and D<sub>1-3</sub> HSZ are shown in Fig. 2-12 to 2-14. There are only two D<sub>1</sub> HSZ mapped in the Swayze greenstone belt: the Fawn and McOwen HSZ; therefore, the statistical analysis of gold with D<sub>1</sub> HSZ may be questionable. The results for distance distribution of gold prospects and the D<sub>1</sub> structures show that the graph of  $D(M)$  (Fig. 2-12A) plots above the upper bound of  $D(N)$ .

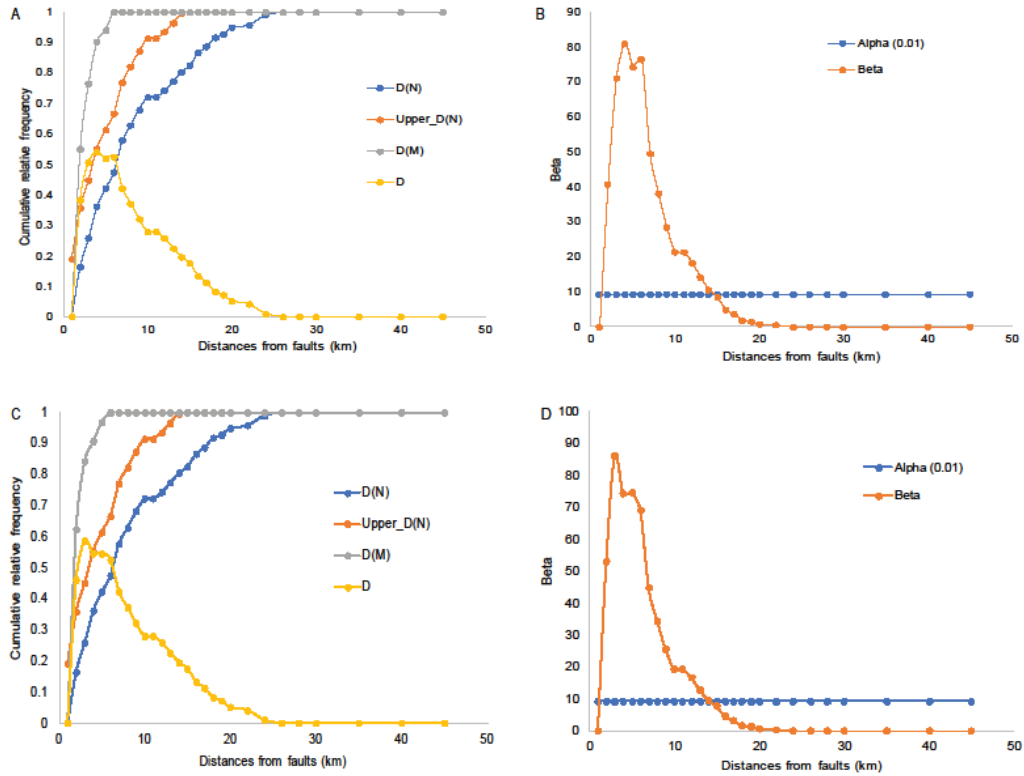


Fig. 2- 11: Cumulative relative frequency curves showing distances of all gold prospects from faults ( $D(M)$ ), relative distances of non-prospects from faults ( $D(N)$ ), the upper statistical bound of non-prospect locations ( $Upper\_D(N)$ ) and the difference ( $D$ ) between prospects and non-prospect density distributions [(A) and (C)]. Graph of  $\beta$ -statistics of differences ( $D$ ) between the cumulative relative frequency of all prospects and non-prospects for distances from faults. The graph shows  $\beta$ -values as well as the intersection of the  $\chi^2$  significance level ( $\alpha=0.01$ ) [(B) and (D)].

Furthermore, evaluation of the spatial correlation between the D<sub>1</sub> HSZ and gold prospects are statistically insignificant at  $\chi^2 = 4.605$  and of  $\alpha = 0.10$  (Fig 2-12B) but statistically significant at  $\chi^2 = 0.21$  and  $\alpha = 0.9$  (i.e., 10% confidence levels). At  $\alpha = 0.9$   $\chi^2$  values, only 17% of gold prospects occur within 9 km from faults meaning that gold prospects do not lie in proximity to the D<sub>1</sub> HSZ.

There are numerous D<sub>2</sub> HSZ have been mapped in the Swayze greenstone belt: the Brett Lake, Ridout, Slate Rock, Rundle and Swayze Lake HSZ. Analysis of spatial and statistical correlations between the D<sub>2</sub> HSZ and the gold prospects show that the latter have a statistically significant spatial correlation with the D<sub>2</sub> HSZ. The results on Fig. 2-13A show that  $D(M)$  plots above  $D(N)$  and the value of  $D$  is positive. Furthermore, Fig. 2-13B shows that the  $\beta$ -statistics values plot about the  $\chi^2 = 9.21$  with 99% confidence levels ( $\alpha = 0.01$ ), indicating a statistically positive spatial correlation between the gold prospects and D<sub>2</sub> HSZ. About 65% and 96% of gold prospects can be found at distances  $< 4$  km and  $< 7$  km from D<sub>2</sub> HSZ, respectively.

Only three D<sub>3</sub> HSZ have been mapped in the Swayze greenstone belt: the Hardiman, Newtown and Wakami HSZ. Similar to the D<sub>1</sub> HSZ, the D<sub>3</sub> HSZ results shows that  $D(M)$  slightly higher than  $D(N)$  but less than upper statistical bound of ( $Upper\_D(N)$ ), and  $D$  values are less than 0.1 indicating an almost random spatial correlation between the gold prospects and D<sub>3</sub> HSZ exists (Fig. 2-14A). The  $\beta$ -statistics at  $\chi^2$  values of  $\alpha = 0.05$  and  $\alpha = 0.01$  show that gold prospects have a statistically insignificant spatial correlation with D<sub>3</sub> HSZ (Fig. 2-14B).

Beta statistics are higher than alpha ( $\alpha = 0.95$ ) with a 5% significance level, showing an optimal distance of 18 km with only 51% of gold found at that distance. The distance distribution

plots show that gold prospects are not spatially correlated with the D<sub>3</sub> HSZ. Most gold prospects occur at distances > 35 km away from the D<sub>3</sub> HSZ and thus the D<sub>3</sub> deformational zones cannot be referred to as a control for mineral prospect distribution.

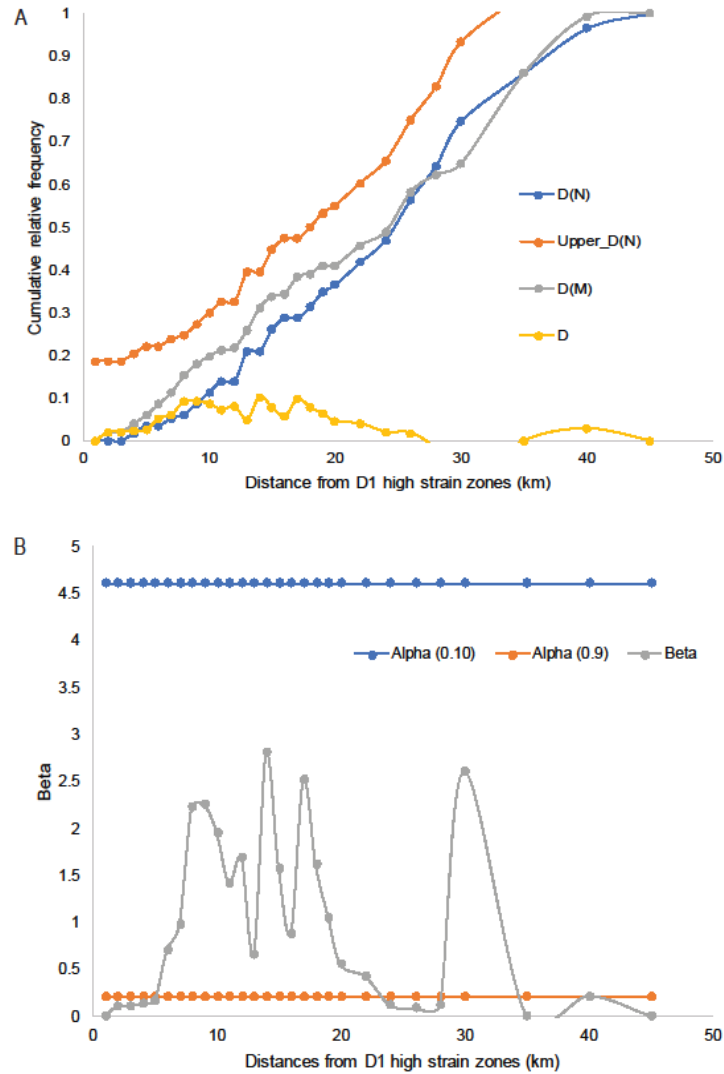


Fig. 2- 12: Cumulative relative frequency curves showing relative distances of all gold prospects from D<sub>1</sub> high strain zones ( $D(M)$ ), relative distances of non-prospects from D<sub>1</sub> high strain zones ( $D(N)$ ), the upper statistical bound of non-prospect locations ( $Upper\_D(N)$ ) and the difference ( $D$ ) between prospects and non-prospect density distributions (A). Graph of  $\beta$  -statistics of differences ( $D$ ) between the cumulative relative frequency of all gold prospects and non-prospects for distances from D<sub>1</sub> high strain zones. The graph shows  $\beta$  values as well as the intersection of the  $\chi^2$  at various significance levels ( $\alpha=0.10$  and  $0.9$ ) (B).

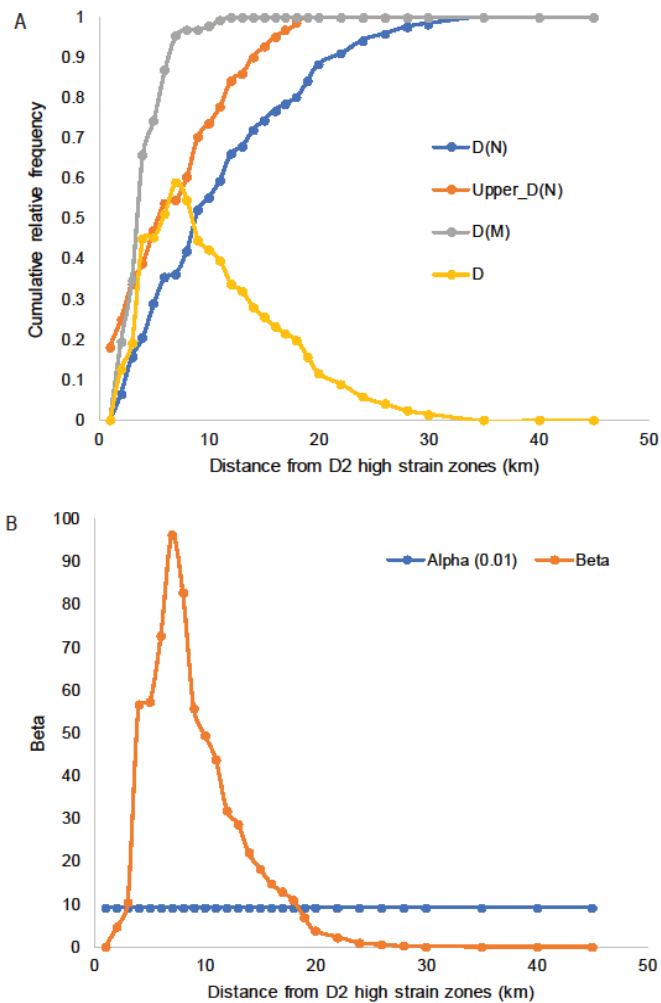


Fig. 2- 13A: Cumulative relative frequency curves showing relative distances of all gold prospects from D<sub>2</sub> high strain zones ( $D(M)$ ), relative distances of non-prospects from D<sub>2</sub> high strain zones ( $D(N)$ ), the upper statistical bound of non-prospect locations ( $Upper\_D(N)$ ) and the difference ( $D$ ) between prospects and non-prospect density distributions (A). Graph of  $\beta$  - statistics of differences ( $D$ ) between the cumulative relative frequency of all gold prospects and

non-prospect for distances from D<sub>2</sub> high strain zones. The graph shows  $\beta$  values as well as the intersection of the  $\chi^2$  at various significance levels ( $\alpha=0.01$ ) (B).

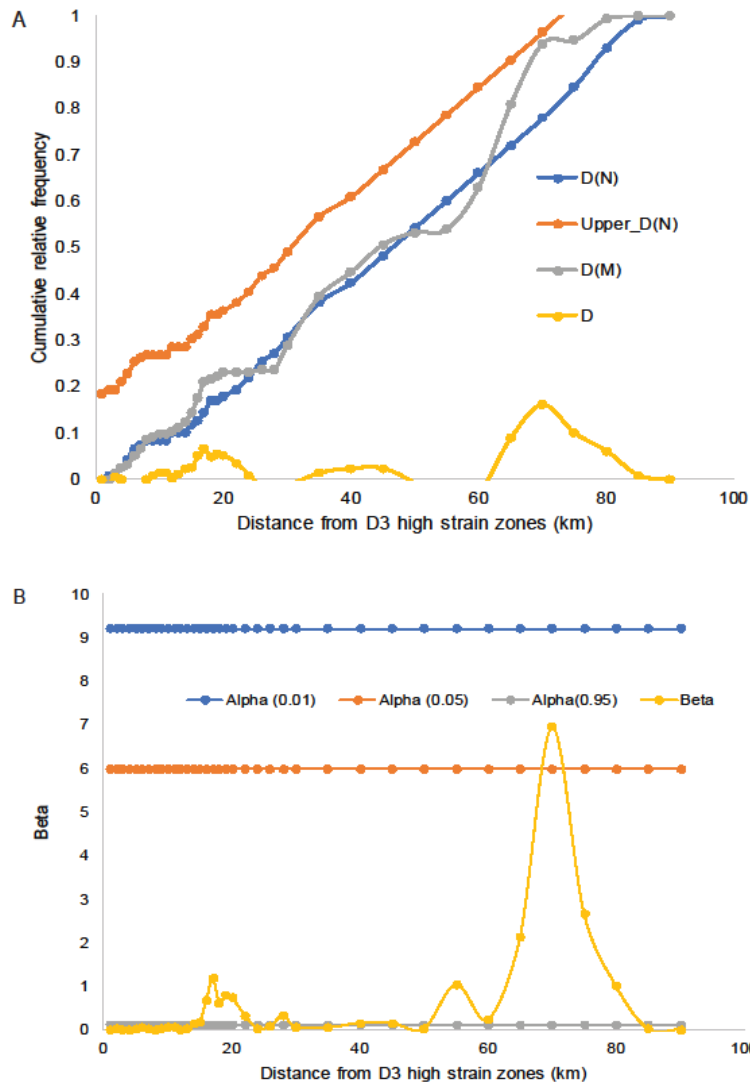


Fig. 2- 14: Cumulative relative frequency curves showing relative distances of all gold prospects from D<sub>3</sub> high strain zones ( $D(M)$ ), relative distances of non-prospects from D<sub>3</sub> high strain zones

( $D(N)$ ), the upper statistical bound of non-prospect locations ( $Upper\_D(N)$ ) and the difference (D) between prospects and non-prospect density distributions (A). Graph of  $\beta$  -statistics of differences ( $D$ ) between the cumulative relative frequency of all gold prospects and non-prospects for distances from  $D_3$  high strain zones. The graph shows  $\beta$  values as well as the intersection of the  $\chi^2$  at various significance levels ( $\alpha=0.01, 0.05$  and  $0.95$ ) (B).

## 2.6 Discussion

Following the guidelines of Singer and Menzie (2010) for selecting permissive tracts for spatial data analysis, the gold deposits, prospects and showings of the Swayze greenstone belt were analyzed to infer their distribution at regional to district to camp scales. The spatial point pattern distributions in the Swayze greenstone belt were analyzed using the multi-distance cluster analysis (Ripley's K-Function), fractal analysis and Fry analysis.

Fractal analysis of orogenic gold prospects revealed that gold prospects in the Swayze greenstone belt display bifractal characteristics (Fig. 2-9). The first fractal dimension occurs at district to regional scales (i.e., distances  $> 8$  km), suggesting the possibility of large-scale geological processes having controlled gold mineralization such as 1st order,  $D_2$  faults the Slate Rock and Ridout HSZ. At these regional scales ( $> 8$  km), hydrothermal fluids are primarily controlled by the crustal-scale shear zones (possibly the 2700 Ma  $D_2$  high strain zones) that have been interpreted from seismic data collected over the Swayze greenstone belt by Cheraghi et al

(2020). These are evident as dipping reflections at > 9 km depths consistent with faults and deformational zones.

The second fractal dimension is evident on the log-log plot at scales of < 8 km opens the possibility that other more district to prospect scale geological controls or features may have influenced the spatial distribution of the gold prospects and resulted in clustering at these scales (e.g., 2nd and 3rd order faults, lithological contacts).

The suggestion that geological controls of gold mineralization in the Swayze greenstone belt operated at fractal dimensions of distances < 8 km are supported by results obtained from Ripley's K-Function, and local-scale Fry analysis results. Modelling point pattern distributions by distance using the Ripley's K-Function within mafic to felsic metavolcanics units revealed that gold prospects are clustered at scales between 2 and 4 km and dispersed at distances > 4 km (Fig. 2-10). The clustering of prospects at scales < 4 km indicates the possibility that small-scaled geological processes (such as 2<sup>nd</sup> and 3<sup>rd</sup> -order structures and lithological contacts) control prospect distributions.

The permissive lithologies that host mineralization such as tholeiitic basalt, feldspar porphyry, that are relatively rich in iron, facilitate the reaction of sulfide-rich fluid with iron-rich host rocks which destabilizes the metal-ligand complex and enables precipitation (Phillips, 1986; Robb, 2005). Furthermore, results from distance distribution analysis between all faults (including small-scale 2<sup>nd</sup> and 3<sup>rd</sup> order faults) and gold prospects in the Swayze greenstone belt show that

there is a statistically positive spatial correlation whereby 96% of gold prospects are found at an optimum distance of 3 km from faults (Fig. 2-11).

According to Table 2-2, at local scales, field evidence shows that orogenic mineral prospects are hosted between lithological contacts, within 2<sup>nd</sup> and 3<sup>rd</sup> order faults, fractures, and sheared and brecciated host rocks (Fumerton and Houle, 1991; Hastie et al., 2015; Love and Robert, 1991).

The regional-scale controls (i.e., defined by second fractal dimension of > 8km) of gold by 1st order, D<sub>2</sub> HSZ assessed using the distance distribution method shows that the relationship between gold prospects and D<sub>2</sub> HSZ is statistically significant (Fig. 2-13) with 65% and 97% of gold prospects found to occur at an optimum distance of 4 and 7 km from D<sub>2</sub> HSZ, respectively. These results suggest that D<sub>2</sub> high-strain zones such as the Slate Rock and Ridout HSZ are the primary pathways responsible for focusing gold-bearing hydrothermal fluids. Additionally, Fry analysis at regional scales (Fig. 2-5 and Fig. 2-6) shows the ESE-WNW, NE-SW (45 – 225 degrees), ENE-WSW (067.5 - 247.5 degrees), and NE -SW (45-225 degrees) that correlate well with the aforementioned D<sub>2</sub> HSZ.

The Fry analysis done for varying grades and scales (Fig. 2-7) were useful for showing intricate details on the controls of the orogenic mineral system at local, district and regional scales. Gold prospects in the Swayze greenstone belt are largely E-W trending which appears to correlate with the geometry and shape of the greenstone belt. According to Heather (2001), the shape of the Swayze greenstone belt is caused by deformational and subsequent magmatic events that followed

an ESE-WNW (112.5-292.5 degrees) orientation. Fry analysis of mineral prospects reveal a strong spatial association with mapped features such as high strain zones, fractures and lower-order faults as seen on Fig. 2-7. The results attained from both Fry and fractal analysis reach the same conclusions in suggesting that ore-forming processes operated at various scales to distribute and cluster gold prospects.

## 2.7 Conclusions

The results of the spatial analyses completed in the Swayze greenstone belt show that orogenic gold prospects are bifractal, have only weak spatial associations with permissive lithologies (i.e., felsic to mafic intrusive rocks) and have strong spatial associations with D<sub>2</sub> HSZ. This observation is consistent with some spatial trends in gold prospect alignment revealed by Fry analysis. The fractal analysis further illustrated that regional-scale processes (> 8 km) controlled gold mineralization. These large-scale processes are modelled with Fry analysis as having predominantly ESE-WNW (112.5-292.5 degrees) and ENE-WSW (067.5 - 247.5 degrees) orientations. Fry analysis results showed other gold mineralization trends exist, for example, N-S (000 - 180 degrees) and NE-SW (45 - 225 degrees), suggesting that there are other factors that controlled gold mineralization.

Supportive field observations show that the flow directions, distributions, and depositional sites of hydrothermal fluid systems were influenced by the presence of 2<sup>nd</sup> and 3<sup>rd</sup>-order faults, breccias, fractures and competency contrasts in host lithologies.

Fractal and Ripley's K-Function analysis supported local scale prospect clustering in the Swayze greenstone belt. Specifically, fractal analysis indicates that there are prospect controls at scales < 8 km. Within these scales, Ripley's K-function show that mineral prospects are clustered at < 4 km and the clustering can be seen along regions with high fault densities.

## 2.8 Acknowledgements

The authors would like to acknowledge the inputs and suggestions from Ore Geology Review journal editor and reviewers for their contributions and insights in improving this manuscript.

We would like to recognize contributions from Leonardo Feltrin as well as research funding from the International Development Research Centre (IDRC), Queen Elizabeth II Diamond Jubilee Scholarship, Ivanhoe Mines, and Goodman School of Mines

## 2.9 References

Agterberg, P.F., 2013. Fractals and spatial statistics of point patterns. *J. of Earth Sci.* 24, 1 -11.

Atkinson, B.T., 2013. The westward extension of the Larder–Cadillac fault through the Kenogamissi batholith, Abitibi sub-province; *in* summary of field work and other activities, 2013, Ontario Geological Survey, Open File Report 6290, p.42-1 to 42-12.

Austin, J.R., Blenkinsop, T.G., 2009. Local to regional scale structural controls on mineralization and the importance of a major lineament in the eastern Mount Isa Inlier, Australia: Review and analysis with autocorrelation and weights of evidence. *Ore Geo. Rev.* 35, 298 – 316.

Ayer J.A, 1995. Precambrian geology northern Swayze greenstone belt; *Ont. Geol. Sur, report 297, pp57*

Ayer, J.A., Trowell, N.F., 2002. Geological compilation of the Swayze, Abitibi greenstone belt; Ontario Geological Survey, Preliminary Map P.3511, scale 1:100 000.

Ayer J., Amelin, Y., Corfu, F., Kamo, S., Ketchum, J.F., Kwork, K., Trowell, N.F., 2002. Evolution of the southern Abitibi greenstone belt based on U-Pb geochronology. Autochthonous volcanic construction followed by plutonism, regional deformation and sedimentation. *Precambrian Res.* 115, 63 – 95.

Ayer, J.A., Berger, B.R., Hall, L.A.F., Houlié, M.G., Johns, G.W., Josey, S., Madon, Z., Rainsford, D., Trowell, N.F., Vaillancourt, C., 2005. Geological compilation of the central

Abitibi greenstone belt: Kapuskasing structural zone to the Québec border; Ontario Geological Survey, Preliminary Map P.3565, scale 1:250 000.

Ayer, J.A., 1995. Precambrian geology, Northern Swayze greenstone belt; Ontario Geological Survey, Report 297, pp57

Bailey, T. C., A. C. Gatrell., 1995 Interactive spatial data analysis. Longman Scientific & Technical, Harlow, U.K. pp 395

Baker T., Lang, J.R., 2001. Fluid inclusion characteristics of intrusion-related gold mineralization, Tombstone-Tungsten magmatic belt, Yukon Territory, Canada. *Miner Deposita*, 36, 563 - 582.

Berman, M., 1977. Distance distributions associated with Poisson processes of geometric figures. *J. Appl. Probab.* 14, 195–199.

Berman, M., 1986. Testing for spatial association between a point process and another stochastic process. *J. Appl. Stat.* 35, 54–62.

Bleeker, W., Atkinson, B.T., Stalker, M., Creek, B., 2014. A “New” occurrence of Timiskaming Sedimentary rocks in the northern Swayze greenstone belt, Abitibi Subprovince — with implications for the eastern continuation of the Porcupine – Destor fault zone and nearby gold mineralization; Ontario Geological Survey, Open File Report 6300, 43.1 -43.10

Blenkinsop, T. G., 1994. The fractal distribution of gold deposits: two examples from the Zimbabwe Archean craton. In: Kruhl J.H (eds) *Fractals and Dynamic Systems in Geosciences*. Springer, Berlin, Heidelberg, pp. 247 – 258.

Blenkinsop, T.G., Tromp, P.L., 1995. Fractal measure for size and spatial distributions of gold mines: economic applications. *Sub-Saharan Econ. Geol. Special Publication Geological Society of Zimbabwe*, 3, 177 – 186

Blenkinsop, T., Sanderson, D.J., 1999. Are gold deposits in the crust fractal? A study of gold mines in the Zimbabwe Craton. *Special publication of the Geological Society of London*. 155, 141 – 151.

Blenkinsop, T.G., 2004. Application of fractal geometry to mineral exploration. In *SEG 2004 Predictive Mineral Discovery Under Cover: Extended Abstracts*. 158 – 11

Breemen, O. V., Heather, K.B., Ayer, J.A., 2006. U-Pb geochronology of the Neoproterozoic Swayze sector of the Southern Abitibi greenstone belt, *Current Research Paper 2006-F1*. Geological Survey of Canada, 1-30.

Calvert, A.J., Ludden, J.N., 1999. Archean continental assembly in the southeastern Superior Province of Canada. *Tectonics*. 18, 412–429.

Carlson, C.A., 1991. Spatial distribution of ore deposits. *Geology* 19, 111–114.

Carranza, E.J.M., 2009. Controls on mineral deposit occurrence inferred from analysis of their spatial pattern and spatial association with geological features. *Ore Geol. Rev.* 35, 383–400.

- Cheng, Q., Agterberg, F.P., Bonham-Carter, G.F., 1996. A spatial analysis method for geochemical anomaly separation. *J. of Geoch. Explor.* 56, 183–195.
- Cheng, Q., 1997. Multifractal modeling and lacunarity analysis. *Math. Geol.* 29 (7), 919 – 932.
- Cheng, Q. M., Agterberg, F. P., 1995. Multifractal Modelling and Spatial Point Processes. *Math. Geol.* 27, 831–845
- Cheng, Q. M., 2008. Non-Linear Theory and Power-Law Models for Information Integration and Mineral Resources Quantitative Assessments. *Math. Geosci.* 40, 195–225, doi:10.1007/s11004-008-9172-6
- Cheraghi, S., Naghizadeh, M., Snyder, D., Haugaard, R., Gemell, T., 2020. High-resolution seismic imaging of crooked two-dimensional profiles in greenstone belts of the Canadian shield: results from the Swayze area, Ontario, Canada. *Geophys. Prosp.* 68, 62 -81.
- Diggle, P.J., 1983. *Statistical analysis of spatial point pattern.* London Academic Press. pp 148
- Diggle, P.J., 2003. *Statistical analysis of spatial point patterns.* Arnold Publishers, London. pp159
- Dixon, P.M., 2002. Ripley's K function. In: El-Shaarawi, A.H., Piegorisch, W.W (Eds.) *Encyclopedia of Envirometrics.* John Wiley & Sons, Chichester, 1796 – 1803
- Dubé, B., Mercier-Langevin, P., Ayer, J., Atkinson, B., Monecke, T., 2017. Orogenic greenstone-hosted quartz-carbonate gold deposits of the Timmins-Porcupine Camp. In: Monecke, T., Mercier-Langevin, P., Dube, B. (eds.), *Archean base and precious metal deposits,*

southern Abitibi greenstone belt, Canada. Society of Economic Geologists, Reviews in Economic Geology. 19, 51 -79.

Ebdon, D., 1988. Statistics in Geography. Blackwell Publishing, Oxford, UK.

Feder, J., 1988. Fractals. Plenum Press, New York. Pp. 265

Ford, A., and Blenkinsop, T.G., 2008. Combining fractal analysis of mineral deposit clustering with weights of evidence to evaluate patterns of mineralization: application to copper deposits of the Mt. Isa inlier, NW Queensland, Australia: Ore Geol. Rev. 33, 435–450.

Fry, N., 1979. Random point distributions and strain measurement in rocks. Tectonophysics, 60, 89-105.

Fumerton, S., Houle, K., 1995a. Mineral prospects of the Swayze greenstone belt Volume 1 - parts of NTS41 O and Volume 2-parts of NTS 41 P, 42 A and 42 B; Ontario Geological Survey, Open File Report 5912, v.1, p.1-372.

Gaboury, D., 2019. Parameters for the formation of orogenic gold deposits. Appl. Earth Sci. 128, 124 - 133

Getis, A., Boots, B., 1978. Models of Spatial Processes. An approach to the study of point, line and area patterns. Cambridge University Press, London.

Getis, A., 1984. Interactive modeling using second-order analysis. Environ. Plan. 16, 173–183.

Gill, G. J., Roots, E. A., Frieman, B. M., Huagaard, R., Craven, J. A., Smith, R. S., Snyder, D.

B., Zhou, X., Sherlock, R., 2021. On Archean craton growth and stabilization: Insights from

lithospheric resistivity structure of the Superior Province. *Earth and Planetary Science Letters*, 562, 1 – 10.

Goldfarb, R.J., Groves, D.I., Gardoll, S., 2001. Orogenic gold and geologic time: a global synthesis. *Ore Geol. Rev.* 18, 1–75.

Groves, D.I., Goldfarb, R.J., Robert, F., Hart, C.J.R., 2003. Gold deposits in metamorphic belts: overview of current understanding, outstanding problems, future research, and exploration significance. *Econ Geol.* 98, 1–29

Groves, D.I., Goldfarb, R.J., Gebre-Mariam, M., Hagemann, S.G., Robert, F., 1998. Orogenic gold deposits: a proposed classification in the context of their crustal distribution and relationship to other gold deposit types. *Ore Geol. Rev.* 13, 7–27.

Groves, D.I., Santosh, M., Zhang, L., 2020. A scale-integrated exploration model for orogenic gold deposits based on a mineral systems approach. *Geosci. Front* in press.

Hanna, S.S., Fry, N., 1979. A comparison of methods of strain determination in rocks from southwest Dyfed (Pembrokeshire) and adjacent areas. *J. Struct. Geol.* 1, 159 - 162

Harris, J.R., 2002. Processing and Integration of geochemical data for mineral exploration\_ application of statistics, geostatistics and GIS technology. PhD thesis, University of Ottawa.

Hastie, E.C.G., Lafrance, B. and Kontak, D.J. 2015. Observations on the Kenty and Rundle deposits, Swayze Greenstone Belt; in summary of field work and other activities 2015, Ontario Geological Survey, Open File Report 6313, .9.1- 9.9.

Hastie E.C.G, 2017. Gold Metallogeny of the Southern Swayze Area, Abitibi greenstone belt: a field trip guidebook: Ontario Geological Survey, Open File Report 6334, pp19.

Hastie, E.C.G., Kontak, D.J., Lafrance, B., 2020. Gold remobilization: Insights from gold deposits in the Archean Swayze greenstone belt, Abitibi Subprovince, Canada. *Econ. Geol.* 115, 241 – 277.

Heather, K., 2001. The geological evolution of the Archean Swayze greenstone belt, Superior Province, Canada. PhD thesis, Keele University

Heather, K.B., 1998. New insights on the stratigraphy and structural geology of the southwestern Abitibi greenstone belts: implications for the tectonic evolution and settings of mineral deposits in the Superior Province; *in* The First Age of Giant Ore Formation: Stratigraphy, Tectonics and Mineralization in the Lake Archean and Early Proterozoic, Prospectors and Developers Association of Canada, 1998 annual meeting volume, 63 – 102.

Hollister, V.F., 1992. On a proposed plutonic porphyry gold deposit model, *Non-renewable Resour*, 1, 293 – 302.

Huugaard, R., Gemmell, T.P., Ayer, J.A., Thurston, P.C., 2017. Lithological and stratigraphic relationships of the north Swayze and Matheson areas, Abitibi greenstone belt. Ontario Geological Survey, Open File Report 6350. 43, 1 -10.

Katz, L.R., Kontak, D.J., Dubé, B., McNicoll, V., 2015. The Archean Côté Gold intrusion-related Au(-Cu) deposit, Ontario: A large tonnage, low-grade deposit centered on a magmatic-hydrothermal breccia. *In*: Targeted Geoscience Initiative 4: Contributions to the understanding of

Precambrian lode gold deposits and implications for exploration, (eds) B. Dubé and P. Mercier-Langevin; Geological Survey of Canada, Open File 7852, 139-155.

Katz, L.R., Kontak, D.J., Dubé, B., McNicoll, V., 2017. The geology, petrology and geochronology of the Archean Côté gold large-tonnage, low-grade intrusion-related Au(-Cu) deposit, Swayze Greenstone Belt, Ontario, Canada. *Can. J. Earth Sci.* 22 -77

Katz, L.R., 2016. Geology of the Archean Côté gold Au (-Cu) intrusion-related deposit, Swayze greenstone belt, Ontario. PhD thesis, Laurentian University.

Knox-Robinson, C.M., Wyborn, L.A.I., 1997. Towards a holistic exploration strategy: Using Geographic Information Systems as a tool to enhance exploration. *Aust. J. Ear. Sci.* 44, 453–463.

Kontak, D.J., Creaser, R.A., Hamilton, M., 2013. Geological and geochemical studies of the Côté Lake Au(-Cu) deposit Area, Chester Township, northern Ontario. *In* Results from the Shining Tree, Chester Township and Matachewan Gold Projects and the Northern Cobalt Embayment Polymetallic Vein Project. Ontario Geological Survey, Miscellaneous Release Data. pp 294.

Kreuzer, O.P., Blenkinsop, T.G., Morrison, R.J., Peters, S.G., 2007. Ore controls in the Charters Towers goldfield, NE Australia: Constraints from geological, geophysical, and numerical analysis. *Ore Geol. Rev.* 32, 37 – 80.

Lang, J.R., Baker, T., 2001. Intrusion-related gold systems: the present level of understanding. *Miner Deposita*, 36, 477 – 489.

- Lester, D.R., Ord, D., Hobbs, B.E., 2012. The mechanics of hydrothermal systems: II. fluid mixing and chemical reactions. *Ore Geol. Rev.* 49, 45 - 71
- Lisitsin, V., 2015. Spatial data analysis of mineral deposit point patterns: applications to exploration targeting. *Ore Geol. Rev.* 71, 861 – 881.
- Love, D.A., Roberts, R.G., 1991. The geology and geochemistry of gold mineralization and associated alteration at the Rundle gold deposit, Abitibi Sub-province, Ontario. *Econ. Geol.* 86, 644–666.
- Mathieu, L., 2021. Intrusion-associated gold systems and multistage metallogenic processes in the Neoproterozoic Abitibi greenstone belt. *Minerals*, 11, 261.
- Mamuse, A., Porwal, A., Kreuzer, O., and Beresford, S., 2010. Spatial statistical analysis of the distribution of komatiite-hosted nickel sulfide deposits in the Kalgoorlie terrane, Western Australia: clustered or not? *Econ. Geol.* 105, 229 -242.
- Mandelbrot, B., 1983. *The Fractal Geometry of Nature*. W.H. Freeman, San Francisco
- McCuaig, T.C., Beresford, S., Hronsky, J., 2010. Translating the mineral systems approach into an effective exploration targeting system. *Ore Geol. Rev.* 38 (3), 128–138.
- McCuaig, T.C., Hronsky, J.M.A., 2014. The Mineral System Concept: The Key to Exploration Targeting. *SEG 2014: Building Exploration Capability for the 21<sup>st</sup> Century*, pp. 153–175.
- Milne, V.G., 1972. *Geology of the Kukatash-Sewell Lake Area: District of Sudbury: Ontario Divisions of Mines, Geological Report 97*, 1 - 116.

Mir, R., Perrouty, S., Astic, T., Bérubé, C. L., Smith, R. S., 2019. Structural complexity inferred from anisotropic resistivity: example from airborne EM and compilation of historical resistivity/IP data from the gold rich Canadian Malartic district, Québec, Canada. *Geophys.* 84 (2), B153–B167.

Mitchel, A., 2005. *The ESRI guide to GIS analysis, Volume 2: spatial measurements and statistics*. ESRI Press. New York

Monecke, T., Mercier-Langevin, P., Dube, B., Frieman, B., 2017b. Geology of the Abitibi greenstone belt. In: Monecke, T., Mercier-Langevin, P., Dube, B. (eds.), *Archean base and precious metal deposits, southern Abitibi greenstone belt, Canada*. Society of Economic Geologists, *Reviews in Economic Geology* 19, 7–49.

Ord, A., Munro, M., Hobbs, B., 2016. Hydrothermal mineralizing systems as chemical reactors: wavelet analysis, multifractals, and correlations. *Ore Geol. Rev.* 79, 155 – 179.

Ord, J.K., Getis, A., 1992. The analysis of spatial association. *Geog. Anal.* 24, 189–206.

O’Sullivan, D., and Unwin, D.J., 2003. *Geographic information analysis: New Jersey*, John Wiley, pp 436.

Phillips, G.N. (1986) Geology and alteration in the Golden Mile, Kalgoorlie. *Econ. Geol.*, 91, 779–808.

Porwal, A., 2006, *Mineral potential mapping with mathematical geological models: The Netherlands*, ITC Ph.D. dissertation, pp289

Pirajno, F., 2009. Hydrothermal processes and mineral systems. Springer, East Perth, Australia.

ISBN: 978-1-4020-8612-0

Raines, G. L., 2008. Are fractal dimensions of the spatial distribution of mineral deposits meaningful? *Nat. Resour. Res.* 17(2): 87–97.

Ripley, B.D., 1977. Modeling spatial patterns. *J. R. Stat. Soc.* 39, 172–192.

Ripley, B. D., 1981. *Spatial Statistics*. John Wiley and Sons, New York

Robert, F., 2001. Syenite-associated disseminated gold deposits in the Abitibi greenstone belt, Canada. *Miner. Deposita*. 36, 503 – 516.

Robert, F., Poulsen, K.H., Cassidy, K.F., Hodgson, J., 2005. Gold metallogeny of the Superior and Yilgarn cratons. In: Hedenquist, J.W., Thompson, J.F.H., Goldfarb, R.J., Richards, J.P. (Eds.), *Economic Geology 100th Anniversary Volume*. Society of Economic Geologists, Littleton, Colorado, pp. 1001–1033.

Sillitoe, R.H., 1991. Intrusion-related gold deposits. In: Foster RP (ed) *Gold metallogeny and exploration*. Blackie, Glasgow, pp. 165 – 209.

Sillitoe, R.H., Thompson, J.F.H., 1998. Intrusion-related vein gold deposits: types, tectono-magmatic settings, and difficulties of distinction from orogenic gold deposits. *Resour. Geol.* 48, 237 – 250.

Silverman, B. W. 1986. *Density estimation for statistics and data analysis*. New York. Chapman and Hall.

- Singer, D.A., and Menzie, W.D., 2008. Map scale effects on estimating the number of undiscovered mineral deposits: *Nat. Resour. Res.* 17, 79–86.
- Singer, D.A., Menzie, W.D., 2010. Quantitative mineral resource assessments — an integrated approach. Oxford University Press.
- Thompson, J.F.H., Sillitoe, R.H., Baker, T., Lang, J.R., Mortensen, J.K., 1999. Intrusion-related gold deposits associated with tungsten-tin provinces. *Miner. Deposita*, 34, 323 – 334.
- Thurston, P.C., Ayer, J.A., Gouttier, J., Hamilton, M.A., 2008. Depositional gaps in Abitibi Greenstone belt stratigraphy: A key to exploration for syngenetic mineralization. *Econ. Geol.* 103, 1097 – 1134.
- Touret, J.L.R., 1992. Carbon-dioxide transfer between the upper mantle and the atmosphere: temporary storage in the lower continental crust. *Terra Nova*, 4, 87 – 98.
- Turcotte, D.L., 1986, A fractal approach to the relationship between ore grade and tonnage. *Econ. Geol.* 81, 1528–1532.
- Vearncombe, J., Vearncombe, S., 1999. The spatial distribution of mineralization: application of Fry analysis. *Econ. Geol.* 94, 475 – 486.
- Vearncombe, J.R., and Vearncombe, S., 2000. The spatial distribution of grade. In: 4<sup>th</sup> International Mining Geology Conference, Proceedings, Australasian Institute of Mining and Metallurgy, 87-93.
- Vearncombe, S. and Vearncombe, J.R., 2001. New methods in 2D and 3D analysis of spatial data. Australian Institute of Geoscientists, Quarterly Newsletter, **63**, 10-12.

- Vearncombe, S., Vearncombe J.R., 2002. Tectonic controls on kimberlite location, southern Africa. *Jour. Struct. Geol.* 24, 1619 – 1625.
- Wyborn, L.A.I., Heinrich, C.A., Jaques, A.L., 1994. Australian Proterozoic mineral systems: essential ingredients and mappable criteria. Australian Institution of Mining Metallurgy Publication Series. 5, 109–115.
- Wyman, D.A., Cassidy, K.F., Hollings, P., 2016. Orogenic gold and the mineral systems approach: Resolving fact, fiction, and fantasy. *Ore Geol. Rev.* 78, 322 – 335
- Zuo, R., Agterberg, F.P., Cheng, Q., Yao, L., 2009. Fractal characterization of the spatial distribution of geological processes. *Int. J. Appl. Earth Obs.* 11, 394 – 402.

# Chapter 3: Support Vector Machine and Artificial Neural Network Modelling of Orogenic Gold Prospectivity Mapping in the Swayze greenstone belt, Ontario, Canada

## 3.1 Abstract

Exploration for new mineral deposits has become increasingly difficult as new discoveries are being found under progressively deeper cover. To better understand and predict orogenic gold mineralization in the Archean Swayze greenstone belt, the essential ingredients of a mineral system are considered: 1) the source of gold and transport fluid ligands, 2) fluid pathways, 3) traps, and 4) the processes responsible for gold precipitation. The aim of this study is to use a mineral-system approach in conjunction to mineral prospectivity mapping to help generate exploration targeting models and corresponding feature importance rankings using a spatial statistical method - weights of evidence (WofE) and data-driven machine learning tools, namely radial basis function neural networks (RBFNN) and support vector machine (SVM). Predictor maps derived from geological, geochemical, structural, and geophysical datasets were used to map expressions of mineral systems in this study. The mineral prospectivity maps generated using the RBFNN and SVM machine learning methods were trained using the K-Fold cross validation approach whereby 10 subsets of the data were used to train and test the model performance. The mean area under receiver operator curve after 10-fold cross-validations were 91% and 94% for the RBFNN models, and the SVM models obtained accuracies of 91% and 87%. Feature importance estimations

obtained from both methods indicate that D<sub>2</sub> and D<sub>3</sub> high strain zones, lithological contacts and D<sub>2</sub> folds (i.e., synclines and anticlines) were found important predictor layers for targeting potential prospective zones of gold mineralization. The machine learning algorithms are novel and pragmatic methods that use the full potential of geoscience datasets in mapping orogenic gold prospectivity.

**Keywords:** Mineral Systems Analysis, Mineral Prospectivity Mapping, orogenic gold systems, machine learning, feature importance, K-Fold cross validation.

## 3.2 Introduction

### 3.2.1 Mineral Prospectivity Mapping

Mineral prospectivity mapping (MPM) can be described as utilising spatial computational techniques to determine the probability of finding a mineral prospect in an area using selected geological layers that show proximity to mineralization (Carranza, 2009). The field of MPM is not new, with early work on a two-staged least-square approach described by Agterberg and Cabilio (1969). Since then, researchers have developed various tools such as Boolean overlay, fuzzy logic, weights of evidence, and artificial neural networks designed to predict the location of new mineral deposits (Bonham-Carter, 1988; 1994; Carranza, 2004). Recent software developments have enabled geoscientists to generate prospectivity maps using geographical information system (GIS) packages. These packages are convenient for spatial data integration and to weight the relationship

of known deposits with input predictor layers, making this a powerful tool for mineral exploration (Bonham-Carter, 1994a; Carranza, 2009).

The methods used for MPM can be classified as either data driven or knowledge-based approach (Bonham-Carter, 1994; Porwal and Kreuzer, 2010). Data-driven techniques are empirical and rely on statistical relationships between input layers and known deposits, while knowledge-driven techniques are more heuristic and rely on expert opinion (Parsa et al., 2017; 2018a; 2018b; Yousefi et al., 2019; Roshanravan et al., 2020). Traditional MPM is done at deposit to district scales (several square kms), where deposit controls are well-defined and understood. MPM is an important tool to assist in the discovery of mineral deposits, as mineral deposit discovery has dramatically decreased even with increasing exploration expenditure. One reason for this is due to exploration being focused on more brownfield areas where mines and deposits already exist (Schodde, 2004; Schodde, 2017; Davies et al., 2020; Groves et al., 2020).

MPM over the Swayze greenstone belt has been carried out by Harris (2002) with a primary focus on effective integration and representation of geochemical datasets during prospectivity analysis. The present study seeks to build on Harris (2002) by considering the mineral systems approach and new geophysical datasets, and assess prospectivity of gold mineralization within the Swayze greenstone belt. This study tests two data-driven machine learning methods and assesses the gold mineralization prospectivity within the Swayze greenstone belt.

The Swayze greenstone belt is regarded as the southwestern extension of the well-mineralized Abitibi greenstone belt. However, workers agree that the Swayze greenstone belt is

not as well mineralized as the world-class gold deposits found in the Abitibi greenstone belt (Ayer et al., 2002; Heather, 2001; Breemen et al., 2006; Hastie, 2017).

The aims of this study are: 1) to outline the critical processes and targeting elements responsible for orogenic gold deposition in the Swayze greenstone belt, 2) to determine the mappable targeting criteria by reviewing the available geoscience data, 3) to use data-driven tools to map mineral prospectivity in the Swayze greenstone belt. The two tools used to predict mineral prospectivity are support vector machine (SVM), and the radial basis function neural networks (RBFNN). The weights of evidence Bayesian statistical method was used to aid in objective estimation of spatial correlations between gold prospects and predictor layers.

### 3.2.2 The geology and stratigraphy of the Swayze greenstone belt

The Archean Swayze greenstone belt is found within the Superior Province of Canada (Fig. 3-1), southwest of the Abitibi greenstone belt. The Swayze greenstone belt is connected to the Abitibi greenstone belt by a narrow septum of metavolcanic and metasedimentary rocks interpreted to be associated with the mineral prolific Porcupine-Destor Fault zone in the north and the Cardillac-Larder lake deformation zone in the southern part of Abitibi (Ayer, 1995, Breemen, 2006). The Porcupine-Destor fault zone is one of the primary controls of the historic orogenic gold mineralization in the Timmins Area - about 11,819 tons of gold can be traced for 300 km (Milne, 1972; Ayer, 1995; Powell et al., 1995; Heather, 2001; Bierlein et al., 2006).

The Swayze is bounded by granitoid complexes namely: the Nat River granitoid complex found in the north, the Ramsey-Algoma complex in the south, the Kenogamissi granitoid complex in the east and in the west, the Kapuskasing structural zone (Heather 2001; Breemen et al, 2006). The separation of the Swayze and Abitibi greenstone belts as two separate belts is due to historical and not geological reasons (Breemen et al., 2006), and as such, work done by Ayer (2002) suggests commonality in ages and rock assemblages within the two greenstone belts and which has led to the Swayze greenstone belt now being regarded as the southwestern extension of the Abitibi (Heather, 2001; Ayer, 2002; Breemen et al., 2006, Thurston, 2008).

The geological evolution of the Swayze greenstone belt consisted of an interplay of volcanic, plutonic, sedimentary, structural, hydrothermal, and metamorphic processes that span between 2750 Ma to 2688 Ma (Heather, 2001). The rocks in the Swayze greenstone belt have been metamorphosed from greenschist to subgreenschist facies with local amphibolite facies rocks found adjacent to synvolcanic and syntectonic intrusions (Heather, 2001; Breemen et al., 2006).

The igneous rocks consist of plutonic and volcanic rocks with mafic to felsic volcanic assemblages with compositions ranging from rhyolitic to komatiitic, while sedimentary rocks occur as clastic and chemical metasedimentary rocks (Heather, 1998, 2001; Ayer et al., 2002; Breemen et al., 2006). The plutonic rocks range from synvolcanic, syntectonic and post-tectonic in age and are found within the greenstone belt as well as in the surrounding granitoid complexes. According to Ayer et al. (2002) and Breemen et al., (2006), both geological mapping and

geochronological studies done in the Swayze greenstone belt support a coherent, upward-facing, autochthonous stratigraphy.

There are six recognized stratigraphic supracrustal groups and 12 associated formations consisting of ultramafic and felsic assemblages that are found within the Swayze greenstone belt with ages ranging from 2740 Ma to 2695 Ma (Heather, 2001; Ayer et al., 2002; Breemen et al., 2006). These are the 2740 Ma Chester, 2735 – 2723 Ma Marion, 2718 – 2713 Ma Biscotasing, 2710 – 2702 Ma Trailbreaker, 2700 – 2695 Ma Swayze and 2690 -2980 Ma Ridout groups that have been correlated with coeval assemblages across the southern Abitibi greenstone belt such as the 2750 – 2735 Ma Pacaud, 2734 – 2724 Ma Deloro, 2719 – 2711 Ma Kidd-Munro, 2710 – 2704 Ma Tisdale, 2704 – 0695 Ma Blake River and the 2677 – 2670 Ma Timiskaming assemblages, respectively (Breemen et al., 2006; Thurston, 2008). Detailed explanation of the correlation of stratigraphic assemblages in the Swayze greenstone belt and the rest of the Abitibi greenstone belt can be found in Thurston et al., (2008).

The stratigraphic section of the Swayze greenstone belt compiled by Heather (2001) is shown on Appendix A and discussed in detail by Heather (2001) and Breemen et al., (2006). The oldest rocks are found in the Chester Group, dated at  $2739 \pm 1$  Ma, which consists of mafic volcanic rocks and are overlain by sedimentary rocks that have been disrupted by younger diorite and tonalite intrusions of the Kenogamissi granitoid complex of  $2722 \pm 1$  Ma (Breemen, 2006). At the top of the Swayze greenstone belt stratigraphic succession lies the Ridout Group that consists of younger sedimentary and volcanic rocks with an age up to  $2688 \pm 2$  Ma. According to Breemen et

al. (2006), sedimentary rocks of the Ridout Group are spatially associated with D<sub>2</sub> and D<sub>3</sub> high-strain zones. Details on the compositions of each stratigraphic group can be found in the following references - Heather, 2001; Ayer et al., 2002; Thurston, 2002, 2008; Breemen et al., 2006. There is currently an ongoing remapping project in the Swayze greenstone belt that aims at improving the current understanding of the geology, stratigraphy and deformational history.

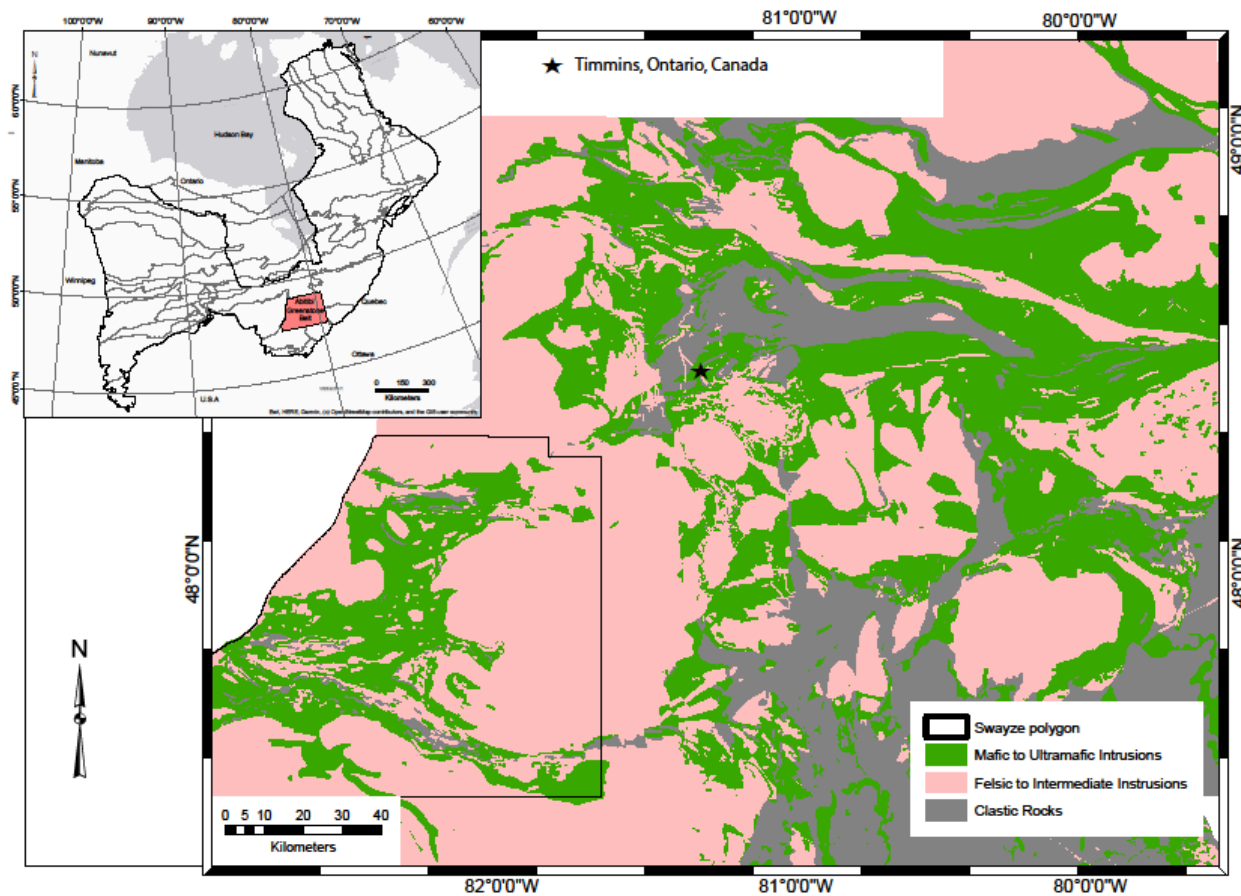


Fig. 3- 1: A simplified regional geological map of the Archean Abitibi greenstone belt found within the Superior Province. The map shows the connection of the Swayze region to the Abitibi greenstone belt by a septum of mafic to ultramafic intrusive rocks (after Ayer et al., 2002, 2005). The thin black line is the outline of the Swayze greenstone belt.

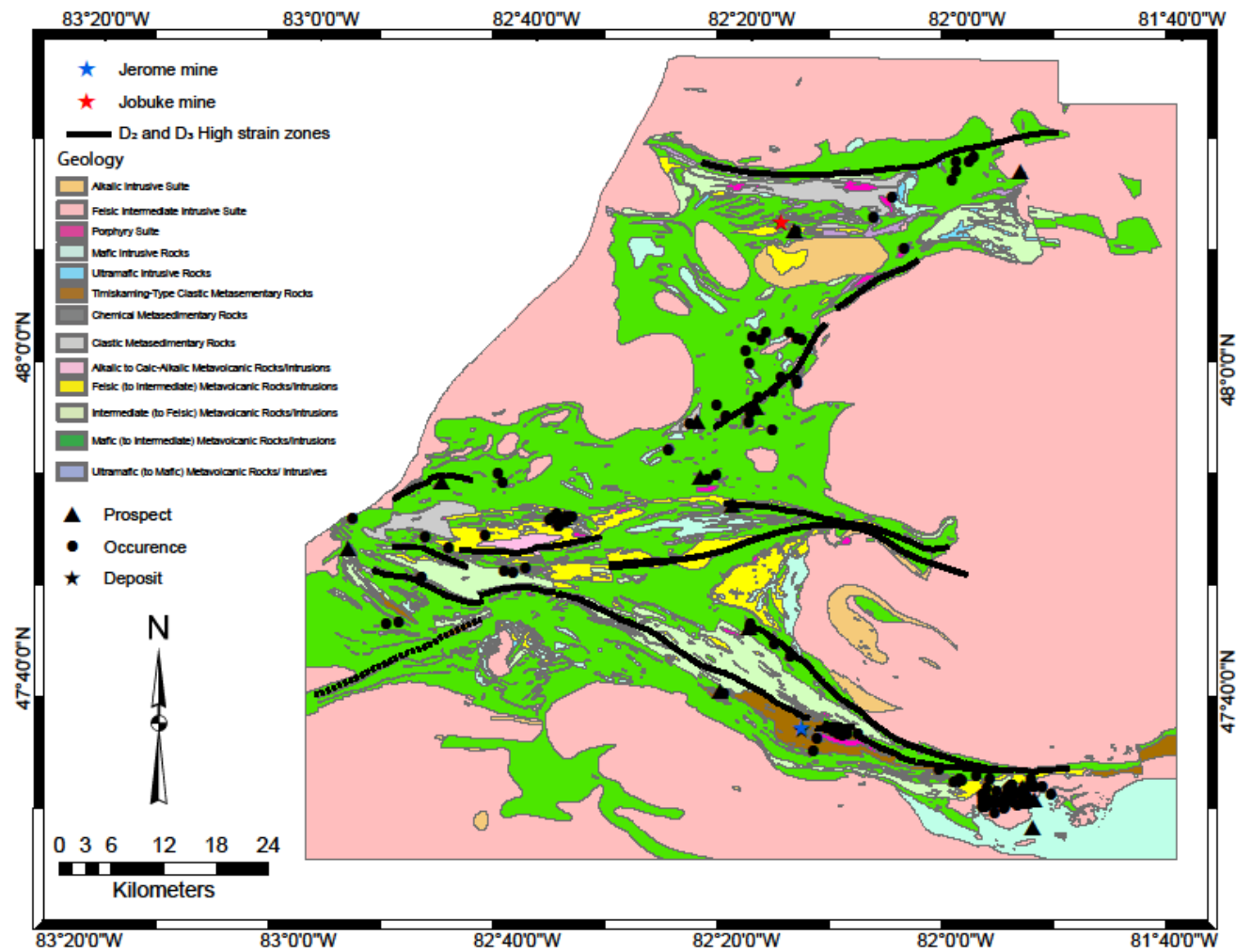


Fig. 3- 2: A) Geological map of the Swayze greenstone belt (after Ayer and Trowel, 2002) showing D<sub>2</sub> and D<sub>3</sub> high strain zones, and locations of gold deposits. The corresponding stratigraphic section is shown on Appendix A.

### 3.2.1 Deformational history of the Swayze greenstone belt

As outlined by Heather (2001) and Ayer (1995), the Swayze greenstone belt has undergone a complex and protracted structural history involving the development of multiple foliations ( $S_1$ ,  $S_2$ ,  $S_3$ , etc.), folds ( $F_1$ ,  $F_2$ ,  $F_3$ , etc.), faulting, as well as the occurrences of major deformational events ( $D_1$ ,  $D_2$ ,  $D_3$ , etc.). According to Heather (2001) the deformation events occurred between 2750 Ma to 2660 Ma. The oldest deformational event  $D_1$  that occurred at 2700 Ma consists of preserved penetrative foliations, intrafolial folds, and contact shear zones (Heather, 2001; Smith, 2016). The second deformational event at 2700 to 2670 Ma resulted in the  $D_2$  high-strain zones (Fig. 3-2) that have a general east-west orientation (Heather, 2001; Breemen et al., 2006). The Ridout high-strain zone has been interpreted as a syn-to late  $D_2$  structure having local association with Ridout Group sedimentary rocks that have been mapped to be associated with the Timiskaming sedimentary assemblages in the Abitibi greenstone belt (Heather, 2001; Ayer et al., 2002).

According to Heather (2001), two types of  $D_2$  high-strain zones are observed in the Swayze greenstone belt, one localised along the limbs of  $F_2$  folds as well as major lithological contacts and another found along the isoclinal geometry of  $F_2$  synclines. Workers in the Swayze greenstone belt have mentioned the occurrences of chloritization, sericitization, sulphidation, carbonatization and tourmalization alterations in some areas along structures associated with the  $D_2$  high strain zones (Heather, 2001; Harris et al., 2000). The  $D_3$  deformation events in the Swayze greenstone belt have prominent N, NE-, ENE- and ESE directions (Heather, 2001). The  $D_3$  deformational events (< 2670 Ma) are associated with NE-striking fractures that are locally associated with felsic and mafic dykes (Heather, 2001).

According to Heather (2001), the Swayze greenstone belt consists of mainly greenschist facies metamorphism; however, transition from amphibolite to greenschist facies metamorphism coinciding with the timing of McOwen and Fawn D<sub>1</sub> high-strain zones and the emplacement of Kenogamissi granitoid complex is also observed. According to Heather (2001), less than 10 % of rocks in the Swayze greenstone belt have experienced amphibolite facies metamorphism. Furthermore, there is retrograde amphibolite to greenschist facies metamorphism along the D<sub>2</sub> and D<sub>3</sub> high-strain zones.

### 3.2.2 Mineral Deposit types in the Swayze greenstone belt

The Swayze greenstone belt hosts a range of Cu-Pb-Zn, Ni-Cu-Fe, Ag and Au prospects and showings, and contains alteration styles, deformations, and mineralization types that are very similar to the mineral-rich Abitibi greenstone belt (Heather, 2001). However, the Swayze greenstone belt lacks significant base metals and precious metals such as Au and Ag (Ayer, 1995; Heather, 2001). The Swayze greenstone belt hosts various gold deposit types ranging from mesothermal, syenite associated, banded iron formation, and greenstone-hosted gold deposits, to intrusion-related gold, similar to gold mineralization in the Abitibi greenstone belt (Fumerton and Houle, 1995; Katz, 2016; Hastie, 2017). The intrusion-related Côté Gold Au(-Cu) deposit is a low-grade large-tonnage deposit hosted in tonalite, diorite and quartz-diorite intrusions (Rodgers et al., 2013; Kontak et al., 2013; Katz, 2016; Smith, 2016).

Current ongoing research suggests that the Jerome, Rundle, and Namex deposits are possibly intrusion-related and are hosted in highly deformed and sheared rock units, along lithological contacts, within quartz veins and near feldspar porphyry units (Fumerton and Houle, 1995; Hastie, 2017; Small et al., 2018). The world-class intrusion related Côté Au-(Cu) deposit is one of the most well studied and documented intrusion-related gold deposits in the Swayze greenstone belt (Kontak et al., 2013; Rogers et al., 2013; Katz, 2016; Smith, 2016).

The gold prospects in the Swayze greenstone belt are hosted in a variety of rocks including feldspar porphyry intrusions and diorites, polymictic conglomerates, iron-rich tholeiitic and breccias, mafic to ultramafic metavolcanics rocks as well as quartz carbonate veins (Fumerton and Houle, 1995; Hastie, 2017). Typical alteration signatures include carbonate, silicification, hematite, chlorite, sericite, and biotite alteration (Hastie, 2017).

The current study was conducted using deposits classified as “mesothermal” according to the 2019 mineral deposit index (MDI) by the Ontario Geological Survey (OGS) (<http://www.geologyontario.mndm.gov.on.ca/index.html>) and Fumerton and Houle (1995). Currently ongoing research studies by Evan Hastie and Daniel Kontak suggests that the Rundle, Namex, and Jerome mines are intrusion-related gold deposits. The original exploration targets in the vicinity of the Côté Au(-Cu) deposit are synchronous with orogenic-style gold mineralization (Rogers et al., 2013; Katz, 2016); however, workers in the region suggest that these gold mineralization’s might actually be of porphyry-type.

The current uncertainty in the deposit type classification of the deposits, prospects, and showings have thus resulted in multiple analysis of orogenic gold prospectivity in the current study. The first analysis is done using the 2019 MDI classification of gold deposits. This classification includes all deposits, prospects, and showings in the Swayze greenstone belt classified as “mesothermal” by the 2019 OGS MDI data. The second analysis is done excluding prospects in the vicinity of the Côté Au(-Cu) deposit and other possibly intrusion-related gold deposits (the Rundle, Jerome, and Namex deposits).

### 3.2.3 Mineral systems analysis of orogenic gold occurrences in the Swayze greenstone belt

#### 3.2.3.1 Exploration targeting approach

The rate of mineral deposit discovery has been drastically decreasing despite massive levels of exploration expenditure (Schodde, 2014, 2017). The low mineral-discovery rate has led the mining and exploration industry to explore for deeper mineral targets in greenfield environments. However, to improve mineral exploration in greenfield environments, the mineral systems approach and processes that operated at regional to district scale to distribute mineral deposits has been developed (Wyborn et al., 1994; Knox-Robinson and Wyborn, 1997; Hronsky and Groves, 2015). Fyfe and Kerrich (1976) were the first to introduce the “systems approach”, however it has become more popular since Wyborn et al., (1994) re-introduced following the establishment and success of the petroleum systems approach used in the oil and gas industry for petroleum exploration (Magoon and Dow, 1991; Wyman et al., 2016).

According to Wyborn et al. (1994), the critical processes that make up a mineral system include: 1) source of the fluid responsible for leaching and transporting metals (meteoric, metamorphic or magmatic fluids), 2) the source of the metals or ores, 3) fluid pathways and traps (high-strain zones and crustal scale faults), 4) thermal and pressure gradient and 5) processes that facilitate deposition. Although mineral systems cannot be observed directly, their expressions and proxies can be translated using available geoscience data in GIS (McCuaig et al., 2010; McCuaig and Hronsky, 2014; Kreuzer et al., 2019).

Recently, the mineral systems approach has been applied in conjunction with MPM as a conceptual approach to help geoscientists to define and express key parameters of a mineral system for the purpose of improving mineral exploration targeting (McCuaig et al., 2010; Hagemann et al., 2016; Wyman et al., 2016; Tessema, 2017; Ford et al., 2019; Groves et al., 2020). Mineral deposits are rare events requiring that their associated mineral systems exist within a fertile lithosphere in the appropriate geodynamic setting (McCuaig and Hronsky, 2014; Groves, 2020). The critical process, constituent process and the targeting element and proxies (such as geoscience predictor and/or evidential maps) that define orogenic gold mineral systems in the Swayze greenstone belt are defined below and in Table 3-1.

#### 3.2.3.2 Source of mineralization fluids and transport ligands

There is no consensus regarding the source of mineralizing fluids associated with orogenic gold deposits due to uncertainty and lack of agreement among various authors. Previous studies postulated several sources of the mineralizing fluid: mantle-derived, magmatic, and metamorphic

devolatilization (Gaboury, 2019; Hagemann et al., 2016; Robb, 2005). Studies by Pitcairn et al., (2006) in the Otago province of New Zealand show that the magmatic-hydrothermal source model cannot fully explain the role of magmatic activity as the source of gold, and magmatic activity cannot provide a universal model for formation of orogenic gold deposits (Pitcairn et al., 2006; Phillips and Powell, 2010; Wyman, 2016; Groves et al., 2020).

The supracrustal metamorphic source model which favours metamorphic devolatilization of hydrated supracrustal rocks at greenschist to amphibolite metamorphic facies has become a generally accepted model for orogenic gold deposits because it corresponds to late metamorphic and deformational timing of gold deposition globally (Goldfarb et al., 2001; Goldfarb, 2015; Groves et al., 2016; Wyman et al., 2016). Evidence from metamorphic devolatilization models of sedimentary rocks (Phillips and Powell, 2010), fluid inclusions (Ridley and Diamond, 2000) and thermodynamic modelling (Tomkins, 2013; Zhong, 2015) shows that sedimentary rocks release large amounts of fluid during transition from greenschist to amphibolite facies metamorphism supporting the devolatilization of sedimentary rocks as sources for orogenic fluids (Gaboury, 2019).

The Swayze greenstone belt is characterized by gold associated with quartz carbonate veining (Ayer, 1995; Heather, 2001) with dominant alterations including Fe-carbonate, sericite, and chlorite (Ayer, 1995; Hastie et al., 2015). All the Archean aged rocks in the Swayze greenstone belt have undergone sub-greenschist to amphibolite facies metamorphism (Heather, 2001) and the metamorphic devolatilization model suggests that the transition between greenschist to amphibolite facies can generate metamorphic fluids (Phillips and Powell, 2010). The exact source of

mineralization fluids and fluid inclusion work in the Swayze greenstone belt is currently still ongoing. Only the intrusion-related Côté Au(-Cu) deposit has been extensively studied and sources of fluids are said to be of magmatic origin (Katz, 2016).

Isotopic studies done by Kerrich (1986) on the mineralization in the Abitibi greenstone belt suggest that gold vein mineralization postdates late alkaline magmatic activities, and the possible source of hydrothermal fluids is late tectonic devolatilization during metamorphism with minor magmatic contributions (Sibson and Poulsen, 1988). Since the Swayze greenstone belt is interpreted to be an extension of the Abitibi, these sources of hydrothermal fluids might hold true in the Swayze greenstone belt as well.

Assay result observations by Hastie (2017) of altered feldspar porphyry veins in the Kenty deposit suggest that gold was originally bound in pyrite and was later remobilized into favourable structural traps, i.e., the mobilization of gold might be due to metamorphic and deformational events. Recent work by Hastie (2020) argues that gold remobilization in the Kenty deposit (Fig. 3-2) might be due to gold being redeposited from a polymetallic sulfide melt and considers unlikely that metamorphic fluids could be the source since metamorphic fluids can only hold less than 100 ppb Au in solution at the Kenty deposit scale (Wagner et al., 2016).

### 3.2.3.3 Source of metals

Orogenic mineral systems are usually found in greenschist to amphibolite facies metamorphosed supracrustal rocks that are structurally controlled with evidence of deep

circulating crustal fluids and strong spatial associations with intrusive rocks (Pirajno, 2008). There is uncertainty and lack of agreement on the source of orogenic gold deposits (Tomkins, 2013a; Gaboury, 2019) with studies suggesting that gold is associated with specific rock types; syenites (Robert, 2001), tonalite-trondhjemite-granodiorite (Katz et al., 2017); and iron-formations (Lambeck et al., 2011) among others (Tomkins, 2013; Gaboury, 2019).

Other suggested sources of gold include primary diagenetic pyrite within sedimentary rocks such as black shale (Pitcairn, 2006; Large et al., 2012; Thomas et al., 2011). Globally, orogenic gold deposits are found in tectonically complex accretionary settings related to subduction of oceanic slab with an underlying sedimentary wedge (Goldfarb and Groves, 2015; Groves et al., 2016; Wyman et al., 2016; Groves et al., 2020). At this geodynamic setting, there is devolatilization of the subducting slab and the oceanic sediment wedge resulting in a release of gold and Ag, As, Bi, Sb, Te and W bearing fluids from pyrite and pyrrhotite in the sediments (Groves et al., 2020). Although Xue et al., (2013), suggest that granitic and other igneous rock types can be the sources of orogenic gold deposits in Archean environments, several authors regard the sedimentary model as a more robust and generally acceptable source of gold (e.g., Gaboury, 2019; Tomkins, 2013).

Gold can be transported by hydrothermal fluids as metal-ligand complexes including chloride ( $\text{Cl}^-$ ) and hydrogen sulfide ( $\text{HS}^-$ ). The hydrothermal fluids are aqueous, dilute, carbonic acid and low salinity fluids with <6 wt. % of NaCl equivalent that contain  $\text{CO}_2 \pm \text{CH}_4 \pm \text{N}_2 \pm \text{H}_2$  and

are generally enriched in S (~1000ppm) but low in Cl (~60 ppm) suggesting metamorphic fluids were formed in the crust (Hagemann and Cassidy, 2000; Kerrich et al., 2000).

Orogenic gold deposits that are found within the Swayze greenstone belts are generally associated with sheared and brecciated felsic intrusive rocks (quartz-feldspar porphyries), quartz veins and intermediate volcanic rocks (diorite). For example, the Jerome mine contains gold hosted in a sheared contact between quartz-feldspar porphyry and epiclastic Timiskaming-type sedimentary rocks (Ayer, 1995). Gold is also associated with chalcopyrite, molybdenite, tetrahedrite, sphalerite and some principal alterations including biotite alteration, hematization, chloritic, carbonatization and silification. At the Rundle mine (a developed prospect with reserves), gold is hosted in cataclastic schist and vein stockworks, and the deposit is associated with the feldspar porphyry intrusive rocks (Hastie, 2015).

Gold is hosted in a variety of rocks that have been sheared and deformed with some mineralization associated with major deformational events (D<sub>2</sub>). Felsic intrusions are believed to be the possible sources of the metal-rich fluids and possibly related to the introduction, remobilization, and concentration of metals in the Swayze greenstone belt (Mamont, 1983). According to Marmont (1983), the possible processes that account for the association of gold with felsic intrusions are: 1) Magmatic association - gold has spatial relationship with felsic intrusions and dikes, so the intrusions may be the source of gold; 2) Metamorphic association - felsic intrusions may have acted as “heat” sources during contact metamorphism, providing heat that caused metal bearing fluid convection; and 3) Assimilation - during emplacement, intrusions may

have assimilated mineralized xenoliths from country rocks. However, Bierlein et al. (2006), suggest that no specific rock type can be considered as the source of gold because available gold can be leached and transported through faults and deposited when the conditions are favorable. Also, Kerrich (1991) noted that some felsic intrusions in the Abitibi greenstone belt pre-date gold deposition and therefore cannot be regarded as sources of gold but rather they serve as physical traps for vein formation (Goldfarb and Groves, 2015).

#### 3.2.3.4 Fluid pathways and conduits

Orogenic mineral systems require a fluid plumbing system that propagates gold bearing fluids to their depositional sites (McCuaig and Hronsky, 2014). Metallogenic provinces hosting world class orogenic gold deposits such as the Abitibi subprovince and the Yilgarn craton have been widely studied and researchers agree that crustal to lithospheric scale faults, shear zones or high-strain zones are required to focus fluids towards their depositional sites (Groves et al., 2005; Goldfarb et al., 2005; Robert et al., 2005; Vearncombe and Zelic, 2015; Groves et al., 2020). Research on fault systems also indicate that the irregularity of major shear zones (such existence of kinks and bends) allows for a transfer of large volumes of fluids through the earth's crust (Vearncombe and Zelic, 2015).

According to Connolly (2010) and Cox (2016), fluid decompression may be the most important event in generating orogenic gold deposits because it helps trigger seismicity resulting in fault reactivation, which allow fluid flow to shallower levels of the crust (Gaboury, 2019). Like

in other Archean orogenic gold deposits, there is evidence that the main pathways for fluids in the Swayze greenstone belt are D<sub>2</sub> high-strain zones, fractures, and faults.

Mineralization in the Abitibi greenstone belt is spatially associated with the D<sub>2</sub> Porcupine-Destor faults and the Cardillac-Larder fault zones. Similarly, the Slate Rock and the Ridout high-strain zones are spatially associated with some gold mineralization in the Swayze greenstone belt (Heather, 2001; Ayer et al., 2002; Hastie, 2017). It is therefore suggested that the large scale D<sub>2</sub> crustal faults may be the regional-scale geological controls that focus fluids to lower-order structures in the Swayze greenstone belt (Breemen et al., 2006; Heather, 2001; Maepa and Smith, 2020). Similar to the Abitibi greenstone belt, the second and third order structures are the district to prospect scale controls of gold mineralization (Heather, 2001; Love, 1991).

Since there is a strong association between structures and gold deposit distribution, the field-based mappable structures as well as faults derived from aeromagnetic data can be used to outline the pathways of deep to shallow circulating fluids. However, there are structures considered to be post-mineralization, and thus, spatial analysis techniques such as Fry analysis and directional distribution were used to determine prominent fault orientations that are spatially and statistically associated with gold mineralization at regional and prospect scales (Parsa and Maghsoudi, 2018; Maepa and Smith, 2020).

An evaluation of controls for gold mineralization using Fry analysis (shown on Fig. 3-3), fractal processes and distance distributions between gold and faults in the Swayze greenstone reveals that gold displays bifractal behaviour at scales <8 km and >8 km. Conclusions by Maepa

and Smith (2020) suggest that 97% of gold being found at distances less than 4 km from second-order faults and fractures, while 96% of gold occur at distances less than 7 km from first-order D<sub>2</sub> high-strain zones. The D<sub>2</sub> high-strain zones and faults are spatially and statistically correlated with mineral deposit distributions with the ESE-WNW, NE – SW, and ENE-WSW strike, which appear to be the preferred orientations of mineral deposits at local to regional scales (Fig. 3-3).

Fry analysis is a spatial autocorrelation technique that can be used to investigate if the spatial distribution of point objects such as gold mines and prospects occur along linear trends. According to this method, for every  $n$  number of points, there would be  $n^2-n$  translations (Hanna and Fry, 1979). Applications of Fry analysis in exploration targeting have proven useful in determining the overall trend of metallogenic processes and the spatial relationships of mineral deposits or prospects (Vearncombe and Vearncombe, 1999; Kreuzer et al., 2007; Carranza, 2009; Parsa et al., 2018; Parsa and Maghoubi, 2018). In this study, Fry translations of mineral prospect distributions are displayed using rose diagram as shown in Fig. 3-3. The scale-integrated Fry analysis gold mines and prospects that was carried out in the Swayze greenstone belt shows that the orientations of mineral prospects vary from ESE - WNW trend to ENE-WSW strike (Maepa and Smith, 2020).

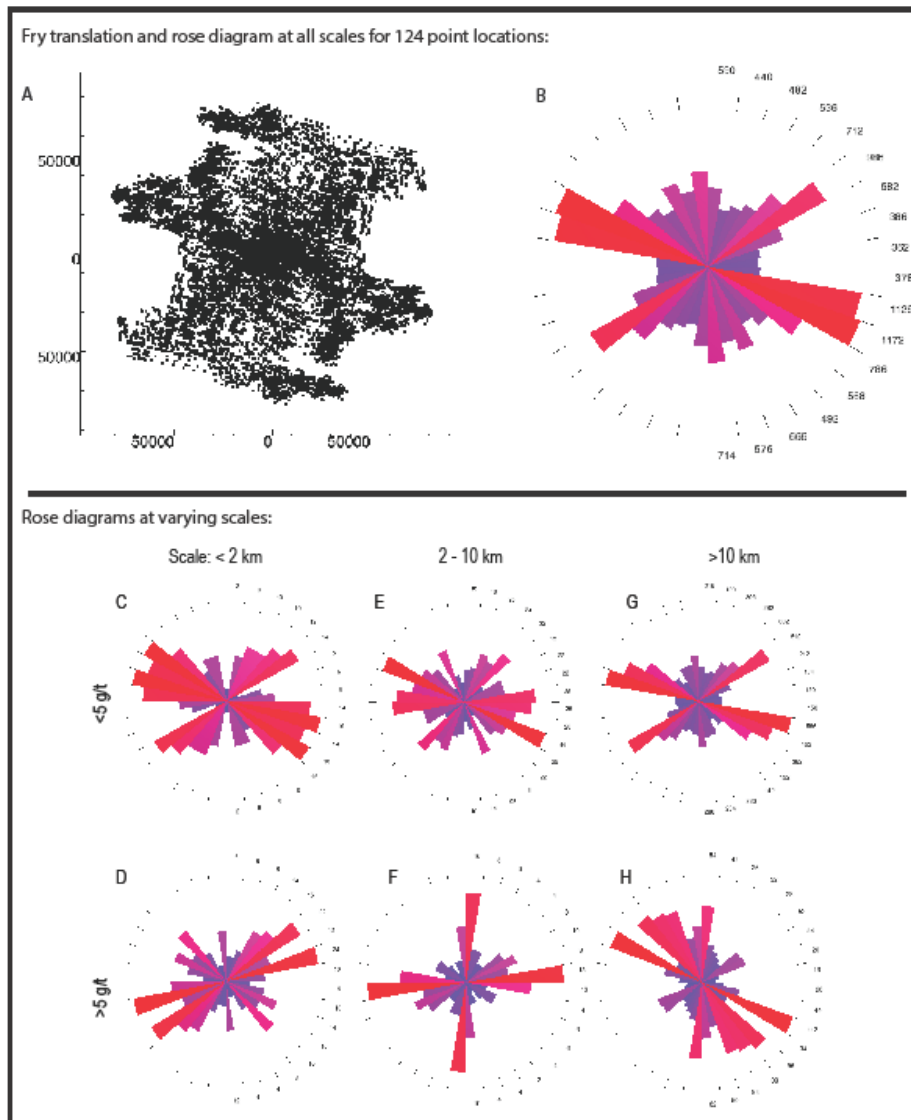


Fig. 3- 3: Fry analysis of all orogenic gold prospects showing a general ESE -WNW and ENE-WSW trend of gold prospect orientations at various scales and grades after Maepa and Smith (2020).

### 3.2.3.5 Mechanisms for gold precipitation

Assuming magmatic-hydrothermal fluid sources, the interaction of hot aqueous fluids with the country rock would result in multiple alteration signatures such as sericite, calcite, chlorite, hematization, silicification, and carbonatization (Gaboury, 2019; Groves et al., 2020). As fluids flow through second and third-order structures and infiltrate planes of weaknesses between lithological contacts, the chemical interaction of hot aqueous fluids with Fe-rich and carbonaceous sedimentary units disturb the  $\text{AuHS}_2$  complexes resulting in metal precipitation (Robb, 2005; Goldfarb and Groves, 2015).

Regardless of the metal-ligand complex in the fluid system, reducing the S content in the fluid, changes in the pH and  $f\text{O}_2$  associated with fluid and rock interactions will affect the solubility of gold resulting in metal precipitation (Gaboury, 2019). Love and Roberts (1991) suggest that the movement of hydrothermal fluids at the Rundle prospect in the Swayze greenstone belt was controlled locally by permeable zones and competency contrast between the felsic porphyry rocks and ductile mafic volcanic rocks. Decreasing temperature and pressure conditions as fluids move through faults and interact with brittle and ductile country intrusive rocks of the Swayze greenstone belt resulted in metal precipitation. The presence of chlorite, calcite and quartz represent reactions of fluids with mafic volcanic and feldspar porphyry rocks which resulted in various alteration signatures that spatially correlate with gold precipitation (Love and Roberts, 1991).

#### 3.2.3.6 Preservation

Finally, to have world-class mineral deposits, there needs to be suitable post-tectonic processes that ensure the preservation of mineralization (Groves et al., 2020). Estimating the degree of preservation is a critical aspect of mineral systems as it can help us determine if deposits remained in their depositional environments or if they were eroded away (Groves et al., 2005).

### 3.3 Methodology

#### 3.3.1 Weights of evidence

Weights of evidence uses Bayesian statistical approaches to define the probability of a variable in question (e.g., a mineral deposit) occurring (Agterberg, 1989; Agterberg, 1990; Bonham-Carter, 1988). Assume that a study area  $A$  covers a 10 000 km<sup>2</sup> extent and contains 100 known areas that contain mineral deposits  $D$ . If each deposit  $D$  is contained within a 1 km<sup>2</sup> cell size, before considering any spatial information such as geoscience datasets, the prior probability that deposits exists in the study area can be expressed using Eq. 1 as outlined by Bonham-Carter (1994a) and Porwal (2006):

$$P \{D| A\} = \frac{P\{D\}}{P\{A\}}, \quad (1)$$

which in our assumed case gives = 100/10 000 = 0.01.

Without any other evidence, this is the probability of a mineral deposit occurring in every cell in the area. If a magnetic intensity map that covers the study area shows that 80 out of 100 mineral deposits lie along high magnetic anomalies, the probability of finding a deposit when there is a high magnetic anomaly increases and the probability decreases when a magnetic anomaly is absent, and thus, the probability of finding deposits in study area  $P\{D\}$  increases and/or decreases on the condition that certain geoscience patterns exists in an area (Bonham-Carter et al., 1989; Bonham-Carter, 1994a). The conditional probability of finding a deposit  $P\{D|E\}$  given the presence of certain geoscience evidence ( $E$ ) can be expressed as:

$$P\{D|E\} = \frac{P\{D \cap E\}}{P\{E\}} \quad (2)$$

where  $P\{D \cap E\}$  is the probability of the deposit and geoscience anomaly existing in the same area, which is proportional to the area where both exist.

The conditional probability increases given that a geoscience anomaly  $E$  exists. The posterior probability is therefore the probability of a mineral deposit occurring after considering spatial evidence,  $E$ . The posterior probability of a deposits occurring in an area when geoscience evidence  $E$  associated with deposits is present can be expressed as (Bonham-Carter, 1994):

$$P\{D|E\} = P\{D\} \times \frac{P\{D|E\}}{P\{E\}}. \quad (3)$$

Conversely, the posterior probability of a deposits occurring in an area when geoscience evidence associated with deposits is absent  $\bar{E}$  can be expressed as:

$$P\{D|\bar{E}\} = P\{D\} \times \frac{P\{D|\bar{E}\}}{P\{\bar{E}\}}. \quad (4)$$

The posterior probability increases and decreases when the geoscience evidence is present and absent, respectively as stated by Bonham-Carter (1994) and Porwal (2006).

The predictor layers that show spatial association with the presence of mineral deposits  $D$  are selected based on the analysis and understanding of the mineral systems involved in the deposition of the metal ore in the study area  $A$ . However, the layers must be spatially correlated with a layer containing the location of known deposits (also known as training points). The input predictor

layers are used to improve the posterior probability value from the prior probability, although it is possible to have layers that do not help improve the posterior probability of the deposit.

In this study, ArcSDM (Spatial Data Modeller), which is an add-on tool to ArcView™ with Spatial Analyst™ were used to carry out the weights of evidence modelling. The weights of evidence model evaluate the spatial relationship between mineral deposits and each input predictor layer such as lithologies, distances from faults, geochemical and geophysical anomalies. The weights defining the spatial relationships between each predictor layer and deposits are computed to determine the weights due to the presence of a mineral deposit  $W^+$ , the weight due to the absence of a mineral deposit  $W^-$  and the strength of the spatial association or the contrast between the two weights,  $W^+$  and  $W^-$ , designated as  $C$ .

Furthermore, the weights of evidence modelling tool computes the studentized contrast, which is the ratio of weights contrast and its standard deviation ( $C/\sigma_C$ ). According to Agterberg et al. (1990), Bonham-Carter (1994) and Porwal et al. (2003), the studentized contrast is an informal measure of certainty that the contrast is correct and therefore provides a more reliable measure of spatial association than the contrast. As stated by Bonham-Carter (1994) a studentized contrast greater than 1.5 or even 2 is ideal. The weight table from weights of evidence can be used to determine the classes with the optimum spatial associations (i.e., high  $W^+$ ,  $C$  and studentized  $C$  values) in multiclass maps (i.e., predictor maps with multiple classes that represent geological features) and thus to determine the cut-off level for converting these maps to binary maps, showing where a deposit is probably present or might be absent. The variance of each  $W^+$  and  $C$  value can

be used to determine the variance and level of uncertainty in the posterior probability maps (Bonham-Carter, 1994).

### 3.3.2 Artificial neural networks (Radial Basis function Neural Networks)

Artificial neural networks techniques were first introduced in the 1940s by McCulloch and Pitts (1943). This technique was designed to emulate the human brain and nervous system in order to learn and classify complex patterns (Andina and Pham, 2008). There are several forms of neural network methods that have been used over the years (McCulloch and Pitts, 1943; Rosenblatt, 1958; Sarle, 1994; Basheer and Hajmeer, 2000; Looney, 2002; Nykänen, 2008; Tessema, 2017), including: multi-layer perception (MLP), probabilistic neural network (PNN), adaptive resonance theory network (ARTN), and more recently radial basis function neural network (RBFNN).

Radial basis functions (RBF) are functions whose responses increase or decrease with distance from a central point  $v$ . A standard form of RBF states that every point  $x$  equidistant from the center  $v$  will yield the same value  $y$ , thus: each  $(x_n, v) \in D$  influences  $y$  based on  $\|x-v\|$  (Orr, 1996; Looney, 2002). The RBF is a Gaussian activation function, with a center  $v$  and a spread parameter  $\sigma$ , which determines the size of the receptive field for RBF as shown on Eq. 6 (Broomhead and Lowe, 1988; Looney, 2002; Porwal et al., 2003) expressed by:

$$y = f(x, v) = - \exp[-\|x - v\|^2 / (2\sigma^2)] . \quad (6)$$

where  $x$  is the vector at the center  $v$  and  $\sigma$  is the spread of the radial receptive field (Looney, 2002). The RBF learning algorithm attempts to find parameters weights  $w_1, \dots, w_N$  that minimises error based on the input training data  $D = (x_1, y_1), \dots, (x_N, y_N)$

$$y = \sum_{n=1}^N w_n \exp [-\gamma \|x - v\|^2 / (2\sigma^2)] . \quad (7)$$

RBFNN is a 3-layer feed-forward non-linear neural networks algorithm (Fig. 3-4A) that consists of an input layer of  $N$  nodes that receives an input feature vector (such as predictor layers), a hidden layer of  $M$  neurons evaluated with an RBF Gaussian activation function, where the input feature vectors are processed and multiplied by synaptic weights produced by the model, and an output layer of  $J$  neurons where the input feature vector is output as a weighted sum average (Looney, 2002; Porwal et al., 2003).

These weights  $u_{mj}$  are the learned weight (gains) applied on the neural network lines which indirectly and directly connect to the outputs. There are also added constants,  $b_j$ , to account for the bias at each output node, which are intended to adjust the output and the weighted sum in an effort to help improve the model performances (Looney, 2002):

$$z_j = \frac{1}{M} [\sum_{m=1}^M u_{mj} y_m + b_j] \quad (8)$$

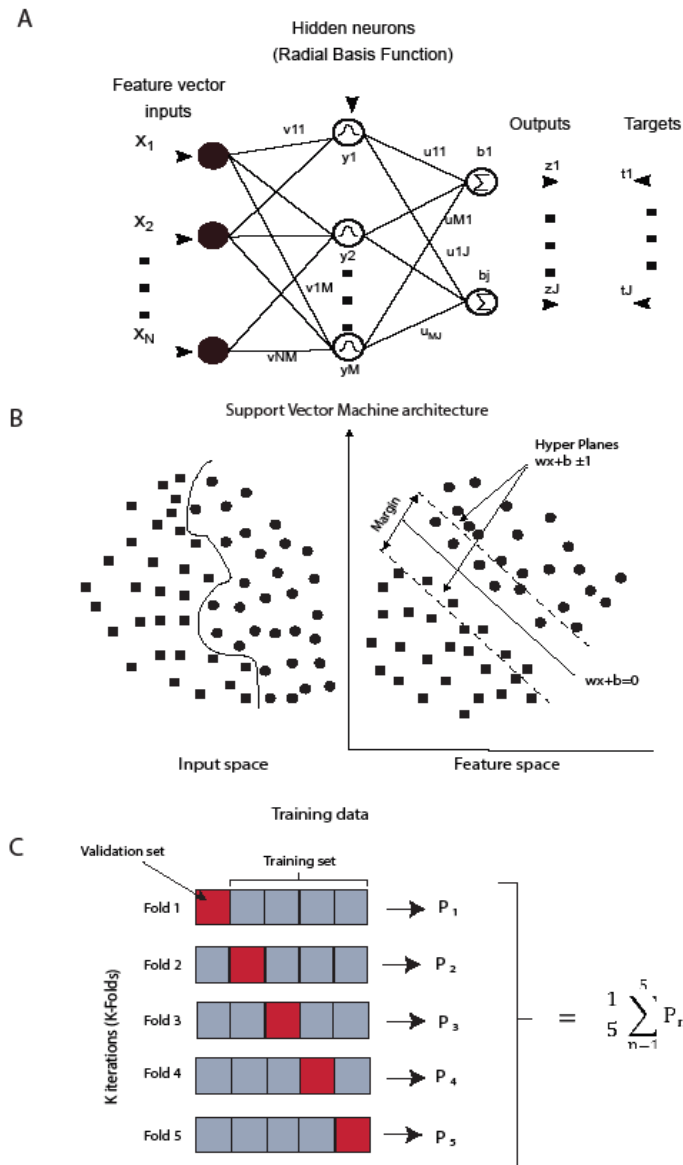


Fig. 3- 4: A) Simplified illustration of the architecture of radial basis function link nets (after Looney, 2002); B) Support vector machine architecture showing the optimum hyperplane for a two-class problem (after Zue and Carranza, 2011); C) Illustration of K-fold cross validation technique whereby  $k=5$  subsets of training and validation data (Kubat, 2017).

In the hidden layer, the elements of the input feature vectors are multiplied by a synaptic weight ( $u_{nj}$ ) which are generated by the model to produce an output layer. The weights are refined by the model in an iterative fashion during training. The algorithm reduces the errors obtained with each iteration by modifying the connection weights to suit the input target values of the deposit and non-deposit points (Looney, 2002).

A variance-based feature importance is used in this study to determine the most contributing predictor layers for mapping gold prospectivity using RBFNN. The variance-based feature importance function introduced by De Sá (2019) provides the changes in weights during neural network training with the assumption that the more important a feature is, the more the weights in a neural network will change during training. The method thus records the variance of every weight connected to the input layer during training and combines with the final layer to obtain a measure of relative feature importance (De Sá, 2019).

### 3.3.3 Support Vector Machines (SVM)

Support Vector Machine is a data-driven supervised machine learning algorithm designed for outlier detection and pattern recognition for solving classification and regression problems. The SVM is a heuristic algorithm based on the statistical learning theory (Vapnik, 1995). The main aim of a SVM algorithm is to find the optimum hyperplane i.e., decision boundary in N-dimensional space that can distinctly separate data points (Fig. 3-4B).

Furthermore, the SVM looks for a hyperplane with the largest maximum distances between data points of different classes i.e., the maximum margins. The support vectors are the data points that lie closest to the hyperplane (as shown on Fig. 3-4B) and determine the orientation of the hyperplane. The dimension of the hyperplane decision boundary depends on the number of input features that require classification (Abedi et al., 2012). For supervised machine learning purposes, the SVM uses prior known class labels i.e., deposit and non-deposit locations to create a hyperplane that can separate input feature data i.e., various geoscience predictor information into multiple classes (Zuo and Carranza, 2011; Abedi et al., 2012).

The definition of a SVM in a two-feature classification problem that involves training set of data containing  $l$  feature vectors, where  $\mathbf{x}_i \in \mathbf{R}^n$ , where  $i (=1,2,3. \dots, n)$  is the number of feature vectors in the training samples. Each sample is assigned to class labeled  $\mathbf{y}_i$  which is equal to 1 for one class and -1 for another class and thus  $\mathbf{y}_i \in \{-1, 1\}$  (Huang et al., 2002; Zuo and Carranza, 2011). If the two classes are linearly separable, a hyperplane i.e., linear separating boundary can derive the classes.

The details of the equations used for separating hyperplane and the SVM algorithm can be found in Vapnik (1995), Tax and Duin (1999), Kavzoglu and Couلكesen (2009), and Zuo and Carranza (2011). There are multiple kernel functions that can be used for computing an SVM classification as discussed by Kecman (2005) and Zuo and Carranza (2011).

In this study, the scikit learn python machine learning library (<https://scikit-learn.org/stable/modules/svm.html>) is used to construct a linear kernel SVM algorithm to map

prospectivity of orogenic gold deposits in the Swayze greenstone belt. With a linear SVM kernel, it is possible to obtain the coefficients (i.e., weights) of the SVM classifier used during training. The absolute sizes of the coefficients help to identify the main features used during classification and thus enable determination of the most contributing predictor layers (Chang and Lin, 2008). The neural network variance-based feature importance function is compared with SVM feature importance estimations.

#### 3.3.4 Model cross validation

Various model cross-validation methods exist to assess the performance and reduce overfitting, such as the leave-out approach and the K-Fold cross-validation method. This study uses the K-Fold cross-validation method for evaluating the performance of the RBNN and SVM methods.

In the leave-out approach (also known as the train test split approach), the target data (i.e., known prospect locations) are randomly split into training and testing sets, ideally the data split is done at 80:20 or 75:25. The model is trained on the training set and the test set is used to evaluate the model's predictive power. The leave-out method has a possibility of introducing bias if there is limited target data.

The K-fold cross validation method generally results in less model bias because the method ensures that the original target information gets a chance to appear in the training and testing set (Kubat, 2017). With the K-Fold cross validation procedure, the target data is split into  $k$  subsets of training and test set as shown on Fig. 3-4C. For example,  $k=5$  means that the data is split into 5

groups, each group gets a chance to participate as a training set and testing (Kubat, 2017). For example, Fold 1 in Fig. 3-4C, groups labelled 2, 3, 4, and 5 are used to train the model while the 1<sup>st</sup> group is used as a testing set. This procedure is done  $k$  times, until all the groups are used as training and test sets. The model performance scores are obtained from each  $k$  fold performance. The mean of the model performance is calculated and used to deduce the overall model performance.

The stratified K-fold cross-validation technique used in this study is a type of K-Fold cross-validation procedure that works to rearrange the data to ensure that each fold contributes to training. The stratified K-Fold cross-validation methods are used frequently in machine learning to avoid model overfitting and data splitting bias. The stratified k-fold procedure used in this study was done is achieved using the scikit-learn library in python (<https://scikit-learn.org/>). The performance of both the RBFNN and the SVM models were evaluated using the stratified K-fold procedure. For RBFNN, the training and validation accuracies and loss (i.e., mean squared error) at each iteration for every  $k$  folds were computed. The mean performance scores after  $k$  number of folds are used as the overall performance of the model.

The receiver operator characteristic curve referred to as ROC curves is used to evaluate the validity of a diagnostic test (Obuchowski, 2003) or a predictive model (Nykänen, 2008, Parsa et al. 2018). A ROC is computed by plotting the sensitivity (the true positive rate) and the 1-specificity (the false positive rate) of a predictive model (Obuchowski, 2003). True positives are values that the model correctly classified to be true and false positive are the false values the model

incorrectly classified as true. The values for the true positive and false positive rates are derived from considering the known deposit and non-deposit areas that were not used to train the model.

The area under the ROC curve (AUC) is used to measure the accuracy and performance of a predictive model. The AUC values vary between 0 and 1, whereby a value of 1 indicates that the model's performance was highly accurate in computing the sensitivity and 1-specificity of a diagnostic test/predictive model (Nykänen et al., 2015), where the sensitivity represents the true positive rate and specificity is an estimate of the true negative rate of a diagnostic test. A completely random model performance would result in an AUC value of 0.5. The sensitivity and 1-specificity of a model can only be determined if adequate deposits and non-deposit sites are available. The RBFNN and SVM machine learning model performances are further evaluated by computing the area under the receiver operator curve (ROC) at each fold. The mean area under curve value of all  $k$  folds is computed as a measure of model performance.

### 3.4 Datasets used and their significance in the Swayze greenstone belt mineral system

#### 3.4.1 Data sources

A variety of datasets obtained from numerous sources that include the Ontario Geological Survey (OGS), which is part of the Ministry of Northern Development, Mines and Forestry (MNDMF) and the Geological Survey of Canada (GSC) were used (Table 3-1). Data processing involve preprocessing and compilation of all available relevant data covering the study area.

### 3.4.2 The distribution of mineral deposit locations and non-deposit data selection

The 2019 MDI together with a database compilation by Fumerton and Houle (1995) consisting of locations of gold deposits prospects showings, and occurrences was used for training RBFNN and SVM. The details of each deposit, prospect and occurrence used in this study are shown on Appendix B.

According to Fumerton and Houle (1995), and the MDI files, the gold locations were grouped into various classes whereby “prospect” was used to refer to an area where exploration has been proposed for mining on a trial basis, “showing and/or occurrence” refers to gold mineralization observed in outcrop or within core samples, and “deposit” refers to regions where gold reserve calculations and feasibility studies have been done. Inactive and active mines were also included in the mineral deposit inventory database. The ranking of the data is therefore subjective and depends on the interpreter’s opinion of the data (Fumerton and Houle, 1995).

For this study, locations of mineral deposits, prospects, and showings were used for training the machine learning algorithms. The gold deposits, prospects, and showings were given rankings between 0 and 1 for the purpose of training machine learning algorithms. Non-prospect locations are points that have been selected to show areas that are most likely unmineralized or known to be no deposits. Selecting these areas can be difficult because they require some sort of ground truthing such as drilling to ensure the absence of a mineral deposit (Porwal et al., 2003; Tessema, 2017).

For generating non-deposit data, a set of randomly distributed points were generated, keeping the location of each point far away from existing mineral deposits, structures and outside the permissive lithological tract (Parsa et al., 2018a, b; Roshanravan et al., 2020). The term “prospect” is used collectively in this study to refer to all classes from showing to mine.

This study created two categories of mineral prospectivity maps. The first group of prospectivity maps used all prospects currently classified as “mesothermal” by currently published work to model orogenic gold prospectivity. The second group of prospectivity maps are derived with prospects, except that those which are suggested to possibly be intrusion-related or porphyry-type have been removed. Specifically, ongoing work proposes that prospects found southeast of the intrusion-related Côté Au(-Cu) deposit might be porphyry-type, and that the Rundle, Namex and Jerome mines/prospects are intrusion-related.

Table 3 - 1 Key datasets used and corresponding description of types, formats and sources.

Dataset	Type	Format	Source	Data description
Mineral deposit index	Gold deposits, mines, prospects, and occurrences	Points	Ontario Geological Survey	Gold deposit occurrences, showings, prospects, and mines
Geology	Bedrock geology	Polygons, and raster	Ontario Geological Survey	Solid 1: 100 000 geological maps compiled by Ayer and Trowell 2002
Geochemistry	Lithogeochemical data	Points, and raster	Geological Survey of Canada	Lithogeochemical dataset containing major oxide and trace element data
Geophysics	Magnetic (1st and second order derivative maps, and analytical signal map) Electromagnetic (decay constant map)	Raster	Ontario Geological Survey	Magnetic and electromagnetic data with Line spacing of 200 m
Structures	High strain zones, faults, and shears	Polylines and raster	Ontario Geological Survey	Structural data compilation mapped in the field and interpreted using geophysics

Table 3 - 2: List of evidential datasets and corresponding weight statistics from the weights of evidence model.

Evidential layers	Description	Weights of evidence statistics					Correlations with gold
		Area (sq. km)	W+	W-	C	Stud C	Field and statistical observations
Lithological data							
Mafic (to intermediate) Metavolcanic rocks	Massive, pillowed, and variolitic flows. High iron tholeiite, tuff breccia and calc alkalic rocks	2083.58	0.67	-0.33	1	5.53	Au is spatially associated with mapped unit
Timiskaming-type lastic metasedimentary Rocks	Arenite, conglomerate, and wacke	66.46	1.72	-0.03	1.75	3.84	Au is spatially associated with mapped unit
Felsic (to intermediate) Metavolcanic intrusions	Tholeiite, massive flows, and tuff breccia	199.25	1.21	-0.05	1.26	3.64	Au is spatially associated with mapped unit
Porphyry Suite	Quartz feldspar porphyry, tonalite, and granodiorite	29.26	1.62	-0.01	1.64	2.29	Au is spatially associated with mapped unit
Permissive lithologies	Distances from permissive lithologies	4707.05	0.06	-1.39	1.46	2.04	Au occurs within 2 km from permissive lithologies
Lithological contacts	Distances from lithological contacts	5601.13	0.11	-2.41	2.53	2.51	Au occurs within 2 km from lithological contacts
Structural data							
First-order D <sub>2</sub> and D <sub>3</sub> high strain zones	Distances from first-order high strain zones (e.g., the Ridout and Slate Rock HSZ)	3663.58	0.17	-2.74	2.91	2.90	Au is spatially correlated within 6450 m from D <sub>2</sub> and D <sub>3</sub> high strain zones
D <sub>2</sub> and D <sub>3</sub> folds	Distances from D <sub>2</sub> and D <sub>3</sub> folds	4683.72	0.07	-2.01	2.09	2.08	Au has statistically positive spatial correlation at distances within 8.5 km from folds
		4522.65	0.53	-3.95	4.48	4.46	

Faults mapped in the field	Mapped (Heather, 2001;							Au occurs at distances within 5km from faulting
Faults interpreted from magnetics	Breemen et al., 2006) and faults interpreted using aeromagnetic data (distances up to 5 km)							

Geophysics data

Distances from reduced to pole magnetics worms (up to 2 km distances from anomalies)	Linear anomalies reflect faulting, sulfide conductors and iron formations (Harris, 2002)	3754.78	0.67	-2.54	3.21	7.04	Au is spatially associated with high magnetic anomalies (100% gold is found within 2.5 km distances from high magnetic anomalies)
--	--	---------	------	-------	------	------	---

Electromagnetic decay constant map (up to 4.5 km from anomalies)	Decay constant reflects conductive surfaces	4757.77	0.45	-3.81	4.26	4.24	Au is spatially associated with conductive surfaces (100% gold found within 5 km distances from conductive features)
--	---	---------	------	-------	------	------	--

Geochemical data (lithochemochemistry)

Major oxide (SiO <sub>2</sub> , MgO, CaO, K <sub>2</sub> O, Na <sub>2</sub> O, FeO) alteration maps	Spitz-Darling alteration (K <sub>2</sub> O+NaO/Al <sub>2</sub> O <sub>3</sub> )	759.67	1.16	-0.27	1.43	6.40	Good spatial correlations
Principal component maps of major oxide	Geochemical principal component 1 (PC1)	201.99	2.01	-0.19	2.19	8.37	Good spatial correlations

### 3.5 Predictor maps and their spatial association with gold based on weights of evidence statistical results and mineral-systems expressions

#### 3.5.1 Proximity to permissive lithologies

Field evidence and exploratory studies by Fumerton and Houle (1995) suggest that orogenic gold prospects in the Swayze greenstone belt are hosted in a variety of lithologies (Fig. 3-2) including iron-rich tholeiitic basaltic rocks, feldspar-porphyry rock units, ultramafic to mafic metavolcanics, and quartz-carbonate veins. From a mineral systems perspective, iron-rich lithologies are favourable for acting as chemical traps in orogenic mineral systems because they have high susceptibility to brittle deformation resulting in a complex set of fractures within which metal-bearing sulfide-rich fluids can react with iron-rich porous rocks to form pyrite, destabilizing the AuHS<sub>2</sub> complex and facilitate metal precipitation (Robb, 2005; Groves et al., 2020).

This study reviewed the statistical relationship between orogenic gold-prospect distributions and all mapped lithologies in the Swayze greenstone belt using weights of evidence method. The overall spatial correlation between orogenic gold prospects and lithologies in the Swayze greenstone belt are shown on Table 3-2. The permissive lithologies with >1.96 studentized contrast (shown on Table 2) were used for further analysis of gold prospectivity. A proximity to host lithologies predictor map (Fig. 3-5) was used as input layer for machine learning prospectivity analysis.

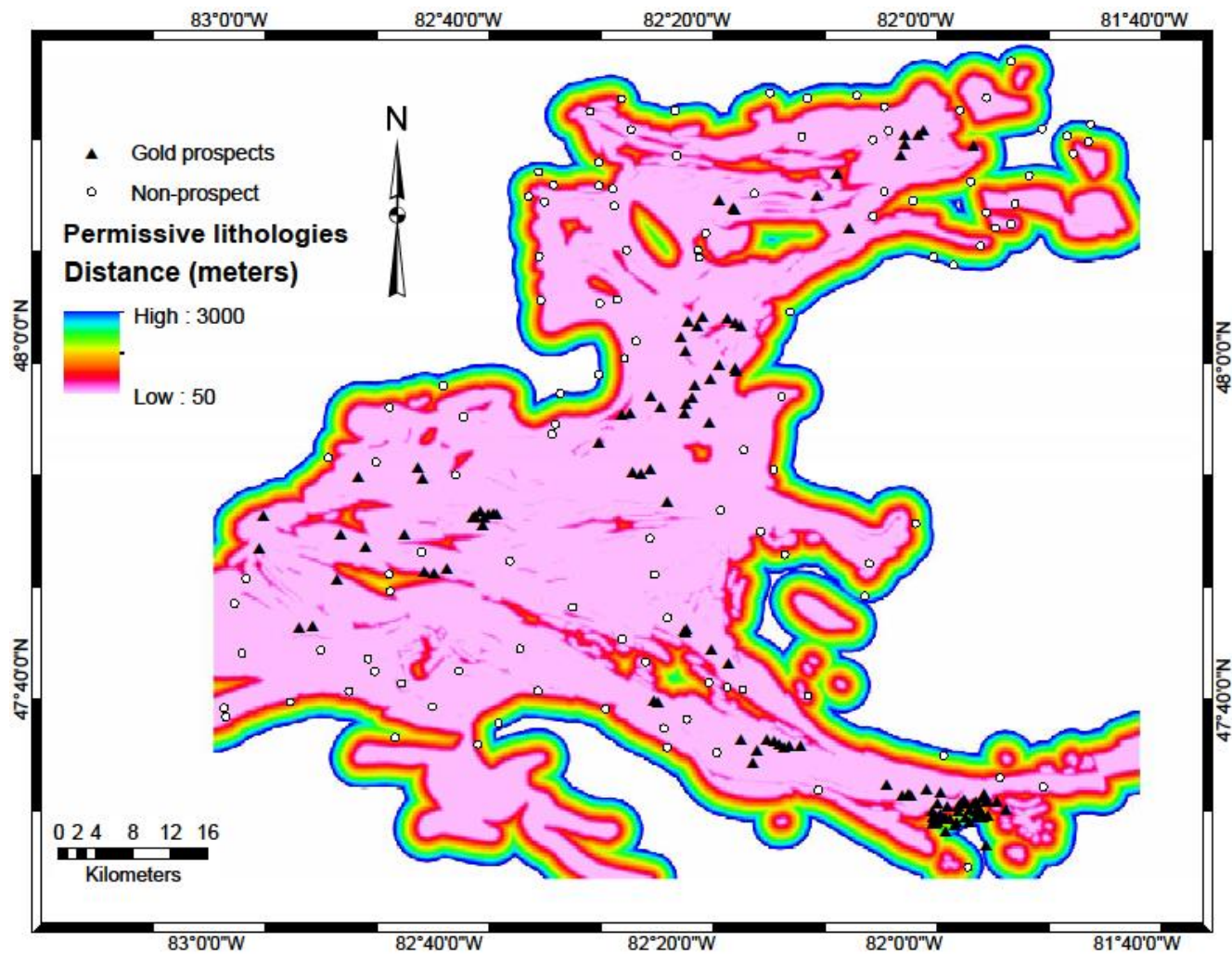


Fig. 3- 5: Proximity to permissive lithologies.

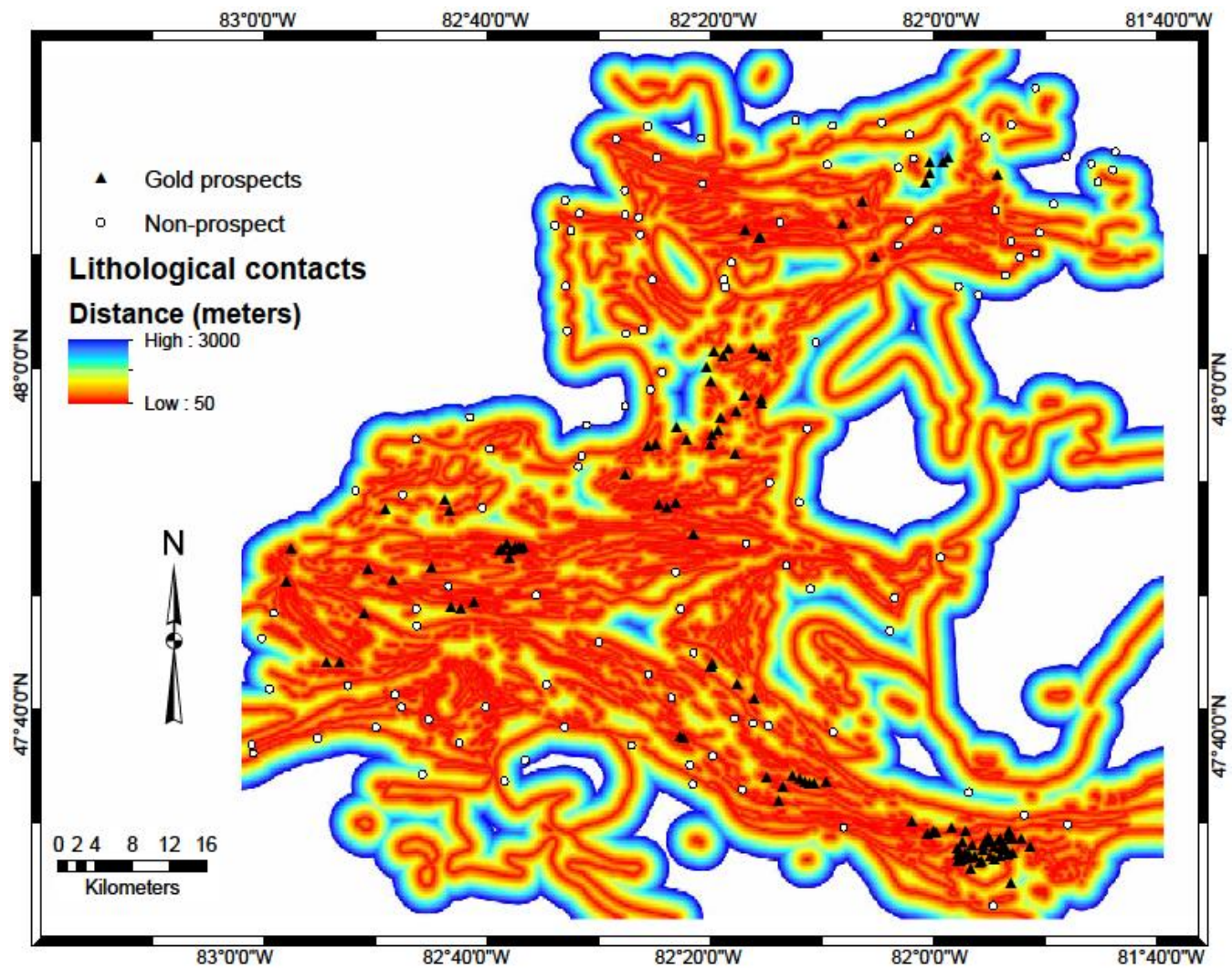


Fig. 3- 6: Proximity to lithological contacts

### 3.5.1.2 Proximity to lithological contacts

According to Groves et al. (2019), metal precipitation from hot aqueous hydrothermal fluids can occur along lithological contacts, and competency contrast between lithologies. Contacts between lithologies such as granitic intrusions and sedimentary rocks represent planes of zone of weaknesses that can localise fluid flux and become the locus of gold mineralization (Groves et al., 2019). In the Jerome deposit, gold prospects are also found along contacts of feldspar porphyry rocks and polymictic conglomerates (Fumerton and Houle, 1991; Hastie et al., 2015; A map of proximity to lithological contacts (Fig. 3-6) reveals that gold may occur at a distances less than 2 km away from contacts (Table 3-2).

### 3.5.3 Structures

#### 3.5.3.1 Proximity to D<sub>2</sub> and D<sub>3</sub> high strain zones

As discussed in section 1.2.1, the Ridout and Slate Rock D<sub>2</sub> high-strain zones in the Swayze greenstone belt are the westward extensions of the gold-rich Porcupine-Destor fault zone and Cardillac-Larder fault zones, respectively in the Abitibi greenstone belt (Heather, 2001; Breemen et al., 2006). A multi-scale spatial analysis of the control of orogenic gold prospects by Maepa and Smith (2020) confirmed that the D<sub>2</sub> high-strain-zones were the primary (1<sup>st</sup>-order) control of gold mineralization, while the influence of D<sub>3</sub> high-strain zone has less significance relative to the D<sub>2</sub> event in controlling the localization of orogenic gold. However, according to Heather (2001), both the D<sub>2</sub> and D<sub>3</sub> events offer potential for hosting gold mineralization.

A map of proximity to high-strain zones that are first-order controls of orogenic gold prospect was included as a predictor layer for gold prospectivity mapping (Fig. 3-7). The weights of evidence statistics indicate that orogenic gold prospects occur within a 6.5 km distance range from both D<sub>2</sub> and D<sub>3</sub> high-strain zones.

#### 3.5.3.2 Proximity to D<sub>2</sub> folds (i.e., F<sub>1</sub> and F<sub>2</sub> folds)

The D<sub>2</sub> deformational event resulted in regional folding and shearing (Heather, 2001) which can be observed from the occurrence of F<sub>1</sub> and F<sub>2</sub> folds cutting across the Swayze greenstone belt in an E-W strike. The map pattern of the Swayze greenstone belt is preserved by regional E - to ESE striking F<sub>2</sub> folds, synclines and anticlines that were interpreted to have formed during orogen-wide shortening (Breemen et al., 2006). According to Heather (2001), the F<sub>2</sub> folds occur along lithological contacts and high rheological contrast between intrusive rocks and greenstones resulting in distinctive cusped-lobate fold geometries. The folding and shearing along bedding planes make folds good conduits for fluid flow and thus the proximity from mapped F<sub>2</sub> folds were included as a predictor map (Fig. 3-8). The results of weights of evidence indicates that there is statistically significant spatial correlation between gold prospects and F<sub>2</sub> within a distance range of 8 km.

### 3.5.3.3 Proximity to faults

The structural field map of Heather (2001) was revised and combined with the faults interpreted from quantitative interpretations of reduced to pole aeromagnetic data (Fig. 3-9). The fault interpretations were done by calculating the 1<sup>st</sup>, 2<sup>nd</sup> and 3<sup>rd</sup>-order vertical-derivative maps and analytical-signal maps from a reduced-to-pole total intensity map. The derivatives were imported into a GIS and using various color gradients and hillside data enhancements to these images, it was possible to interpret and digitize linear structural features, and offsets / displacements in geological features. The interpreted faults and mapped discontinuities were compared and evaluated using the current geological map and faults previously mapped in the field by Heather (2001), and published by Ayer and Trowell (2002).

Fry analysis was applied to discrete points that represent the mineral prospects in the area. The resulting Fry analysis provided the major orientation of the patterns of orogenic gold prospects in the area. The faults that are consistent with the major orientations of the Fry analysis were considered as possible pathways along which a mineralized fluid interacted with the host rocks. The results obtained from Maepa and Smith (2020) were used to generate an optimum buffer distances map. According to the weights of evidence statistics, gold prospects occur within 5 km distances from mapped and interpreted faults with a studentized contrast value of 4.46 (Table 3-2).

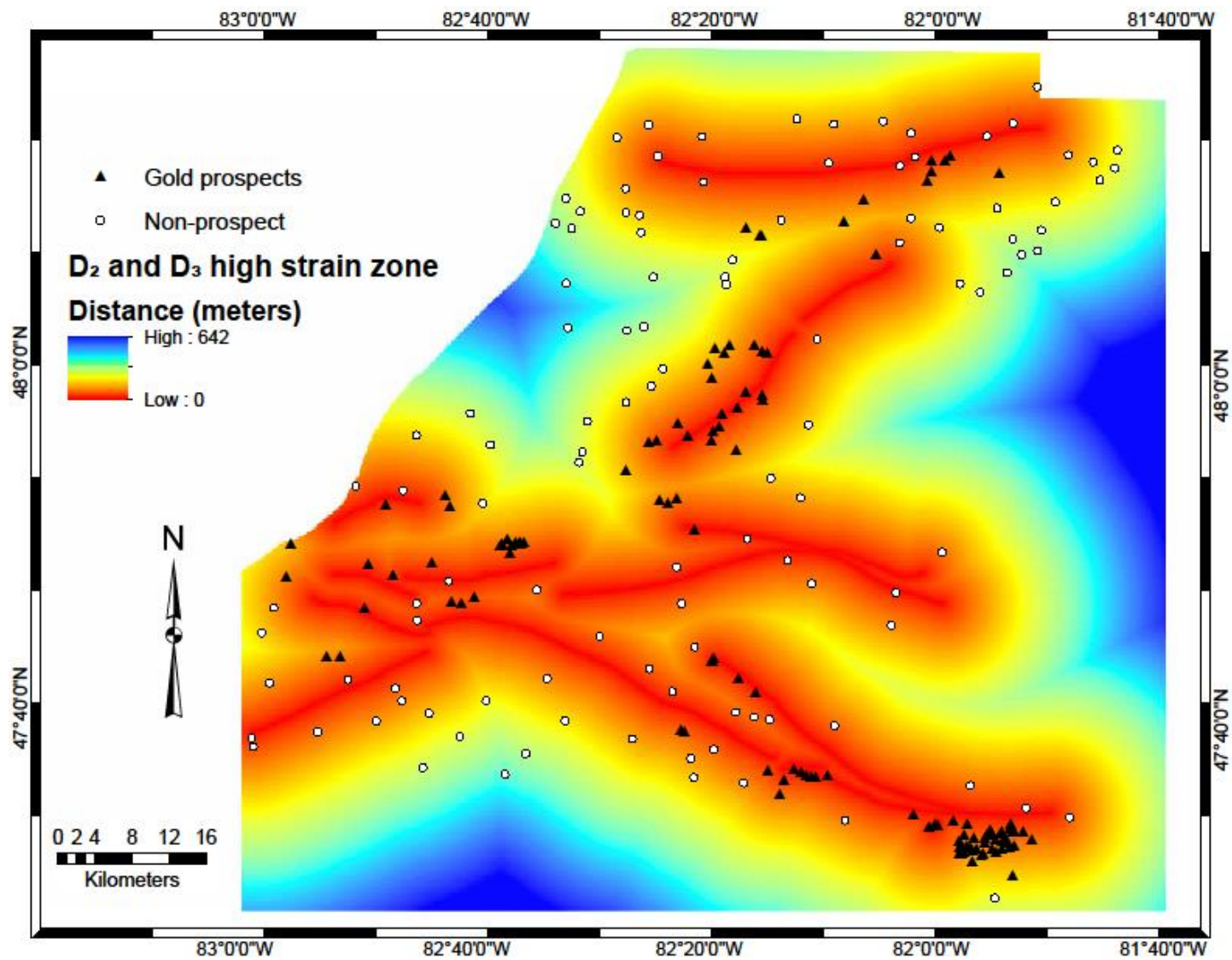


Fig. 3- 7: Proximity to D<sub>2</sub> and D<sub>3</sub> high strain zones.

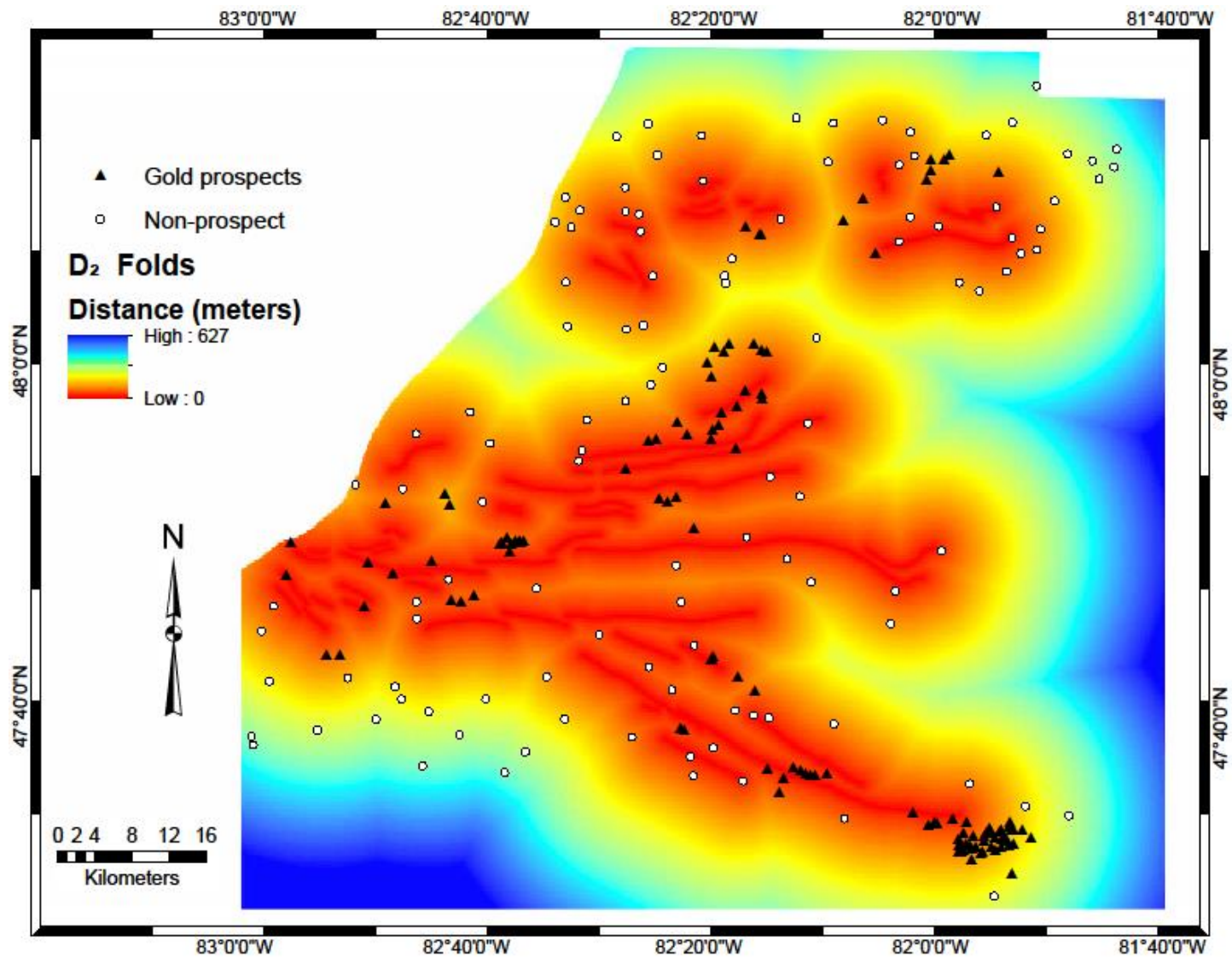


Fig. 3- 8: Proximity to D<sub>2</sub> folds

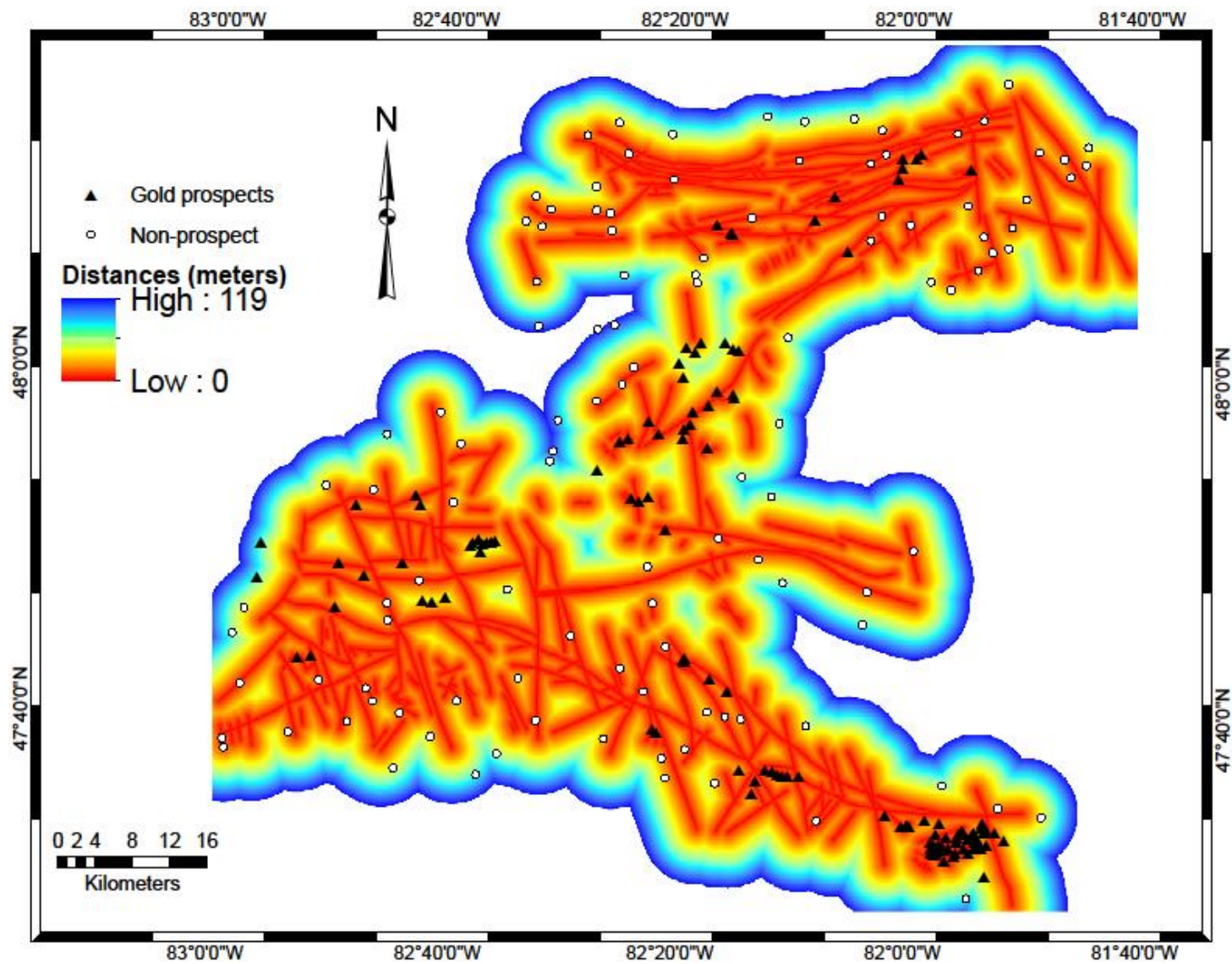


Fig. 3- 9: Proximity to faults.

### 3.5.4 Geophysics

#### 3.5.4.1 Aeromagnetic data: Proximity to magnetic worms

The data preprocessing steps for aeromagnetic data involved removal of the regional using the international geomagnetic reference field (IGRF), micro-levelling, and levelling the data to the Ontario master aeromagnetic grid. The reduced to pole (RTP) total magnetic intensity (TMI) map was used to determine regions with high magnetite content or destruction of magnetic susceptibility of rocks caused by interaction between hydrothermal fluid and the host rocks.

This allows to map areas where fluid-rock interaction destabilized gold-metal ligand complexes, which probably created a condition for precipitation of metals such as gold and associated minerals. Regions with high magnetic anomalies spatially correlate with i) chemical metasedimentary rocks which represent iron formations, and sulfide facies, and ii) mafic and ultramafic intrusive rocks (i.e., gabbro, peridotites and pyroxenitic rocks).

To generate magnetic worms, the RTP TMI data was upward continued (Fig. 3-10) to multiple elevations (i.e., 2 km, 2.5 km, 3 km, 3.5 km and 4 km), and the first-vertical derivative was calculated at each upward continuation level. The RTP total magnetic intensity magnetic worms map (Fig. 3-11) was created to represent multi-scale edges from the potential-field data (Roshanravan et al., 2020; Archibald et al., 1999; Fitzgerald and Paterson, 2013). The magnetic worms extracted from 2 km upward continuation (UC) were interpreted to represent upper crustal (i.e., within 1 km depth) fluid pathways and shear zones at the current erosional level.

Orogenic gold prospects form at a depth  $> 2$  km within the earth's crust and thus, upward continuation up to 2 km (Fig. 3-10) would help reveal structures operating between 1 -2 km below the current surface-level exposure. A proximity to magnetic worm's map (Fig. 3-12) was generated to show spatial statistical correlations. According to the studentized contrast (Table 3-2), there is a high spatial correlation between magnetic worms and gold prospects within a distance range of 1750 m.

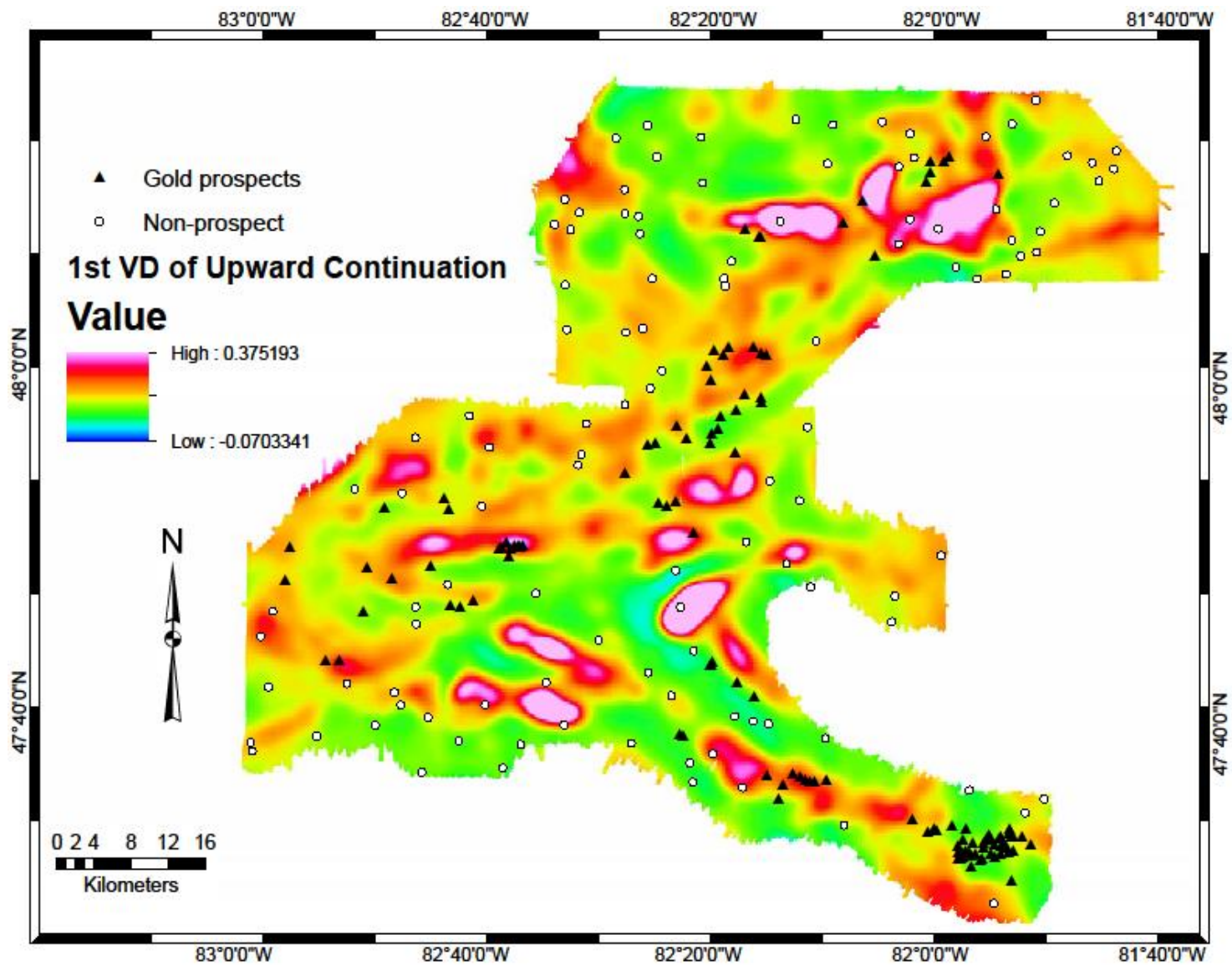


Fig. 3- 10: The first vertical derivative of the 2 km upward continued RTP total magnetic intensity.

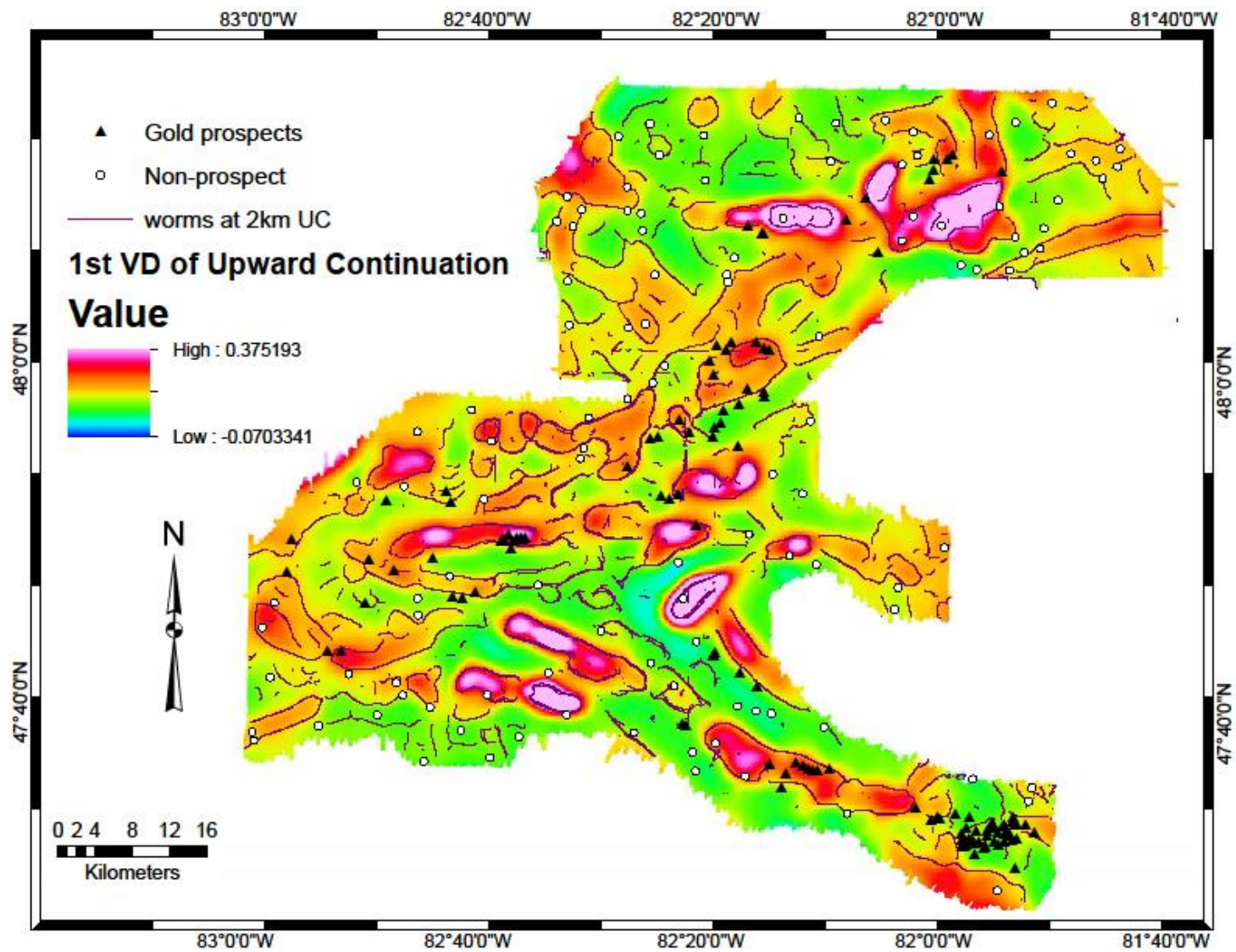


Fig. 3- 11: Magnetic worms overlying the 2 km upward continued map.

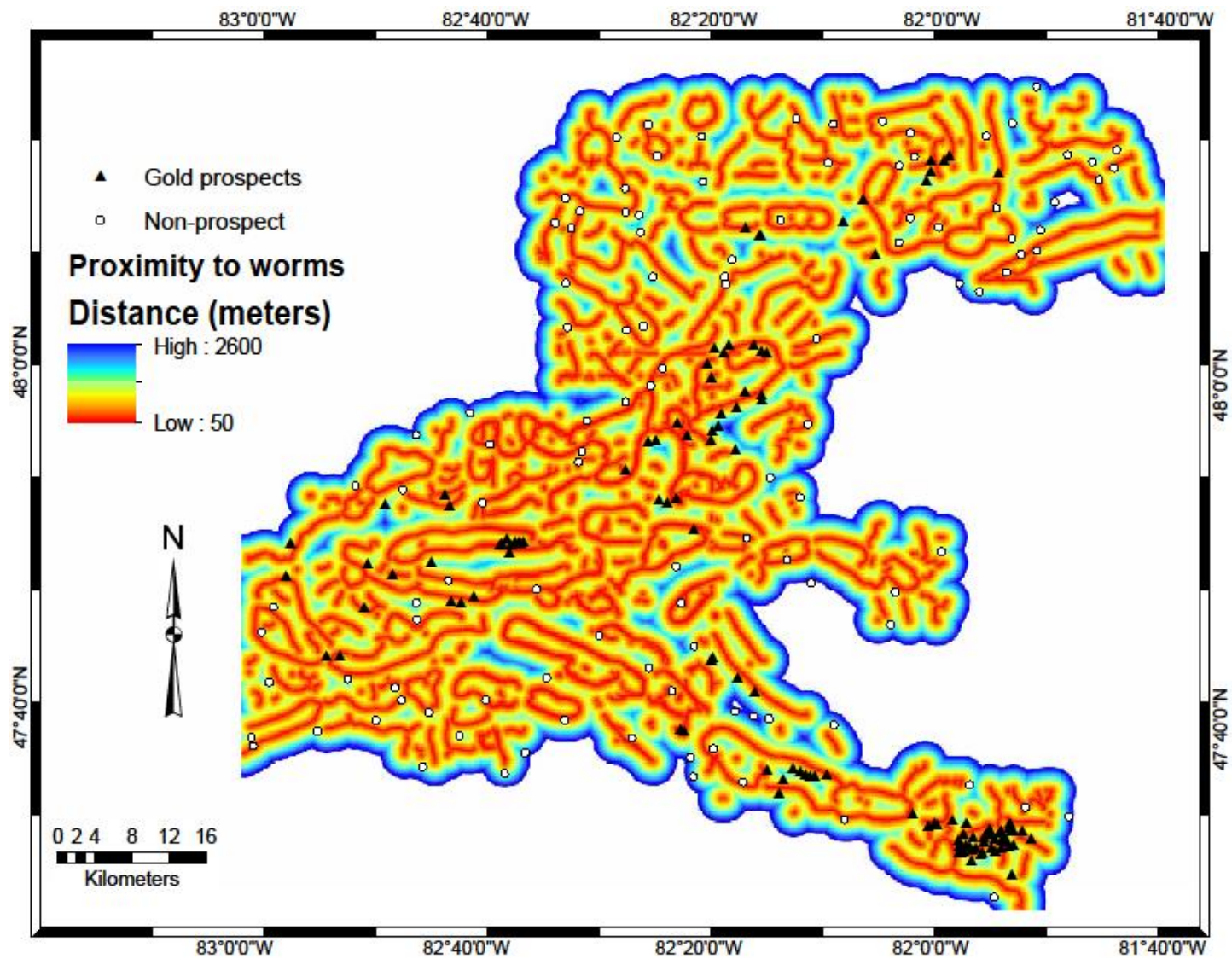


Fig. 3- 12: Proximity to magnetic worms.

#### 3.5.4.2 Electromagnetic conductivity

The INPUT and GEOTEM II systems were used to measure electromagnetic (EM) conductivity in the southern and northern parts of the Swayze greenstone belt, respectively. These systems are designed to detect conductive volcanogenic massive sulfides in the Canadian shield, primarily from off-time data collected after an excitation pulse has been turned off (Ontario Geological Survey, 2003). An improvement of the GEOTEM II system in the 1990s allowed an on-time data acquisition, which enable detection of weakly conductive overburden, previously considered as geological noise, and difficult to measure during the early off time mode (Ontario Geological Survey, 2003; Smith, 2000).

The apparent decay constant map shows the EM conductivity of the near-surface material (Ontario Geological Survey, 2003; Vaughan, 1988). From a mineral-system perspective, highly conductive features might be indicative of zones that were altered by fluids, graphic shear zones, regions of hydrothermal fluid flow, and/or lithologies that may be metal trap sites. These features representing high EM decay-constants (Fig. 3-13) were extracted and grouped for further processing.

This was followed by creation of buffer map defining cumulative distances from high EM conductivities (Fig. 3-14). According to weights of evidence statistics, 100% of gold prospects occur within 5 km distances from EM decay constant anomalies (Table 3-2). Conductive features shown on the decay constant map (Fig. 3-13) spatially correlate with chemical metasedimentary rocks which include iron formations, sulfide facies, oxide, and silicate facies. .

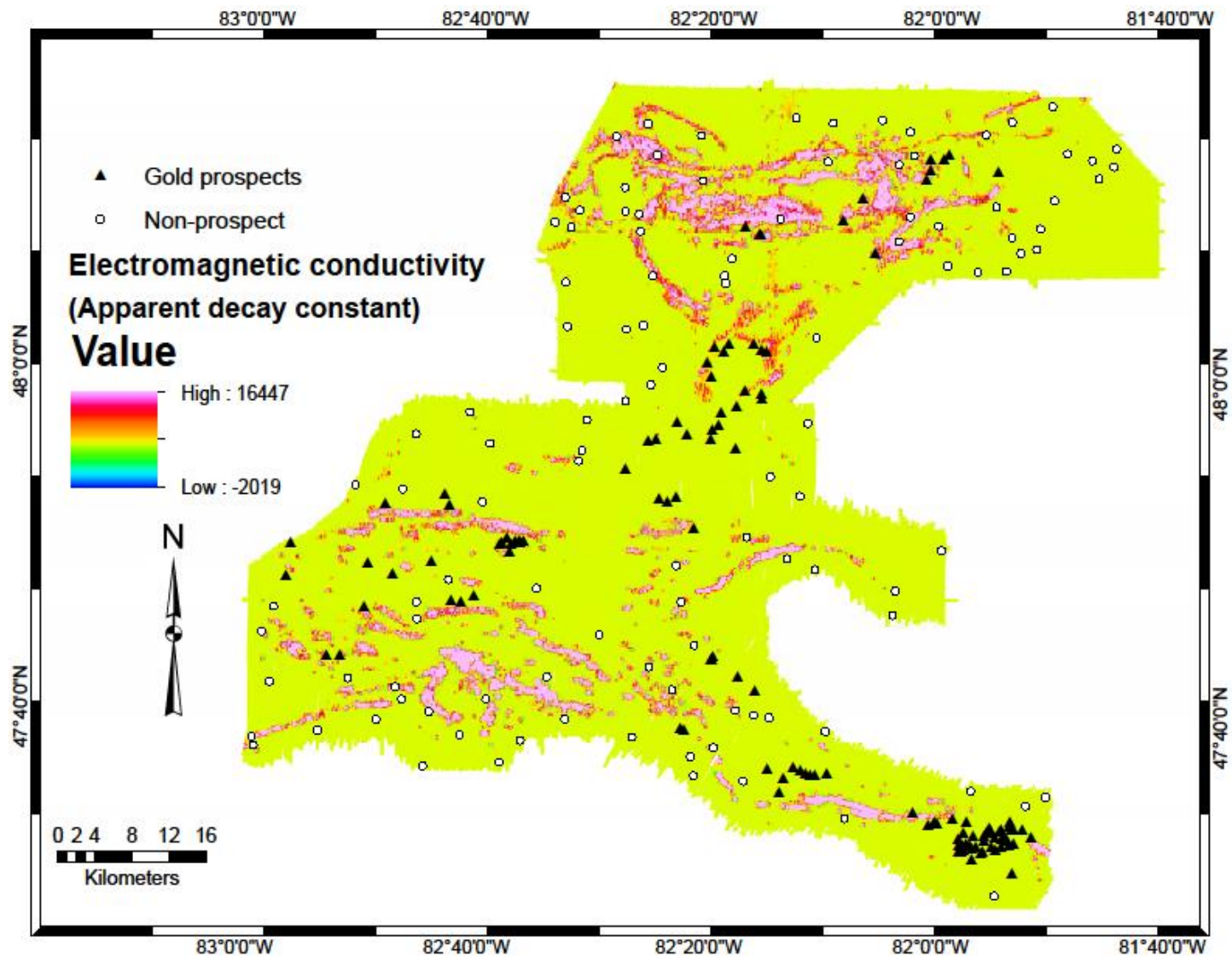


Fig. 3- 13: Electromagnetic decay apparent conductivity map.

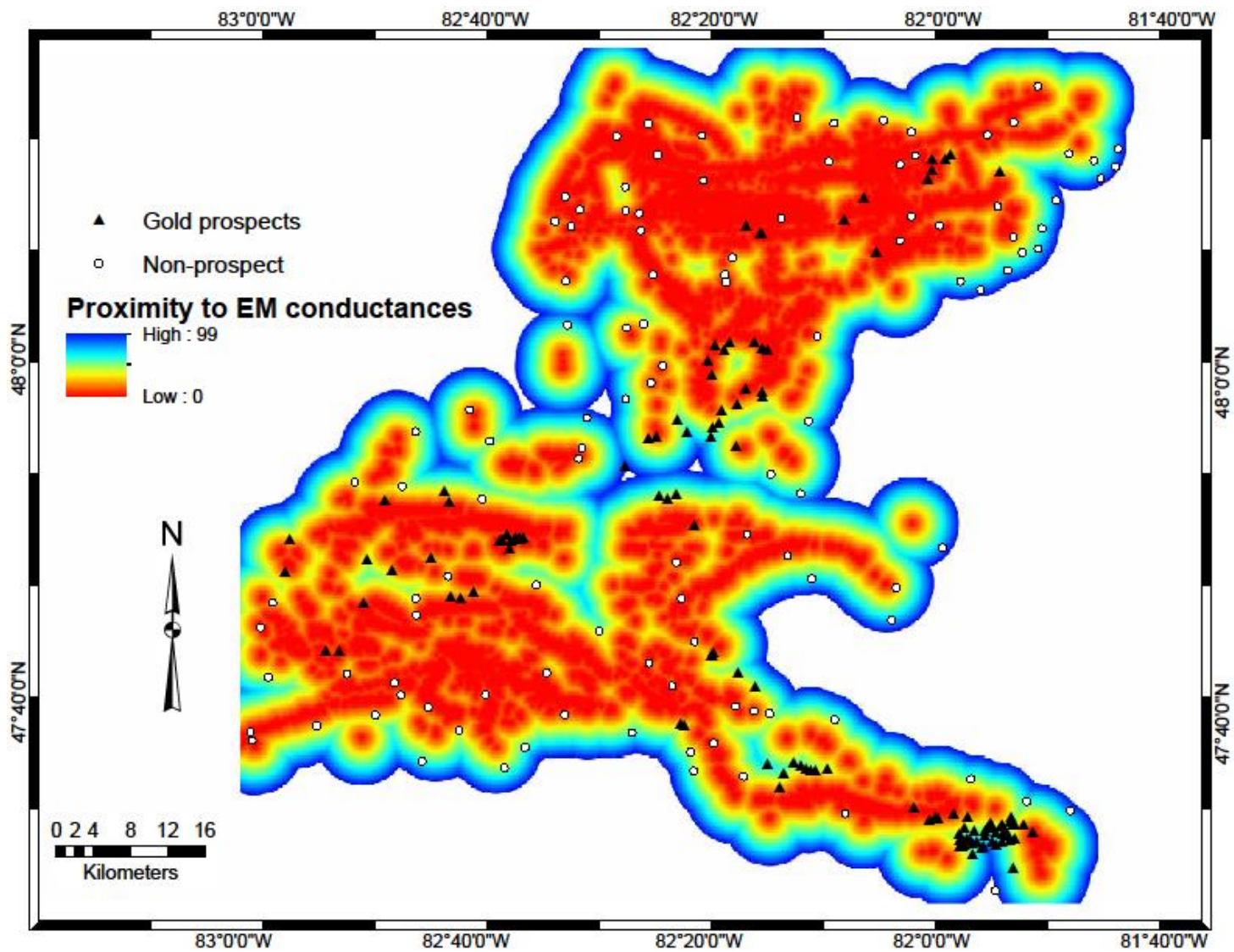


Fig. 3- 14: Proximity to Eelectromagnetic decay high apparent conductivities.

### 3.5.5 Geochemistry

The lithochemical data used in this study consists of major element oxides and the distribution of geochemical data used is seen on Appendix D. Major oxide geochemical data can help to show the elemental gains and losses during processes of hydrothermal alteration. Gold-prospects in the Swayze greenstone belt are characterised by a variety of alteration types such as chlorite, sericite, silicification, Fe-carbonate, sulfidation, carbonatization, tourmalization, and albite alteration (Harris, 2001; Heather, 2001, Appendix B). The geochemical data was transformed using centred log-ratio analysis in CoDaPack freeware (<http://www.compositionaldata.com/codapack.php>). Principal components analysis (PCA) was computed from the log-ratio transformed datasets. The centered logratio transformation (Aitchison, 1986) uses the geometric mean to remove the effect of closure from the compositional data and to project compositional data to real number space, allowing for statistical techniques such as PCA to be better applied (Grunsky, 2010).

The PCA method has been widely used in multielement geochemical data analysis (Grunsky, 1986, Grunsky, 2010). The statistical analysis reduces data dimensionality from a large correlated matrix to much smaller uncorrelated variables called principal components that highlight observed variations in the data (Jolliffe, 2002; Davis, 2002; Grunsky, 2010) and retain the variation of the original data.

The first, second and third principal components (PC) transformations derived from major oxide data were interpolated using the kriging algorithm to generate continuous surface maps

showing the distributions of PC values. The interpolated PC data and calculated geochemical alterations were evaluated using weights of evidence to review their spatial correlations with gold.

The first three principal components account for 72% of the variance and were analysed for spatial correlations with gold using weights of evidence (Table 3-3). Only the first PC had a good spatial correlation with gold as shown on Table 3-2, with a studentized contrast of 8.37. Table 3-3 shows the relative and actual contributing variables, PC1 shows that Fe<sub>2</sub>O<sub>3</sub>, MgO, MnO and SiO<sub>2</sub> were the strongest contributors. The bi-plots on Fig. 3-15 shows that Al<sub>2</sub>O<sub>3</sub> and SiO<sub>2</sub> have the largest negative correlations and contributions to each other while CaO, MgO, Fe<sub>2</sub>O<sub>3</sub> and MnO show large positive contributions and correlations. Furthermore, Fe and Mg display the strongest positive contributions to the PC1 variation which may indicate formation of chlorite. There is also a contribution to PC1 by CaO which may reflect carbonatization alteration seen in various locations within the greenstone belt (Appendix B).

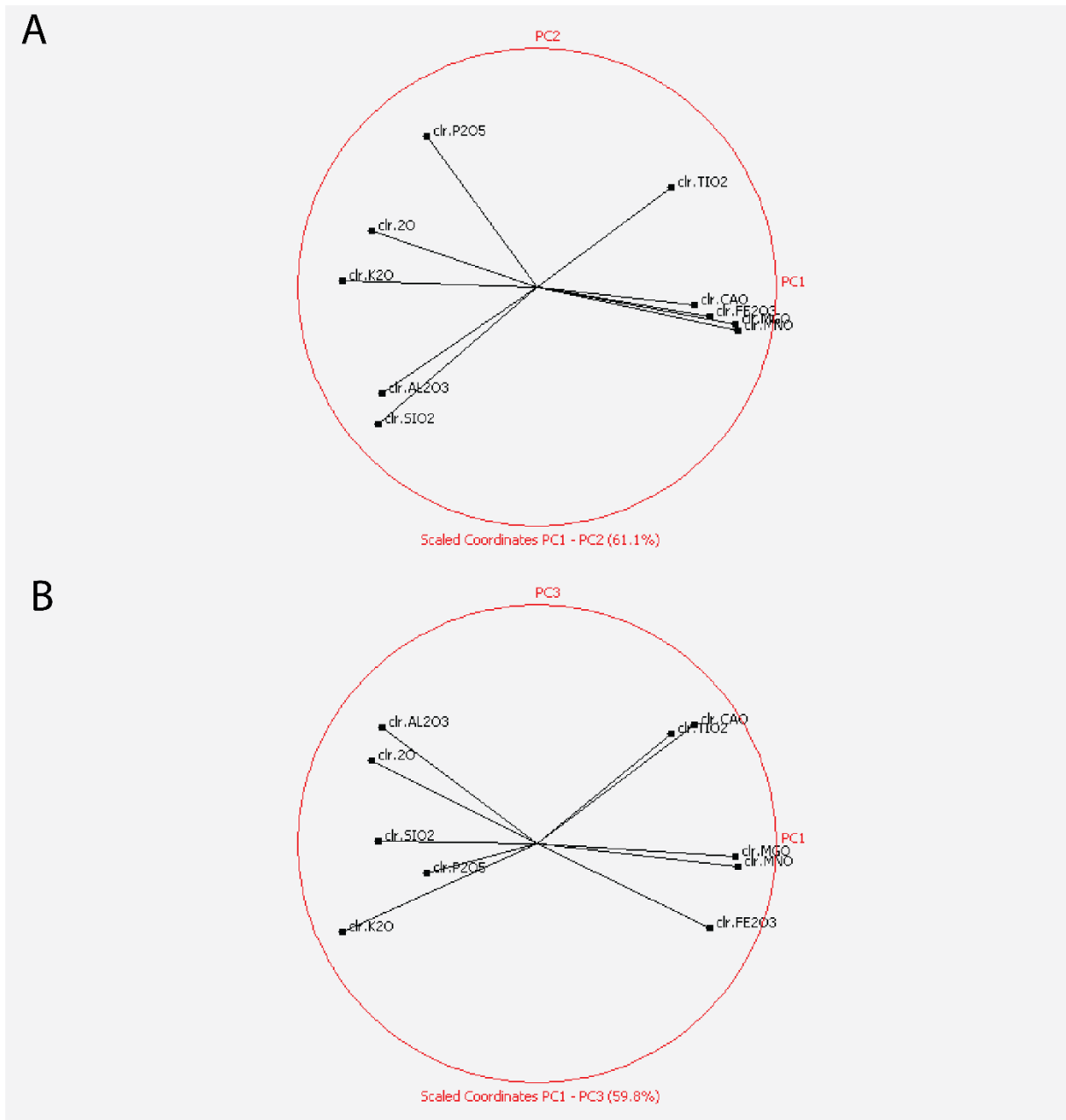
Alteration signatures and principal components with the best spatial associations (i.e., high *C* and studentized contrast *C* values) were used for further analysis of prospectivity. Table 3-2 shows good spatial correlation between gold and the first principal component map (Fig. 3-16). The Spitz-Darling ( $K_2O+NaO/Al_2O_3$ ) alteration (Spitz-Darling, 2011) is added to show alkali enrichment with Al<sub>2</sub>O<sub>3</sub> depletion in rocks. On a regional scale, there might be correlation with gold (Fig. 3-17).

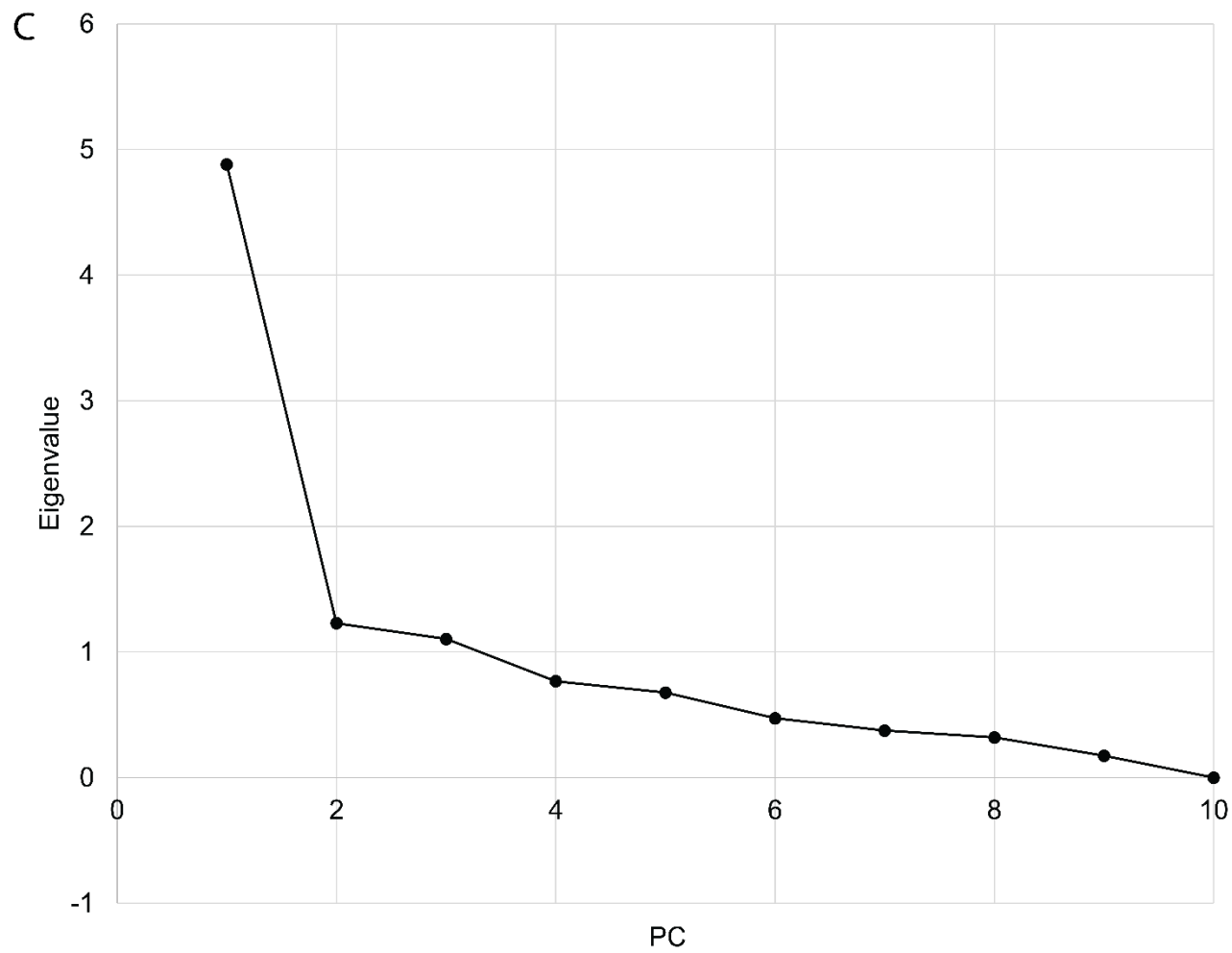
The geochemical data approach in this study could benefit more from calculations of alterations and PCA analysis on individual lithologies to help highlight elemental gains and losses with respect to regional scale geochemistry projects.

Table 3 - 3: Principal components of normalized lithochemical major oxide data from the Swayze greenstone belt.

Eigenvectors	PC1	PC2	PC3	PC4	PC5	PC6	PC7	PC8	PC9	PC10
SiO <sub>2</sub>	-0.301	-0.515	0.008	0.437	0.052	0.151	-0.102	0.053	-0.624	0.16
Al <sub>2</sub> O <sub>3</sub>	-0.292	-0.4	0.464	0.218	0.183	-0.126	0.196	-0.128	0.607	0.138
Fe <sub>2</sub> O <sub>3</sub>	0.327	-0.113	-0.334	-0.073	0.551	0.239	0.343	-0.426	-0.026	0.321
MgO	0.376	-0.14	-0.051	0.182	-0.245	0.279	-0.655	-0.092	0.303	0.369
CaO	0.298	-0.067	0.471	-0.176	-0.548	0.022	0.375	-0.278	-0.265	0.257
Na <sub>2</sub> O	-0.313	0.214	0.333	-0.444	0.229	0.511	-0.103	0.297	-0.054	0.366
K <sub>2</sub> O	-0.368	0.025	-0.353	-0.237	-0.17	-0.529	-0.065	-0.089	0.002	0.601
TiO <sub>2</sub>	0.255	0.374	0.438	0.243	0.425	-0.451	-0.254	-0.041	-0.244	0.185
P <sub>2</sub> O <sub>5</sub>	-0.209	0.57	-0.115	0.606	-0.194	0.258	0.295	-0.037	0.104	0.218
MnO	0.38	-0.164	-0.094	0.108	0.011	-0.125	0.313	0.784	0.081	0.27
Eigenvalues	4.9	1.2	1.1	0.8	0.7	0.5	0.4	0.3	0.2	0
Cumulative %	48.8	61.1	72.1	79.8	86.6	91.3	95.1	98.3	100	100

Fig. 3- 15: The bi-plots of the first and second principal component (A), first and third principal component (B) and a scree plot (C) for the logratio centered Swayze greenstone belt major oxide data.





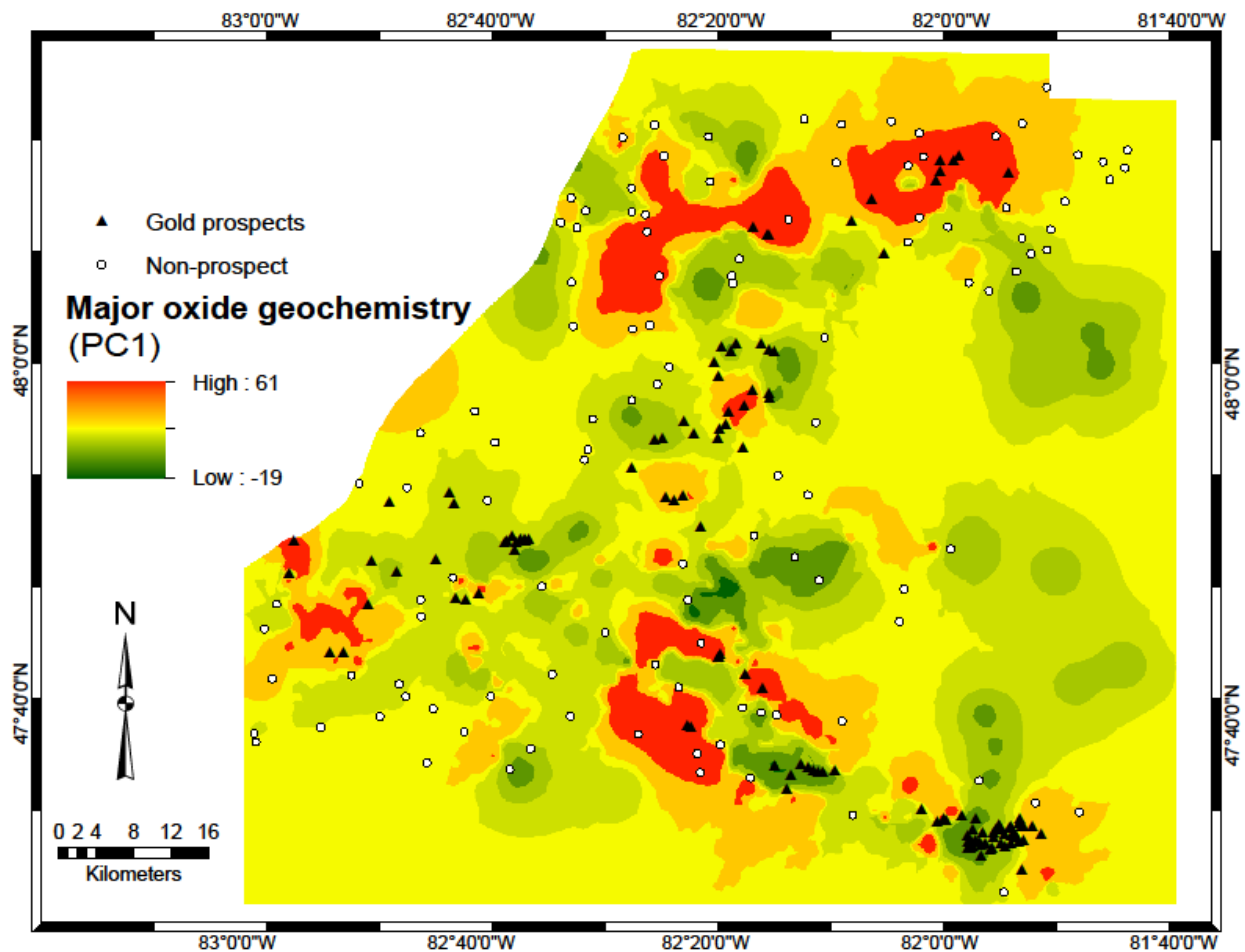


Fig. 3- 16: The first principal component PC1 of major oxide geochemistry. The geochemical data point locations are shown on Appendix D, E, and F.

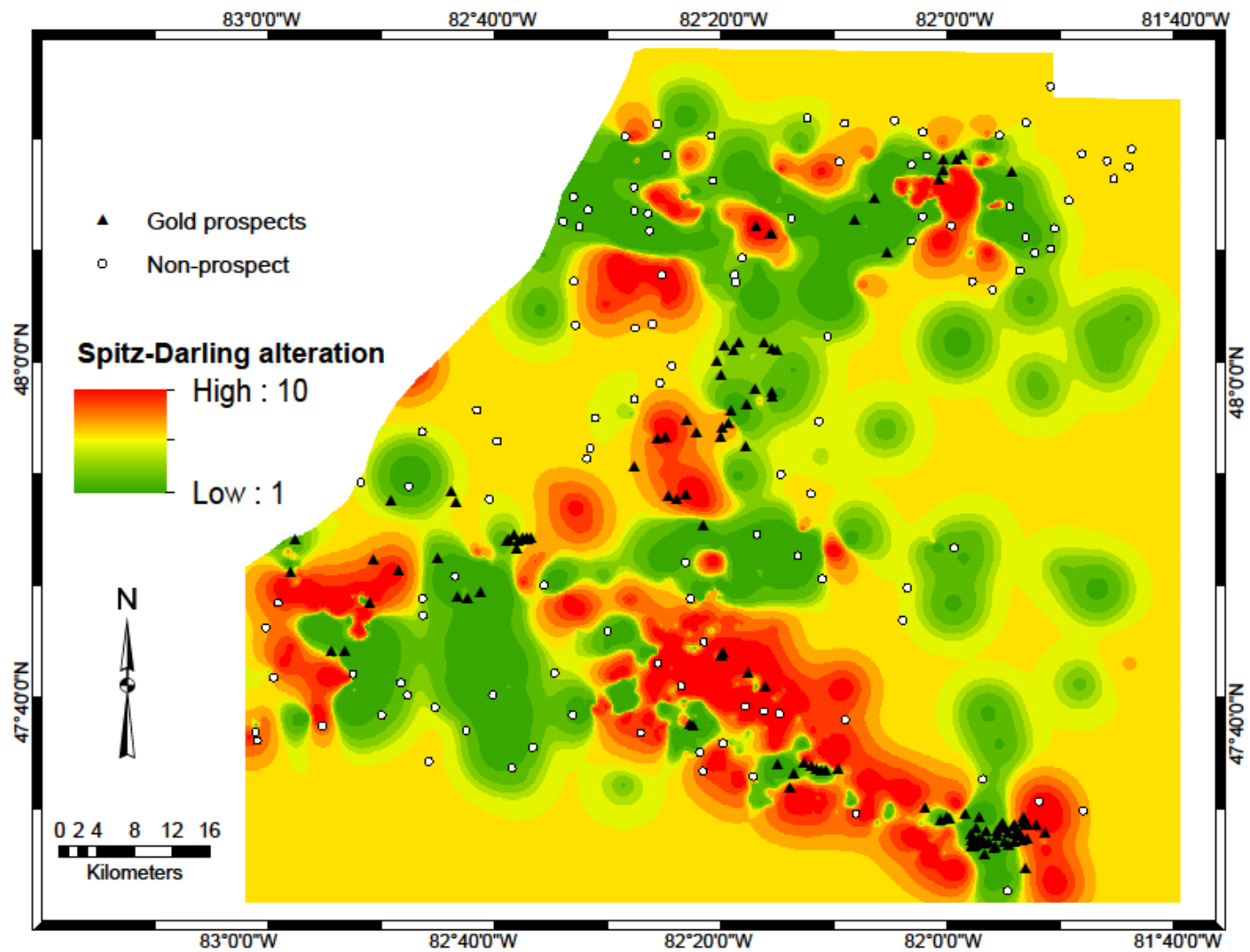


Fig. 3- 17: Spitz-Darling alteration index map.

### 3.6 Results

To avoid possibly mixing various mineral deposits types, multiple mineral prospectivity maps were created using both radial basis function neural networks and support vector machines.

The first set of mineral prospectivity maps (Figs. 3-18, 3-19, and Figs, 3-20 and 3-21) were created using the 2019 OGS mineral deposit inventory which classifies the Rundle, Namex, and Jerome deposits as well as prospects in the southeastern Swayze greenstone as mesothermal (i.e., orogenic gold prospects). This collection of deposits is termed “classification type 1” below.

The second set of mineral prospectivity maps (Fig. 3 -26and Fig. 3 – 27) were created with exclusion of the Rundle, Namex, and Jerome deposits as well as prospects in the southeastern Swayze greenstone because currently ongoing research suggest that these prospects might actually represent intrusion-related and porphyry-type prospects. (termed “classification type 2” below).

#### 3.6.1 Prospectivity modeling using prospect classification type 1

Using classification type 1, four gold prospectivity maps were created with and without geochemistry predictor layers (Figs. 3-18 and 3-19, and Fig. 3-20 and 3-21, respectively). The training and validation accuracies and losses (i.e., mean squared error) for the RBFNN models are shown on Fig. 3-22. Following the 10-fold cross validation approach, the training mean and validation accuracy of RBFNN model 1 is 80% (Fig. 3-18), with a standard deviation of 10.12% (Figs. 3-22A and 3-22B). The RBFNN model 2 created without the geochemical predictor layers (Fig. 3-21) yield a mean accuracy of 82% with standard deviation of 6.80% (Figs. 3-22C and 3-22D) after 10-fold cross validation.

Both SVM models were cross-validated using 10-fold cross-validation. The SVM model 1 (i.e., with geochemical data) shown on Fig. 3-19, obtained a mean kernel performance of 80% and standard deviation of 0.09%. The SVM model 2 (i.e., without geochemical predictor layers) shown on Fig. 3-21, obtained a mean kernel performance of 80.3% and standard deviation of 0.10%.

Cross-validation for RBFNN and SVM was also done using receiver operator curves as shown on Fig. 3-23. The area under the curve for RBFNN model 1 and 2 are 91% and 94%, respectively (Fig. 3-23A), while the SVM model 1 and 2 show mean AUC values of 91% and 87%, respectively (Fig. 3-23C). The ROC shows that both models performed well in defining gold prospectivity. The results show that the performance of the two models is comparable when geochemical data is included into the predictor layers. However, the RBFNN show better performance than the SVM without the inclusion of geochemical data. Furthermore, the standard deviations for both models went down when geochemistry was excluded indicating a reduction in model uncertainty.

Feature importance estimations were obtained for both RBFNN and SVM models (Fig. 3-23B and Fig. 3-23D, respectively). The RBFNN model considered folds, lithological contacts and D<sub>2</sub> and D<sub>3</sub> high-strain zones as the most influential predictor maps for mapping gold prospectivity (Fig. 3-23B). Similarly, the D<sub>2</sub> and D<sub>3</sub> high-strain zones and lithological contacts scored high in the feature importance estimations for the SVM prospectivity model. The least contributing predictor maps were geochemical PC1 map and the Spitz-Darling alteration map.

Regions of exploration interest in the northern and southern Swayze greenstone belt are shown using an ellipse and black box (Fig. 3-24). The high prospectivity zones modelled by RBFNN and SVM are characterized by proximity to D<sub>2</sub> HSZ, occurrences of magnetic worms and high lithological contrast. The locations of existing mines and new exploration targets that require

detailed appraisal are shown on Fig. 3-25. The spatial overlay of predictor features shown on Fig. 3-25 displays how prospective zones correlate with EM conductivity, magnetic worms, folds, and high-strain zones.

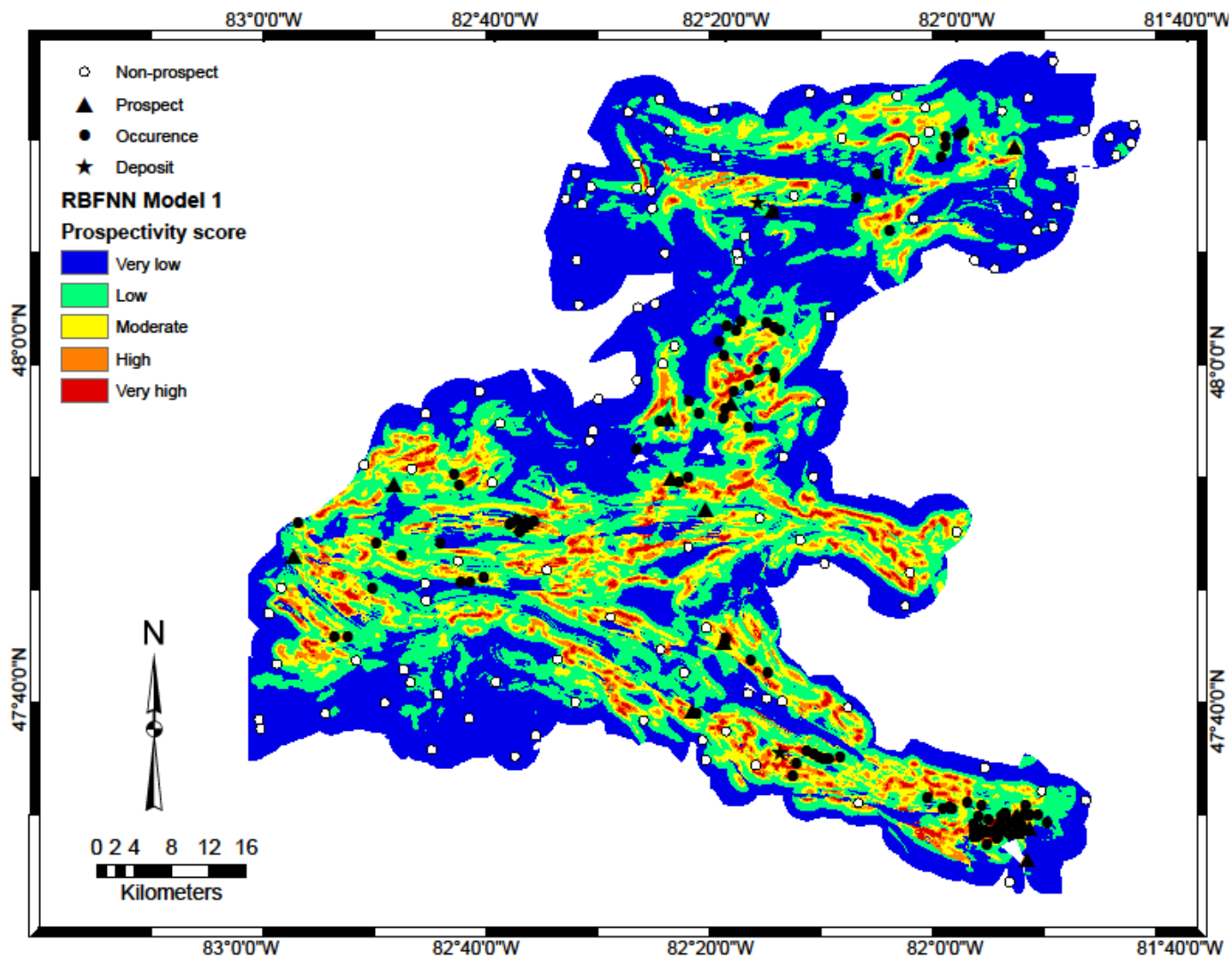


Fig. 3- 18: Mineral prospectivity map derived from radial basis function neural networks learning with geochemistry predictor layers included. This prospectivity model was created using the prospect classification type 1.

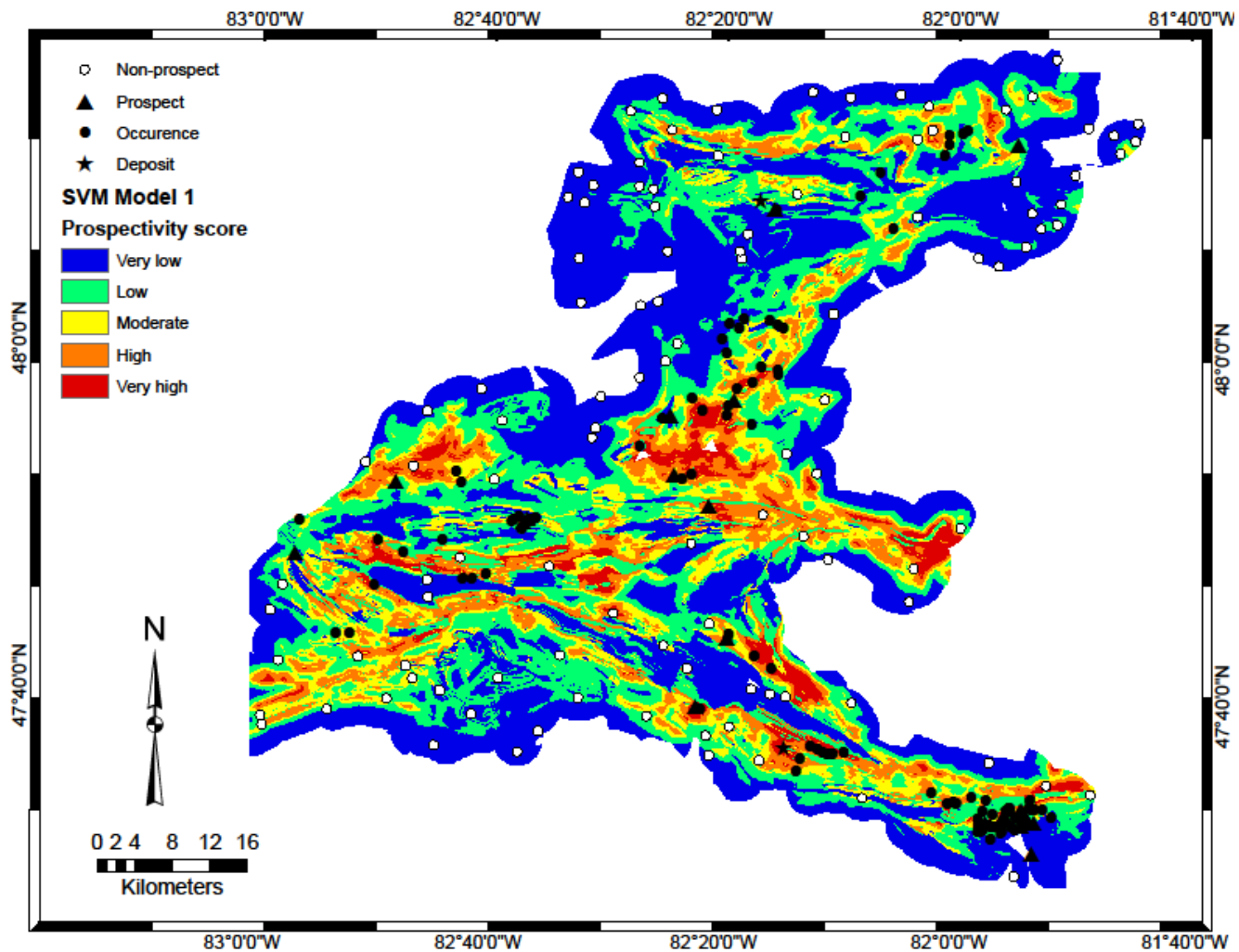


Fig. 3- 19: Mineral prospectivity map derived from support vector machine with geochemistry predictor layers excluded. This prospectivity model was created using the prospect classification type 1.

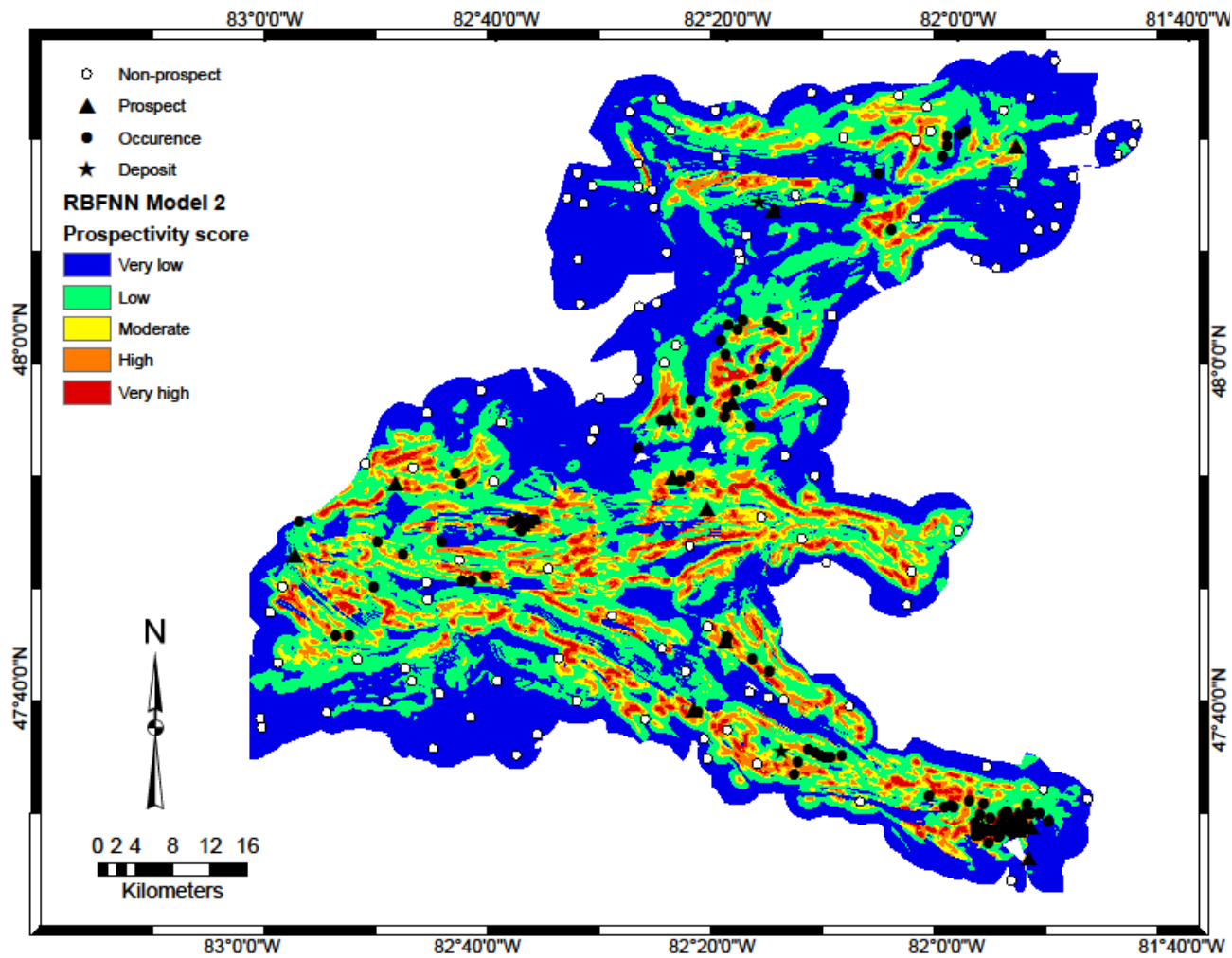


Fig. 3- 20: Mineral prospectivity map derived from radial basis function neural network machine learning with geochemistry predictor layers included. This prospectivity model was created using the prospect classification type 1.

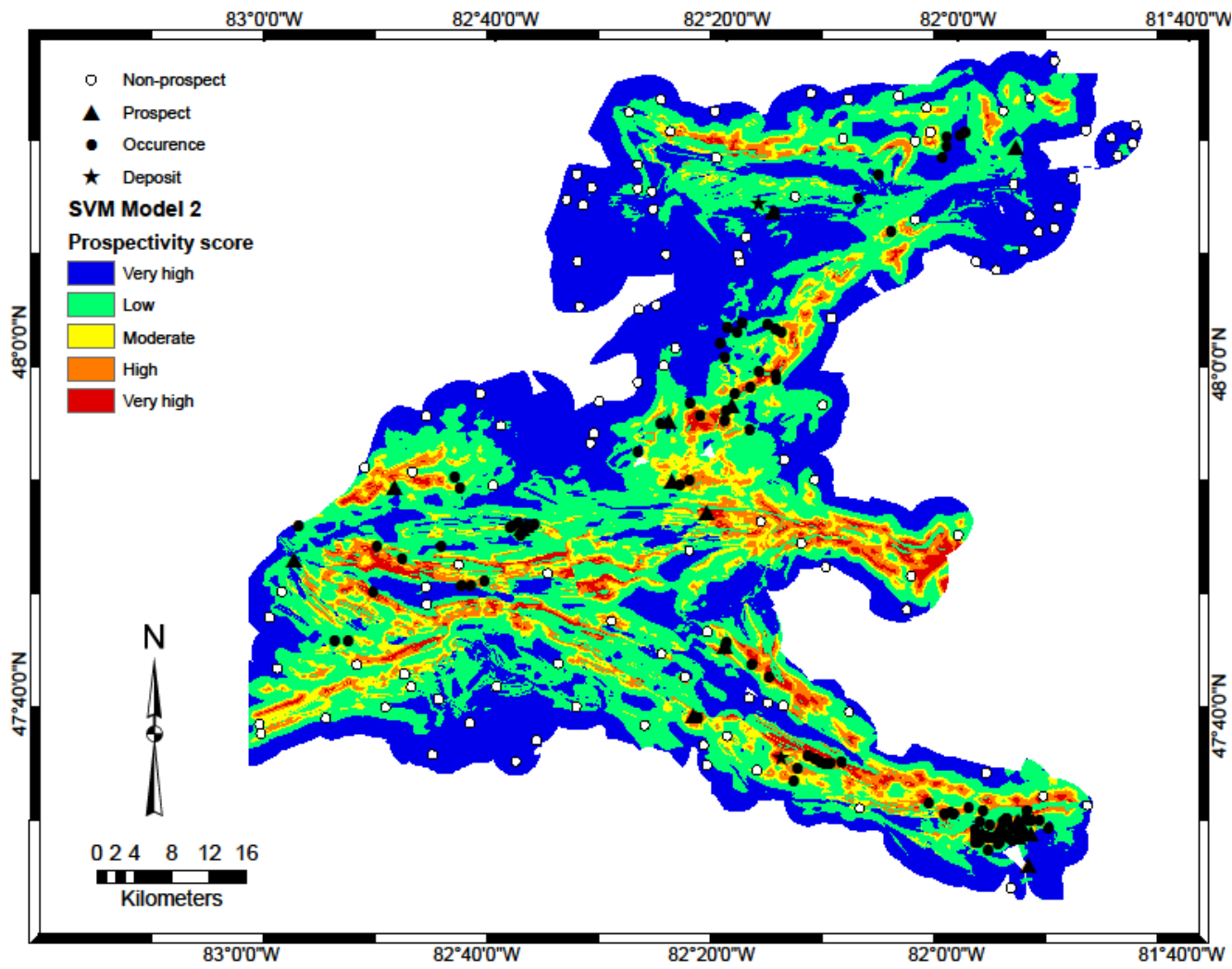


Fig. 3- 21: Mineral prospectivity map derived from support vector machines machine learning with geochemistry predictor layers excluded. This prospectivity model was created using the prospect classification type 1.

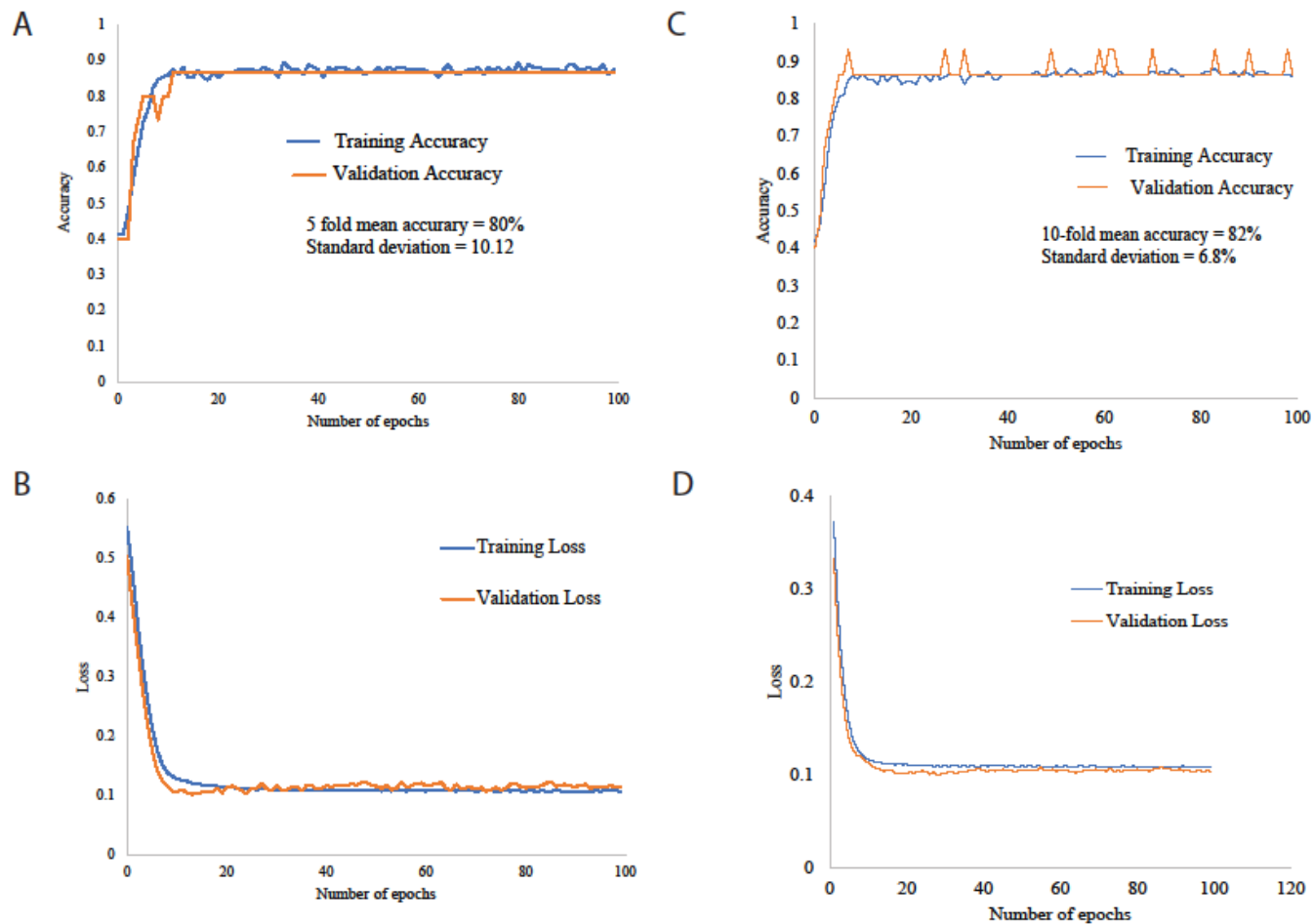


Fig. 3- 22: Training and validation plots from the radial basis function neural network models showing the mean training and validation accuracies, losses, and the standard deviation for RBFNN model with geochemistry (A and B) and RBFNN model without geochemistry (C and D).

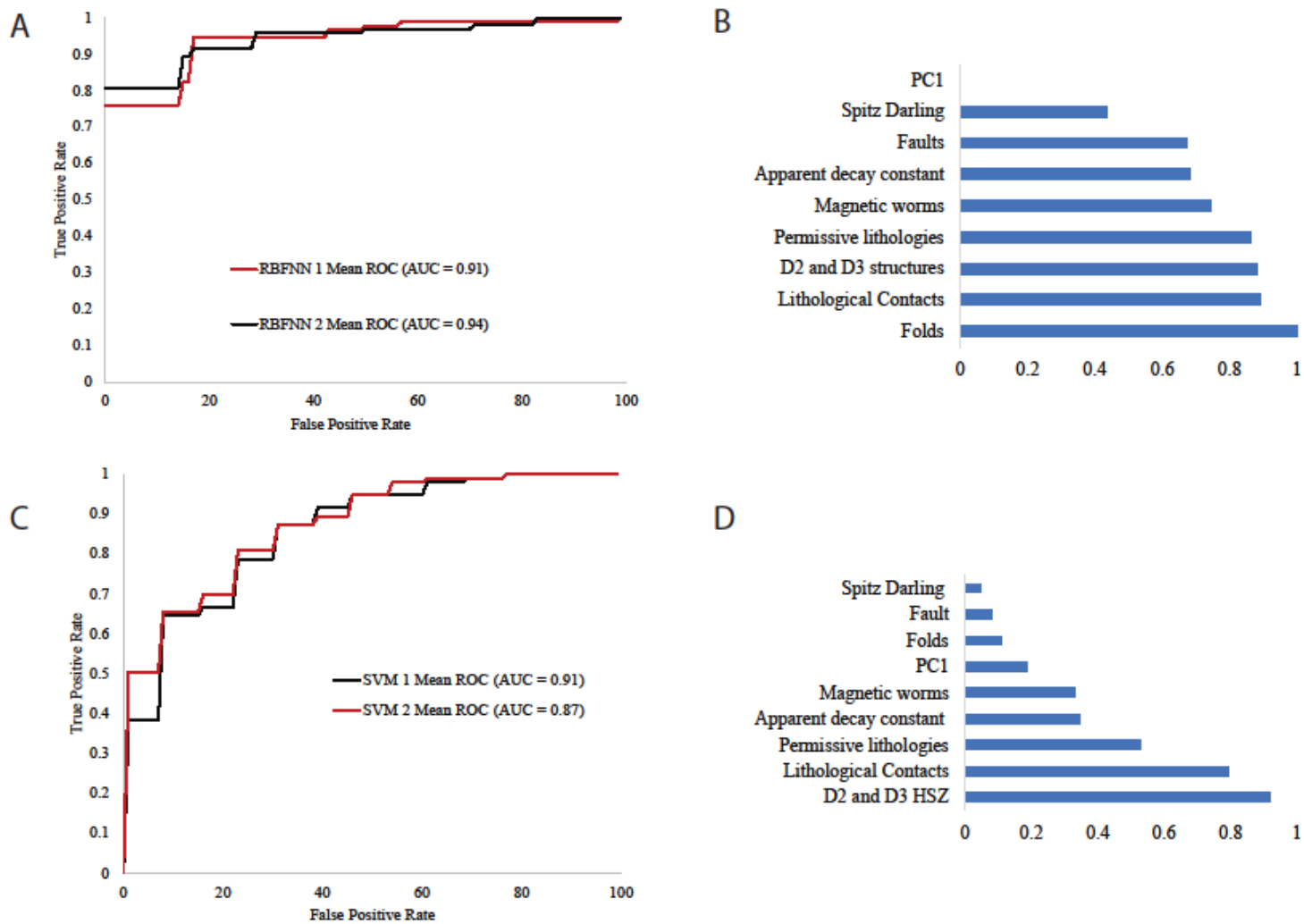


Fig. 3- 23: The mean area under receiver operator curves for RBFNN models (A) and SVM models (C). and Feature importance scores derived from RBFNN (D) and SVM (D) models.

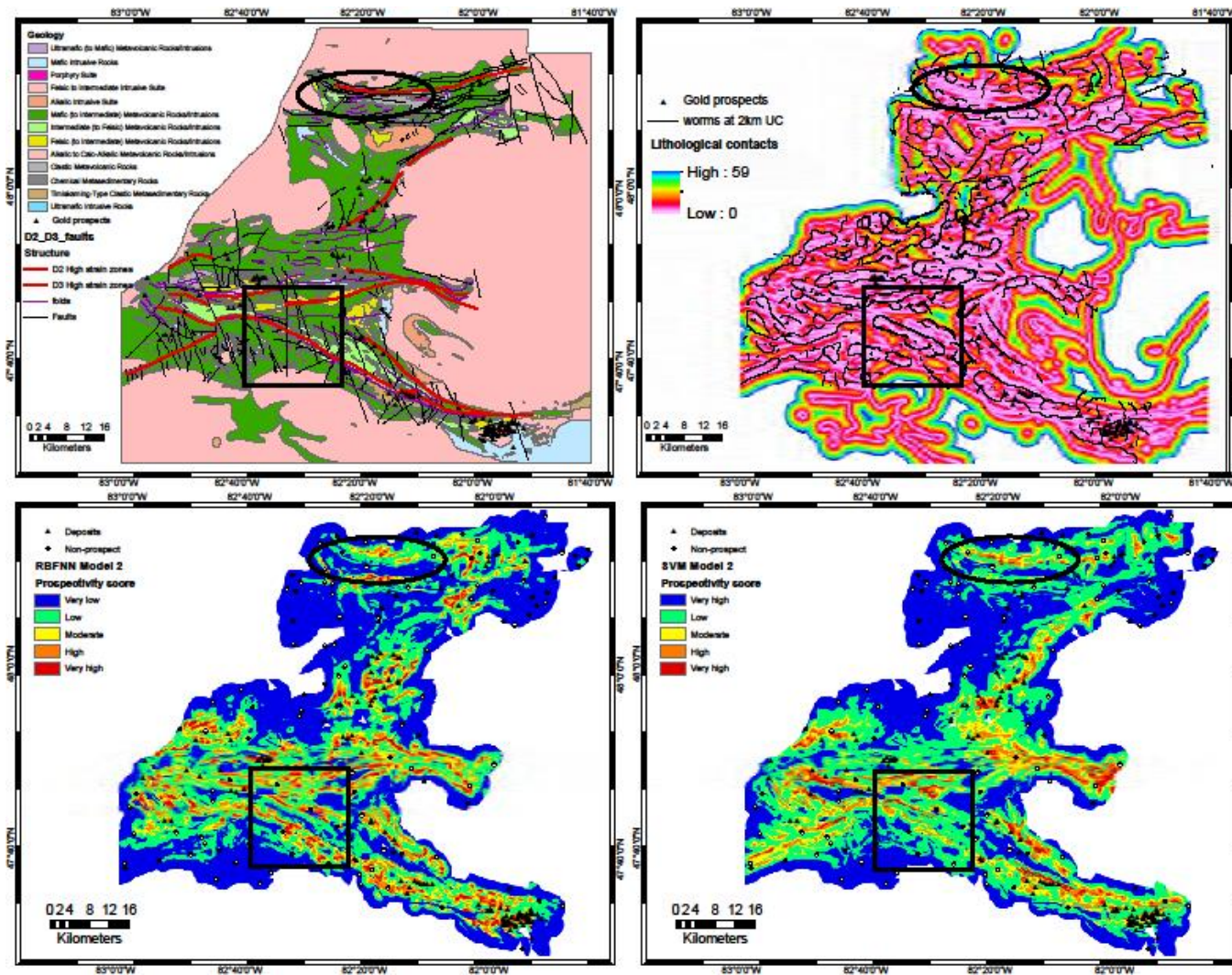


Fig. 3- 24: Comparison of the RBFNN and SVM prospective sites. The black boxed area shows predictions from both SVM and RBFNN and geological processes that may have contributed to the predictions.

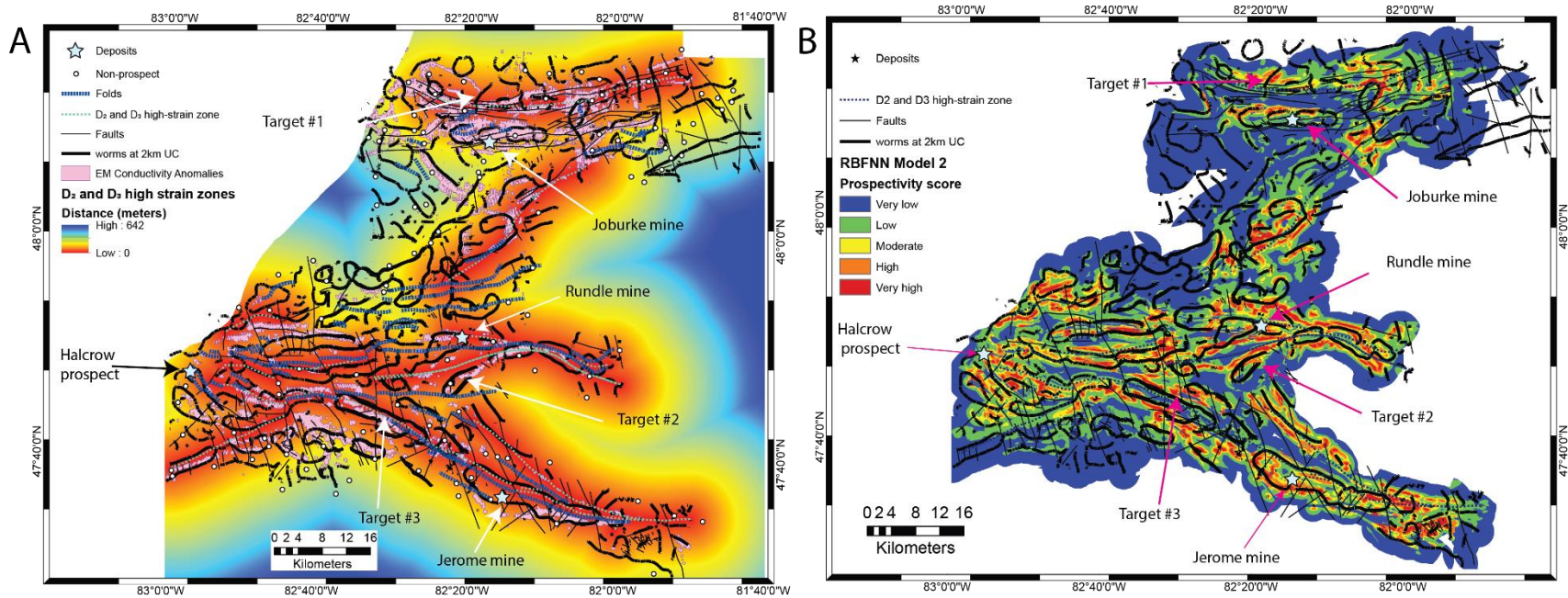


Fig. 3- 25: The RBFNN mineral prospectivity map and predictor features; high strain zones, EM conductivities, magnetic worms and faults are shown on (A) and (B). The locations of new prospective regions (Target #1, Target #2 and Target #3) and existing mines and prospects (Joburke, Rundle, Jerome and Halcrow) are also overlain.

### 3.6.2 Prospectivity modelling using prospect classification type 2

The SVM and RBFNN models created with the prospect classification type 2 as defined above (excluding intrusion-related and porphyry-style deposits) are shown on Fig. 3-26 and 3-27, respectively. Both models were created with geochemical data included and the model metrics show that the mean performance after k=10 cross-validation for RBFNN and SVM are 81% and 90% area under curve, respectively. The standard deviation for the RBFNN and SVM models after k=10 subsets of training are 0.06 and 0.08, respectively suggesting that there is less variance between the k-fold subsets during training and thus lower model uncertainty.

Visual inspection of the prospectivity maps on Fig. 3-26 and Fig. 3-27 shows that the high prospectivity scores spatially correlate with the known gold prospects in the Swayze greenstone belt. Similar to the first set of prospectivity maps created in this study, these maps (on Fig. 3-26 and Fig. 3-27) also demonstrate that certain regions may be prospective for hosting gold. For examples, the RBFNN map (Fig. 3-30) shows that there is a high prospectivity prediction west of the Joburke mine. This area may represent a place that could be investigated further in the future for hosting gold.

Feature importance generated from the SVM and RBFNN show that the machine learning models considered faults, magnetic worms and electromagnetic conductivity as important predictors while the Spitz-Darling alteration shows lower influence.

### 3.6.3 Comparison of prospectivity models from prospect classification type 1 and type 2

There are recognizable differences between mineral prospectivity maps created using the prospect classification type 1 (Fig. 3-18, 19, 20 and 3-21) and type 2 (Fig. 3-26 and Fig. 3-27).

The RBFNN prospectivity models created using gold prospect classification type 1 have significantly high measures of uncertainty (i.e., standard deviations of 6.8) than models created with classification type 2 (i.e., standard deviations of 0.08). The differences in uncertainty measurements shows that the possible mixing of mineral prospect types affected the ability of the RBFNN machine learning methods during training and classification. Removal of the prospect, prospects, and occurrences that represented potentially different prospect types minimized machine learning model uncertainty.

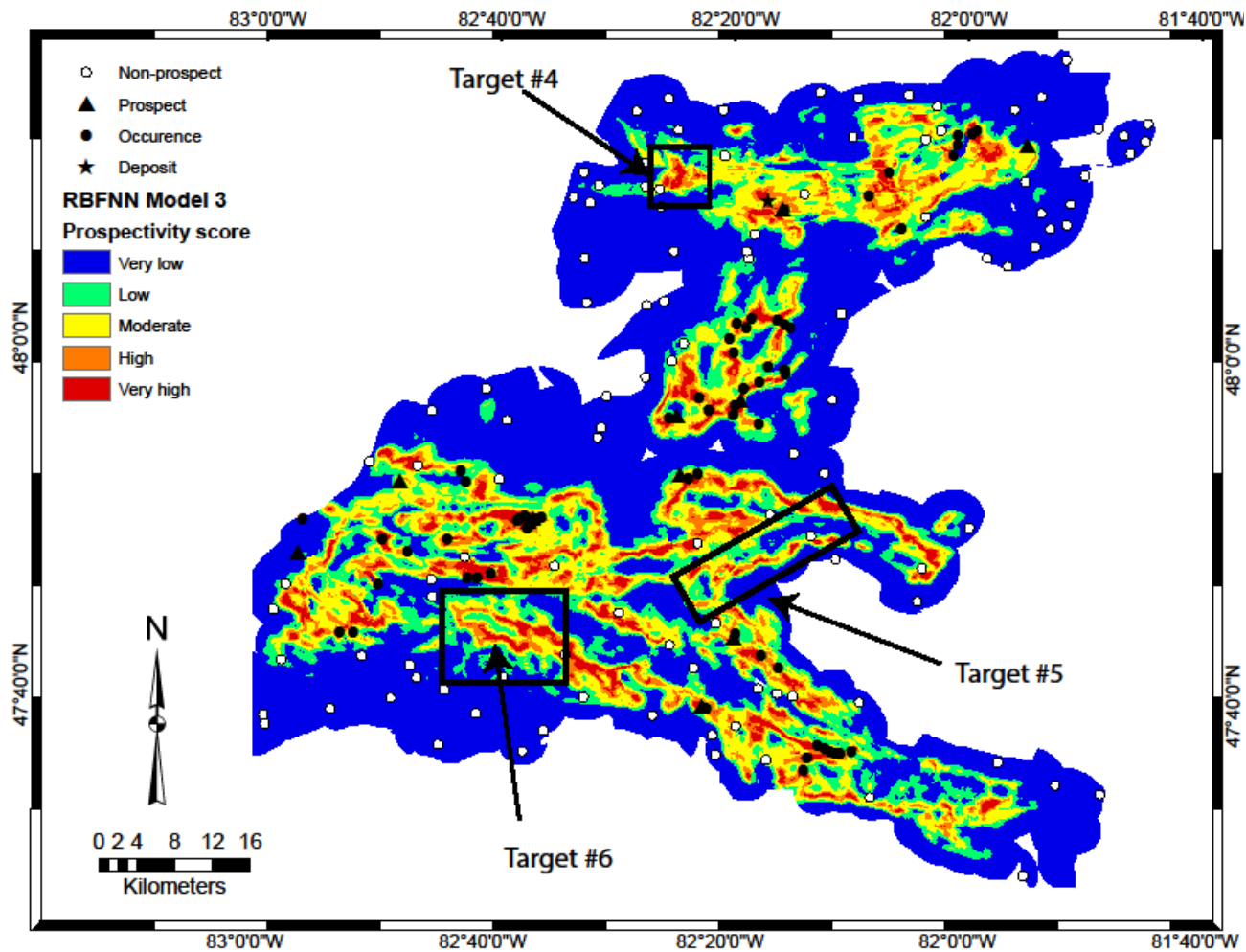


Fig. 3- 26: Mineral prospectivity map derived from the radial basis function neural network model with geochemistry predictor layers included. The prospectivity map indicates three potential targets in the area. This prospectivity model was created using the prospect classification type 2.

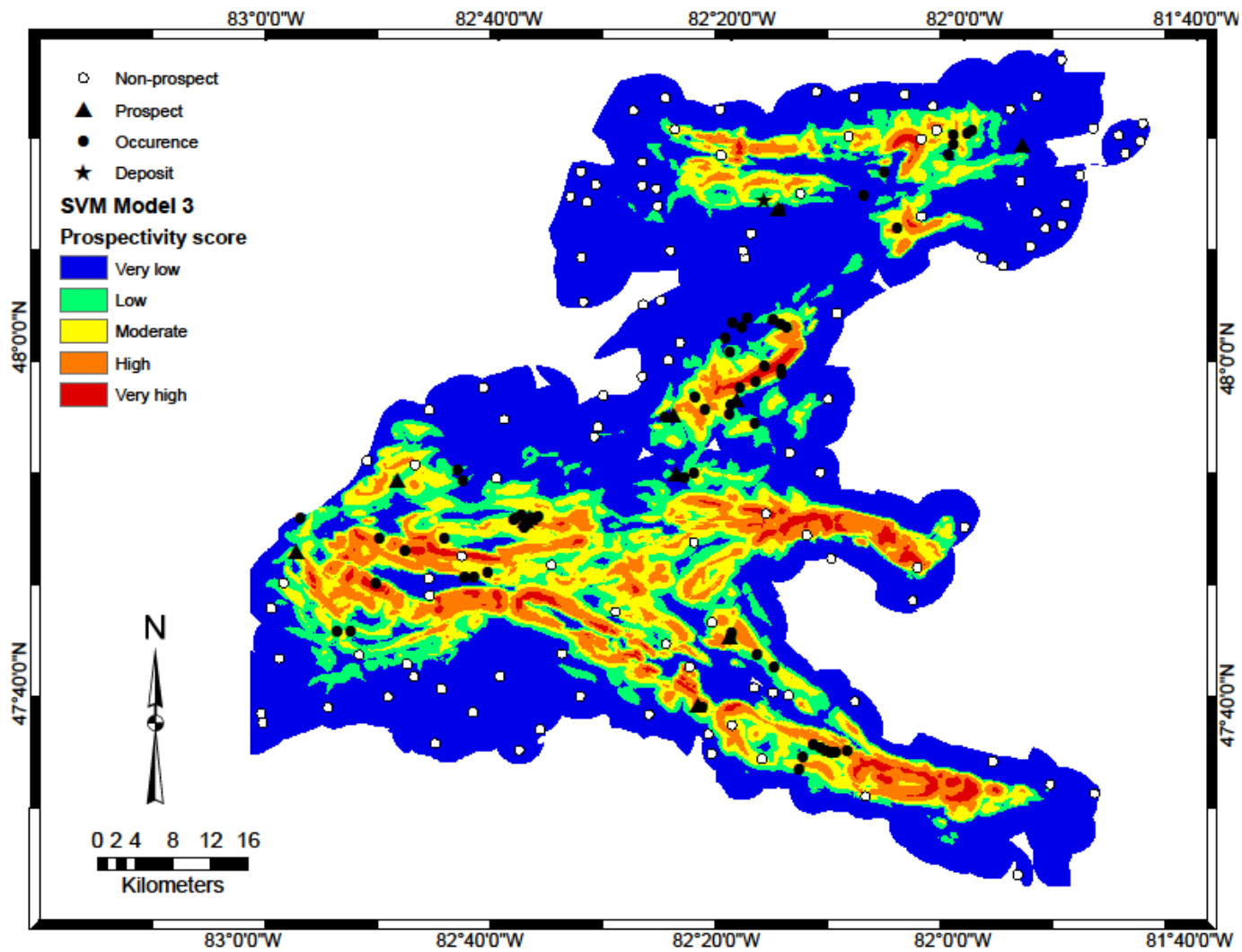


Fig. 3- 27: Mineral prospectivity map derived from the support vector machines model with geochemistry predictor layers included.

This prospectivity model was created using the prospect classification type 2.

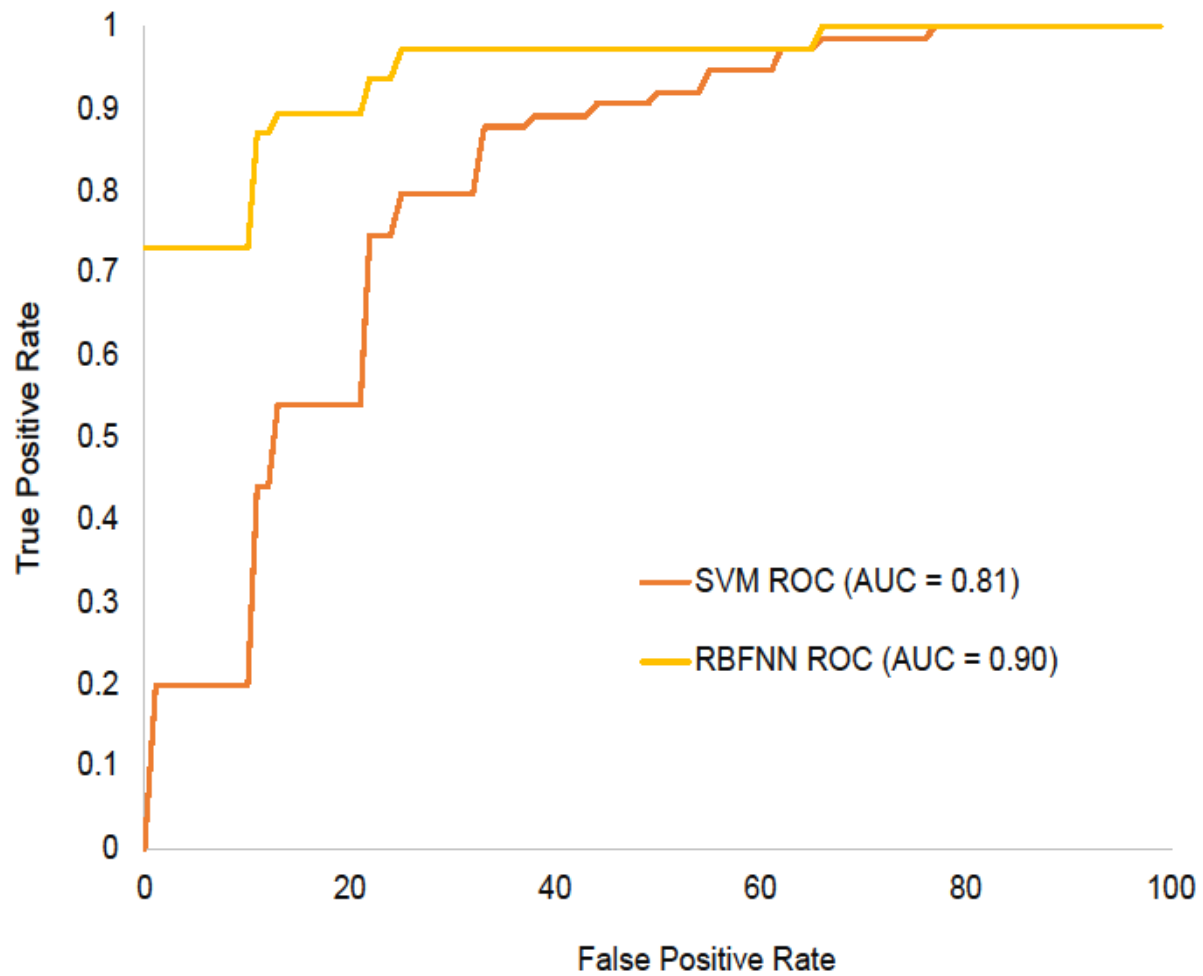


Fig. 3- 28: The mean area under receiver operator curves for RBFNN models and SVM models after k=10 subsets after training with prospect classification type 2.

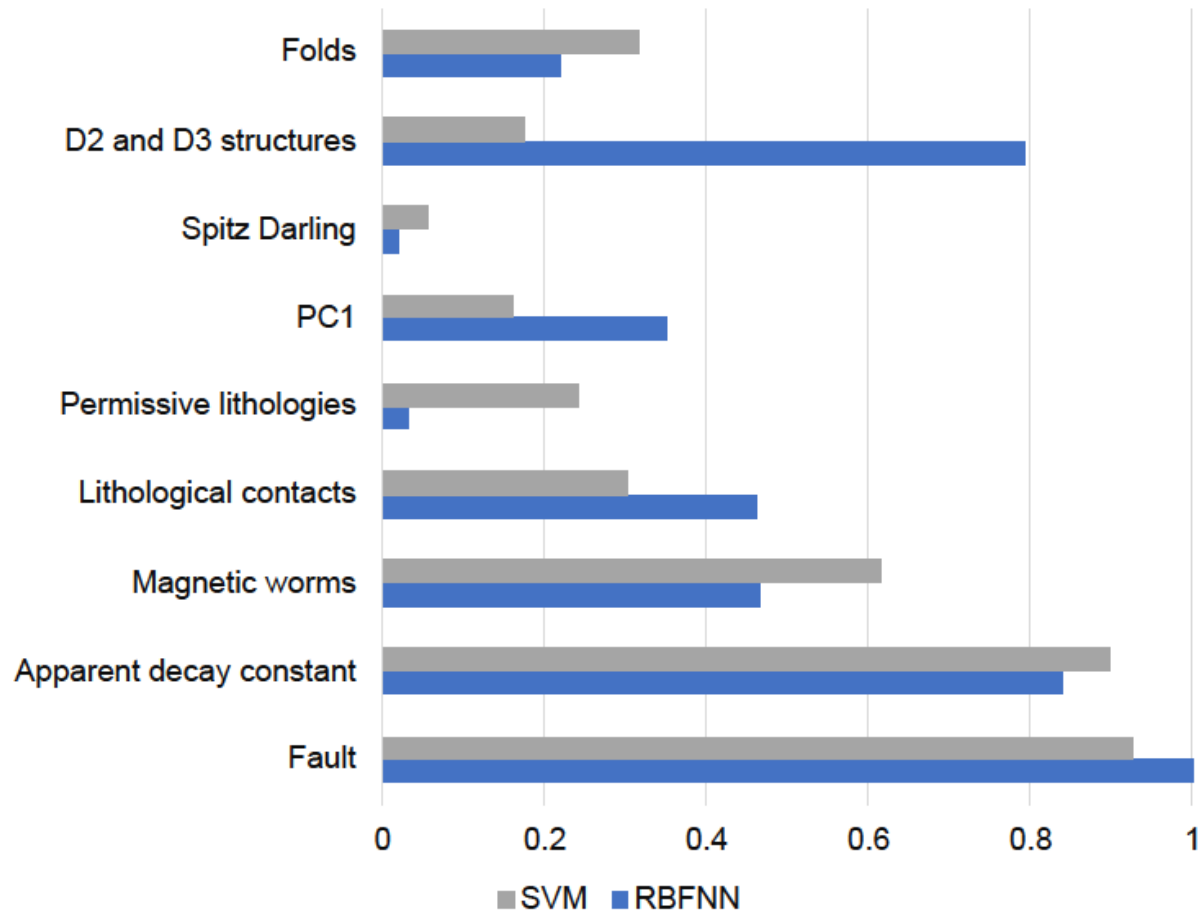


Fig. 3- 29: Feature importance estimations derived from the RBFNN and the SVM prospectivity models after training with prospect classification type 2.

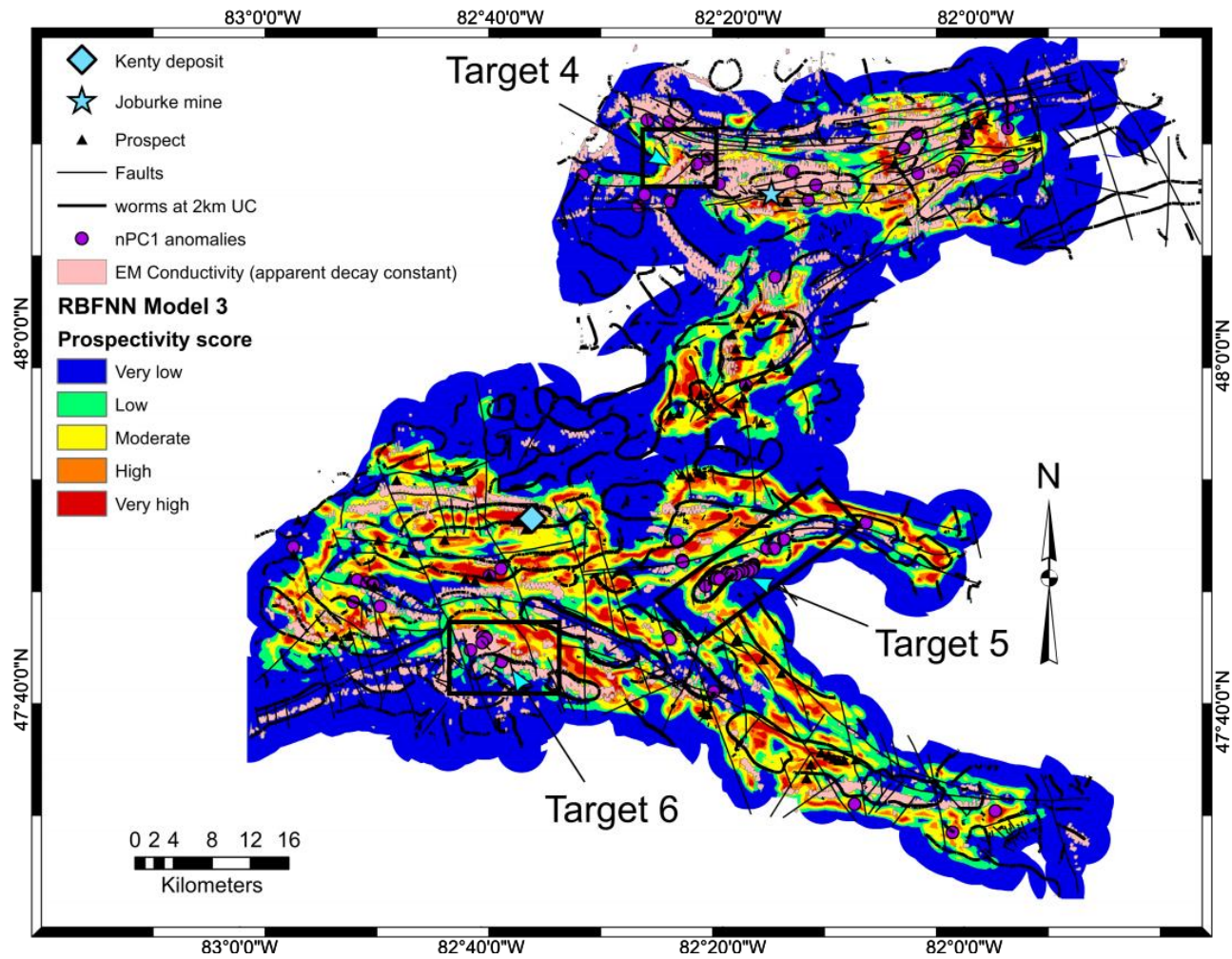


Fig. 3- 30: The RBFNN model showing prospectivity predictions overlain by faults and magnetic worms. The past producing Joburke mine and Kenty prospects are shown

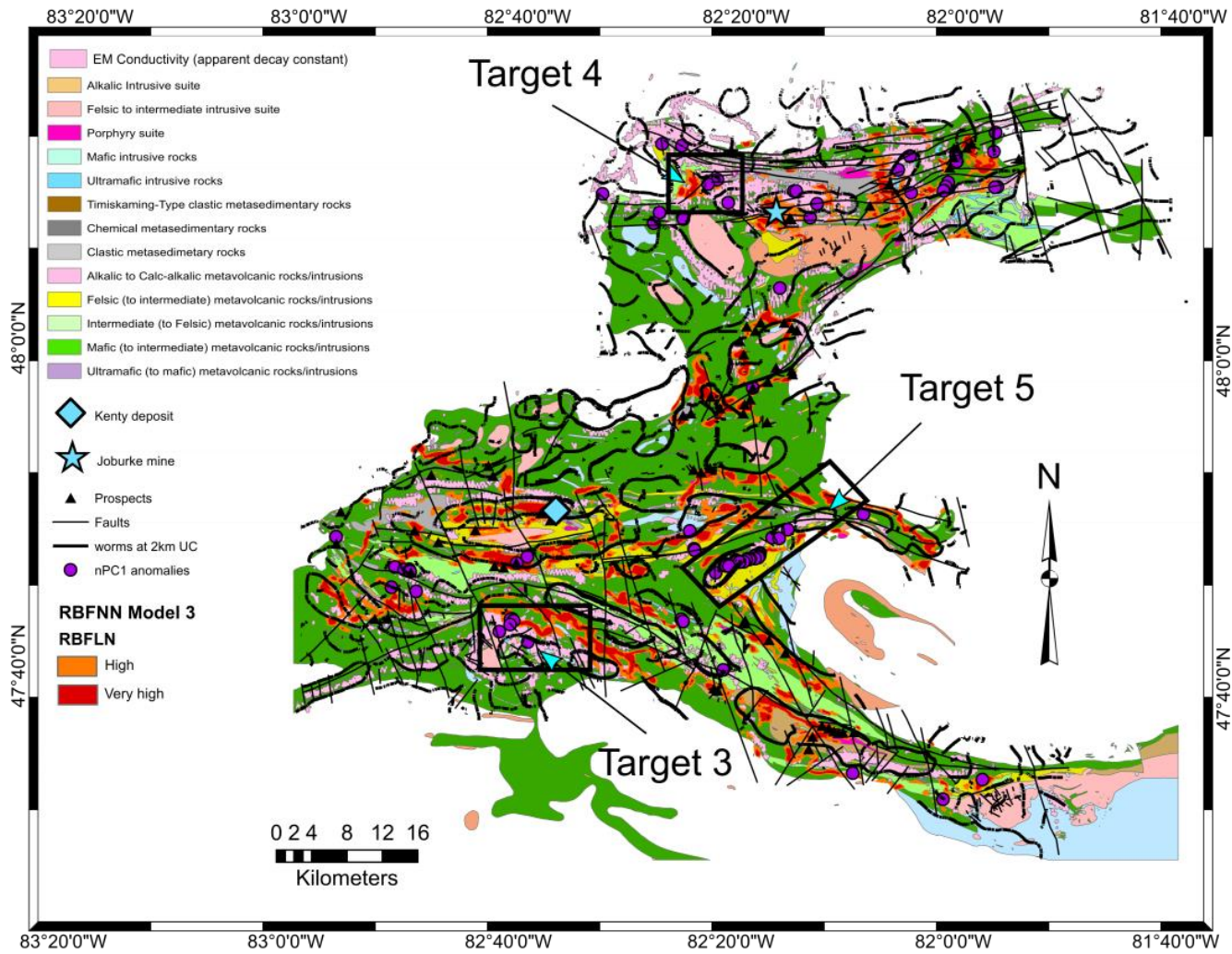


Fig. 3- 31: The high RBFNN model predictions are shown overlying the geological map of the Swayze with faults, EM conductivities, anomalous PC1 samples, and magnetic worms. The past producing Jorburke mine and Kenty prospect are shown.

## 3.7 Discussions

### 3.7.1 Mineral prospectivity mapping overview

Results from classification type 1 show that the SVM and RBFNN models used in this study performed well in mapping prospectivity of gold in the Swayze greenstone belt. The performance metrics of both models (i.e., the mean AUC and mean accuracy scores) are high, >80%, indicating excellent model performances. The standard deviation of SVM with and without geochemical data show well defined and tightly clustered accuracy scores with respect to the mean. This suggests that the level of error introduced into the model due to uncertainty in model parameters is relatively low compared to the RBFNN.

The feature importance scores generated from both SVM (Fig. 3-23B) and RBFNN (Fig. 3-23D) were vital in establishing gold exploration targeting criteria. The high to low feature importance scores agree that major structures such as D<sub>2</sub> and D<sub>3</sub> HSZ and folds, followed by lithological contacts, permissive lithologies, EM apparent decay constant conductivity, and magnetic worms are important datasets to consider while targeting orogenic gold prospects in the Swayze greenstone belt.

Similarly, results from classification type 2 (Fig. 3-26 and Fig. 3-27) also show high classification and prediction performances (> 80% area under curve) and low model variances (<0.08 standard deviations). The feature importance estimations (Fig. 3-29) also indicate that faults, apparent decay constant (i.e., electromagnetic conductivity, D<sub>2</sub> and D<sub>3</sub> high strain zones and magnetic worms) were the most important layers used by the models to predict prospectivity.

According to the feature importance scores, the exploration criteria for orogenic gold prospects in the Swayze greenstone belt require delineating lithospheric-scale high-strain zones. These features represent fluid pathways, and exploration targeting should focus within 6.5 km

distance from the 1<sup>st</sup> order structures which are presumed to be the control of gold mineralization. Within the permissive distance range, areas with high rheological contrasts, proximal to high EM conductivity and magnetic worms could likely suggest the presence of prospective areas for gold mineralization. Both the high EM conductivities and magnetic worms are suitable datasets for regional-scale mapping of sulfide, oxide and silicate facies that are associated with gold mineralization.

The EM conductivities also spatially correlate with chemical metasedimentary rocks such as iron formation which are highly reactive with hydrothermal fluids. The magnetic worms and EM conductivity maps highlight the expressions of metal deposition and preservation of gold mineralization resulting from the interaction between hydrothermal fluid and the host rocks. The lithological contacts scored high in feature importance analysis for both SVM and RBFNN demonstrating the significance of complexity gradient along which fluid-rock interaction has taken place prior to metal precipitation.

### 3.7.3 Implications for exploration and target delineations

#### 3.7.3.1 Targets delineation using prospect classification type 1

The Joburke mine is located in the northern part of the Swayze greenstone belt (Fig. 3-25A), and lies on an east-west striking high EM conductive zone, which extends over a strike length of about 30 km. The high conductive zone strongly correlates with ENE-WSW major fault zone as observed from field geological mapping and processed magnetic map. According to previous studies, the prospect is hosted in quartz-carbonate veins, basalt, and near quartz-feldspar porphyry (Hastie, 2017). This suggests that at regional scales, gold mineralization around the Joburke mine possibly controlled by high-strain zones along which metalliferous fluid flow and

chemical reaction with the host rocks might have taken place. The high EM conductivity therefore suggests the expressions of chemical reaction with the host and also help map strong conductors reflecting disseminated pyrite and/ magnetite at shallow depths (Müller et al., 2021), which consequently contributed to high EM conductivity along the fluid flow path.

Three regional-scale potential targets for follow-up exploration were identified based on the results of SVM and RBFN. These are, Target #1, Target #2, and Target #3 (Fig. 3-25A and 3-25B). Target #1 is proximal to D<sub>2</sub> Slate rock high-strain zone in the north, and its expression is exhibited by high EM conductivity and magnetic worms. This target also lies at the contact between clastic metasedimentary rocks and mafic to intermediate metavolcanic rocks (is shown with an elliptical shape polygon on Fig. 3-24). There are multiple E-W striking 2<sup>nd</sup> and 3<sup>rd</sup>-order faults that correspond to the Slate rock high-strain zone and folds proximal to Target #1. All the four prospectivity maps derived from the SVM and RBFNN consistently highlight the significance of Targe #1 as one of important follow-up areas for gold mineralization.

Target #2 is located at the contact between chemical metasedimentary rocks (i.e., banded iron formation) and mafic to intermediate metavolcanic rocks. The high EM conductivity also suggests the expressions of highly reactive and iron-rich chemical metasedimentary rocks. Target #2 is approximately 2 km away from the D<sub>2</sub> Brett lake high-strain zone, which is characterized by high EM conductivity and magnetic worms.

The area marked as Target #3 on Fig. 3-25 (and the region shown using the black box on Fig. 3-24) can be recommended as one of follow-up exploration targets based on similar interpretation attributed to the Jerome, Rundle, and Joburke mines. This target is situated along the D<sub>2</sub> high-strain zone, F<sub>2</sub> folds which are exhibited by magnetic worms, and high EM

conductivities. In addition, there are multiple cross-cutting faults and contacts between feldspar porphyry and felsic to intermediate metavolcanic rocks proximal to Target #3.

The spatial association between predictive maps and orogenic gold training points were determined using WofE. The results show that there are number of permissive lithologies and lithospheric-scale weak zones that show statistically strong correlation with gold mineralization. On a regional-scale, the predictor maps such as proximity to D<sub>2</sub> and D<sub>3</sub> HSZ, and D<sub>2</sub> folds show strong spatial correlation with gold at a distance  $\leq 8$  km from high-strain zones and major folded structures. This result is consistent with the recent study of Maepa and Smith (2020) in that gold prospects are fractal at a regional-scale, and controlled by 1<sup>st</sup>-order D<sub>2</sub> high-strain zones.

The proximity to faulting, high EM conductivity, and magnetic worms show high spatial correlations with gold prospects. The predictor maps derived from magnetics and electromagnetic data (e.g., mapped structure and apparent decay conductivity) scored high based on SVM and RBFNN feature importance estimates, thus indicating the importance of geophysical data for mapping fluid pathway in orogenic mineral systems.

### 3.7.3.2 Targets delineation using prospect classification type 2

From the prospectivity models derived using prospect classification type 2 (Fig. 3-26 and Fig. 3-27), three new possible target areas (Target #4, #5, and #6) were selected for future exploration. Each target (shown on Fig. 3-230 and Fig. 3-31) correlates with high EM conductivity, magnetic worms, faults, lithological complexity gradients, and the presence of PC1 anomalies. The PC1 anomalies plotted on Fig. 3 – 30 was obtained by plotting a Q-Q probability plot in the GIS and separating the anomalous PC1 values from the background. The anomalous values are seen to spatially correlate with the high prospectivity values. Future exploration of

Targets #4, #5, and #6 might benefit from more detailed geochemical sampling, geological mapping, drilling, and possibly more prospect-scale geophysical analysis.

#### 3.7.4 Comparison with previous study by Harris et al., (2001)

Harris et al (2001) used WoE modelling approach and generated mesothermal gold prospectivity maps of the Swayze greenstone belt. Although the predictor layers used and the modelling approaches are different, the results of the present study are consistent with the previous work. For example, areas labelled as *L*, *D*, *JB*, *Q*, *G1*, and *G2* on Fig. 3-32A correspond to the high prospective zones shown on Fig. 3-32B. The RBFNN model defined larger area as highly prospective compared to Harris et al., 2002 (Figs. 3-32A and 3-32B). However, the differences between the two sets of prospectivity maps can be attributed to: 1) the use of new geophysical data which were not available in the previous study; 2) differences in predictor layers and GIS spatial data pre-processing techniques. For example, Harris et al. (2001) map shown on Fig. 3-32A was derived using point geochemical data instead of spatial interpolation applied to point geochemical data.

According to Harris et al (2001), the use of point geochemical data as a layer of evidence provides better model performance than predictor layers generated using spatial interpolation. In addition, Harris et al. (2001) used more geochemical predictor maps than the present study. Weights of evidence assumes conditional independence among various predictor layers used for prospectivity mapping (Bonham-Carter et al., 1989). A violation of conditional independence may result in inflated posterior probability predictions in certain regions. However, in this study, lithological contacts and geophysical data (EM conductivity and magnetic worms) are more favourable as predictor layers than geochemical data.

Furthermore, artificial neural network model calculates weights and classifies the input feature vectors differently from WoE methods, and this may have contributed to discrepancy between the results of the previous study and the present work. In addition, the present study used K-fold cross-validation technique for training, while train test split approach was implemented in the previous study. The K-fold cross validation technique was more effective when training RBFNN and SVM models because K-Fold helps to minimise bias during selection of training and validation data. The K-Fold enables to improve model performance and output predictions, particularly when working with artificial neural network models that are prone to overfitting.

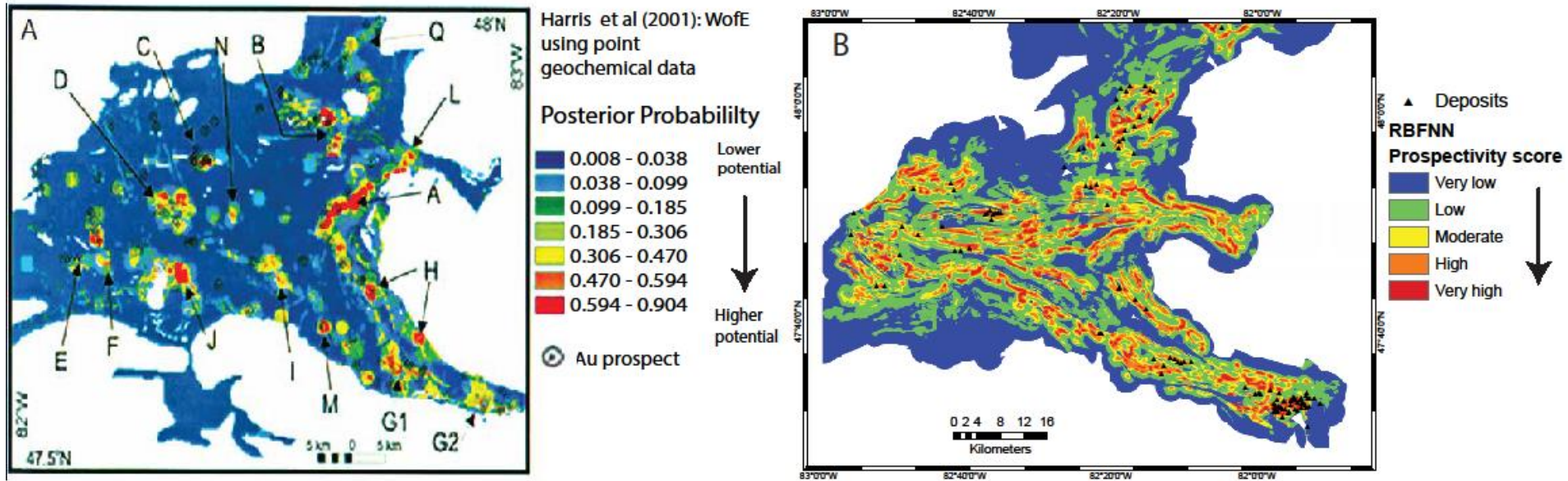


Fig. 3- 32: Comparison of current prospectivity maps with the weights of evidence prospectivity mapping results from Harris (2001). The mineral prospectivity maps of the southern Swayze greenstone belt are shown side by side indicating prospectivity scores from weights of evidence (Harris et al., 2001) and the current radial basis function neural network study (right).

### 3.7.4 Comparison of model performances

Overall, our implementation of the data-driven methods was successful in helping to define predictor maps and generate meaningful gold prospectivity maps of the Swayze greenstone belt. Comparison of the results of SVM with RBFNN highlights strong spatial correlation with respect to high prospective areas and accuracy scores. However, the results of RBFNN reveal more extensive highly prospective areas as compared to the SVM. The standard deviation derived from accuracy estimations at each fold are lower for SVM ( $< 0.10$ ) than for RBFNN ( $< 10.12$ ).

This suggests that SVM accuracy scores are clustered around the mean, which suggests that the 10-fold used for training the machine learning tools exhibit lower model variance and uncertainty. The RBFNN models show higher standard deviation than SVM after 10 folds cross-validation, which implies that high variance in the accuracy scores resulting in a spread around the mean, hence the SVM performance was statistically better than RBFNN.

The model performance plots for RBFNN (Fig. 3-22) show an improved accuracy scores with increasing number of iterations. The mean training and validation accuracy and mean squared error loss scores are comparable signifying good performances. The ROC plots on Fig. 3-23 for both RBFNN and SVM indicate that both models performed very well in distinguishing between true positives and false positives scores.

### 3.8 Conclusions

The weights of evidence statistics together with machine learning feature importance estimations are useful in determining predictor layers that best outline prospective areas for gold mineralization. The feature importance scores outlined the decision process of the data-driven

methods and reduced the lack of transparency of machine learning methods (especially artificial neural networks).

Overall, the prospectivity predictions from both methods are comparable and the metrics scores are almost similar. Both methods prove to be robust and perform well in defining new prospective regions (as shown on Fig. 3-24 and Fig. 3-25). The SVM method shows lower standard deviation of the accuracy scores than RBFNN indicating lesser model uncertainty as compared to RBFNN. Using the first mineral prospect classification from the Swayze greenstone belt, it was established from the data integration and machine learning that the geological, structural and geophysical characteristics of Targets #1, #2, and #3 are similar to Jerome, Joburke, and the Rundle mines.

These targets lie proximal to regional-to-district-scale 1<sup>st</sup> and 2<sup>nd</sup>-order high-strain zones, which can be interpreted as fluid pathways in the mineral systems analysis. The major structures are characterized by high EM conductivity and magnetic worms representing regions of hydrothermal fluid circulations. The targets spatially correspond to rocks with high rheological contrasts and chemically reactive rock units.

The second prospect classification method derived the same conclusions with a slightly lower uncertainty measurement and thus better model predictions metrics. The data integration and predictive models indicated new potential targets that also lie proximal to EM conductivities, magnetic gradients, and nearer to faults. Prospectivity maps derived from the first and second classification type were almost similar, except for predictions in the southeastern Swayze. Using legacy geoscience data, the expressions of mappable proxies of orogenic mineral systems were defined and an exploration targeting approaches that utilize multiple data-driven techniques was

established. The Bayesian weights of evidence, SVM and RBFNN machine learning tools, were significant in defining regional-scale prospective areas for gold mineralization.

### 3.9 Acknowledgements

This work was financially supported by the International Development Research Centre (IDRC); Queen Elizabeth II Diamond Jubilee Scholarships; Ivanhoe Mines and Goodman School of Mines. We thank Charles Scott Spath III for proofreading the manuscript.

### 3.10 References

- Abedi, M., Norouzi, G., Bahroudi, A., 2012. Support vector machines for multi-classification of mineral prospectivity areas. *Comput. Geosci.*, 46, 272 – 283.
- Agterberg, F.P., Cabilio, P., 1969. Two-Stage Least-Squares Model for the Relationship Between Mappable Geological Variables. *J. Int. Ass. for Math. Geosci. I*, 138–153.
- Agterberg, F.P., 1989. Systematic approach to dealing with uncertainty of geoscience information in mineral exploration: Proceedings 21st APCOM Symposium, Las Vegas, March 1989, Chapter 18. 165 - 178
- Agterberg, F.P., Bonham-Carter, G.F., Wright, D.F., 1990. Statistical pattern integration of mineral exploration. *Comput. Geosci.* 1 - 21.
- Andina, D., Pham, D.T., 2008. *Computational intelligence: For engineering and manufacturing*, Springer, Boston, pp. 212.

Ayer, J., 1995. Precambrian geology northern Swayze greenstone belt. Ontario Geological Survey, Open File Report 297, pp. 57. Available from: <http://www.geologyontario.mndmf.gov.on.ca/>.

[Accessed: 14 April 2020]

Ayer J.A., Trowel N.F., 2002. Geological compilation of the Swayze area, Abitibi greenstone belt; Ontario Geological Survey, Preliminary Map P.3511, scale 1:100 000. Available from : <http://www.geologyontario.mndm.gov.on.ca/> [Accessed: 14 April 2020].

Basheer, I.A., Hajmeer, M., 2000. Artificial neural networks: fundamentals, computing, design, and application. *J. of Microbiol. Methods.* 43, 3-31.

Bierlein, F.P., Groves, D.I., Goldfarb, R.J., Dubé, B., 2006. Lithospheric controls on the formation of provinces hosting giant orogenic gold deposits. *Miner. Deposita.* 40, 874–886.

Bonham-Carter, G.F., Agterberg, F.P., Wright, D.F., 1989. Weights of evidence modelling: a new approach to mapping mineral potential. Geological Survey of Canada, Paper no. 89-9, 171-183.

Bonham-Carter, G.F., 1994. *Geographic Information Systems for Geoscientists: Modelling with GIS.* Computer and Geosciences. Pergamon, New York, pp. 416.

Bonham-Carter, G.F., Agterberg, F.P., Wright, D.F., 1988. Integration of Geological Data Sets for Gold Exploration in Nova Scotia. *Photogramm. Eng. Rem. S.* 54, 1585–1592.

Breemen., O.V., Heather., K.B., Ayer., J.A., 2006. U-Pb geochronology of the Neoproterozoic Swayze sector of the southern Abitibi greenstone belt. Geological Survey of Canada. *Nat. Resour. Res.* pp. 32.

Broomhead, D.S., Lowe, D., 1988. Multivariate functional interpolation and adaptive networks, *Complex Syst.* 2, 321 – 355

Calvert, A.J., Ludden, J.N., 1999. Archean continental assembly in the southeastern Superior Province of Canada. *Tectonics*. 18, 412–429.

Carranza, E.J.M., 2009. *Geochemical Anomaly and Mineral Prospectivity Mapping*, 1st Edition. ed. Elsevier Science, Amsterdam, pp. 368.

Carranza, E.J.M., 2004. Weights of evidence modeling of mineral potential: A case study using small number of prospects, Abra, Philippines. *Nat. Resour. Res.* 13, 173–187.

Cheraghi, S., Naghizadeh, M., Snyder, D., Haugaard, R., Gemell, T., 2020. High-resolution seismic imaging of crooked two-dimensional profiles in greenstone belts of the Canadian shield: results from the Swayze area, Ontario, Canada. *Geophys. Prosp.* 68, 62 -81.

Condie, K.C., 1986. Geochemistry and tectonic setting of early Proterozoic supracrustal rocks in the southwestern United States. *J. Geol.* 94, 845–864.

Connolly, J.A.D., 2010. The mechanics of metamorphic fluid expulsion. *Element*. 6, 165–172.

Chang, Y., Lin, C., 2008. Feature ranking using linear SVM. *JMLR: Workshop and Conference Proceedings*. 3, 53 -64.

Cox, S.F., 2016. Injection-driven swarm seismicity and permeability enhancement: implications for the dynamics of hydrothermal ore systems in high fluid-flux, over-pressured faulting regimes - An invited paper. *Econ. Geol.* 111, 559–587.

Davies, R.S., Groves, D.I., Trench, A., Dentith, M., 2020. Towards producing mineral resource-potential maps within a mineral systems framework, with emphasis on Australian orogenic gold systems. *Ore Geol. Rev.* 119, 103 – 369.

Davis, J.C., 2002. *Statistics and Data Analysis in Geology*. 3rd edition. John Wiley & Sons Inc, New York, pp. 656.

De Sá, C.R., 2019. Variance-based feature importance in neural networks, in Novak, P.K., Šmuc, T., Džeroski, S., ed., *Discover Science 2019: Switzerland*, Springer Nature, 306 - 315.

Ford, A., Peters, K.J., Partington, G.A., Blevin, P.L., Downes, P.M., Fitzherbert, J.A., 2019. Translating expressions of intrusion-related mineral systems into mappable spatial proxies for mineral potential mapping: Case studies from the southern New England Orogen, Australia. *Ore Geol. Rev.* 111, 102943.

Fumerton, S., Houle, K., 1995. Mineral Prospects of the Swayze greenstone belt, Volume 1 - parts of NTS 41 O, and Volume 2- parts of NTS 41 P, 42 A and 42 B: Ontario Geological Survey, Open File Report 5912, 1, pp. 372. Available: <http://www.geologyontario.mndmf.gov.on.ca/> [Accessed: 14 April 2020].

Fyfe, W.S., Kerrich, R., 1976. Geochemical prospecting: extensive versus intensive factors. *J. Geochem. Explor.* 6, 177–192.

Gaboury, D., 2019. Parameters for the formation of orogenic gold deposits. *Appl. Earth Sci.* 128, 124 – 133.

Goldfarb, R.J., Groves, D.I., Gardoll, S., 2001. Orogenic gold and geologic time: a global synthesis. *Ore Geol. Rev.* 18, 1 – 75.

Goldfarb, R.J., Baker, T., Dube, B., Groves, D.I., Hart, C.J.R., Gosselin, P., 2005. Distribution, character, and genesis of gold deposits in metamorphic terranes. *Econ. Geol.* 100, 407–450.

Goldfarb, R.J., Groves, D.I., 2015. Orogenic gold: common or evolving fluid and metal sources through time. *Lithos.* 233, 2–26.

Groves, D. I; Goldfarb R.J; Gebre-Mariam, M; Hagemann, S.G; Rober, F., 1998. Orogenic gold deposits: A proposed classification in the context of their crustal distribution and relationship to other gold deposits. *Ore Geol. Rev.* 13, 7–27.

Groves, D.I., Condie, K.C., Goldfarb, R.J., Hronsky, J.M.A., Vielreicher, R.M., 2005. 100th Anniversary special paper: Secular changes in global tectonic processes and their influence on the temporal distribution of gold-bearing mineral deposits. *Econ. Geol.* 100, 203–224.

Groves, D.I., Goldfarb, R.J., Santosh, M., 2016. The conjunction of factors that lead to formation of giant gold provinces and deposits in non-arc settings. *Geosci. Front*, 7, 303 – 314.

Groves, D.I., Santosh, M., Zhang, L., 2020. A scale-integrated exploration model for orogenic gold deposits based on a mineral systems approach. *Geosci. Front* in press.

Grunsky, E.C., 1986. Recognition of alteration in volcanic rocks using statistical analysis of lithochemical data. *J. Geochem. Explor.* 25, 157 - 183.

Grunsky, E.C., 2010. The interpretation of geochemical survey data. *Geochem. Explor. Env. A*, 10, 27 - 74.

Ontario Geological Survey, 2003. Ontario airborne magnetic and electromagnetic surveys geophysical data set 1005 - Revised. Available: <http://www.geologyontario.mndm.gov.on.ca/>.  
[Accessed: 14 April 2020]

Hagemann, S.G., Cassidy, K.F., 2000. Archean orogenic lode gold deposits. In: Hagemann, S.G., Brown, P.E. (Eds.), *Gold in 2000*. Society of Economic Geologists, Reviews in Econ. Geol. 13, 9–68.

Hagemann, S.G., Lisitsin, V.A., Huston, D.L., 2016. Mineral System Analysis: Quo Vadis. *Ore Geol. Rev.* 76, 504 – 522.

Harris, J.R., Wilkinson, L., Grunsky, E.C., 2000. Effective use and interpretation of lithochemical data in regional mineral exploration programs: Application of Geographic Information Systems (GIS) technology. *Ore Geol. Rev.* 16, 107–143.

Harris, J.R., Wilkinson, L., Heather, K., Fumerton, S., Bernier, M.A., Ayer, J., Dahn, R., 2001. Application of GIS processing techniques for producing mineral prospectivity maps – a case study: mesothermal Au in the Swayze greenstone belt, Ontario, Canada.

Harris, J.R., 2002. Processing and integration of geochemical data for mineral exploration: application of statistics, geostatistics, and GIS Technology. PhD thesis, University of Ottawa.

Hastie, E.C.G., Lafrance, B., Kontak, D.J., 2015. Project Unit 14-009. Observations on the Kenty and Rundle Deposits, Swayze Greenstone Belt, Ontario Geological Survey, Open File Report 6280. Available: <http://www.joshuagoldresources.com/>. [Accessed: 14 April 2020].

Hastie E.C.G., 2017. Gold metallogeny of the southern Swayze area, Abitibi greenstone belt: A field trip guidebook. Ontario Geological Survey, Open File Report 6334. Available: <http://www.geologyontario.mndmf.gov.on.ca/>. [Accessed: 14 April 2020].

Hastie, E.C.G., Kontak, D.J., Lafrance, B., 2020. Gold remobilization: Insights from gold deposits in the Archean Swayze greenstone belt, Abitibi Subprovince, Canada. *Econ. Geol.* 115, 241 – 277.

Heather, K.B., 1998. New insights on the stratigraphy and structural geology of the southwestern Abitibi greenstone belt: implications for the tectonic evolution and setting of mineral deposits in the Superior Province; in *The First Age of Giant Ore Formation: Stratigraphy, Tectonics and*

Mineralization in the Later Archean and Early Proterozoic, Toronto, Prospectors and Developers Association of Canada Annual Convention, p. 63 – 101.

Heather, K., 2001. The geological evolution of the Archean Swayze greenstone belt, Superior Province, Canada. PhD Thesis. Keele University.

Huang, C., Davis, L.S., Townshend, J.R.G., 2002. An assessment of support vector machines for land cover classification. *Int. J. Remote Sens.* 23, 725–749.

Ikechukwu, M.N., Ebinne, E., Idorenyin, U., Raphael, N.I., 2017. Accuracy assessment and comparative analysis of IDW, spline and kriging in spatial interpolation of landform (topography): An experimental study. *J. Geogr. Syst.* 9, 354–371.

Jolliffe, I.T., 2002. *Principal Components Analysis*. 2nd Edition, Springer, New York. pp. 271

Katz, L.R., 2016. Geology of the Archean Côte Gold Au (-Cu) intrusion-related deposit, Swayze greenstone belt, Ontario. PhD Thesis, Laurentian University, Canada, pp. 347.

Katz, L.R., Kontak, D.J., Dubé, B., McNicoll, V., 2017. The geology, petrology, and geochronology of the Archean Côte Gold large-tonnage, low grade intrusion-related Au(-Cu) deposit, Swayze greenstone belt, Ontario, Canada. *Can. J. Earth Sci.* 54, 173 – 202.

Kavzoglu, T., Colkesen, I., 2009. A kernel functions analysis of support vector machines for land cover classification. *Int. J. Appl. Earth Obs. Geoinf.*, 11, 352 – 359.

Kecma, V., 2005. *Support vector machines: Theory and Applications*. Springer. Berlin, Heidelberg. 1 – 47.

Kerrick, R., 1986. Fluid infiltration into fault zones: Chemical, Isotopic, and Mechanical Effects. *Pure Appl. Geophys.* 124, 1-2. 225 - 28.

Kerrick, R., 1991. Mesothermal gold deposits: a critique of genetic hypotheses. In: Robert, F., Sheahan, P.A., Green, S.B. (Eds.), *Greenstone Gold and Crustal Evolution: Geological Association of Canada, NUNA Conference Volume*, 13–31.

Kerrick, R., Goldfarb, R., Groves, D., Garwin., 2000. The geodynamics of world-class gold deposits: characteristics, space-time distribution, and origins. In: Hagemann, S.G., Brown, P.E. (Eds.), *Gold in 2000*. Society of Economic Geologists, *Reviews in Econ. Geol.*13, 501 - 551.

Knox-Robinson, C.M., Wyborn, L.A.I., 1997. Towards a holistic exploration strategy: Using Geographic Information Systems as a tool to enhance exploration. *Aust. J. Ear. Sci.* 44, 453–463.

Kontak, D.J., Creaser, R.A., and Hamilton, M.A., 2013, Section 2: Geological and geochemical studies of the Côté Lake Au(-Cu) deposit area, Chester Township, Northern Ontario, *In: Results from the Shining Tree, Chester Township and Matachewan Gold Projects and the Northern Cobalt Embayment Polymetallic Vein Project*. Ontario Geological Survey, Miscellaneous Release – Data 294.

Kreuzer, O.P., Buckingham, A., Mortimer, J., Walker, G., Wilde, A., Appiah, K., 2019. An integrated approach to the search for gold in a mature, data-rich brownfields environment: A case study from Sigma-Lamaque, Quebec. *Ore Geol. Rev.* 111, 1 – 23.

Kubat, M., 2017, *An introduction to machine learning*: Springer International Publishing, 348p.

Lambeck A, Mernagh TP, Wyborn L. 2011. Are iron-rich sedimentary rocks the key to the spike in orogenic gold mineralization in the Paleoproterozoic? *Econ Geol.* 106:321–330.

Large R, Thomas H, Craw D, Henne A, Henderson S. 2012. Diagenetic pyrite as a source for metals in orogenic gold deposits, Otago Schist, New Zealand. *New Zealand. J Geol Geophys.* 55:137–149.

- Looney, C.G., 2002. Radial basis functional link nets and fuzzy reasoning. *Neurocomputing*, 48, 489–509.
- Love, D.A., Roberts, R.G., 1991. The geology and geochemistry of gold mineralization and associated alteration at the Rundle gold deposit, Abitibi Sub-province, Ontario. *Econ. Geol.* 86, 644–666.
- Maepa, M.F., Smith, R.S.S., 2020. Examining the controls on gold deposit distribution in the Swayze greenstone belt, Ontario, Canada, using multi-scale methods of spatial data analysis. *Ore Geol. Rev.* 125. 1 – 21.
- Magoon, L.B., Dow, W.G., 1994. The Petroleum Mineral System. *AAPG Mem.* 60, 3 -24
- Marmont, S.C.A., 1983. The role of felsic intrusions in gold mineralization, Ontario Geological Survey, Miscellaneous Paper 110. Ontario Geological Survey, Miscellaneous Paper 110. Available: <http://www.geologyontario.mndmf.gov.on.ca/>. [Accessed: 14 April 2020].
- McCulloch, W.S., Pitts, W., 1943. A logical calculus of the ideas immanent in nervous activity. *Bull. Math. Biol.* 5, 115–133.
- McCuaig, T.C., Beresford, S., Hronsky, J., 2010. Translating the mineral systems approach into an effective exploration targeting system. *Ore Geol. Rev.* 38, 128 – 138.
- McCuaig, T.C., Hronsky, J.M.A., 2014. The Mineral System Concept: The Key to Exploration Targeting. *SEG 2014: Building Exploration Capability for the 21<sup>st</sup> Century*, 153–175.
- Milne, V.G., 1972. Geology of the Kukatush-Sewell Lake Area, District of Sudbury; Ontario Division. Mines, GR97, 1-116. Accompanied by Maps 2230, 2231, scale 1 inch to 1/2 mile. Available: <http://www.geologyontario.mndmf.gov.on.ca/>. [Accessed: 14 April 2020].

Müller, D., Kwan, K., Groves, D.I., 2021. Geophysical implications for the exploration of concealed orogenic gold deposits: A case study in the Sandy Lake and Favourable Lake Archean greenstone belts, Superior Province, Ontario, Canada, 128,

Nykänen, V., 2008. Radial basis functional link nets used as a prospectivity mapping tool for orogenic gold deposits within the central Lapland greenstone belt, Northern Fennoscandian shield. *Nat. Resour. Res.* 17, 29–48.

Nykänen, V., Lahti, I., Niiranen, T., Korhonen, K., 2015, Receiver operating characteristics (ROC) as validation tool for prospectivity models – A magmatic Ni-Cu case study from the Central Lapland greenstone belt, Northern Finland, *Ore Geol. Rev.*, 71, 853 – 850.

Obuchowski, N.A., 2003. Receiver Operating Characteristic Curves and Their Use in Radiology. *Radiology* 229, 3–8.

Oliver, M., 1990. Kriging: A method of interpolation for Geographical Information Systems. *Int. J. Geogr. Inf. Syst.* 4, 313–332.

Pearson, K./ 1901. On lines and planes of close fit to systems of points in space. *Philos. Mag.* 11, 559 -572.

Parsa, M., Maghsoudi, A., Yousefi, M., 2017a. An improved data-driven fuzzy mineral prospectivity mapping procedure; cosine amplitude-based similarity approach to delineate exploration targets. *Int. J. Appl. Earth Obs.*, 58, 157-167.

Parsa, M., Maghsoudi, A., Yousefi, M., Carranza, E.J.M., 2017b. Multifractal interpolation and spectrum–area fractal modeling of stream sediment geochemical data: Implications for mapping exploration targets. *J. Afr. Earth Sci.*, 128, 5-15.

- Parsa, M., Maghsoudi, A., Carranza, E.J.M., Yousefi, M., 2017c. Enhancement and mapping of weak multivariate stream sediment geochemical anomalies in Ahar Area, NW Iran. *Nat. Resour. Res.* 26(4), 443-455.
- Parsa, M., Maghsoudi, A., Yousefi, M., 2018a. A receiver operating characteristics-based geochemical data fusion technique for targeting undiscovered mineral deposits. . *Nat. Resour. Res.* 27(1), 15-28.
- Parsa, M., Maghsoudi, A., Yousefi, M., 2018b. Spatial analyses of exploration evidence data to model skarn-type copper prospectivity in the Varzaghan district, NW Iran. *Ore Geol. Rev.* 92, pp.97-112.
- Phillips, G.N., Powell, R., 2010. Formation of gold deposits: a metamorphic devolatilization model. *J. Metamorph. Geol.* 28, 689 - 718.
- Pirajno, W., 2008. *Hydrothermal Processes and Mineral Systems*. Geological Survey of Western Australia. Perth, Australia.
- Pitcairn, I.K., Teagle, D. A. H., Craw, D, Olivo, G.R., Kerrich, R., Brewer, T.S., 2006. Sources of metals and fluids in orogenic gold deposits: Insights from the Otago and Alpine Schists, New Zealand. *Econ Geol.* 101, 1525–1546.p
- Porwal, A.K., Carranza, E.J.M., Hale, M., 2003. Artificial Neural Networks for Mineral-Potential Mapping: A Case Study from Aravalli Province, Western India. *Nat. Resour. Res.* 12, 155–171.
- Porwal, A.K., Kreuzer, O.P., 2010. Introduction to the Special Issue: Mineral prospectivity analysis and quantitative resource estimation. *Ore Geol. Rev.* 38, 121–127.

Powell, W.G., Carmichael, D.M., Hodgson, C.J., 1995. Conditions and timing of metamorphism in the southern Abitibi greenstone belt, Quebec. *Can. J. Earth Sci.* 32, 787 - 805.

Phillips, G.N., Powell, R., 2010. Formation of gold deposits: a metamorphic devolatilization model. *J Metam Geol.* 28,689–718.

Porwal, A.K., Kreuzer, O.P., 2010. Introduction to the Special Issue: Mineral prospectivity analysis and quantitative resource estimation. *Ore Geol. Rev.* 38, 121 – 127.

Ridley, J.R., Diamond, L.W., 2000. Fluid chemistry of orogenic lode gold deposits and implications for genetic models. *Rev Econ Geol.* 13, 146–162.

Robb L.J., 2005. *Introduction to Ore-Forming Processes*, Blackwell Publishing.

Robert, F., 1989. Internal structure of the Cardillac tectonic zones southeast of Vald'Or, Abitibi greenstone belt, Quebec. *Econ. Geol.* 26, 2661 – 2675.

Robert, F., 2001. Syenite-associated disseminated gold deposits in the Abitibi greenstone belt, Canada. *Miner. Deposita.* 36, 503 – 516.

Rogers, J.R., Beilhartz, D., Kontak, D.J., Katz, L., Dubé, B., and McNicoll, V., 2013, The Côté Gold deposit: discovery of a new generation low-grade, multi-million-ounce gold resource in the Archean Superior Province of Canada [ext. abs.]. *NewGenGold Conference*, Perth, Australia, 2013, *Extended Abstracts*, p. 159-174.

Roshanravan, B., Kreuzer, O.P., Bruce, M., Davis, J., Briggs, M., 2020. Modelling gold potential in the Granites-Tanami Orogen, NT, Australia: A comparative study using continuous and data driven techniques. *Ore Geol. Rev.* 125, 1 – 49.

Rosenblatt, F., 1958. The perceptron: A probabilistic model for information storage and organization in the brain, *Psychol. Rev.* 65, 6, 386-408

Sarle, W.S., 1994. Neural networks and statistical models. Proceedings of the nineteenth annual SAS Users Group International Conference. Cary: NC, SAS Institute Inc., 1538-1550. Available: [https://people.orie.cornell.edu/davidr/or474/nn\\_sas.pdf](https://people.orie.cornell.edu/davidr/or474/nn_sas.pdf). [Accessed: 14 April 2020].

Sibson, R.H., Poulsen, F.R.K., 1988. High-angle reverse faults, fluid-pressure cycling, and mesothermal gold-quartz deposits. *Geology*. 16, 551 - 555.

Sawatzky, D., Raines, G., Bonham-carter, G., 2010. Spatial Data Modeller. U.S Geological Survey, Geological Survey of Canada. Available: <https://www.ige.unicamp.br/sdm/ArcSDM10/source/ReadMe.pdf>. [Accessed: 14 April 2020].

Schodde, R. C., 2004. Discovery performances of the western world gold industry over the period 1985–2003. PACRIM 2004 Proceedings, Melbourne.

Schodde, R., 2014. Uncovering exploration trends and the future: where is exploration going? *In*: Abstract Rimfire Pacific Mining AGM, Melbourne, 14th Nov 2014: 1–36.

Schodde, R., 2017. Long term trends in global exploration-Are we finding enough metals? *In*: 8th Fennoscandian Exploration and Mining Conference. Levi, Finland. 1–66.

Smith, R.S., 2000. The realizable resistive limit: A new concept for mapping geological features spanning a broad range of conductance's. *Geophysics* 65, 1124–1127.

Small, C.R., McDonald, A.M., Hastie, E.C.G., 2018. The Rundle Intrusive Complex: Investigating oxidation processes related to gold mineralization in an archean alkalic intrusive setting, Ontario Geological Survey, Open File Report 6350, 1 - 8

Spitz, G., Darling, R., 2011. Major and minor element lithogeochemical anomalies surrounding the Louven copper deposits, Val d'Or, Quebec, Can. J. Earth Sci. 15, 1161 – 1169.

Tax, D., Duin, E., 1999. Support vector domain description. Pattern Recognit. Lett., 20, 1191 - 1199.

Tessema, A., 2017. Mineral Systems Analysis and Artificial Neural Network Modeling of Chromite Prospectivity in the Western Limb of the Bushveld Complex, South Africa. Natural Resources Research. 26, 465–488.

Thurston, P.C., 2002. Autochthonous development of superior province greenstone belts? Precambrian Res. 115, 11 – 36.

Thurston, P.C., Ayer, J.A., Gouttier, J., Hamilton, M.A., 2008. Depositional gaps in Abitibi Greenstone belt stratigraphy: A key to exploration for syngenetic mineralization. Econ. Geol. 103, 1097 – 1134.

Thomas, H.V., Large, R.R., Bull, S.W., Maslennikov, V., Berry, R.F., Fraser, R., Froud, S., Moye, R., 2011. Pyrite and pyrrhotite textures and composition in sediments, laminated quartz veins, and reefs at Bendigo gold mine, Australia: Insights for ore genesis. Econ Geol. 106, 1–31.

Tomkins, A.G., 2013. On the source of orogenic gold. Geology. 41,1255–1256.

Vapnik, V., 1995. Nature of statistical learning theory. John Wiley and Sons, Inc, New York.

Vaughan, C., 1988. A Novel Approach to AEM Data Compilation, Proceedings of the USGS sponsored AEM Workshop, Denver, Colorado.

Vearncombe, J., Vearncombe, S., 1999. The spatial distribution of mineralization: application of Fry analysis. Econ. Geol. 94, 475-485,

Vearncombe, J., Zelic, M., 2015. Structural paradigms for gold: do they help us find and mine? *Appl Earth Sci.* 124, 2 -19.

Wagner, T., Fusswinkel, T., Wälle, M., and Heinrich, C.A., 2016. Microanalysis of fluid inclusions in crustal hydrothermal systems using laser ablation methods: *Elements*. 12, 323–328.

Wyborn, L.A., Heinrich, C.A., Jaques, A.L., 1994. Australian proterozoic mineral systems essential ingredients and mappable criteria. *AusIMM Public.* 109–115.

Wyman, D.A., Cassidy, K.F., Hollings, P., 2016. Orogenic gold and the mineral systems approach: resolving fact, fiction, and fantasy. *Ore Geol. Rev.* 78, 322–335.

li

Xue, Y., Campbell, I.H., Ireland, T.R., Holden, P., and Armstrong, R., 2013. No mass-independent sulfur isotope fractionation in auriferous fluids supports a magmatic origin for Archean gold deposits: *Geology*, 41, 791–794.

Yousefi, M., Kreuzer, O.P., Nykanen, V., Hronsky, J.M.A., 2019. Exploration information systems – A proposal for the future use of GIS in mineral exploration targeting. *Ore Geol. Rev.* 111, 1 -14.

Zhong, R., Brugger, J., Tomkins, A.G., Chen, Y., Li, W., 2015. Fate of gold and base metals during metamorphic devolatilization of a pelite. *Geochim. Cosmochim Acta.* 171, 338–352.

Zuo, R., Carranza, E.J.M., 2011. Support vector machine: a tool for mapping mineral prospectivity. *Comput. Geosci.*, 37, 1967 – 1975.

## Chapter 4: Investigating the applications of Deep Neural Networks, Random Forest, and Transfer Learning for exploration targeting in the Abitibi greenstone belt, Canada.

### 4.1 Abstract

Mineral exploration has evolved thanks to the application of data integration and machine learning, however, machine learning typically requires that the region of interest have a reasonable number of known deposits for training in order to make subsequent predictions. This paper seeks to apply machine learning tools [deep neural networks (DNN), random forest (RF) and deep transfer learning (DTL)] for mineral exploration targeting. To perform DTL, a DNN model is trained on predictor and target variables from a data-sufficient region and the model weights and parameters are saved, and later used to make subsequent predictions on a new area without prior knowledge of target distributions. Exploration targeting models in this study were built using DNN and RF machine learning models to derive gold prospectivity of two regions within the Abitibi greenstone belt, specifically the Swayze and Matheson regions. The DNN and RF results obtained using the area under the receiver operator curve gave 90% and 89% prediction accuracies over the Swayze region, respectively. A transfer learning model pre-trained using data from the Swayze region with 80% area under receiver operator curve was used to make further predictions in the Matheson region. The pre-trained model obtained 68% success rate for predicting gold deposits in the Matheson region without prior knowledge of gold deposit distributions. Overall, harvesting the power of DNN and DTL yields good predictions that could help geoscientists to implement machine learning models over greenfield areas that have little

target variables to train on, provided the tools are trained on areas with similar geology and similar mineral system expressions in the predictor data.

Keywords: Deep neural networks, random forest, feature importance, transfer learning, mineral prospectivity mapping, source domain, and target domain

## 4.2 Introduction

Machine learning (a popular subfield of artificial intelligence) is defined as a method that gives computers the ability to learn without being explicitly programmed (Domingos, 2012; Raschka and Mirjalili, 2017; Chollet, 2018). The machine learning techniques have been applied in various fields to automate and improve the way human beings accomplish simple everyday tasks. In the geoscience, mining, and mineral exploration communities, machine learning tools have been applied with increasing interest in both academia and industry. The motivation for this has been that the rate of mineral deposit discovery is vastly decreasing due to shallow deposits being depleted and targets being sought deeper in the earth's crust; hence, geologists are looking at new ways of finding mineral deposits (Schodde, 2017; Desharnais et al., 2018). Mining companies, government surveys and academic institutions collect large amounts of data aimed at helping geoscientists to understand the mineral systems involved in the distribution and deposition of mineral deposits near the earth's surfaces. Several studies have been done using knowledge-driven and data-driven machine learning methods to generate mineral prospectivity maps (Agterberg and Cabilio, 1969; Bonham-Carter, 1994; Harris, 1999; Harris, 2002; Carranza, 2009; Porwal and Carranza, 2015; Carranza and Laborte, 2015). Other more recent studies have applied the mineral

systems approach as a conceptual exploration targeting method in conjunction with mineral prospectivity mapping to outline the expressions of ore-forming mineral systems at various scales (McCuaig et al., 2010; McCuaig and Hronsky, 2014; Kreuzer et al., 2019). This study uses data-driven machine learning tools such as artificial neural network (ANN) methods and random forest classifiers to make data classifications and predictions. The random forest decision tree classifiers are popular data-driven machine learning method used for exploration targeting due to their ability to generalise and make accurate prospectivity predictions (Rodriguez-Galiano et al., 2014; Rodriguez-Galiano et al., 2015; Carranza and Larborte, 2015). The ANN consist of input nodes, one or more hidden layer of neurons with an activation function used to generate weights in order to create classification and prediction outputs (McCulloch and Pitts, 1943; Sarle, 1994; Basheer and Hajmeer, 2000). Several types of ANN have been proposed and used in the AI community, each constructed to help improve data classification and predictions. The different types of ANN that exist today include multilayer perception, radial basis functions neural networks, and probabilistic neural networks among others (Basheer and Hajmeer, 2000; Looney, 2002; Nykänen, 2008; Tessema, 2017). Some more recent advancements in neural networks are deep neural networks (DNN), convolutional neural networks (CNN), and recurrent neural networks (RNN) which are neural network models with multiple hidden layers that are used to analyze complex features in data. The first few layers in a deep learning model usually learn general or simple features in data while the remaining layers tend to learn more complex features, making deep learning a powerful method in artificial intelligence and machine learning.

Traditional machine learning for mineral prospectivity mapping requires that there be adequate input data (predictor layers such as geophysics, lithology, structures, geophysics, and geochemistry) as well as known locations of mineral deposits to aid in making classifications and

predictions. The predictor layers and deposits traditionally lie within the same map area. In cases where adequate deposit location information is not available the concept of transfer learning can be applied to extract weights and features from a pre-trained model and using the learned information to make predictions on a new area (Pan and Yang, 2010; Weiss et al., 2016). A more detailed description of transfer learning can be found in Pan and Yang (2010). Deep transfer learning is suitable for cases when there is i) a *source domain* that contains adequate data (i.e., predictor and target variables) for training a machine learning classification model and ii) a *target domain* with similar input predictor variable data but limited known deposit locations. The source and target domains, however, must contain the same predictor layer information (i.e., the same input shape) to make the necessary predictions. Transfer learning should also be applied on two domains that are known to have similar expressions of mineralization in predictor layers or predictor variables. Therefore, transfer learning should be applied in regions that contain similar deposit types, geological controls and regions that have comparable data distributions (Weiss et al., 2016). There have been several applications of transfer learning to image classification and text sentiment classification (Pratt, 1993; Torrey and Shavlik, 2009; Weiss et al., 2016; Zhu et al., 2011; Pan and Yang, 2011) but this study seeks to introduce the application of transfer learning to mineral exploration, specifically gold exploration in the Abitibi greenstone belt. The objectives of this study are to: i) to generate mineral prospectivity maps for the Swayze region using the DNN and random forest machine learning methods, ii) to use the pre-trained models to make prospectivity predictions over the Matheson region, iii) to derive and compare feature importance's from both DNN and random forest models, and iv) to discuss the limitations of using DNN and transfer learning techniques on mineral exploration datasets.

### 4.3 Regional geology of the Abitibi greenstone belt

The study areas are found within the Abitibi Sub-province and form part of the mineral prolific southern Abitibi greenstone belt, in Ontario and Quebec, Canada (Fig. 4-1). The Abitibi greenstone belt is the largest Neoproterozoic greenstone belt in the world that hosts a variety of mineral deposits including orogenic gold deposits and volcanogenic massive sulfide deposits (Monecke et al., 2017). The Swayze region is found in the southwest of the Abitibi greenstone belt and the Matheson region is located at the central part of the Abitibi greenstone belt, east of the city of Timmins, Ontario (Fig. 4-1). The Abitibi greenstone belt consists of east-trending extrusive and intrusive units overlain by sedimentary rocks that have been substantially folded, highly deformed, and metamorphosed between sub-greenschist to amphibolite facies (Monecke et al., 2017). The Abitibi greenstone belt consists of seven volcano-stratigraphic assemblages with ages ranging from 2750 to 2695 Ma that can be traced and correlated using geochronological U-Pb age dating across the greenstone belt between Swayze and Matheson regions (Ayer et al., 2005; Thurston et al., 2008; Monecke et al., 2017). The Abitibi greenstone belt stratigraphy consists mainly of mafic and felsic volcanic units overlapping with significant laterally extensive clastic and chemical sedimentary units that are used as stratigraphic markers (Thurston et al., 2008). The tectonic history of the Abitibi greenstone belt is defined by complex late-stage strike-slip deformation which resulted in major faults and shear zones (Monecke et al., 2017). The ductile-brittle fault zones cut across the Abitibi greenstone belt in an E-W orientation. The fault zones include the Porcupine-Destor Fault zone, Larder – Cadillac fault zone, and the Pipestone Fault (shown on Fig. 1) and together with second and third order faults, they control and host major orogenic gold deposits (Monecke et al., 2017; Dubé et al., 2017). The Porcupine-Destor Fault zone cuts across the Matheson region and is interpreted to extend towards the southwestern Abitibi greenstone into

the Swayze where it is referred to as the Slate Rock high strain zone. Similarly, the Cadillac-Larder fault zone is interpreted to extend into the Swayze where it is known as the Ridout high strain zone (Milne, 1972, Heather, 2001; Breemen et al., 2006; Monecke et al., 2017; Dubé et al., 2017).

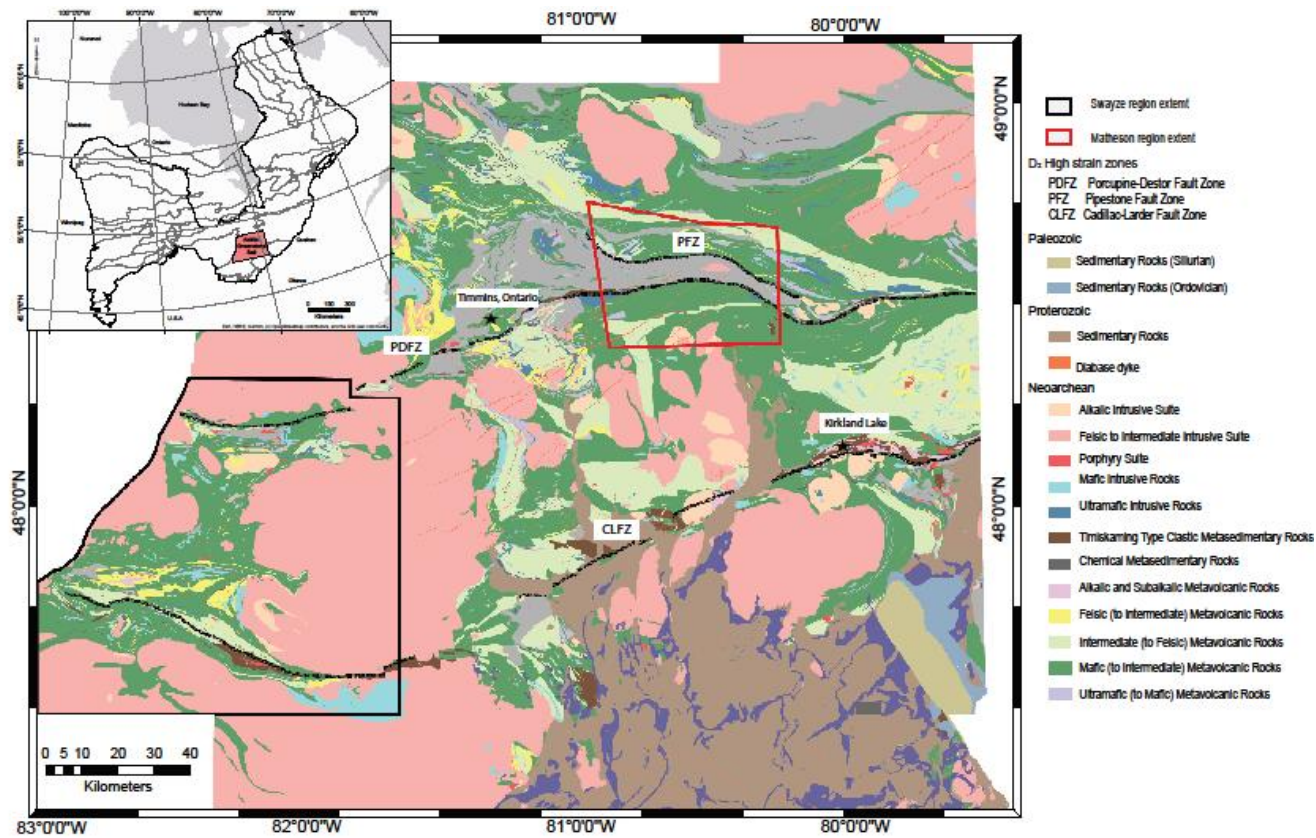


Fig. 4- 1 : Regional geological map of the Abitibi greenstone belt after Ayer et al (2002, 2005) showing the location of the Abitibi greenstone belt within the Superior Province, Canada. On the map, the locations of the Swayze greenstone belt and the Matheson greenstone belt are shown in a black and red outline, respectively. The E-W trending D<sub>2</sub> high strain zones are shown cutting across the Abitibi greenstone belt.

#### 4.2.1 Local geology of the Swayze greenstone belt

The Swayze region (shown in a black outline on Fig. 4 -1 and in more detail on Fig. 4 - 2) makes up the south western section of the mineral-prolific Abitibi greenstone belt, with field mapping and geochronological studies suggesting commonality in stratigraphy and deformational history (Huagaard et al., 2018; Breemen et al., 2006; Ayer et al., 2005; Heather, 2001). The geology, stratigraphy, and deformational history of the Swayze region has been field mapped by Heather (2001) as part of a PhD thesis, further mapping and U-Pb geochronological studies were done by Huagaard et al (2018), Ayer et al (2005) and Breemen et al., (2006). Similar to the rest of the Abitibi greenstone belt, the Swayze region consists of a range of intrusive and extrusive rock types, including felsic to ultramafic intrusions, metasedimentary rocks and clastic sedimentary rocks with ages ranging between 2740 and 2695 Ma (Breemen et al., 2006; Heather, 2001). The rocks in the Swayze region are highly deformed and have been metamorphosed at grades between subgreenschist to amphibolite facies (Ayer et al., 2005; Breemen et al., 2006). There are several gold-deposit types found in the Swayze region, namely; the recently discovered intrusion-related Côté Au-(Cu) deposit (Katz, 2016; Smith, 2016; Kontak et al., 2013a; Rodgers et al., 2013), possibly intrusion-related gold deposits (e.g., Jerome and Rundle deposits), iron-formation-hosted gold deposits (e.g., the 4K deposit), and greenstone-hosted gold deposits (e.g., Kenty deposit) (Katz et al., 2015; Hastie., 2017; Love and Roberts, 1991). The Swayze region also hosts occurrences of Cu-Pb-Zn, Ni-Cu-Fe and Ag, with Au being the principal commodity in most mineral occurrences (Heather, 2001). The Swayze region underwent multiple deformational events involving developments of multiple foliations, it consists of several high strain zones known to be associated with gold emplacement. The oldest deformation event, D<sub>1</sub> is associated with penetrative foliation, shear zones and intrafolial isoclinal folds (Breemen et al., 2006). The most important

event is the D<sub>2</sub> deformational event because it is responsible for formation of D<sub>2</sub> high strain zones that are synchronous with gold mineralization in the Swayze region and the rest of the Abitibi greenstone belt (including the Matheson region). The D<sub>2</sub> high strain zones such as the Slate Rock high strain zone found in the northern Swayze region and the Ridout high strain zone found in the southern Swayze region are regarded as the first-order controls of metal-rich fluids (Milne, 1972, Heather, 2001; Breemen et al., 2006; Monecke et al., 2017; Dubé et al., 2017). Similar to the rest of the Abitibi greenstone belt, orogenic gold deposits in the Swayze region are hosted in second- and third-order structures, quartz-carbonate veins, and between lithologies with high competency contrast. Details on the stratigraphy, structural history, and geology of the Swayze region can be found in Heather (2001) and Breemen et al., (2006). Machine learning techniques have been applied previously to the Swayze region by Harris (2002) who used geochemical and lithological predictor layers to generate mineral prospectivity maps. Maepa et al (2020) found that a single hidden-layer radial basis function neural networks and the support vector machines techniques were helpful in defining possible exploration targets, with weights of evidence being especially useful at determining predictor maps that have the best spatial correlations with gold deposits. Other spatial analysis of the deposit locations has been undertaken by Maepa and Smith (2020) to determine the controls of mineral deposits in the Swayze region using Fry, fractal analysis, and distance-based point-pattern analysis. The study found that mineral deposits in the Swayze region are bifractal at 8 km, and mineralization controls vary with the scale of observation, and the prominent deposit alignments are seen along ESE-WNW, ENE-WSW, NE-SW directions).

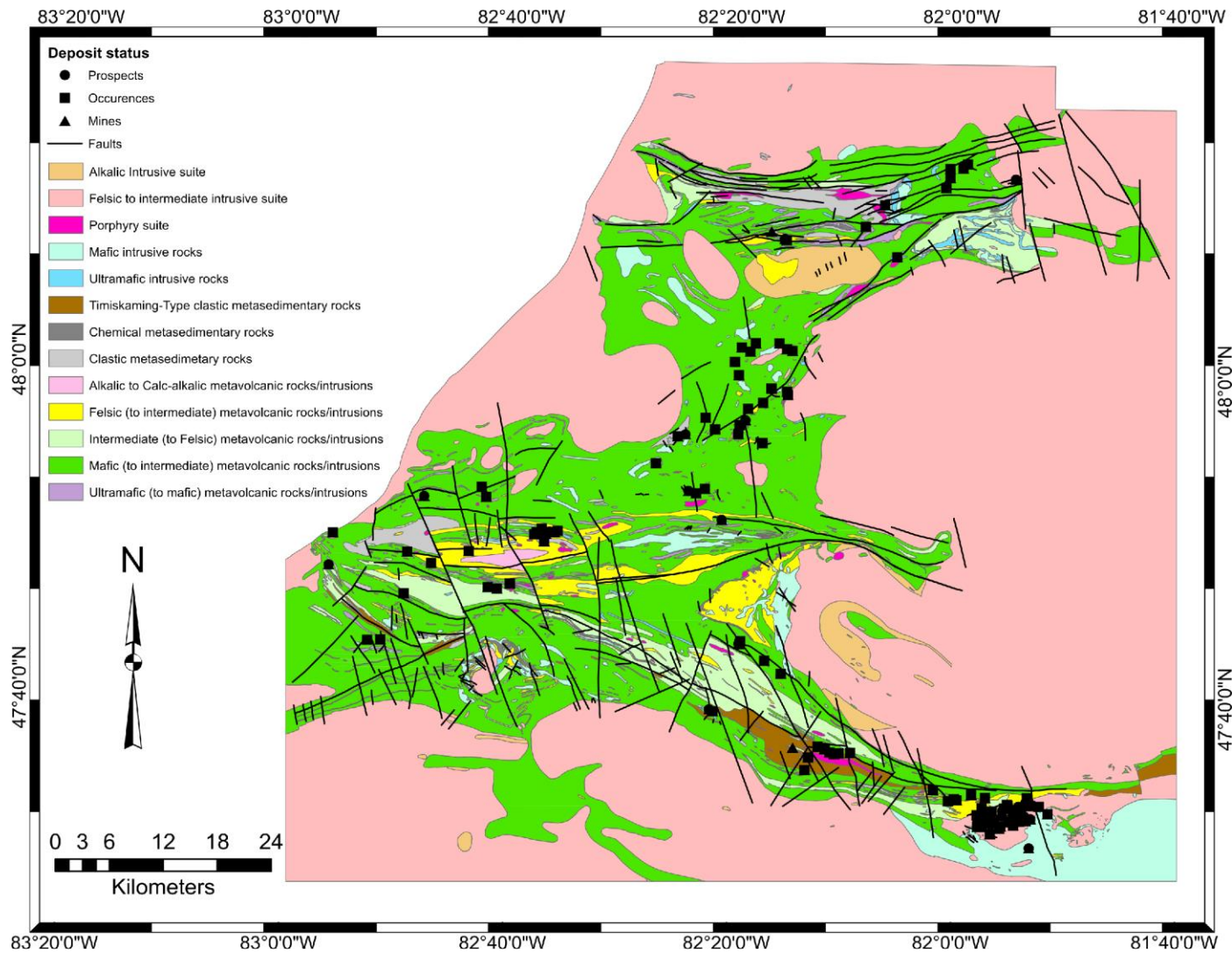


Fig. 4- 2: Geological map of the Swayze greenstone belt showing felsic to ultramafic intrusions and clastic metasedimentary rocks after Ayer and Trowell, (2002). The distributions of mineral deposits and mapped faults are overlain as points and polylines.

#### 4.2.2 Local geology of the Matheson greenstone belt

The Matheson region (shown as a red outline on Fig. 4 -1 and in more detail on Fig. 4 - 3) is in northeast Ontario, east of the city of Timmins and centered in the Matheson township (McClenaghan, 1990). The Matheson region, also located within the mineral prolific Abitibi greenstone belt, shares geological similarities with the Kirkland Lake and Larder Lake gold camps to the south of Matheson township (McClenaghan, 1991; McClenaghan et al., 1992). The bedrock geology of the Matheson region is extensively covered by glaciolacustrine clays and sands deposited in glacial lakes as well as thick and complex sequences of quaternary sediments that were investigated using overburden drilling (Vagner, 1983; McClenaghan et al., 1992; Ayer et al, 1999). Geochemical work was done by McClenaghan et al., (1992) on the youngest till unit in the region referred to as the 'Matheson till'. The composition of the till units shows that there are different sequences of till that appear to be derived from distinct mafic and felsic rock sources (McClenaghan et al., 1992). The felsic till unit is found at the top of the stratigraphy and is interpreted to be sourced from granitic and gneissic bedrocks north of the Matheson region, while mafic till units found lower in the stratigraphy are deduced to be sourced from local mafic intrusive and volcanic bedrock (McClenaghan et al., 1992). The Archean bedrock geology of the Matheson region is interpreted primarily from geophysical maps and constrained by field mapping and bedrock drilling. The Matheson region consists of mafic to ultramafic rocks as well as several tonalite-trondjemite-granodiorite intrusions that are covered by glacial sediments (McClenaghan et al., 1992).

The Porcupine-Destor fault zone and the Pipestone fault zone (McClenaghan et al., 1992) cut across the Matheson region in an E-W manner and are known to be associated with gold mineralization (Vagner, 1983; Whittaker, 1986; McClenaghan et al., 1992). The mineral

occurrences in the Matheson region include epigenetic gold and silver as well as rare occurrences of volcanogenic massive sulfide deposits (Whittaker, 1986; McClenaghan et al., 1992). Gold is the dominant commodity element in the majority of mineral occurrence in the Matheson region (Bath, 1990). Gold deposits are found along the Porcupine-Destor fault zone and associated with quartz-carbonate veins and as inclusions in pyrite (McClenaghan et al., 1992). Overburden sampling revealed anomalous concentrations of gold with rutile in older till sampling suggesting similar bedrock sources such as the rest of the Abitibi greenstone belt (McClenaghan et al., 1992). There are several gold producing mines that exist in the area as well as numerous gold occurrences, prospects, and showings. The mines in the area include (McClenaghan, 1990): 1) the Holt-McDermott (Au-Ag) mine, the Hislop West Au mine, the Croesus (Au) mine and the Ross (Au, Ag, Cu) mine. According to the mineral deposit inventory published by the Ontario Geological Survey (OGS), most of the gold mines, deposits and occurrences in the Matheson region are associated with felsic to intermediate intrusions, mafic to ultramafic intrusions and alkaline intrusive rocks.

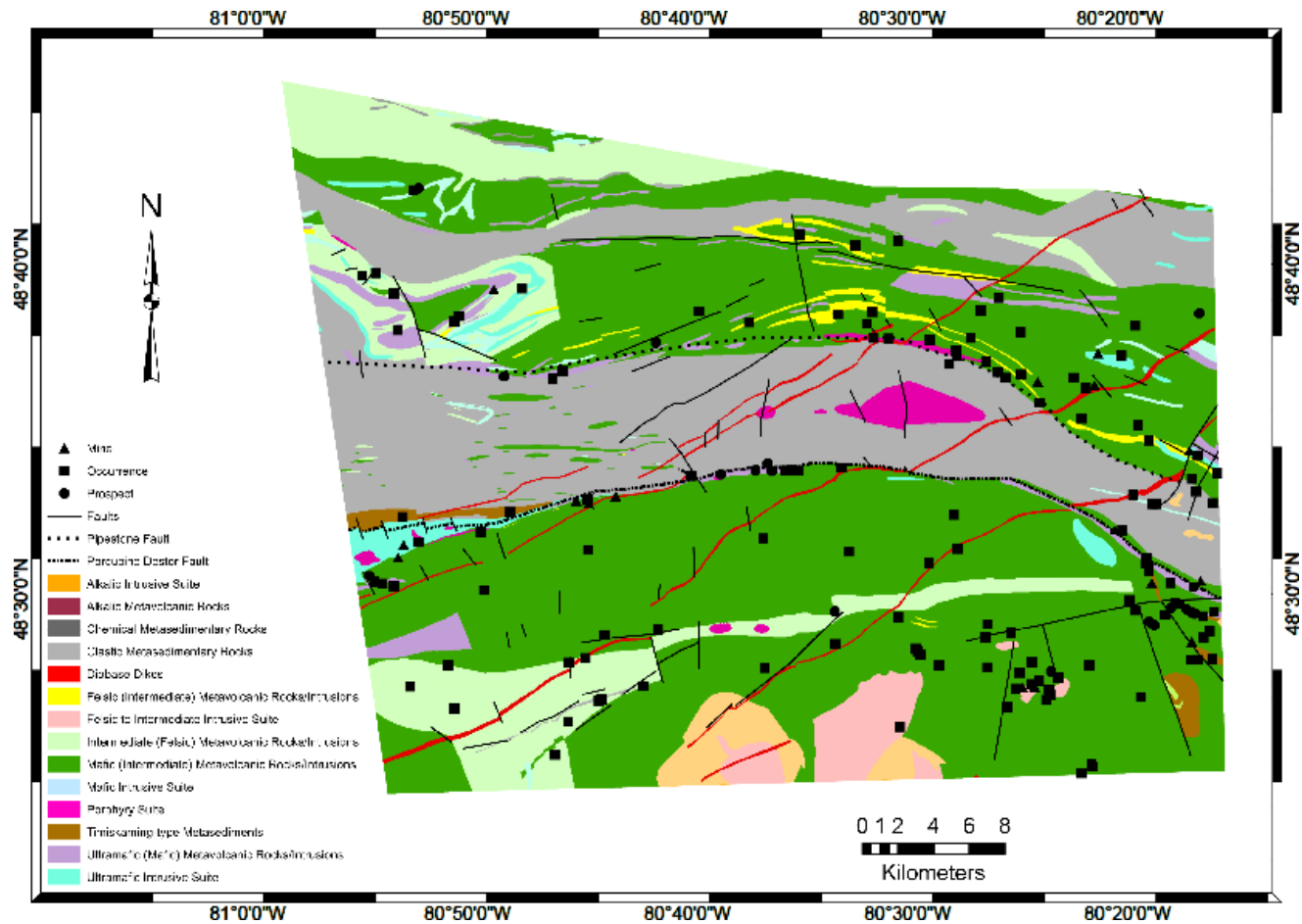


Fig. 4- 3 : Geological map of the Matheson greenstone belt showing bedrock lithologies with felsic to ultramafic intrusions from a compilation of the Abitibi greenstone geology by Ayer et al. (1999). The map is overlain by mapped faults and mineral deposit distributions.

### 4.3 Available data

The study utilized historical geoscience data collected over both the Swayze and the Matheson region obtained from multiple organizations as outlined in Table 4-1, Fig. 4-4, Fig. 4-6, and Fig. 4-7.

#### 4.3.1 Available data in the Swayze greenstone belt

The geology and fault data from the Swayze region were field mapped and compiled at a scale of 1:50 000 by Heather (2001); Ayer and Trowell (2002); and Breemen et al. (2006). The geological map (Fig. 4-2) contains ultramafic to felsic intrusive rocks as well as clastic metasedimentary rocks mapped in the Swayze region.

A litho-geochemistry database obtained from the Geological Survey of Canada (GSC) was used to map geochemical signatures related to mineralization processes in the Swayze region. Litho-geochemical data from the Swayze region were centered log-ratio normalized using [CoDaPack](#). A principal component analysis (PCA) transformation of log-transformed geochemical data (Pearson, 1901; Grunsky, 1986; Grunsky, 2010) discussed in Maepa et al (2020) was carried out using [IoGAS](#) geochemical processing software to highlight elemental anomalies and the variances in the major oxide data.

The first three principal components (Table 4-3 and Fig. 4-5) have the highest elemental variances and were thus used to highlight processes associated with hydrothermal alteration and mineralization (Grunsky, 2010). Since the data is sparsely distributed and will thus introduce bias in kriging interpolation, distances from anomalous principal component maps were derived (Fig. 4-4) and used for prospectivity analysis. A normal probability plot was used to extract anomalous principal component from the background data (Grunsky, 2010). The distribution of anomalous principal component values is overlain on top the Swayze region geological map (Fig. 4-4A), the

derived proximity to PC1, PC2 and PC3 anomalies are shown on Fig. 4-4B, Fig. 4-4C and Fig. 4-4D, respectively.

The aeromagnetic data preprocessing steps by the OGS included International Geometric Reference Field (IGRF) removal, levelling, micro-levelling, and gridding (Fig. 4-6B). Using a total magnetic intensity map that has been reduced to the pole and the calculated 1<sup>st</sup>, 2<sup>nd</sup> and 3<sup>rd</sup> order vertical derivative maps and analytical signal maps, the faults in the Swayze region were further remapped and interpreted in geographical information systems (GIS) for this study. The derivatives were integrated with and overlain on a geological map and field-mapped faults in the GIS. Using various color gradients and hillside data enhancements on these maps, linear structural features, and offsets / displacements in geological features were identified and digitized. Faults were most evident as discontinuities and displacements seen on dikes, magnetic rock units, and intrusions. Furthermore, regions of higher and lower magnetic intensities and geological offsets were scrutinized by zooming in and out of the GIS view window to ensure that important geological features related to deformation are captured (Isles and Rankin, 2013). The interpreted faults were confirmed and extensions identified in such a way that they were consistent with the overlapping geological map and faults previously mapped in the field by Heather (2001), and published by Ayer and Trowell (2002). The interpreted faults together with faults mapped in the field were combined and evaluated for further use in this study (Fig. 4-6A). The aeromagnetic data (Fig. 4-6B) was also used to derive magnetic worms from the Swayze and Matheson regions, which helped to define upper crustal (~1 km) fluid pathways and shear zones (Roshanravan et al., 2020; Archibald et al., 1999). The first vertical derivative of a 2 km upward continued total magnetic intensity RTP data (Fig. 4-6C) was used to calculate the magnetic worms (Fig. 4-6D) as discussed in detail in Maepa et al., (2020).

Other geophysical datasets used in this study include the electromagnetic (EM) apparent-decay-constant map covering the entire Swayze region. The electromagnetic data preprocessing by the OGS included EM data filtering, data corrections, and apparent-decay-constant calculations. The decay constant raster grid is used to map and outline conductive features in the near surface within the Swayze region. A distance to EM conductivity map (Fig. 4-6E) derived from the electromagnetic decay constant data (Fig. 4-6F) were also added as predictor maps. Other predictor maps used to derive mineral prospectivity maps were the proximity to intrusive rocks (Fig. 4-6G) and the apparent magnetic susceptibility map (Fig. 4-6H). Finally, a mineral deposit inventory dataset compiled by Fumerton and Houle (1995) as part of the OGS data collection projects was used to review mineral deposits and prospects covering the Swayze region.

#### 4.3.2 Available data in the Matheson greenstone belt

A geological compilation map of the Lake Abitibi area by Ayer et al (1999) covering the Matheson region compiled at a scale of 1:100 000 was used to represent the lithologies in the region. The lithological map (Fig. 4-3) was compiled using geophysical data interpretations constrained with field mapping and overburden drilling as part of the Discover Abitibi initiative (Johnstone, 1991; McClenaghan, 1992; Berger, 2002; Ayer et al., 2005).

The reduced to pole total magnetic intensity map (Fig. 4-7A) was preprocessed by the OGS, including IGRF removal, levelling, micro-levelling, and reduction to pole. Similar to the Swayze region, the aeromagnetic data in the Matheson region was upward continued to 2 km and a first vertical derivate map was calculated and used to determine magnetic worms (Fig. 4-7B). The distances from magnetic worms (Fig. 4-7D) used to map magnetic gradients in the Matheson region was used as a predictor map.

Other data included fault maps showing minor and major faults cutting across the Matheson region in an E-W direction. The fault data was primarily field mapped by the OGS and further interpreted using geophysics (Berger, 2002; Ayer et al., 2005). The authors further reinterpreted faults within the region using the reduced to pole total magnetic intensity map, and the calculated 1st, 2nd, and 3<sup>rd</sup> vertical derivative maps. A distance from fault map (Fig. 4-7C), the apparent magnetic susceptibilities (Fig. 4-7E) and distances from lithological contacts (Fig. 4-7F) were all included as predictor maps for deep transfer learning over the Matheson region.

Both the Swayze and Matheson regions contain mineral deposit inventory data showing locations of current and past-producing mines, gold deposit prospects, showings, and occurrences. The terms ‘occurrences’ and ‘showings’ are used to show regions where traces of gold mineralization have been observed in outcrop or core. A ‘prospect’ represents a location where ore has been mined on a trial basis, while a ‘deposit’ represents regions where reserve calculations have been made (Fumerton and Houle, 1995). For this study, the ‘deposits’, ‘prospects’, and ‘occurrences’ were all during training but were given different weightings between 0 and 1.

Table 4- 1: A summary of the data used in the study from the Swayze greenstone belt and the Matheson greenstone belt.

Dataset	Description	Format	Source
Swayze greenstone belt			
Geology	Bedrock geology mapped at scale of 1:100 000	GIS vector (polygons)	Ontario Geological Survey
Mineral deposits	Locations of mineral deposits, drilled prospects, and assayed Au showings/occurrences	GIS vector (points)	Ontario Geological Survey
Structures	Mapped in the field by Heather (2001). Some data was interpreted using aeromagnetic data by the OGS and the authors	GIS vectors (polylines)	Ontario Geological Survey
Litho geochemistry	Major oxide and trace element geochemical data	GIS vectors (points)	Geological Survey of Canada
Magnetic	Total magnetic intensity map reduced to the pole.	raster grids	Ontario Geological Survey
Electromagnetic	A decay constant map showing conductance's derived from EM	raster grids	Ontario Geological Survey
Gamma-ray spectrometry	Canada wide Gamma-ray spectrometry grid data	raster grids	
Matheson greenstone belt			
Geology	Bedrock geology mapped and compiled at scale of 1:100 000 and interpreted using geophysics	GIS vector (polygons)	Ontario Geological Survey
Mineral deposits	Mineral deposits (i.e., mines) and drilled prospects.	GIS vector (points)	Ontario Geological Survey
Structures	Faults and structures compiled by the Ontario Geological Survey. Faults were also interpreted using aeromagnetic data (1st, 2 <sup>nd</sup> , and 3rd order derivative maps) by the OGS and the authors.	GIS vectors (polylines)	Ontario Geological Survey
Magnetic	Total magnetic intensity map reduced to the pole.	raster grids	Ontario Geological Survey
Gamma-ray spectrometry	Canada wide Gamma-ray spectrometry grid data	raster grids	Geological Survey of Canada

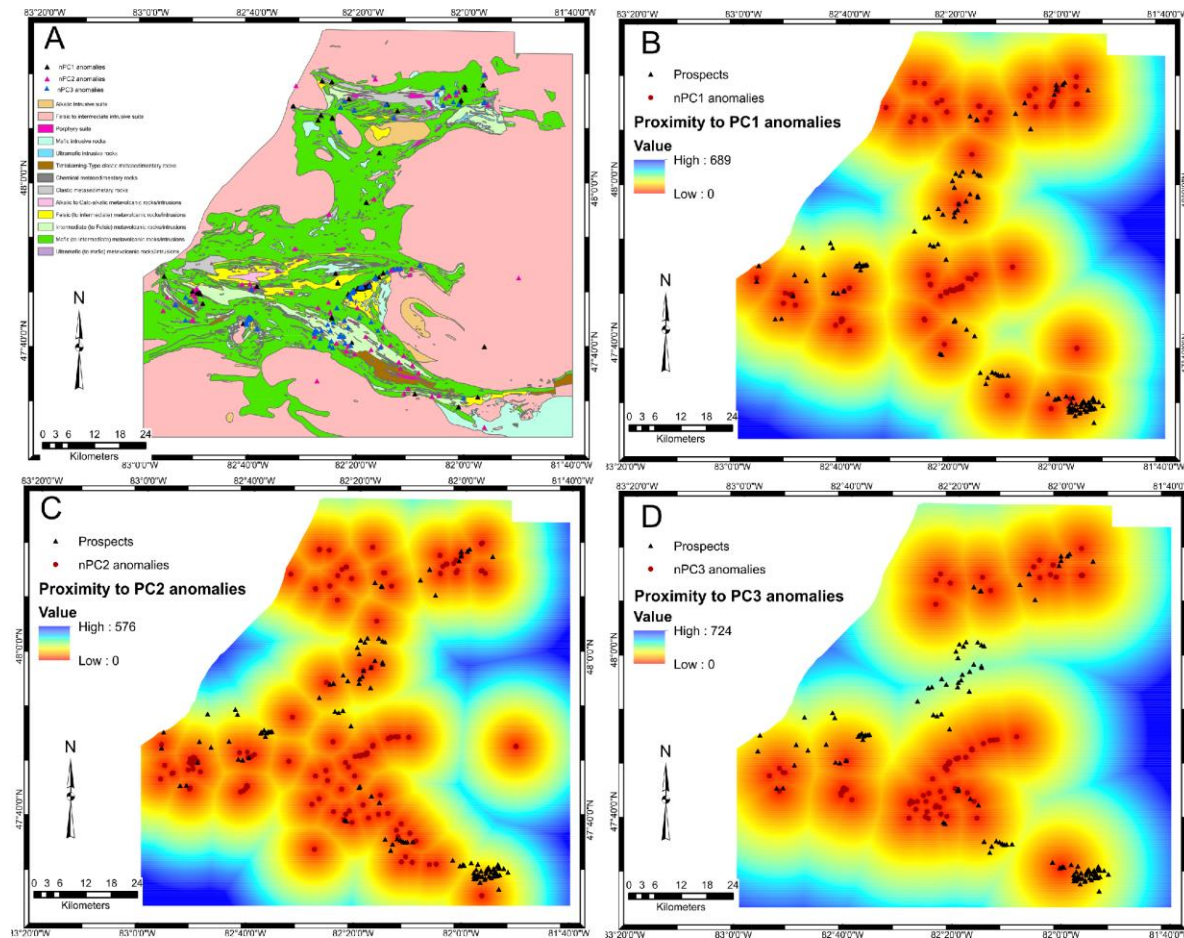
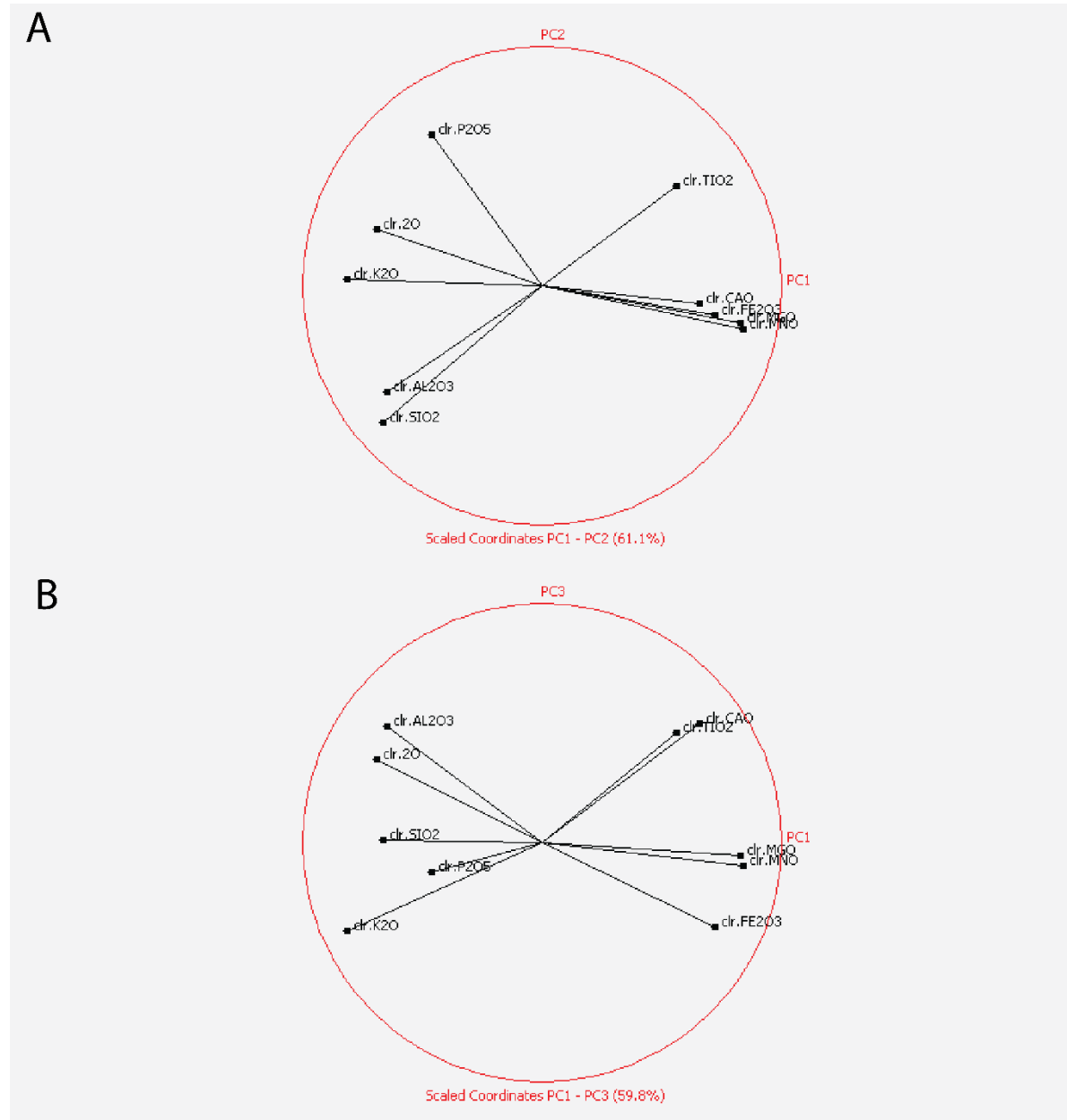


Fig. 4- 4 : Swayze region predictor maps derived from lithogeochemistry overlain by gold prospect locations. The maps show the distributions of principal component anomaly points overlain on the Swayze geological map (A), a proximity from PC1 anomalies map (B), a proximity from PC2 anomalies map(C), and a proximity from PC3 anomalies map (D).

Fig. 4- 5: The bi-plots of the first and second principal component (A), first and third principal component (B) and a scree plot (C) for the logratio centered Swayze greenstone belt major oxide data.



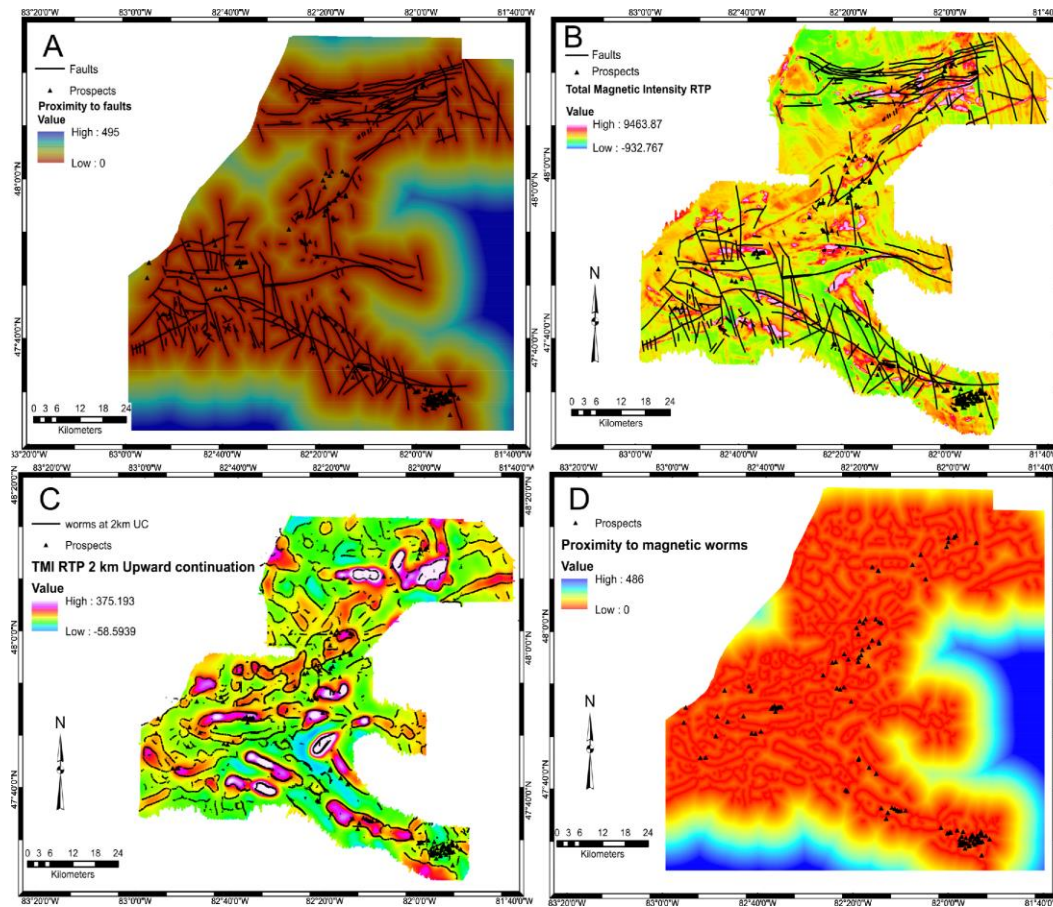


Fig. 4- 6 : Swayze region predictor maps of distances from faults (A), a reduced-to-pole total magnetic intensity map (B), a reduced to pole total magnetic intensity map that has been upward continued to 2 km overlain by the derived magnetic worms (C), proximity to magnetic worms (D), distances from high electromagnetic conductivity map (E), electromagnetic conductivity map (F), proximity to intrusive suites map (G), and the apparent magnetic susceptibility map (H).

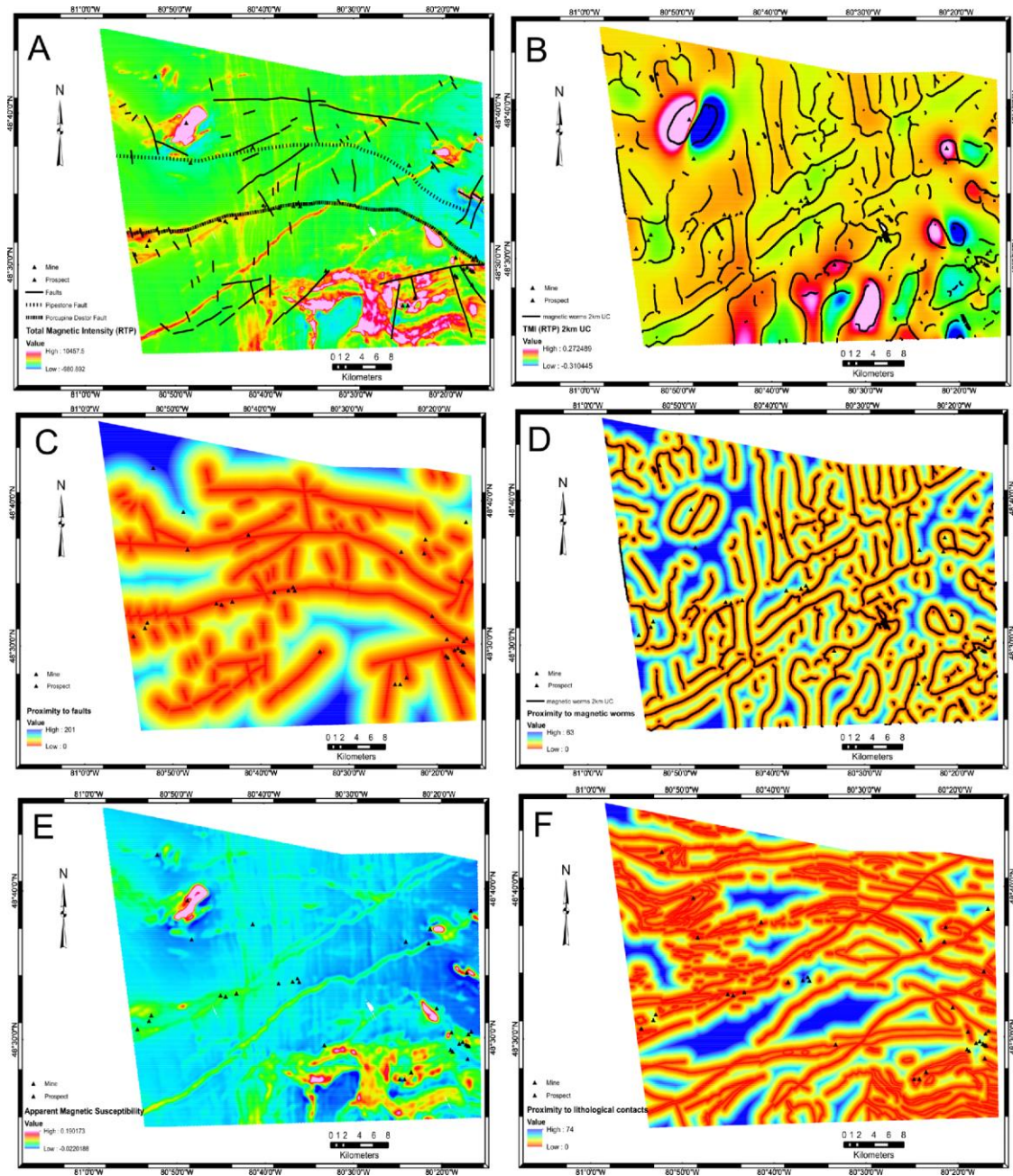


Fig. 4- 7 : Matheson region predictor layers showing the reduced-to-pole total magnetic intensity map (A), a 2 km upward continued reduced to pole total magnetic intensity map overlain by the derived magnetic worms (B), distances from faults (C), distances from magnetic worms (D), the apparent magnetic susceptibility map (E), and proximity to lithological contacts (F)

## 4.4 Methodology

A summary of the exploration targeting workflow followed in this study is outlined on Table 4-2 and shows steps from data preprocessing to generation of DNN models as well as deriving transfer learning predictions. The exploration workflow is explained in more detail below:

### 4.4.1 Fry analysis

Fry analysis (Fry, 1979) is a spatial autocorrelation technique that has been widely used to determine the distributions of point patterns representing mineral prospects and their associated structural controls (Vearncombe and Vearncombe, 1999; Kreuzer et al., 2007; Carranza, 2009; Maepa and Smith, 2020). For  $n$  number of points in a dataset, there are  $n^2-n$  translations, and the Fry translations can be used to determine the overall spatial distributions of the point datasets. Fry analysis can be done manually using a sheet of paper and tracing paper and marking each point as an origin for translation or digitally using a specialized point distribution software (Carranza, 2009).

This study used SpaDIS software (developed by Julian Vearncombe, discussed in Vearncombe and Vearncombe, 1999) to map Fry translations and to generate rose diagrams showing the primary spatial distributions of mineral prospects at regional scales. After determining the overall spatial alignments of mineral prospects, the fault data that have the same orientation as the Fry rose diagram distributions of gold were selected to represent fluid pathways for hydrothermal mineral systems (Fig. 4-8).

To determine the overall regional-scale spatial orientations of gold deposit points in the Swayze and Matheson regions, Fig. 4-8A and Fig. 4-8B are used to show Fry translations and

rose diagrams for the Swayze region, respectively. On Fig. 4-8C and Fig. 4-8D the Fry analysis translations and corresponding rose diagrams for gold deposit points in the Matheson region is shown. The spatial controls of gold prospects in the Swayze region are discussed in more detail by Maepa and Smith (2020). Faults that had a similar orientation as the gold deposit distributions were used to map the controls of fluids in a hydrothermal mineral system.

#### 4.4.2 Selection of training data for machine learning (deposit versus non-deposit point)

Deep learning models require that there be deposit [1] and non-deposit [0] data to use during training. The deposit locations are known locations where mineral prospects and/or mines exist, historically determined from field mapping and surface drilling. The non-deposit data represent regions where prospects do not exist. Normally, a non-deposit location data is obtained by ground-truthing in the field either by drilling or field mapping for certainty that the location does not host a deposit. However, due to the limitation of this study, generation of non-deposit points involved using a random set of points that had to be far from known gold prospects and outside permissive lithologies (Roshanravan et al., 2020; Maepa et al., 2020).

Table 4- 2: The mineral exploration workflow that was followed in the study from data preprocessing to building deep learning models.

Deep Transfer Learning Workflow	
Data Preprocessing	<p>Lithochemical data: Normalize to lithology (Harris, 2000); log-ratio normalization, dimensionality reduction, and kriging (Maepa and Smith, 2020).</p> <p>Faults: Field mapped faults, Qualitative and quantitative fault interpretations using aeromagnetic, Fry Analysis</p> <p>Geophysics: Gridding aeromagnetic reduction to pole and decay constant data, apparent magnetic susceptibility calculations</p> <p>Geological: Field mapped lithologies</p> <p>Mineral deposit inventory: Define deposit data using fuzzy classification between 0[non deposit], showings/occurrences [0.8] and 1[deposit]</p>
GIS Integration	<p>Georeferenced and integrate geoscience data</p> <p>convert shapefile data to raster's (i.e., create predictor maps)</p> <p>Generate a unique conditions raster mapping the combinations of the predictor layers using ArcGIS '<a href="#">Combine</a>' tool</p>
Exporting to python environment	<p>Export unique conditions raster map using the 'Neural Networks Input file' tool in ArcMap to create normalized training and classification files for ML</p> <p>Convert training and classification data to .csv file format</p>
ML Pre-processing	<p>Load, standardize and transform data predictor information (train model on training file)</p> <p>One hot encoding of target data</p> <p>Define number of stratified K-Fold splits, and data balancing to ensure that each fold contains a good representation of the training data</p> <p>Balance the data to ensure each contains a good representation of each input target variable [0, 0.8, 1]</p>
Deep learning procedure	<p>Build Deep learning model, train for multiple epochs, evaluate model accuracies and loss values on training and validation datasets for each fold</p>
Save model weights and parameters and make predictions	

Import new unseen data from new domain (the target domain data must have the same predictor datasets (i.e., same shape) as the source domain data used for training the model.

#### Transfer Learning

Preprocess the data using steps outlined above (standardization, normalization, one hot encoding)

Use pre-trained model to make predictions on target domain data

Cross-validate model and evaluate accuracy of model predictions if unseen target labels exist for that region

---

Export predictions from python environment back into GIS environment

Use the Neural Network Output file tool in GIS to combine model predictions with the unique condition's raster mapping the combinations of the evidence

Visualize model prediction spatially in GIS as a raster map.

---

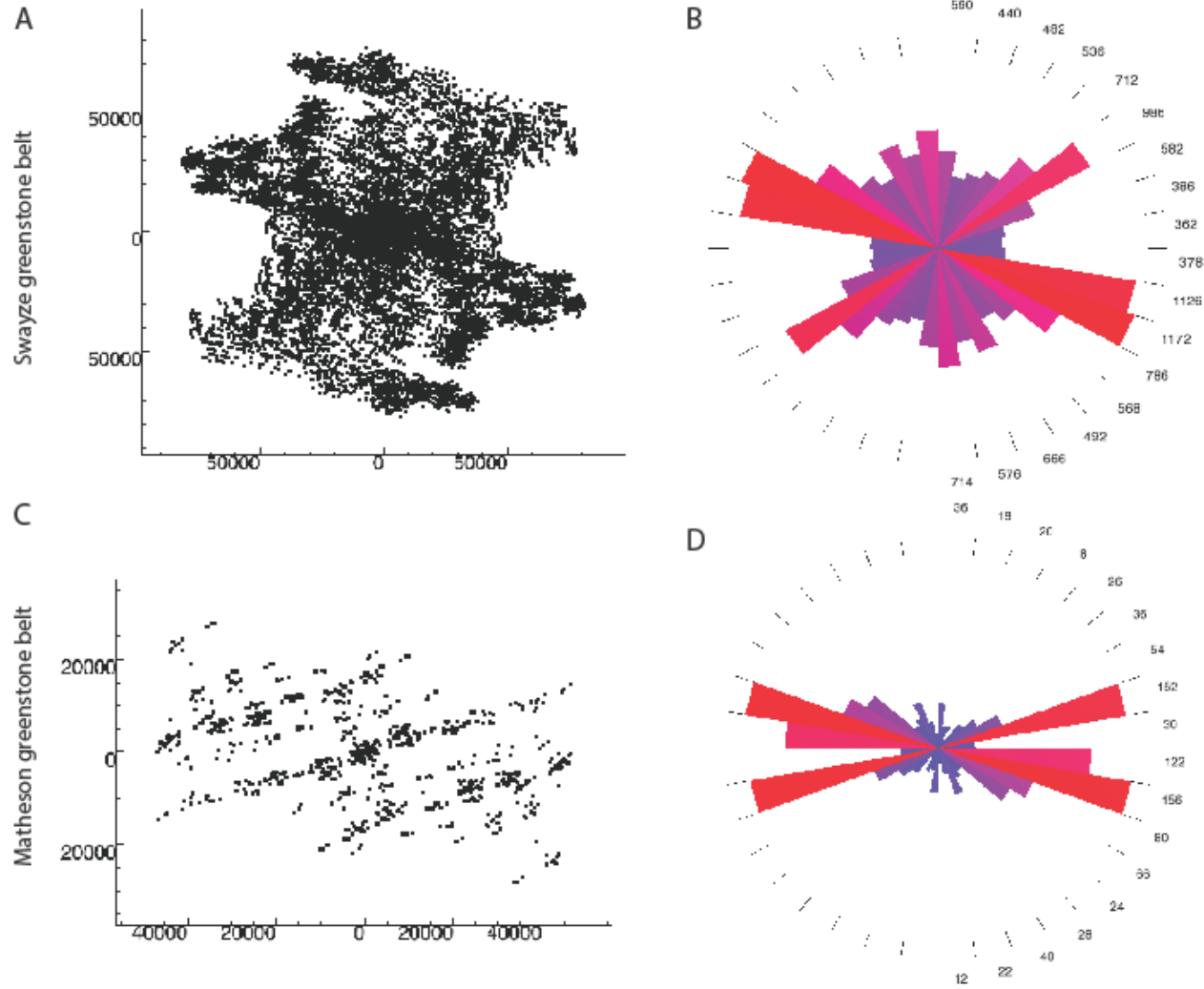


Fig. 4- 8 : Regional scale Fry analysis of gold deposit point distributions indicated using Fry translations and corresponding rose diagrams for the Swayze greenstone belt (A and B) and the Matheson greenstone belt (C and D).

#### 4.4.3 Preprocessing steps in GIS

The geoscience data used was integrated, georeferenced, and prepared in a GIS, specifically [ArcGIS](#) Desktop. All predictor data (Fig. 4-4, Fig. 4-6, and Fig. 4-7) including lithological, geophysical (aeromagnetic data and electromagnetic decay constant data), faults, geochemistry were converted into integer raster datasets of equal pixel sizes and map dimensions. The predictor datasets delineating mineralization processes were combined using the ArcGIS combine tool into a single unique-condition raster map for both areas. The [neural network input](#) tool in ArcGIS (originally created for GeoXplore software) was used to generate and export a training and classification files that contain a normalized representation of predictor layers and deposit targets. The ‘training data file’ represents a subset of the predictor data information that spatially correlate with the gold deposit training and non-training data, this is used for training machine learning classifiers. The ‘classification file’ represents a subset of the predictor data where spatial correlations with deposit locations is unknown. Selection of the training file is defined by intersection of training data with the unique condition’s raster map (Swatzky et al., 2010). In the training file, the deposit data locations are shown as a fuzzy belief classes (i.e., between 0 to 1) showing that an input predictor feature either has complete membership [1] or no membership [0] with deposit locations. The created classification file represents remaining predictor layer data in the study area with unknown target values (i.e., there is no knowledge of whether a deposit exists in this site or not). Both the training and classification files are converted to a (.csv) file formats, and the training file is used to train and validate the machine learning algorithm using feature and target variables in the data. Once a suitable accuracy is obtained from the training file, the model is used to make subsequent predictions with the classification file.

#### 4.4.4 Data preprocessing steps in python

The tools in Google [Tensorflow](#) and the [keras](#) functional application programme interface (API) and [Python](#) programming language were used to run the DNN on geoscience datasets from the Swayze and the Matheson regions. Keras is a high-level API written in python and capable of running Tensorflow DNN models (Chollet, 2018). Upon loading data into a deep learning environment in python, using the [scikit-learn](#) data preprocessing library, predictor information is standardized and rescaled to comparable data ranges. The data standardization method used is called Z-normalization where sparse datasets are put in the same ranges and data are scaled down from large magnitudes to much lower values (Brownlee, 2016; Scikit-learn, 2019). The Z-normalization transformation from scikit-learn used is defined as:

$$\text{Z-normalization} = \frac{\text{Value} - \mu}{\sigma} \quad (1)$$

Where  $\mu$  and  $\sigma$  are the mean and the standard deviation of the feature, respectively (Brownlee, 2016; Scikit-learn, 2019).

The preprocessing procedure for the target variables includes ‘one-hot encoding’ and/or ‘label encoding’ (Raschka and Mirjalili, 2017). For example, for one-hot-encoding, the target variables are converted to a binary column matrix with two categories, so that for example a deposit is represented as [0, 1] and a non deposit as [1, 0]. The target data in this study are locations of mineral deposits, prospects and non-deposits represented at a scale between 0 and 1, whereby 1 means deposit/mines, 0.8 represented gold prospects and 0 represented non-deposit.

#### 4.4.5 Deep neural networks

The idea behind ANN came from the perceptron learning rule which was aimed at mimicking the biology of a living neurons, where a neuron in the brain is expected to either fire or not fire (Rosenblatt, 1958). The perceptron learning rule consists of a single neuron with an input vector  $\mathbf{x}$  ( $x_1, x_2, x_3, \dots, x_n$ ) with corresponding weights  $\mathbf{w}$  ( $w_1, w_2, w_3, \dots, w_n$ ) that are multiplied and summed,  $z = w_1x_1 + w_2x_2 + w_3x_3 \dots + w_nx_n$  in the node (Rosenblatt, 1958). The summed values  $z$  are transferred to the next layer containing the activation function which determines if the neuron should be activated or not. For the weights in the input evidence to generate an output, the value of the weighted sum  $z$  must be either greater or less than a certain threshold. If the weighted sum is less than the threshold,  $z < threshold$ , the output will be 0, and if the weighted sum,  $z > threshold$ , then the output prediction will be 1. Artificial neural networks can also introduce a bias,  $b$ , to adjust the weights and help to reduce the output prediction error, whereby the output with regards to the bias can be defined as (Goodfellow et al., 2016):

$$\text{Output} = \begin{cases} 0 & \text{if } z + b \leq 0 \\ 1 & \text{if } z + b > 0 \end{cases} \quad (3)$$

There are different types of activation functions (linear, sigmoidal, binary step, non-linear etc.) and they work to help adjust the weights and help to normalize the output values of each neuron to specific ranges such as between 0 and 1 or -1 to 1 (Nair and Hinton, 2010; Goodfellow et al., 2016; Nwankpa et al., 2018).

A typical neural network model consists of multiple input neurons and an output layer. The middle layer called the hidden layer consists of the activation function, where during training with input  $\mathbf{x}$  the weights  $\mathbf{w}$  are adjusted iteratively for the chosen activation function to derive the desired output prediction (McCulloch and Pitts, 1943; Basheer and Hajmeer, 2000). Simple

neural networks have just one hidden layer. A DNN (Appendix E) represent a powerful neural network comprising of multiple hidden layers that are capable of analyzing a large number of input datasets for classifications and making predictions on complex features (Domingos., 2012; Chollet, 2018; Raschka and Mirjalili (2017). In this study, the DNN input layers represent the predictor layers or predictor variables (such as geophysical signatures, certain ore bearing lithologies and geochemical alterations that may signify the existence of a mineral deposit) and the output layer contains the model predictions. A DNN also contains hidden layers of nodes with weights appropriately adjusted to account for the structural similarities and correlations between the input data and the known (training) output (Goodfellow et al., 2016). Lines called neurons connect data from the inputs to the hidden layers, each line represents a weight that is multiplied with an activation function (Chollet, 2018). Activation functions capture non-linearities in a model and are used to compute the weighted sums of input datasets to determine an output prediction.

4.4.5.1 Rectilinear activation function (ReLU) Activation functions compute the sum of inputs and biases to manipulate the data in order to derive an output classification (Nwankpa et al., 2018). The activation function used in this study is the rectified linear unit (ReLU) activation function. ReLU is used in the hidden layers of deep neural networks while a softmax activation function (described below) is used in the output layer to make classifications. ReLU is defined by (Nair and Hinton, 2010):

$$f_r(x) = \max(0, x) = \begin{cases} x, & \text{if } x \geq 0 \\ 0, & \text{if } x < 0 \end{cases}, \quad (4)$$

where in this equation  $x$  is the weighted sum of inputs and biases input to the hidden layer node. The ReLU is a non-linear activation function that performs a threshold operation on each input

feature element which forces all values in the input that are less than zero to zero (Nwankpa et al., 2018), making it a more robust activation function because it maintains the properties of linear model units. Although the ReLU activation function performs faster and better, a major limitation compared to other activation functions is that it easily overfits to the training data, thus certain regularization techniques such as dropout (Srivastava et al., 2014) and batch normalization (Ioffe and Szegedy, 2015) are introduced to reduce model overfitting (Srivastava, 2014).

#### 4.4.5.2 Softmax activation function

The softmax activation function is used at the output layer of a deep neural networks to make output classification of features and it is used to make output probabilities (Nwankpa et al., 2018). Softmax is used in multivariate classification of features with classes ranging in values between 0 and 1:

$$f_s(x_i) = \frac{\exp(x_i)}{\sum_j \exp(x_j)}, \quad (5)$$

where in this equation  $x_i$  is the weighted sum of inputs and biases input to the  $i$ th output node and the sum over the  $j$  in the denominator is the sum over the weighted sums of inputs and biases for all the output nodes. Further details on the softmax activation function can be found in Goodfellow et al. (2016) and Nwankpa et al. (2018).

#### 4.4.6 Loss functions and weight optimization

During model training, a loss function (or a close equivalent a cost function) is computed to determine the error of the model, defined as the difference between the predicted value and the target value (Goodfellow et al., 2016). The loss function is defined as a measure of a model's

predictive performance and can be represented by:  $J(w)$  where  $w = p - \hat{p}$ ,  $p$  is the target value and  $\hat{p}$  is the predicted value (Ruder, 2016; Goodfellow et al., 2016). The lower the loss function of a model, the better the model is performing. A well-performing model has a loss function that is continuously decreasing as the model learns to improve its parameters (weights and biases) and the predicted values start to match the target values (Rumelhart et al., 1986; Goodfellow et al., 2016).

The loss function used in this study is the cross-entropy loss function (Nielsen, 2018). It is used to define the probability value  $f(x)_p$  of an event occurring with target values ranging between 1 for true and 0 for false. The cross-entropy loss function is a gradient descent loss function that adjusts the models' parameters by measuring the changes in weights with regards to changes in the error to help find the optimum weights during training (Rumelhart et al., 1986; Goodfellow et al., 2016). The gradient descent algorithm evaluates the slope of the loss function, the larger the slope of the function is, the faster the model can learn to minimize the loss function; however, when the slope of the loss function is zero, the model stops learning because the predictions cannot be made smaller. A learning rate can be adjusted and introduced to allow the model to make small or large changes in the direction of the gradient towards finding optimum weights. If a learning rate is too small, it will result in the model running for too long trying to find the optimal weights and if the learning rate is too big, it could result in missing the chances of finding minimum error and optimum weight value. In this study, we used an optimization algorithm called *Adam* to optimize the learning rate, because work by Kingma and Lei Ba (2015) consider it to be effective.

#### 4.4.7 Model cross validation

Machine learning models need to be checked and cross validated to determine their performances in making new predictions on unseen datasets. Cross validation is a method of evaluating the performance of a machine learning model by splitting the input data into training and validation sets. Usually, a *train-test split* or *hold-out* approach is used during model training which requires splitting input data into two subsets, one for training and the other for testing model performance (Kuhn and Kjell, 2013). Since deep learning models are prone to overfitting, other cross validation methods such as K-fold cross validation are commonly preferred to create a more robust model. For this study, [a stratified K-fold](#) cross-validation technique was used to train and validate the deep-learning model. The stratified K-fold technique is performed by splitting data into a  $k$  number of equally sized subsets referred to as folds (e.g.,  $k=5$ ). The model is trained  $k$  number of times, whereby each time, a subset is removed during training and used only for testing the model (Maepa et al., 2020; Kubat, 2017). The model training is done  $k$  number of times until all subsets have been used to train and test the model. The average and standard deviation values of the model's accuracy results are computed to give an overall model performance and the model's degree of uncertainty. The K-Fold cross validation approach has been shown to improve model precision and reduce bias and model overfitting (Kuhn and Kjell, 2013). Furthermore, the training data was balanced to ensure that each fold obtains an equal amount of training classes, for example, in a domain with deposits classified as fuzzy classifications of 0, 0.8 and 1 representing non-deposit, a prospect and a mine respectively, balancing ensures that each fold gets an equal representation of the input training datasets. After training, the mean accuracy of each fold and the standard deviation are computed to show the

overall performance of the model. The average model training and validation accuracy and training and validation loss for  $k$ -folds of training are used to define the model metrics.

The receiver operator curve (ROC) was also used to evaluate the DNN and random forest predictive performance in this study. The ROC computes a model's ability to distinguish between true positives rate (i.e., sensitivity) and the false positive rate (i.e.,  $1 - \text{specificity}$ ) of the model (Obuchowski, 2003). The area under the receiver operator curve is computed to get an estimation of the model's performance. The area under curve (AUC) values range between 0 and 1, where 1 represents excellent performance, 0.5 represents random classification and near 0 is poor performance (Obuchowski, 2003). In this study, the area receiver operator curve is computed for the different K-fold cross validation splits making it possible to determine the mean AUC and the standard deviation of the model.

#### 4.4.8 Transfer learning: The definitions of transfer learning for mineral exploration

Transfer learning is a subset of machine learning that allows for learning and extracting features from a source task and applying the knowledge to a target task (Pan and Yang, 2010; Tan et al., 2018). While machine learning requires that there be an adequate amount of input data to train and classify a learning system, with transfer learning, knowledge gained from different machine learning tasks can be used as a starting point of a new but somewhat related task. The notations and definitions of transfer learning shown in this paper are explained in detail by Pan and Yang, (2010), for the purpose of this study, the explanations are in a mineral exploration context:

Given a domain  $D$  with feature space  $\mathcal{X}$  and marginal probability  $P(X)$ , where  $X = \{x_1, x_2, x_3, \dots, x_n\} \in \mathcal{X}$ . The domain  $D$  represents the field of exploring for gold deposits and  $\mathcal{X}$  is all possible learning feature vectors such as all possible geoscience signatures representing a mineral deposit.

Specifically,  $\mathcal{X}$  are datasets or maps indicating geoscience signatures -- for example, a feature proximity map of faults or a gridded geophysical map of magnetic signatures are represented by  $X$  and  $x_i$  is the  $i^{\text{th}}$  feature vector instance corresponding to the  $i^{\text{th}}$  geophysical class value of a pixel  $i$  in a gridded geophysical map. For a given domain  $D = \{ \mathcal{X}, P(X) \}$ , there is a task  $T$  consisting of a label space  $Y$  and an objective predictive function  $f(\cdot)$  denoted  $T = \{Y, f(\cdot)\}$ , which can be learned from training data consisting of pairs  $\{x_i, y_i\}$  where  $x_i \in X$  and  $y_i \in Y$  (Pan and Yang, 2010; Weiss et al., 2016). In mineral exploration,  $Y$  represents the labeled data of mineral deposits, prospects and/or mine locations with values classified between 0 and 1, where 0 represents the absence of mineral deposit feature and 1 represents the presence of a mineral deposit feature. The function  $f(\cdot)$  can be used to predict corresponding labels of  $f(x)$  of a new instance  $x$  (Pan and Yang, 2010; Weiss et al., 2016). An area that contains adequate amounts of training data will be referred to as the source domain ( $D_s$ ) while the data deficient region will be referred to as the target domain ( $D_T$ ). The source and target domains representing a brownfield and greenfield exploration site respectively can be shown as (Pan and Yang, 2010; Weiss et al., 2016; Tan et al., 2018):

$$D_s = \{(x_{s_1}, y_{s_1}), \dots, (x_{s_n}, y_{s_n})\}, \text{ where } x_{s_i} \in \mathcal{X}_s \text{ and } y_{s_i} \in Y_s$$

Similarly,  $D_T = \{(x_{T_1}, y_{T_1}), \dots, (x_{T_n}, y_{T_n})\}$  where  $x_{T_i} \in \mathcal{X}_T$  and  $y_{T_i} \in Y_T$ . In terms of data availability:  $0 \leq n_T \leq n_s$ .

According to the above definition, transfer learning aims to improve learning and prediction for the target predictive function  $f_T(\cdot)$  in  $D_T$  using knowledge acquired from models generated using  $D_s$  and  $T_s$ , where the  $D_s \neq D_T$  or  $T_s \neq T_T$  (after Pan and Yang, 2010). See Appendix F for illustration of transfer learning.

#### 4.4.9 Random Forest classifier

The random forest algorithm is a method that uses multiple decision trees to solve both classification and regression machine learning problems (Brieman, 2001). The random forest method randomly splits training data into multiple decision trees whereby each tree uses a subset of the training data (i.e., predictor variables and targets) to make predictions and classifications. The random forest algorithm uses bagging procedure (i.e., bootstrapping statistics) by randomly resampling training data into subsets and assigns them to the different trees, each tree therefore obtains slight variations of the original input data which helps to increase prediction accuracies and reduce generalisation errors (Gislason et al., 2006; Rodriguez-Galiano et al., 2015). According to Carranza and Laborte (2015), about two-thirds of the target variables are assigned to decision trees for training and the remaining data is used for model validation. The algorithm determines the model performance by voting and obtaining the average performance metrics of all trees. The random forest algorithm has been previously applied in mineral prospectivity mapping (Rodriguez-Galiano et al., 2014; Rodriguez-Galiano et al., 2015; Carranza, 2015) and is regarded as a highly accurate and robust machine learning approach with low likelihood of overfitting. An essential aspect of random forest is its ability to determine the relative importance of input predictor features used during training. Random forest can determine feature importance by varying and omitting each input predictor variables during training while keeping the rest constant and noting the changes in model accuracy and errors estimates (Briema, 2001; Rodriguez-Guliano et al., 2015). According to Rodriguez-Guliano et al., (2015), this procedure allows the model to identify the best prospectivity predictor variables in the input geoscience datasets. The random forest accuracy metrics, prospectivity predictions, and feature importance results are compared with those obtained from deep neural network outputs in this study.

#### 4.4.10 Deriving feature importance in the deep neural network model

A [variance-based feature importance method](#) proposed by De Sá (2019) was used to determine the relative feature importance from the deep learning models. The feature importance in a neural network is determined by computing the variance of features from the calculated weights during training. Artificial neural networks and deep neural networks make data classifications by multiplying the input features with a random set of weights and adjusts these weights using an activation function with every epoch of training to reduce the loss or error. The variance-based feature importance approach is done with the assumption that important features in a neural network will have the highest variances during training (De Sá, 2019), and thus the variances of weights and the final weights are combined to determine the relative feature importance. A study by De Sá (2019) showed that the variance-based feature importance scores correlate well with the variable importance approach obtained from the random forest algorithm.

Following De Sá (2019), this study used the Welford's online algorithm (Welford, 1962) to update the mean and variances of weights in the DNN models and thus determine the important features responsible for influencing the final predictions of deep learning models. Details on the use of variance-based feature importance method can be found in De Sá (2019).

#### 4.5 Results

Deep learning and random forest prospectivity maps were created using various available geoscience data outlined on Table 4-4. Furthermore, the important predictor variables that influenced the model predictions were determined using the random-forest feature importance algorithm and the neural-network variance-based feature importance estimator. The machine learning models were created to show: i) the ability of DNN and random forest to map gold

prospectivity in the Swayze region, ii) to test the ability of a model pretrained on the southern Swayze region to make prospectivity predictions on the northern Swayze region, iii) to determine if transfer learning from the Swayze region to the Matheson region is possible, iv) to determine and compare feature importance estimates derived from DNN and random forest models in mapping mineral prospectivity.

#### 4.5.1 Deep learning and random forest prospectivity analysis over the Swayze greenstone belt

Two mineral prospectivity maps were created for the whole of the Swayze region using DNN and random forest models (Fig. 4-9 and Fig. 4-10, respectively). The DNN model was trained with a stratified k-fold cross validation subset of  $k=10$  and results show model training and validation accuracies of 79% and 81%, respectively and model training and validation loss of 0.14 and 0.13, respectively after 100 epochs of training (Fig. 4-11). The random forest algorithm gave a classification accuracy of 81%. Both mineral prospectivity maps show prospectivity classifications on a color spectrum from red to green representing high to low prospectivity, respectively. To further evaluate and compare the performance of the random forest and DNN predictive maps, the area under the receiver operator curve were calculated and plotted on Fig. 4-12A. The area under the receiver operator curve for the DNN model and random forest models are 90% and 89%, respectively, suggesting that deep learning did a slightly better job at determining the most prospective regions.

Table 4- 3: Principal components of normalized lithogeochemical major oxide data from the Swayze greenstone belt. Shaded blocks show anomalous correlations between major oxide data and principal components. The corresponding principal component analysis data showing the amount of variance associated with each principal component of the major oxide datasets (results from Maepa et al., 2020).

Eigenvectors	PC1	PC2	PC3	PC4	PC5	PC6	PC7	PC8	PC9	PC10
SiO <sub>2</sub>	-0.301	-0.515	0.008	0.437	0.052	0.151	-0.102	0.053	-0.624	0.16
Al <sub>2</sub> O <sub>3</sub>	-0.292	-0.4	0.464	0.218	0.183	-0.126	0.196	-0.128	0.607	0.138
Fe <sub>2</sub> O <sub>3</sub>	0.327	-0.113	-0.334	-0.073	0.551	0.239	0.343	-0.426	-0.026	0.321
MgO	0.376	-0.14	-0.051	0.182	-0.245	0.279	-0.655	-0.092	0.303	0.369
CaO	0.298	-0.067	0.471	-0.176	-0.548	0.022	0.375	-0.278	-0.265	0.257
Na <sub>2</sub> O	-0.313	0.214	0.333	-0.444	0.229	0.511	-0.103	0.297	-0.054	0.366
K <sub>2</sub> O	-0.368	0.025	-0.353	-0.237	-0.17	-0.529	-0.065	-0.089	0.002	0.601
TiO <sub>2</sub>	0.255	0.374	0.438	0.243	0.425	-0.451	-0.254	-0.041	-0.244	0.185
P <sub>2</sub> O <sub>5</sub>	-0.209	0.57	-0.115	0.606	-0.194	0.258	0.295	-0.037	0.104	0.218
MnO	0.38	-0.164	-0.094	0.108	0.011	-0.125	0.313	0.784	0.081	0.27
Eigenvalues	4.9	1.2	1.1	0.8	0.7	0.5	0.4	0.3	0.2	0
Cumulative %	48.8	61.1	72.1	79.8	86.6	91.3	95.1	98.3	100	100

Table 4- 4: A summary of evidential layers used for machine learning and transfer learning and the respective model performance accuracies of each analysis.

Predictor datasets	Entire Swayze greenstone belt	Entire Swayze greenstone belt	Southern Swayze greenstone belt	Northern Swayze greenstone belt	Entire Swayze greenstone belt	Matheson greenstone belt
Method	Deep Neural Network	Random Forest	Deep Transfer learning (Source domain)	Deep Transfer learning (Target domain)	Deep Transfer Learning (Source domain)	Deep Transfer Learning (Target domain)
PC1	X	X	X	X		
PC2	X	X	X	X		
PC3	X	X	X	X		
Distances from D2 and D3 high-strain zones	X	X	X	X		
Distances from D2 and D3 folds	X	X	X	X		
Lithologies	X	X	X	X	X	X
Lithological contacts	X	X	X	X	X	X
Apparent magnetic susceptibility					X	X
Distance from faults (up to 6km)	X	X	X	X	X	X
Distance from magnetic worms	X	X	X	X	X	X
Distance from electromagnetic anomalies	X	X	X	X		
Mineral Deposit Index	X	X	X	X	X	
Training Accuracy	79%	81%	81%		70%	
Validation Accuracy	81%		82%		77%	
Training Loss	0.14		0.11		0.2	
Validation Loss	0.13		0.12		0.18	
Area under the ROC	90%	89%	90%		80%	
Efficiency of prediction after transfer learning					77%	68%

#### 4.5.2 Feature importance estimates from deep neural networks and random forest in the Swayze greenstone belt

The most important features responsible for mapping prospectivity were determined from both random forest and DNN. A comparison of the feature importance estimates by DNN and random forest predictive models is shown on Fig. 4-12B. The DNN model considered the EM conductivity, distances from igneous intrusive suites, distances from PC3, and distances from D<sub>2</sub> and D<sub>3</sub> high-strain zones as the most important predictors of prospectivity whereas random forest decision trees deemed D<sub>2</sub> and D<sub>3</sub> high-strain zones, distances from PC1 and igneous intrusive suites as the best predictors. The random forest model considered the geological map (i.e., lithologies) as a less effective predictor map. The variance based DNN feature importance approach and random forest feature importance estimators show comparable results, except that DNN considered magnetic worms to have minor significance compared to random forest. The feature importance results indicate that monitoring the variance of weights in a neural network is a useful way of determining important predictor variables.

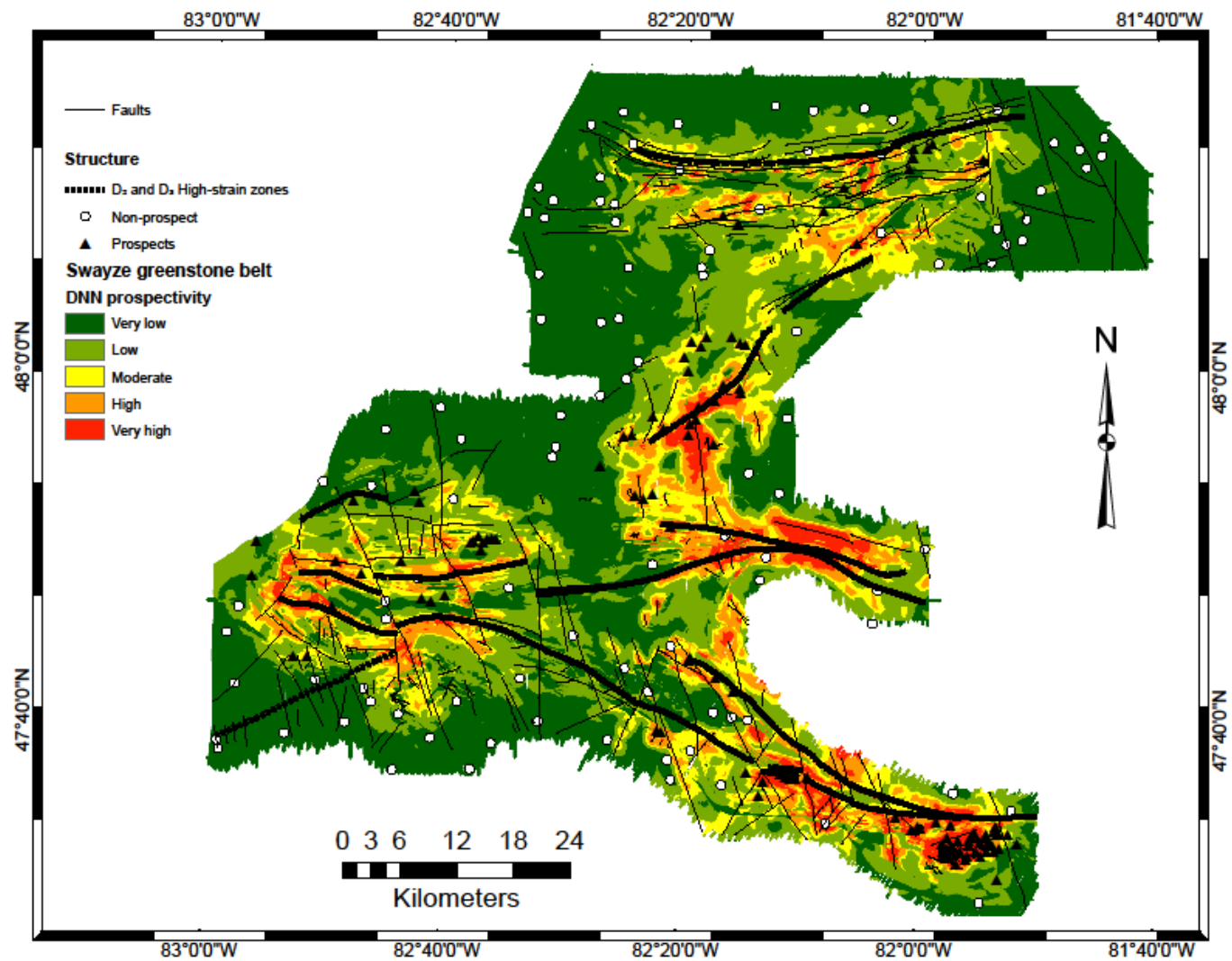


Fig. 4- 9 : Mineral prospectivity map created using a deep neural network with data from the entire Swayze region as defined on Table 4-4.

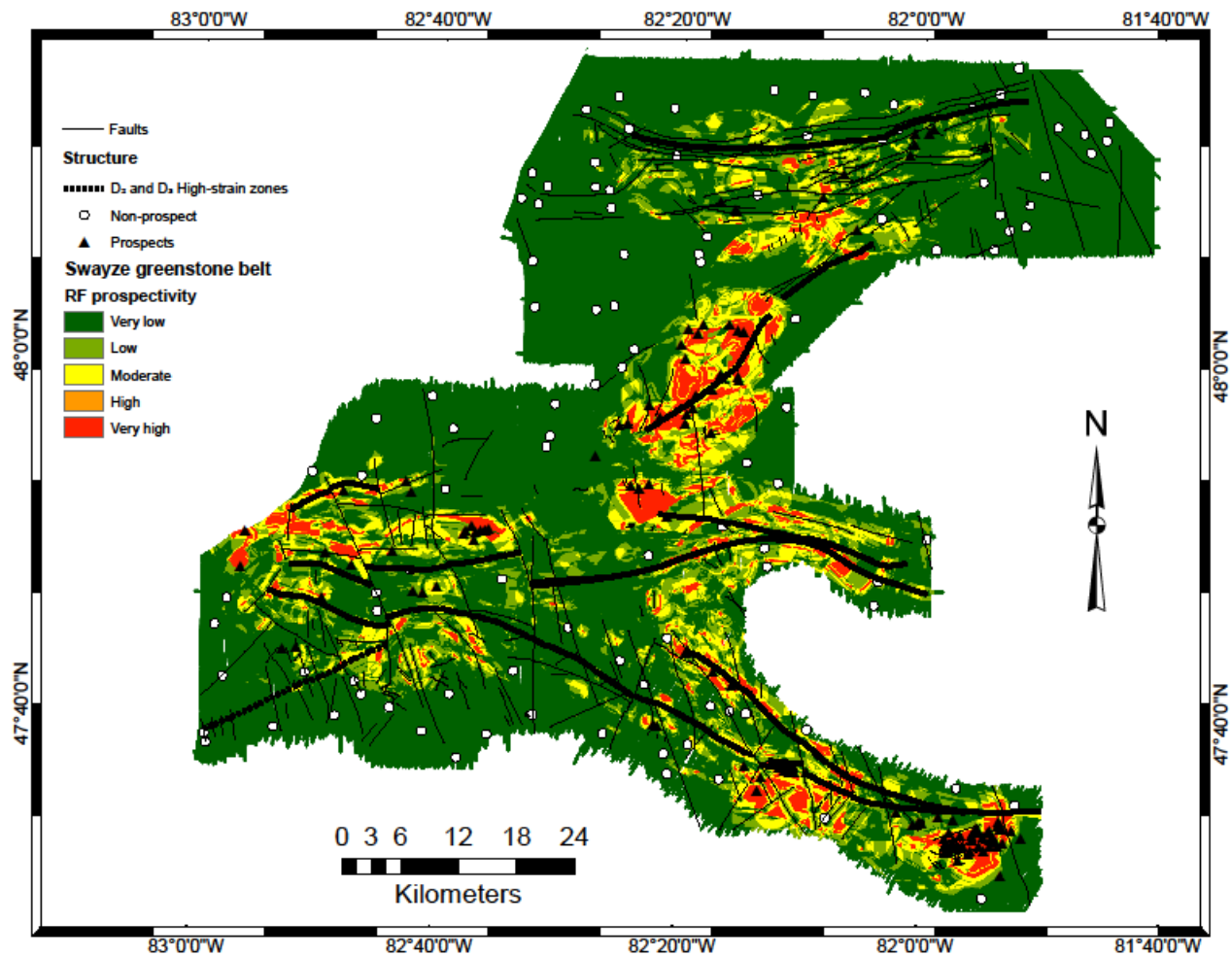


Fig. 4- 10 : Mineral prospectivity map created using the random forest algorithm with data from the entire Swayze regions defined on Table 4-4.

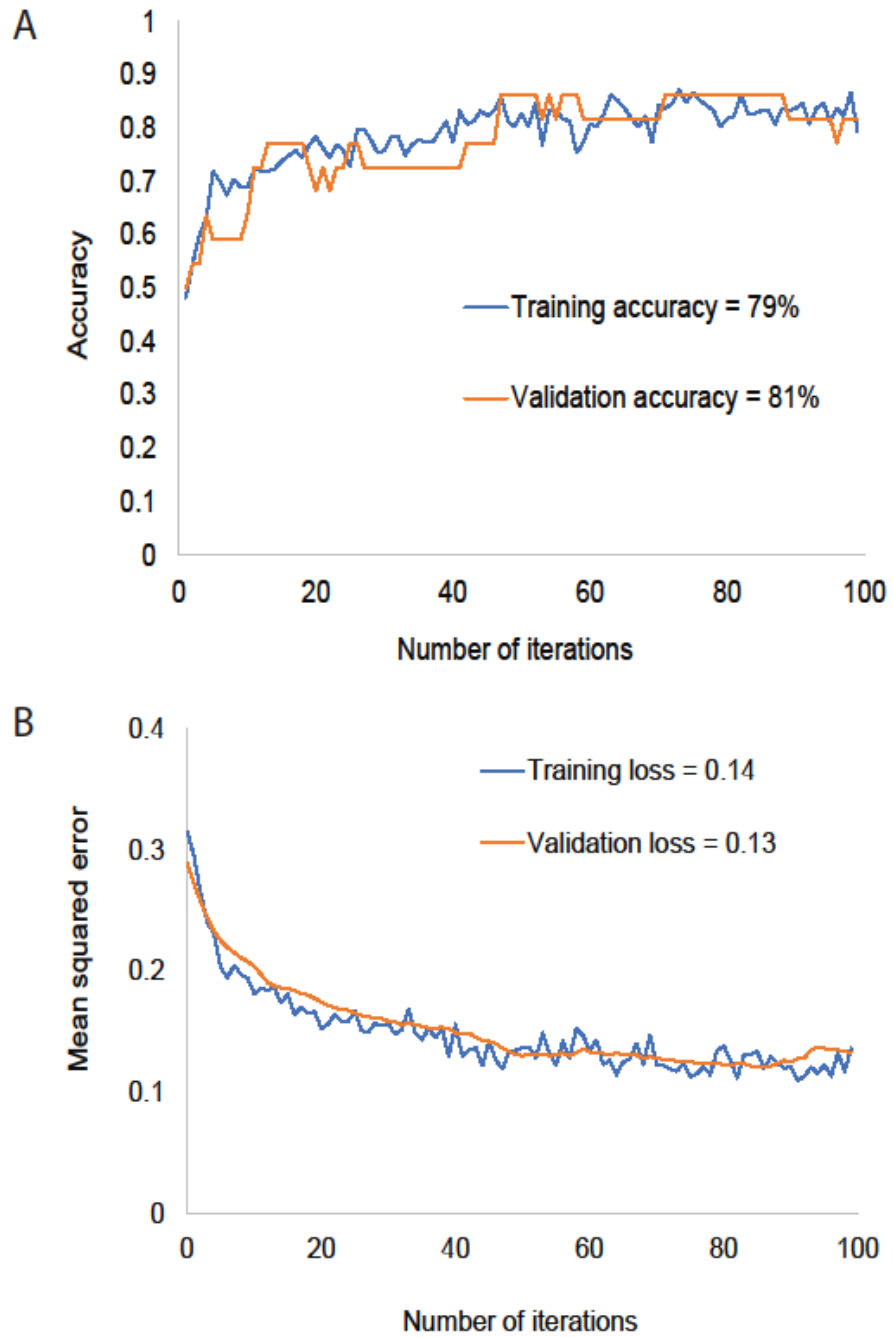
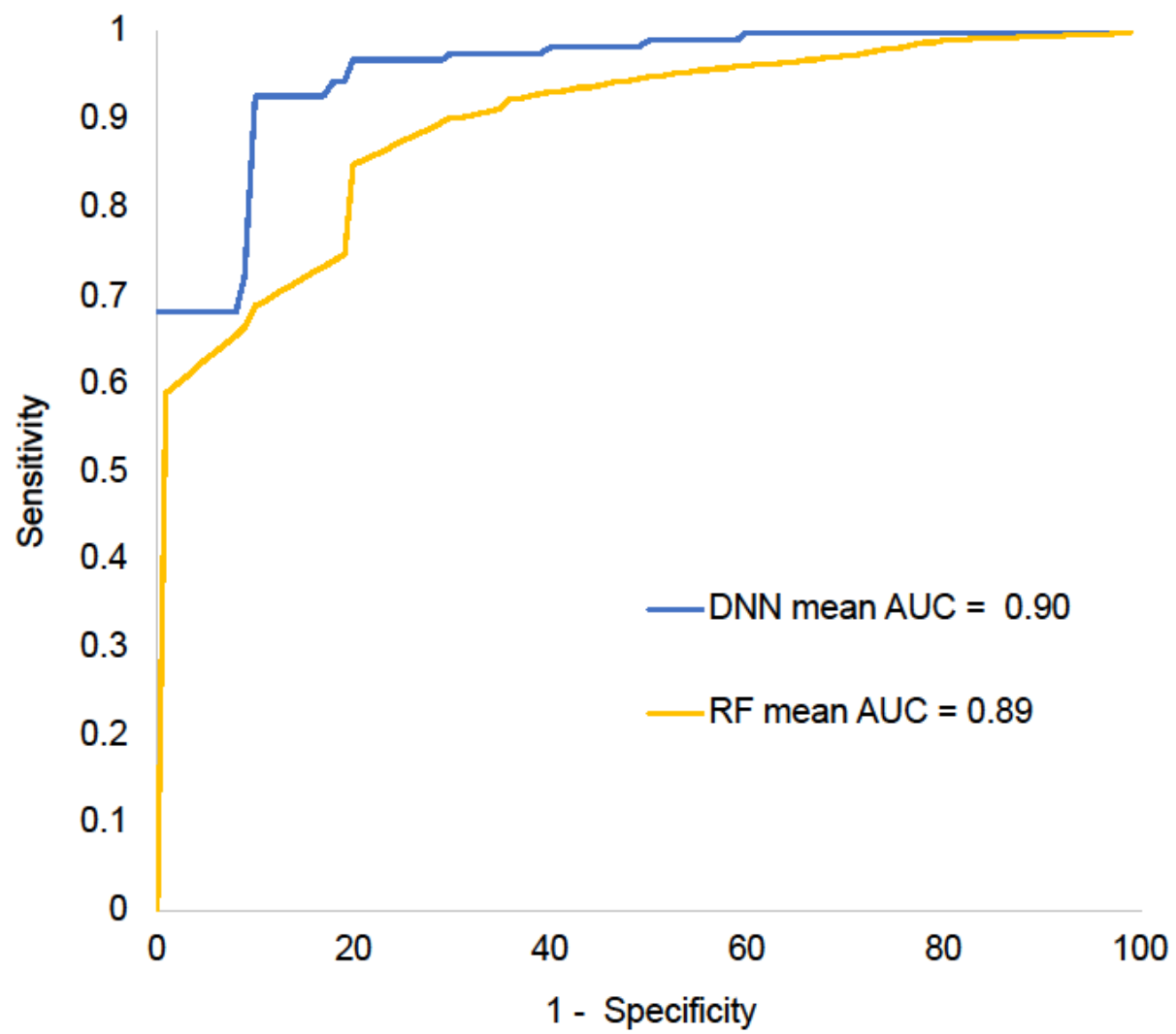


Fig. 4- 11: Deep neural network model performance metrics showing the training and validation accuracy plots (A) and the training and validation loss plot (B) for a model trained on the entire Swayze region with predictor layers shown on Table 4-4.



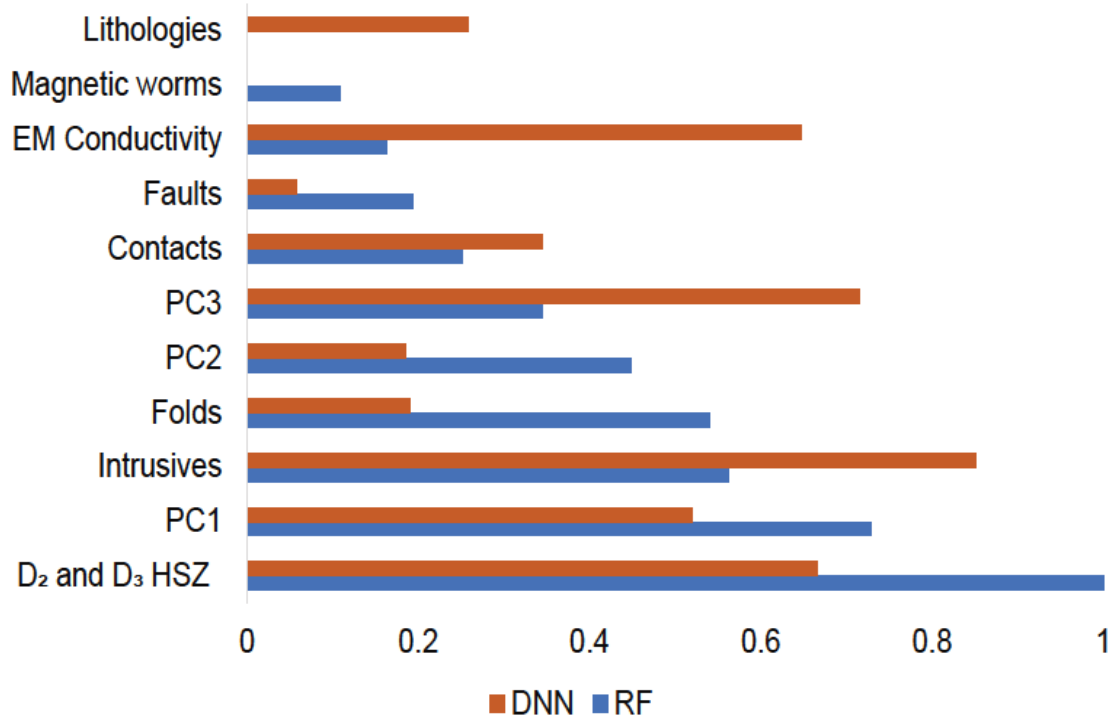


Fig. 4- 12 : A) Receiver operator curves derived from deep neural networks and random forest in the Swayze region. The curves with greater area under the curves indicate that the model’s predictive performance is greater. B) The feature importance plot estimations derived from deep neural networks and random forest graph shows how much each predictor variables contributed towards making prospectivity predictions for each machine learning method.

#### 4.5.3 Transfer learning between the north and south of the Swayze greenstone belt

Deep transfer learning was attempted first on data from the north and south of the Swayze regions to determine if datasets derived from the southern Swayze region can be used to train a deep learning model and later be used to predict prospectivity in the northern Swayze region. This experiment was done on the north and south Swayze regions because both the north and southern regions are assumed to have experienced similar, but perhaps slightly different geological and deformational processes related to gold mineralization, in comparison with the Matheson area. Using data covering the southern Swayze region as defined in Table 4-4, a deep learning model was trained using K-Fold subset of  $k = 10$ . The deep learning model results showed the average accuracy of 10-fold subsets is 80% accuracy and standard deviation of 7.98. The model training and validation accuracies are 81% and 82% (Fig. 4-13A) and the models training, and validation losses are 0.11 and 0.12 (Fig. 4-13B) after 100 epochs of training. After training, the model weights parameters were saved and evaluated on new unseen data from the northern Swayze region, the evaluation score results gave a 77% prediction accuracy and 0.18 prediction error. The model prospectivity predictions in the northern Swayze region are shown on Fig. 4-14 in the solid black box and the predictions for prospectivity in the southern Swayze region are seen on the dotted black box on Fig. 4-14. The evaluation scores show that the model was effective enough in making predictions on a new area with previously unseen deposit locations.

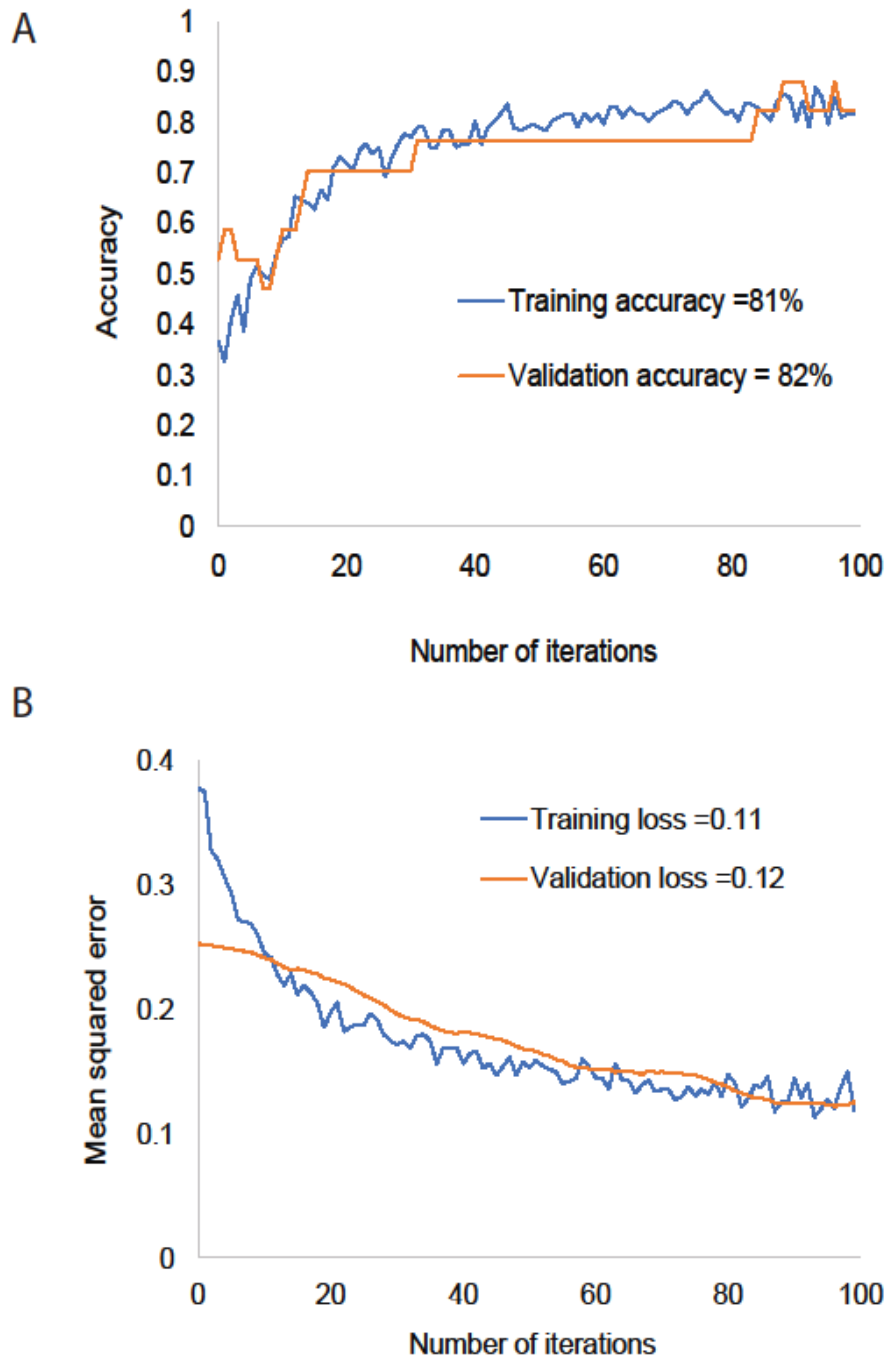


Fig. 4- 13 : Deep neural network model performance metrics showing the training and validation accuracy plots (A) and the training and validation loss plot (B) for a model trained on the southern Swayze region generated for transfer learning from the south to the north Swayze regions with predictor layers shown on Table 4-4.

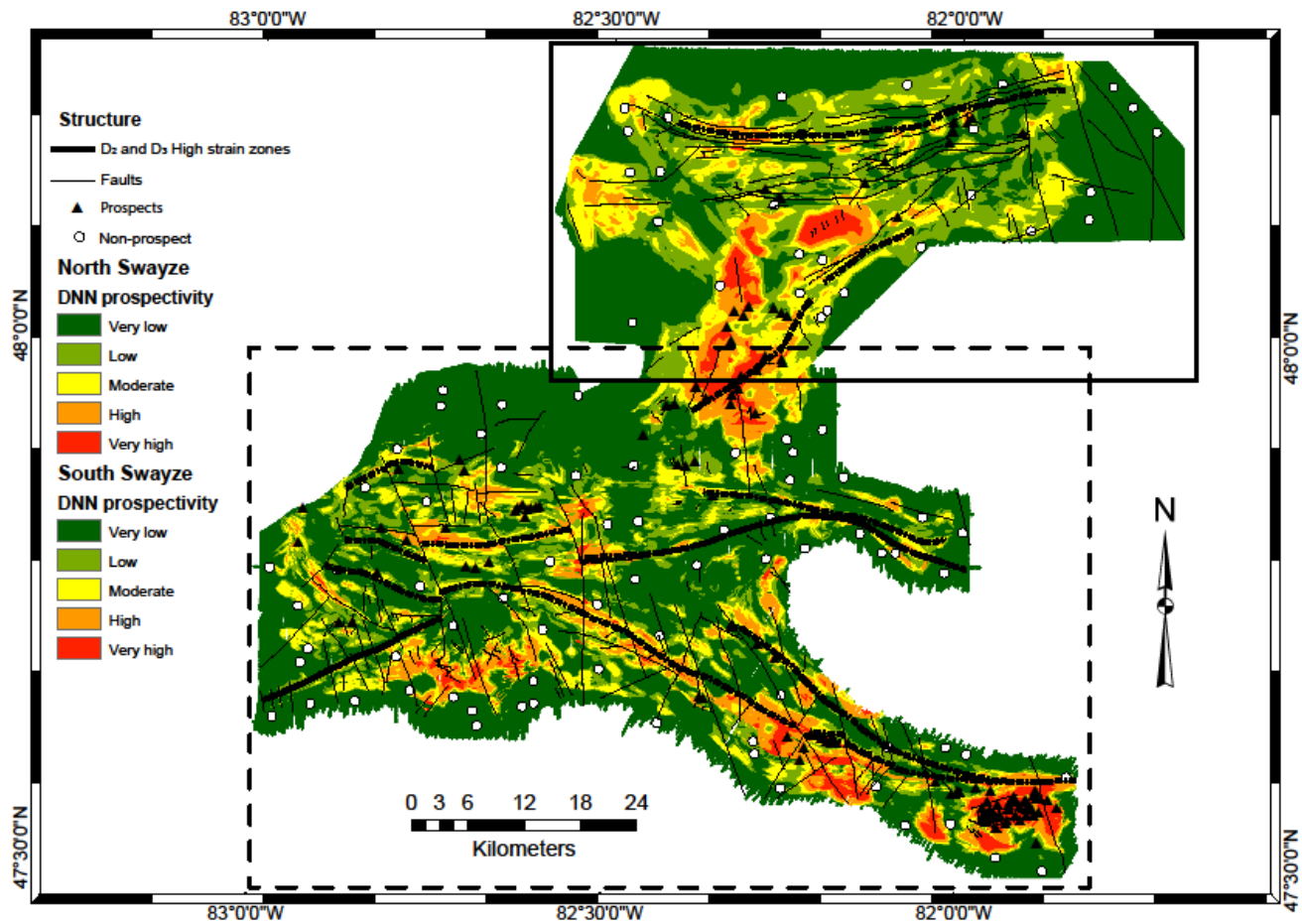


Fig. 4- 14 : Mineral prospectivity map created using deep transfer learning from the southern to the northern Swayze regions. The southern prospectivity predictions is the colour image shown inside the dashed rectangle. The transfer learning prospectivity predictions in the northern Swayze region is shown in a solid rectangle. The area where the rectangles overlap (i.e., central Swayze region) is from the northern Swayze region transfer learning prediction results.

#### 4.5.4 Transfer learning between entire Swayze and Matheson greenstone belts

Deep transfer learning was attempted next on the Matheson region using a model pre-trained on data from the entire Swayze region. Both regions were selected because they form a part of the Abitibi greenstone belt, and thus are assumed to have similar geological and mineralization controls such as the D<sub>2</sub> Porcupine-Destor Fault zone. The drawback of using the Matheson region is that there is no lithogeochemical data available in the region to map alteration. As mentioned previously, to derive new predictions using deep transfer learning, the source domain's predictive model must be trained using similar datasets found in the target domain. Thus, only the predictor variables that are available (i.e., fault, lithological map, magnetic worms, and apparent magnetic susceptibility map) in the Matheson region were used to train the deep learning model on the Swayze region. The pre-trained model generated using data from the entire Swayze region obtained a training and validation accuracy of 70% and 77% respectively and a training and validation loss of 0.20 and 0.19 after 100 epochs of training (Fig. 4-15). The mean area under the receiver operator curve obtained an 80% prediction accuracy of the Swayze pre-trained model (Fig. 4-16). The Swayze region pre-trained model was used to predict gold prospectivity in the Matheson region after seeing only predictor maps and without prior knowledge of mineral deposit distributions (shown on Fig. 4-17) and the resulting model-evaluation score was 68% prediction accuracies and 0.35 prediction error. According to the accuracy metric results obtained, a model pre-trained on the Swayze region data was successful in predicting at least 68% of the deposits in the Matheson region without prior knowledge of the deposit distributions. Furthermore, Fig. 4-18 shows that gold mineral prospectivity predictions in the Matheson region lie along major fault zones such as the Porcupine-Destor fault zone and Pipestone fault are shown cross cutting the region in an E-W orientation as dotted lines. The

influence of faulting, closeness to lithological contacts and magnetic gradients is supported by Fig. 4-18 which summarises important features used by the pretrained DNN to make classification of gold prospectivity in the Swayze region and predictions in the Matheson region.

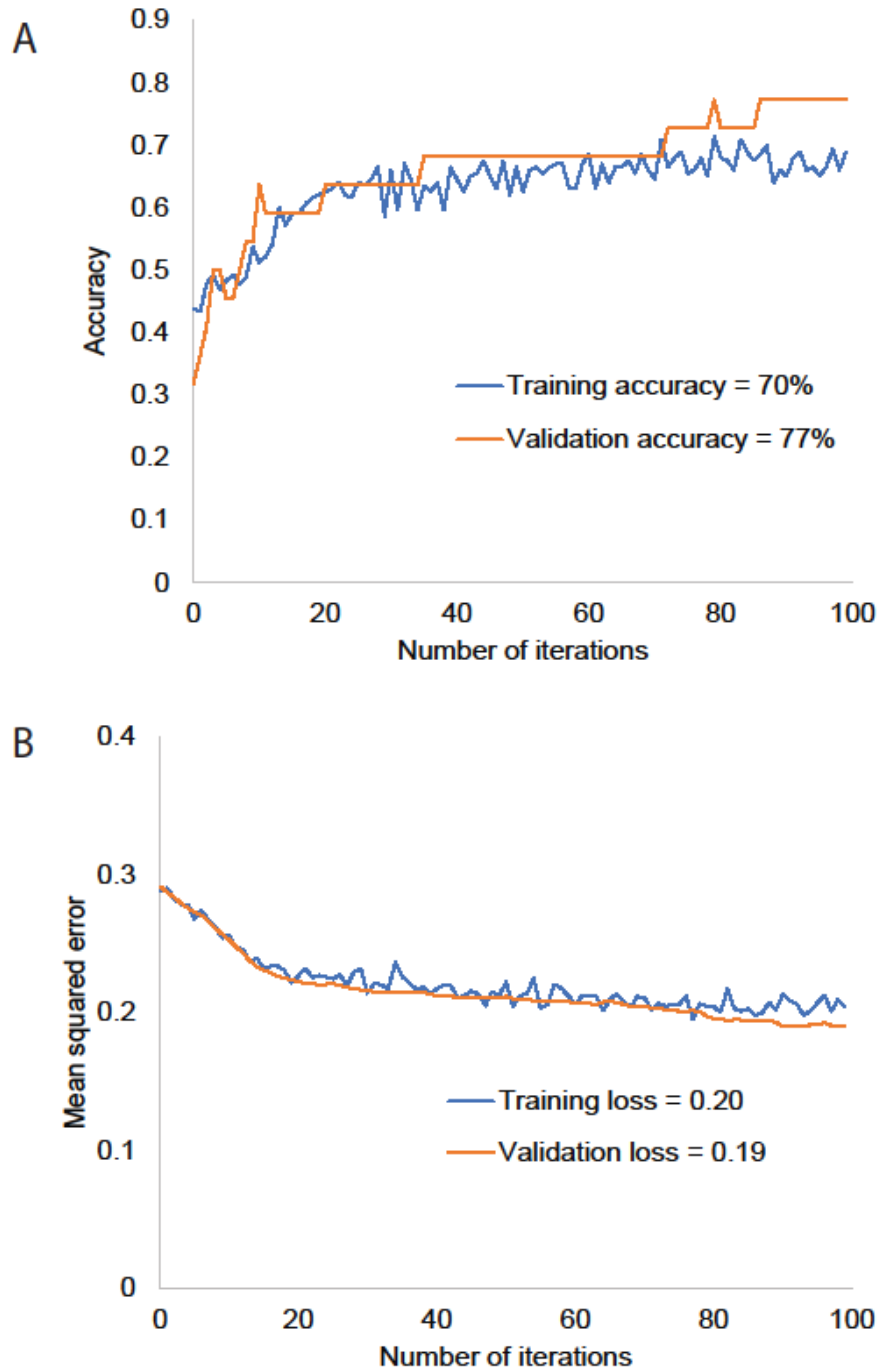


Fig. 4- 15 : Deep neural network model scores showing the training and validation accuracy plots (A) and the training and validation loss plot (B) for a model trained on the entire Swayze region for transfer learning from the Swayze region to the Matheson region with evidential layers defined on Table 4-4.

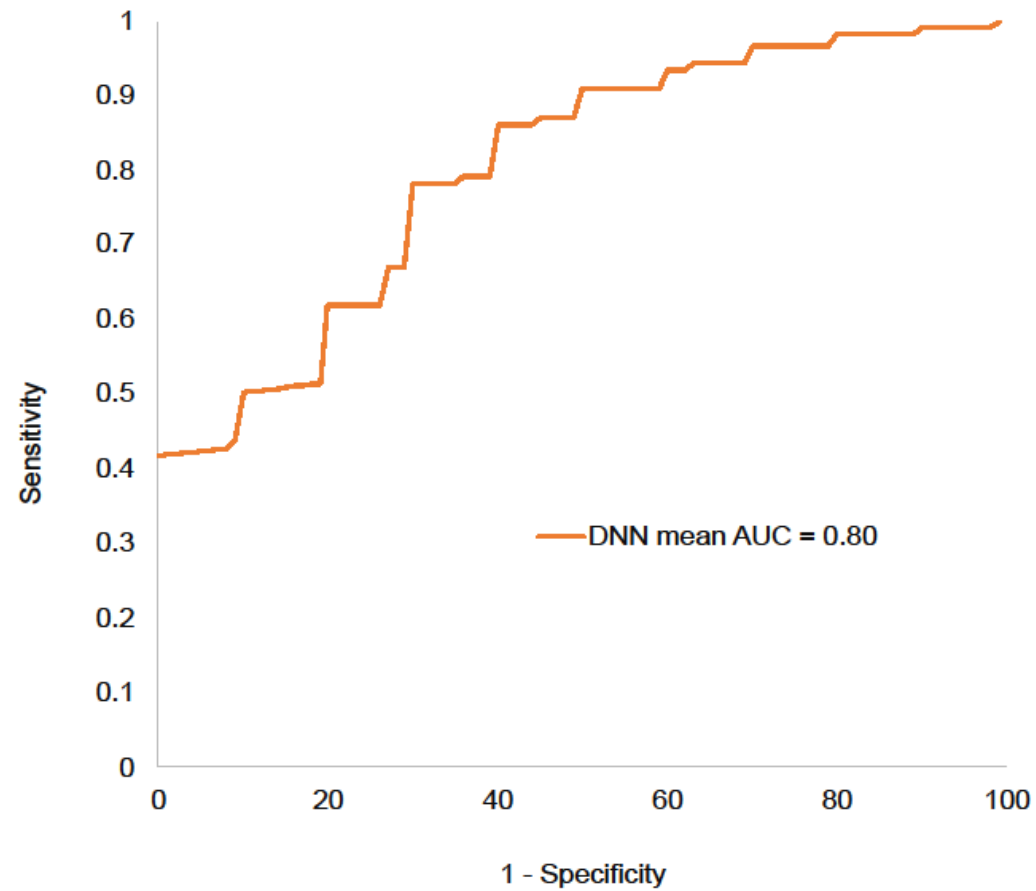


Fig. 4- 16 : The receiver operator curve metrics from a model pre-trained on the Swayze region for transfer learning shows an area under the receiver operator curve of 80%.

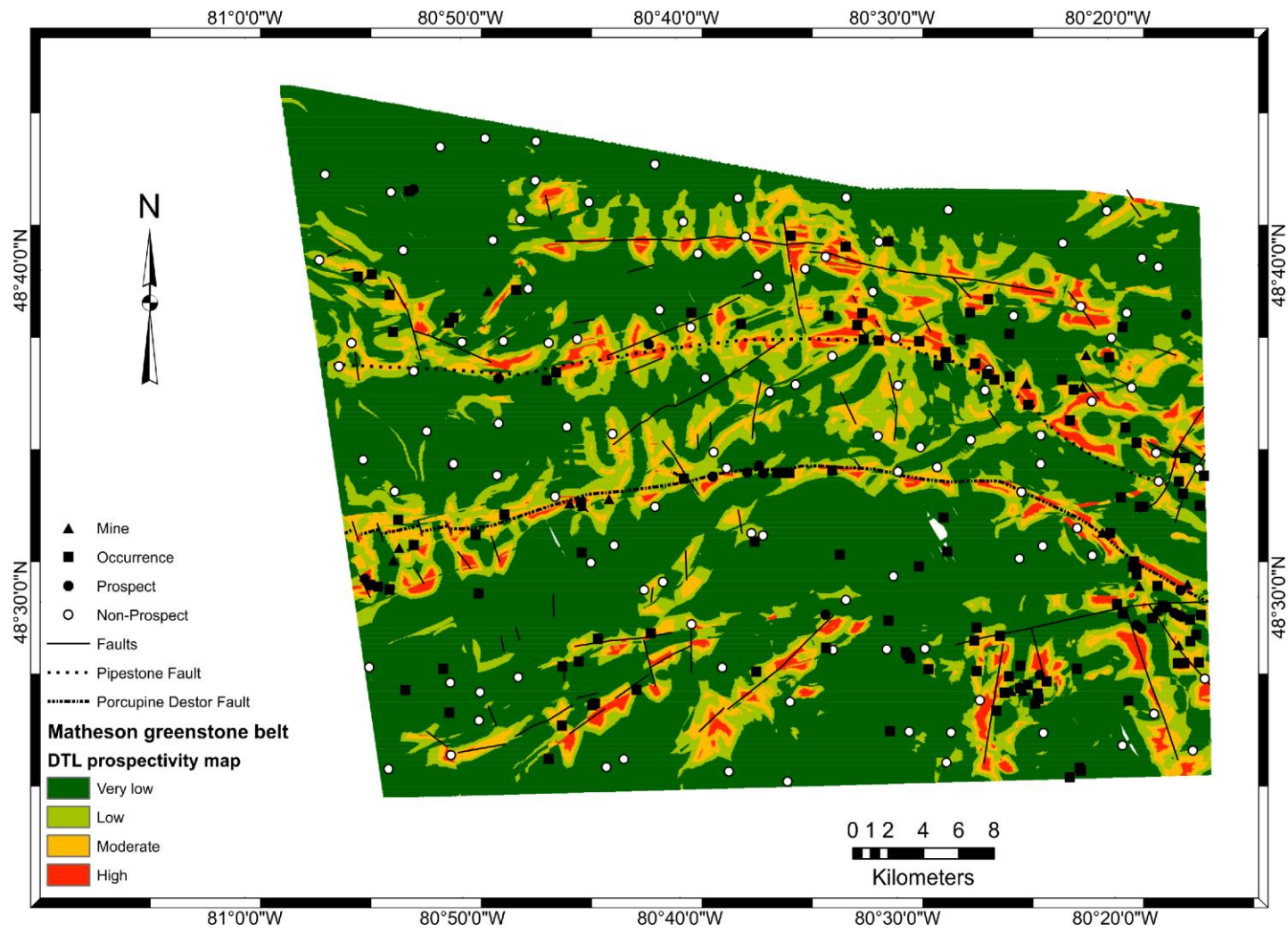


Fig. 4- 17 : The prospectivity predictions in the Matheson region obtained from the pre-trained (i.e., deep transfer learning) model in the Swayze region.

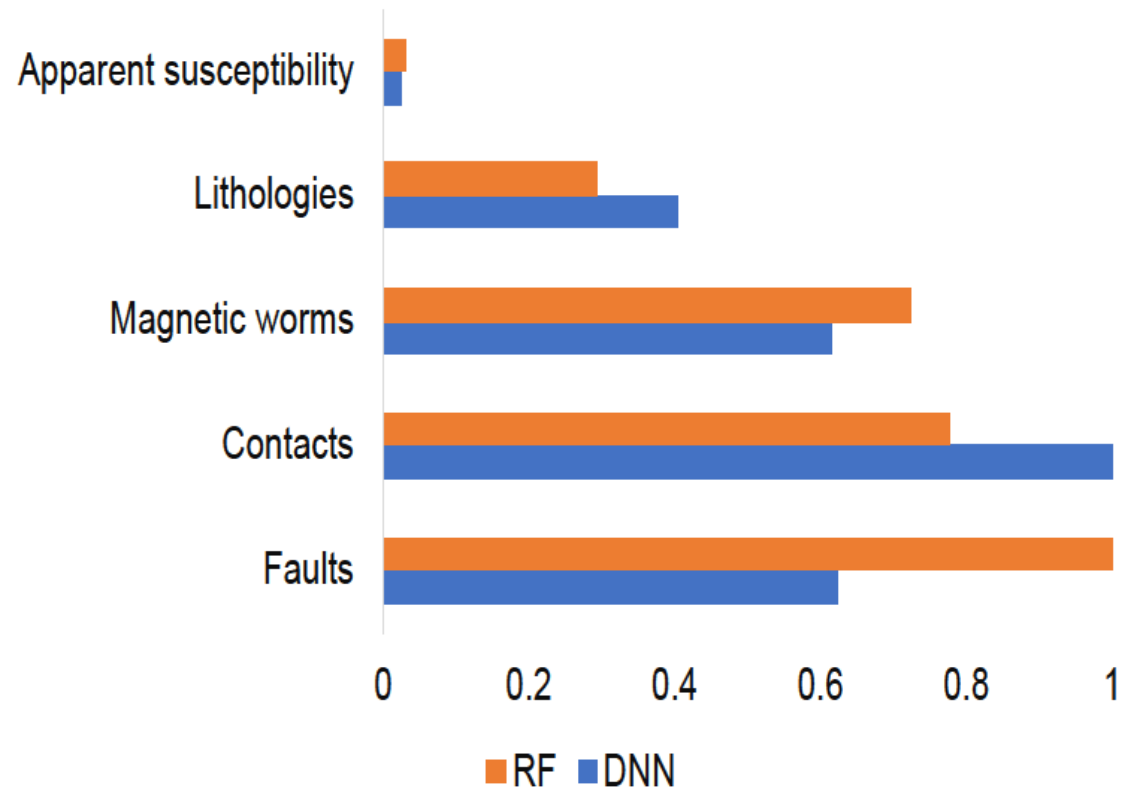


Fig. 4- 18 : The feature importance estimations derived from the deep transfer learning model and random forest on the pre-trained Swayze region. The plot shows how much each predictor variables contributed towards making prospectivity predictions for transfer learning from the Swayze to the Matheson region.

## 4.6 Discussions

The results indicate that DNN performed well in determining mineral prospectivity (Fig. 4-9, Fig. 4-10A and Table 4-4). When compared with random forest, the DNN showed slightly higher prediction accuracies (Fig. 4-12A) and both models have defined similar and spatially overlapping regions as prospective. Normally, one of the drawbacks of using neural networks procedures has been the black box nature of the models (Rodriguez-Galiano et al., 2014; Carranza and Laborte, 2015), however, the implementations of the variance-based feature importance algorithm with Welford's online algorithm (De Sá, 2019; Welford, 1962) helps to mitigate the problem.

The results showed that using the variance-based feature importance approach for DNN is not only possible but is comparable to the feature importance estimations derived from the random forest classification models (Fig. 4-12B) A key limitation of using DNN is that they take longer to train than random forest models and are subject to overfitting if proper cross-validation techniques such as stratified K-Fold techniques are not used.

In an effort to determine if models pre-trained on one region can be used to predict occurrences of gold prospects in another separate but geologically related region, the Swayze region was divided into north and south at 480'00" N. The southern Swayze region was used as a source domain on which a deep learning model was trained and the northern Swayze region was regarded as the target domain. According to the results presented above, the transfer learning process gave prediction accuracy and error of 77% and 0.17. Predictions made for the northern Swayze region are shown on Fig. 4-14 within the solid black box. The area on Fig. 4-14 where the rectangles overlap (i.e., central Swayze region) is from the northern Swayze region transfer learning prediction results.

Visual inspection shows that there is moderate spatial correlation between highly prospective areas derived from transfer learning predictions for the northern Swayze region (Fig. 4-14) compared with the predictions of regular DNN (Fig. 4-9) and random forest (Fig. 4-10) prospectivity maps. The similarity in prospective regions, and the high prediction accuracy scores show that deep transfer learning can be applied in mineral exploration. Instead of only implementing machine learning in regions where adequate predictor and targeting variables are available, researchers and exploration geoscientists can use models pre-trained on well understood regions to make prospectivity predictions on new areas with limited target information.

The only drawback is that transfer learning requires that the target domains have similar predictor layers used to create the pre-trained models and that the geological processes involved in creating the mineral prospects be expressed well in the predictor layers information. Thus, transfer learning can be used to serve as a guide for focusing exploration projects in greenfield regions that lack adequate target information for machine learning.

Transfer learning attempted on the Matheson region from a model pre-trained on the Swayze region yielded promising results. Although the Swayze and Matheson regions are both a part of the Abitibi greenstone belt, contain rocks of similar ages and both have D<sub>2</sub> high strain zones controlling gold distributions and mineralization at regional scale, the Swayze and Matheson regions are more distal from one another than the north and south Swayze region, and thus might possess different district- to prospect-scale geological controls of gold mineralization.

However, using data that outline regional-scale mineralization controls in the Swayze region, a DNN model was created using predictor and target variables with an area under the receiver operator curve of 80% (Fig. 4-16). The model was used to model regional scale prospectivity in the Matheson region, resulting in transfer learning prediction accuracy of 68%.

According to feature importance estimators (Fig. 4-18), mineral prospectivity was influenced by faulting, lithological contacts, and magnetic worms. The model used for transfer learning was trained on “low resolution” geoscience data that can easily be acquired at early stages of exploration before detailed mapping, geochemical and geophysical surveys can be done. The results are promising and indicate that transfer learning should be considered in orogenic gold deposit systems that are highly fault controlled and when the faults can be interpreted from the magnetic or electromagnetic data.

One observation of the prospectivity map of the Matheson region derived from transfer learning is that a large portion of the map has been defined as highly prospective (i.e., red colors on Fig. 4-17) and this is due that the DNN pre-trained model recognised the importance of faults and geological contacts in orogenic mineral systems and the Matheson region has high fault densities. One way to select the more important areas to focus an exploration program on would be to concentrate on mapping fault densities and deriving a robust structural framework to guide exploration, as suggested by the feature importance results. Magnetic worms and lithological contacts also scored high in feature importance estimations suggesting the need for monitoring magnetic gradients and lithological complexity gradients when exploring in orogenic mineral-deposit environments.

Suggestions for future work would be to use CNN to model mineral prospectivity and for transfer learning. CNN are regarded as better predictors, and more highly robust and accurate models than DNN models, and thus their applications in exploration targeting could be beneficial. However, CNN techniques are significantly more work than DNN, so we preferred the latter.

### *Limitations of the study*

The following limitations have been observed in this study and are crucial when doing exploration targeting with deep neural networks and deep transfer learning:

i) Training DNN models require a vast amount of data to learn important data parameters and to make predictions, if a model is not given adequate data to learn from, it may underfit resulting in poor classifications and predictions.

ii) Selecting non-deposit datasets can become a subjective process if the study area has not been highly explored. The current study used random set of points as non-deposit training data because it is a less bias approach and has become the accepted method by researchers (Roshanravan et al., 2020).

iii) Transfer learning could only be done if the input data from the Matheson region had the same number of predictors layers as training data used to create the pre-trained Swayze region model. Thus, the Swayze region was trained with the same number of available geoscience data as the Matheson region to make predictions.

iv) Transfer learning further requires that predictor maps from both the source and the target domains have similar value domains. For example, aeromagnetic data values from the source region to the target region may vary and this may skew the transfer learning prediction results. Normalization of the data was crucial for helping with equating geoscience data from two different regions as emphasized in the *Data preprocessing steps in python* section. Another method this study used to correct for the distinction in data values was using proximity to feature maps instead of raw continuous datasets. For instance, instead of using a reduced to pole aeromagnetic map as an input predictor map, the aeromagnetic data was refined to create magnetic worms' maps for

both the Swayze and Matheson regions, this helped to simplify the impact of extreme values of data from different domains. The distances from magnetic worm's map were useful for mapping magnetic gradient and upper crustal fluid pathways in both regions.

v) Other limitations involve deriving faults from aeromagnetic data in highly covered terranes. There is bias associated with interpreted data versus data obtained from field mapping. Such uncertainties in data can be improved with rigorous and high-resolution data acquisition, in-depth analysis and further detailed field mapping where possible. However, if the area to which transfer learning is being applied is a greenfield area, then this detailed geological information will not be available in the early stages. The transfer learning can help to prioritize areas for this type of detailed geological mapping. Predictive models are governed by data availability and can be improved as new detailed information becomes available throughout an exploration project.

#### 4.7 Conclusions

Exploration targeting works to improve mineral exploration and define new targets using scale-integrated machine-learning approaches. This study reviewed DNN as a potential tool for generating targets and compared it with a popular machine learning classifier, random forest. Observations from this study indicate that DNN performances are comparable with random forest in defining mineral prospectivity. The model training and validation accuracies derived from using a stratified K-Fold cross validation technique gave  $> 80\%$  model performance accuracies and  $< 0.2$  model losses. By computing the mean and variances of the model weights obtained during training of DNN, feature importance's can be derived to determine predictor variables that guided the deep neural networks towards making classifications. The variance-based neural network feature

importance method was compared with feature importance estimates derived from the random forest algorithm, and the results are somewhat comparable and accurate.

Transfer learning between the northern and southern Swayze region was investigated and the results show that a model pre-trained on data from the southern Swayze region was able to predict ~77% of gold prospects unseen by the model during training in the northern Swayze region. The transfer learning prospectivity predictions spatially correlate with predictions made from traditional machine learning models, DNN and random forest prospectivity maps, on Fig. 4-9 and Fig. 4-10, respectively.

Prospectivity estimations attained from using transfer learning from the Swayze region to the Matheson region was also successful. The deep learning pre-trained model was able to make new prospectivity predictions using only predictor layers and with no knowledge of mineral deposit distributions in the Matheson region. The pre-trained model was able to predict at least 68% of the unseen gold prospects in the Matheson region confirming that transfer learning is possible in mineral exploration targeting. This study indicate that transfer learning should be considered as an exploration targeting tool in defining prospectivity in greenfield areas that lack enough deposit examples to perform traditional machine learning.

#### 4.8 Acknowledgements

We would like to acknowledge funding for this study from the International Development Research Centre (IDRC), Queen Elizabeth II Diamond Jubilee Scholarship, Ivanplats Mines, and Goodman School of Mines.

#### 4.9 References

Agterberg, F.P., and Cabilio, P., 1969, Two-Stage Least-Squares Model for the Relationship Between Mappable Geological Variable: IAMG, 1, 138–153.

Ayer, J.A, 1995, Precambrian Geology Northern Swayze Greenstone Belt; Ontario Geological Survey, Report 297, 1-57

Ayer, A.J., Trowell, N.F., Berger, B., Madon, Z., Zalnierius, R., and Valade, L., 1999, Geological compilation of the Lake Abitibi area, Abitibi greenstone belt; Ontario Geological Survey, Miscellaneous Release – Data 46. ISBN 0-7778-8875-0

Ayer, J.A, and Trowel N.F, 2002, Geological compilation of the Swayze area, Abitibi greenstone belt; Ontario Geological Survey, Preliminary Map P.3511, scale 1: 100 000.

Ayer, J.A., Berger, B.R., Hall, L.A.F., Houlé, M.G., Johns, G.W., Josey, S., Madon, Z., Rainsford, D., Trowell, N.F., and Vaillancourt, C., 2005, Geological compilation of the central Abitibi greenstone belt: Kapuskasing structural zone to the Québec border; Ontario Geological Survey, Preliminary Map P.3565, scale 1:250 000.

Breemen, O.V., Heather, K.B., and Ayer, J.A., 2006, U-Pb Geochronology of the Neoproterozoic Swayze Sector of the Southern Abitibi Greenstone Belt, Current Research Paper 2006-F1; Geological Survey of Canada, 1-30.

Bonham-Carter, G.F., 1994, Geographic Information Systems for Geoscientists: Modelling with GIS: Canada, Pergamon e-book ISBN: 9781483144948

Brownlee, J., 2016, Machine Learning Mastery with Python; Australia, Jason Brownlee, 1- 179.

- Basheer, I.A., and Hajmeer, M., 2000, Artificial neural networks: fundamentals, computing, design, and application: *J. Microbiol. Methods*, 43, 3-31.
- Bath, A.C., 1985, Black River-Matheson economic geologist program: in *Summary of Field Work and Other Activities 1985*, Ontario Geological Survey, Miscellaneous Paper 132, 421 – 430.
- Briemen, L., 2001. Random forests. *Machine Learning*, 45, 5 – 32
- Carranza, E.J.M., 2009, *Geochemical Anomaly and Mineral Prospectivity Mapping*: Amsterdam Elsevier Science, 365 p.
- Carranza, E.J.M., and Laborte, A.G., 2015, Random forest predictive modeling of mineral prospectivity with small number of prospects and data with missing values in Abra (Phillipines): *Comput and Geosci*, 74, 60 – 70.
- Chollet, F., 2018, *Deep learning with python*: United States of America, Manning Publications Co, 384 p.
- Chung, C.J.F., and Fabbri, A.G., 1993, The representation of geoscience information for data integration. *Non-renewable Resour.*, 2, 22–139.
- De Sá, C.R., 2019, Variance -based feature importance in neural networks, in Novak, P.K., Šmuc, T., Džeroski, S., ed., *Discover Science 2019: Switzerland*, Springer Nature, 306 – 315.
- Desharnais, G., Paiement, J.P., and Poupant, N., 2018, Mining Big Data: The Future of Exploration Targeting Using Machine Learning: In Tschirhart, V., Thomas. M.D., ed., “Proceedings of Exploration 17: Sixth Decennial Conference on Mineral Exploration”, 319 – 323.

- Domingos, P., 2012, A few things to know about machine learning: *Communications of the ACM*, 55, 78 – 87.
- Fumerton, S., Houle, K., 1995a. Mineral prospects of the Swayze greenstone belt Volume 1 - parts of NTS41 O and Volume 2-parts of NTS 41 P, 42 A and 42 B; Ontario Geological Survey, Open File Report 5912, 1, 1-372.
- Gislason, P.O., Benediktsson, J. A., and Sveinsson, J.R., 2003, Random Forest for land cover classification: *Pattern Recogn.Lett.*, 27, 294 – 300.
- Grunsky, E.C., 1986, Recognition of alteration in volcanic rocks using statistical analysis of lithochemical data: *J. Geochem. Explor.* 25, 157 - 183.
- Grunsky, E.C., 2010, The interpretation of geochemical survey data: *GEEA*, 10, 27 - 74.
- Goodfellow, I., Bengio, Y., and Courville, A., 2016, Deep learning, in Dietterich., ed., *Adaptive Computation and Machine Learning*: Massachusetts, MIT Press, 801p.
- Harris, D., and Pan, G., 1999, Mineral favorability mapping: A comparison of artificial neural networks, logistics regression, and discriminant analysis: *Nat. Resour. Res.*, 8, 93 – 109.
- Harris, J.R., 2002, Processing and integration of geochemical data for mineral exploration: application of statistics, geostatistics and GIS technology, PhD Thesis, University of Ottawa, 332 p.
- Hastie, E.C. G., 2017, Gold Metallogeny of the Southern Swayze Area, Abitibi greenstone belt: A Field Trip Guidebook: Ontario Geological Survey, Open File Report 6334, 1 – 19.
- Heather, K., 2001, The Geological Evolution of the Archean Swayze Greenstone Belt, Superior Province, Canada: Unpublished PhD thesis, Keele University, Keele, England. 370 p.

Katz, L.R., 2016, Geology of the Archean Côté Gold Au (Cu) Intrusion-Related Deposit, Swayze Greenstone Belt, Ontario. PhD thesis, Laurentian University, Sudbury, Canada, 328p.

Kingma, D.P., Lei Ba, J., 2015, Adam: A method for stochastic optimization. 1- 15.

Kreuzer, O.P., Buckingham, A., Mortimer, J., Walker, G., and Wilde, A., 2019, An integrated approach to the search for gold in a mature, data-rich brownfields environment: A case study for Sigma-Lamaque, Quebec: *Ore Geol. Rev.*, 111, 102977.

Kubat, M., 2017, An introduction to machine learning: Springer Sci. Rev. 348p.

Kuhn, M., and Johnson, K., 2013, Applied predictive modelling: New York, Springer, 600p.

Looney, C.G., 2002, Radial basis functional link nets and fuzzy reasoning: *Neurocomputing*, 48, 489–509.

McClenaghan, M.B., 1990, Summary of results from the Black-River-Matheson (BRiM) reconnaissance surface till sampling program: Ontario Geological Survey, Open File Report 5749, 1 – 255.

McClenaghan, B.M., 1991, Geochemistry of tills from the Black-River-Matheson (BRiM) sonic overburden drilling program and implications for exploration: Ontario Geological Survey, Open File Report 5800, 1 – 263.

McCuaig, T.C., Beresford, S., and Hronsky, J., 2010, Translating the mineral systems approach into an effective exploration targeting system: *Ore Geol. Rev.*, 38, 128 – 138.

McCuaig, T.C., and Hronsky, J.M.A., 2014, The mineral system concept: the key to exploration targeting., in Karen, D.K., Kelley, H.C.G., ed., *Building Exploration Capability for the 21<sup>st</sup> Century*, 18, 153–175.

McClenaghan, B.M., Lavin, O.P., Nichol, I., and Shaw, J., 1992, Geochemistry and clast lithology as an aid to till classification, Matheson, Ontario, Canada: J. Geoch. Explor., 42, 237 - 260.

McCulloch, W.S., and Pitts, W., 1943, A logical calculus of the ideas immanent in nervous activity: Bulletin of Mathematical Biophysics, 5, 115-133.

Maepa, F.M., and Smith, R.S., 2020, Examining the controls on gold deposit distributions in the Swayze greenstone belt, Ontario, Canada, using multi-scale methods of spatial data analysis: Ore Geol. Rev., 125, 103671  
Milne, V.G., 1972, Geology of the Kukatush-Sewell Lake Area: District of Sudbury: Ontario Divisions of Mines, Geological Report 97, 1 - 116.

Nair, V., and Hinton, G.E., 2010, Rectified linear unit improve restricted Boltzmann machines: Proceedings for the 27<sup>th</sup> International Conference on Machine Learning, p. 807 – 814.

<https://www.cs.toronto.edu/~fritz/absps/reluICML.pdf>. (Accessed 27 Nov 2019)

Nykänen, V., 2008, Radial basis functional link nets used as a prospectivity mapping tool for orogenic gold deposits within the central Lapland greenstone belt, Northern Fennoscandian shield: Nat. Resour.Res., 17, 29–48.

Nwankpa, C. E., Ijomah, W., Gachagan, A., and Marshall, S., 2018, Activation functions: comparison of trends in practice and research for deep learning, p. 1 - 20.

<https://arxiv.org/abs/1811.03378> (Accessed 27 Nov 2019).

Pan, S.J., Yang, Q., 2010, A survey of transfer learning: IEEE Transactions on Knowledge and Data Engineering, 22, 1345-1359

Pan, W., Liu, N., Xiang, E.W., and Yang, Q., 2011, Transfer learning to predict missing ratings

via heterogeneous user feedbacks: Proceedings of the Twenty-Second International Joint Conference on Artificial Intelligence, Hong Kong, 3, 2318 – 2323.

Pearson, K., 1901, On lines and planes of close fit to systems of points in space: *Philos. Mag. Lett.* 2, 559 -572.

Porwal, A., and Carranza, E.J.M., 2015, Introduction to the Special Issue: GIS-based mineral potential modelling and geological data analyses for mineral exploration: *Ore Geol. Rev.*, 71, 477–483.

Pratt, L.Y., 1993, Transferring previously learned back-propagation neural networks to new learning task: PhD thesis, New Brunswick, USA, Rutgers University, 163p.

Raschka, S., Mirjalili., V., 2017, Python Machine Learning: Birmingham, Packt Publishing Ltd, 622p,

Rodriguez-Guliano, V.F., Ghimier, B., Rogan, J., Chica-Olmo, M., and Rigol-Sanchez, J.P., 2012, An assessment of the effectiveness of a random forest classifier for land-cover classification.: *ISPRS J. Photogramm.*, 67, 93 – 104.

Rodriguez-Guliano, V.F., Chica-Olma, M., and Chica-Rivas, M., 2014, Predictive modelling of gold potential with the integration of multisource information based on random forest: a case study on the Rodalquilar area, Southern Spain: *Int. J. Geogr. Inf. Sci.*, 28, 1336 – 1354.

Rodriguez-Guliano, V.F., Sanchez-Castillo, M., Chica-Olmo, M., and Chica-Rivas, M., 2015, Machine learning predictive models for mineral prospectivity: An evaluation of neural networks, random forest, regression trees and support vector machines: *Ore Geol. Rev.* 71, 804 – 818.

Rosenblatt, F., 1958, The perceptron: A probabilistic model for information storage and organization in the brain: *Psychol. Rev.*, 65, 386-408

Ruder, S., 2016, An overview of gradient descent optimization algorithms, Insight Centre for Data Analytics, Dublin, Aylien Ltd, 1, 1 – 14. <https://arxiv.org/abs/1609.04747> [Accessed: 06/03/2021]

Sawatzky, D., Raines, G., and Bonham-Carter, G., 2010, Spatial Data Modeller (SDM): ArcMap 9.3 geoprocessing tools for spatial data modelling using weights of evidence, logistic regression, fuzzy logic, and neural networks.

<https://www.ige.unicamp.br/sdm/ArcSDM10/source/ReadMe.pdf>

Sarle, W.S., 1994, Neural networks and statistical models: Proceedings of the nineteenth annual SAS Users Group International Conference, Cary, USA, SAS Institute, 1538-1550.

[https://people.orie.cornell.edu/davidr/or474/nn\\_sas.pdf](https://people.orie.cornell.edu/davidr/or474/nn_sas.pdf) [Accessed: 06/03/2021]

Schodde, R., 2017., Long term trends in global exploration-Are we finding enough metals? In: 8th Fennoscandian Exploration and Mining Conference. Levi, Finland. 1–66.

Tan, C., Sun, F., Kong, T., Zhang, W., Yang, C., and Liu, C., 2018, A survey on deep transfer learning: State Key Laboratory of Intelligent Technology and Systems, 1-10.

<https://arxiv.org/abs/1808.01974> [Accessed: 06/03/2021]

Tessema, A., 2017, Mineral Systems Analysis and Artificial Neural Network Modeling of Chromite Prospectivity in the Western Limb of the Bushveld Complex, South Africa: *Nat. Resour. Res.* 26, 465–488.

Torrey, L., and Shavlik, J., 2009, Transfer learning. Handbook of Research and Machine Learning Application. In: Soria, E., Martin, J., Magdalena, R., Martinez, M., Serrano, A., ed.,

Handbook of Research on Machine Learning Applications: IGI Global, 1 – 22.

ISBN:1605667668 9781605667669

Vagners, U.J., 1984, Quaternary geology of the Matheson area, District of Cochrane; Ontario Geological Survey, Map P.2835: Geological Series-Preliminary Map. Scale 1:50 000, Geology 1983.

Weiss, K., Khoshgoftaar, T. M., and Wang, D, 2016, A survey of transfer learning: Journal of Big Data, 3, 1-40.

Zhu, Y., Chen, Y., Yu, Z., Pan, S.J., Xue, G., Yu, Y., and Yang, Q., 2011, Heterogeneous transfer learning for image classification: Proceedings of the Twenty-Fifth AAAI Conference of Artificial Intelligence, 1304 - 1309.

## Chapter 5: Concluding statements

### 5.1 Summary and conclusions

This thesis sought to apply various data science and machine learning techniques for mineral exploration targeting. The main study areas discussed in this thesis are the Swayze and Matheson regions found within the Abitibi greenstone belt.

The mineral deposits in the Swayze greenstone belt are believed to have formed by hydrothermal mineral systems which typically display strong spatial association with faults at various crustal scales. This study set out to quantify the mineralization controls and the scale at which deposits occur in the Swayze greenstone belt, as such knowledge will help to increase exploration targeting success. Using spatial analysis techniques at various scales, it was observed that gold deposits in the Swayze greenstone belt are bifractal at local  $< 8$  km and regional  $> 8$  km scales. This implies that at large crustal scales ( $> 8$  km) geological features responsible for distributing mineralization fluids were later “overtaken” by much smaller-scaled features ( $< 8$  km) which likely channeled fluids within the upper crust towards favorable depositional sites. This quantifies and validates the observations of many geologists that typically, orogenic mineral systems are controlled by second- to third-order faults in the Swayze greenstone belt.

At large crustal scales,  $> 8$  km, hydrothermal mineral systems are distributed by first-order fault systems such as the D<sub>2</sub> HSZ (i.e., Ridout, Slate Rock, Rundle and Swayze Lake HSZ), this is recognized from:

- i) The ESE-WNW, NE-SW (45 – 225 degrees), ENE-WSW (67.5 - 247.5 degrees), and NE-SW (45-225 degrees) gold deposit alignment of Fry analysis at regional scales which correlates well with the D<sub>2</sub> HSZ.

- ii) Distance distribution analysis results indicating that the relationship between gold deposits and D<sub>2</sub> HSZ is statistically significant with 65 – 97% of gold deposits found within 4 km – 7 km distances from D<sub>2</sub> HSZ.

At small scales, < 8 km, various geological features such as second and third order faults, fractures, competency contrast between lithologies, and brecciation in lithologies controlled gold deposits distributions from district to local scales, this indicated by:

- i) Gold deposits clustered at scales between 2 -4 km and dispersed at > 4 km scales.
- ii) Density analysis maps shows that gold deposits are clustered at regions with high densities of lower-order faults.
- iii) Gold deposits have statistically positive spatial correlations with second and third-order faults, with 96% of gold deposits found within 3 km distances from lower-order faults.
- iv) Local scale Fry analysis displays variability in spatial orientations of gold deposits such as N-S (000 - 180 degrees) and NE-SW (45 - 225 degrees) orientations in addition to ESE-WNW (112.5-292.5 degrees) and ENE-WSW (67.5 - 247.5 degrees) orientations observed at all scales.

Mineral prospectivity mapping studies for gold deposits in the Swayze greenstone belt using support vector machines and the radial basis function neural networks were helpful in defining regions that have the highest likelihood of hosting mineral deposits. The spatial statistical weights of evidence method helped to estimate the spatial associations between gold deposits and predictor maps. Following the mineral systems approach, the critical and constituent processes that define hydrothermal mineral systems were reviewed and mappable targeting parameters were defined.

The weights of evidence statistics (i.e., contrast and studentized contrast) show the spatial correlations between mineral deposits and the input predictor layers. These statistics indicate that certain rock units such as massive iron tholeiites, tuff breccias, Timiskaming-type clastic metasedimentary rocks, quartz-feldspar porphyry, granodiorite, and diorites have positive and statistically significant spatial correlations with gold. The best predictors of gold prospectivity however were the maps of distances from geologically mapped deformational zones and faults that have an ESE-WNW, ENE-WSW and NE-SW orientations observed from: i) Fry analysis; and ii) the map of distance mapped with magnetic and electromagnetic apparent decay constant maps. The optimum distances of positive spatial association (i.e., high contrast and studentized contrast) were found between gold and lithological contacts, magnetic worms, fault distance buffer, and electromagnetic distance buffers were 1.7 km, 2.5 km, 5 km, and 4.5 km, respectively. The electromagnetic decay constant map was used to map conductivity of near-surface features such as sulfides, iron formations, alteration and facies associated with hydrothermal fluid flow.

Other recognized predictor layers that were essential for gold prospectivity mapping include the calculated Spitz-Darling ( $K_2O+NaO/Al_2O_3$ ) alteration map derived from major oxide lithogeochemical data. The first three principal components accounted for 72% of the variance in the data, and helped to show enrichment of MgO, Fe<sub>2</sub>O<sub>3</sub>, MnO, and CaO which are associated with alteration and mineralization processes in the greenstone belt. The mineral prospectivity predictions created using radial basis function neural networks and support vector machines showed similarities in defining prospective regions. All the prospectivity maps generated showed prediction accuracies of > 80% according to the area under the receiver operator curves. The prospectivity analysis correlated with fractal analysis in showing that at regional scales, D<sub>2</sub> and D<sub>3</sub> high strain zones and folds were essential first order controls.

An additional study for modelling gold prospectivity mapping was done using more robust machine learning methods, such as deep neural networks and random forest. Deep neural networks are becoming increasingly popular in the fields of artificial intelligence and data science. Deep learning models are considered as highly accurate machine learning methods today; however, there are limited numbers of deep neural networks applications for mineral exploration targeting. This study examined the use deep neural networks for mineral prospectivity mapping while simultaneously comparing deep neural network model performances with random forest classification method.

The random-forest algorithm is a recommended modelling tool for use in mineral exploration targeting because it is less likely to overfit during training and can generate a feature importance table showing the predictor variables that were crucial for making data classification and predictions. Furthermore, by also using the variance-based feature importance estimator to monitor the variances of computed weights during training of deep neural networks, feature importance estimations can be derived from the deep neural networks. In the case of the Swayze greenstone belt, the important features for both random forests and deep neural networks were faults and magnetic and electromagnetic anomaly buffer maps.

The deep neural networks and random forest prospectivity maps generated over the Swayze greenstone belt are highly comparable. The prediction accuracies of deep-neural-networks and random-forest models are 86 and 82% suggesting slightly better performance by deep learning.

One of the drawbacks of using machine learning for exploration targeting is that there needs to be sufficient training data to generate mineral prospectivity maps. This thesis tackled a new subset of artificial intelligence called transfer learning, which allows data scientists to use the knowledge acquired from pre-trained models in making predictions on new but related tasks. Deep

transfer learning was applied in this study by first training a deep neural network model on the southern Swayze greenstone belt and using the learnt weights and parameters to predict the occurrence of gold deposits in the northern Swayze greenstone belt without prior knowledge of distributions of gold deposits in the north. The pre-trained model was able to predict at least 74% of unseen gold deposits in the northern Swayze greenstone belt. Assuming that the northern and southern Swayze greenstone belt are geologically similar, then comparable prediction capabilities in another area also similar to the Swayze greenstone belt can be expected.

A model trained using data from the entire Swayze greenstone belt was transferred to similar predictor layers from the Matheson region, the model was able to predict 77% of gold deposits in the Matheson region without prior knowledge of the location of these mineral deposits. Using a variance-based feature importance algorithm, a ranking of the features used by the model to understand gold prospectivity was derived and the results indicate that deep neural networks considered faulting, distances from high magnetic intensities, and lithological contacts to be the best predictors of gold prospectivity in the Swayze and Matheson region. . The predictor variables used for transfer learning from the Swayze greenstone belt to the Matheson region are from data sets that are representative of data normally found at the early stages of mineral exploration, there was no whole rock geochemical data or high-resolution geophysical data to use for training and predicting prospectivity between the source and target domains.

## 5.2 Implications for mineral exploration

The thesis research has highlighted the importance of a scale-integrated evaluation of geological controls in a hydrothermal mineral system. Viewing mineral deposits as expressions of large mineral systems and determining variations in spatial associations of deposits with distance

from geological features can help field geologists to vector their exploration projects to lie along or close to the highly prospective areas, such as the D<sub>2</sub> HSZ in the Swayze (and hence Matheson region).

The weights statistics from the weights of evidence, the feature-importance information derived from random forest and the variance-based feature importance estimations from deep neural networks also have positive implications for exploration targeting. Exploration geoscientists can determine spatial correlations between deposits and predictor variables as well as identify the predictor variables that are recommended as important by artificial intelligence tools such as deep neural networks. The variance-based feature-importance algorithm shifts deep learning models from “black box” approaches to machine learning methods that can communicate the parameters used to make final decisions.

This study demonstrated that deep transfer learning is possible for regional scale exploration in orogenic greenstone belts. For exploration purposes, transfer learning will allow geoscientists to generate machine learning models and predict for new targets in under-explored geological environments. The knowledge obtained from well explored and data rich environments can be harvested and used to help guide future exploration studies in academia and industry.

Feature-importance estimation is significant because it can be used to guide the acquisition of the next data set in an exploration program. For example, if a brownfield environment with significant geological, geochemical, and geophysical information exists, a “data science exploration model” can be generated using data from the brownfield area and the feature importance estimations obtained from the trained model can assist geoscientists in establishing the most cost-effective way to acquire data in geologically similar but relatively greenfield areas where there is little or no training data available. Lower cost and high-resolution data with uniform spatial

coverage such as aeromagnetic data may be used to map regional to district scale faults zones and fluid pathways in orogenic ore systems.

Furthermore, using the feature importance estimations as a guide, the next most important data set to focus the exploration along that fault might be electromagnetics or geochemistry. If the electromagnetics is significantly cheaper then it may be more cost effective to collect this prior to the geochemical data. When the geochemistry is collected, then this would mean putting a crew onto the ground for more district to local scale surveys around prospective regions. The next most important data could be collected, for example, magnetic susceptibility, detailed structural geological mapping and eventually drilling. This reliance of the feature importance of the data allows the decision-making process to be driven in a cost-effective way by the data already collected in a “data science exploration model” area.

### 5.3 Applications of the thesis workflow in greenfield exploration programs and suggestions for future work

Applications of the workflows presented in this thesis from an academic to a greenfield exploration setting is possible. Benefits would also accrue in brownfield environments, as these areas can have decades of legacy and proprietary data that is hardly utilized. Industry application of the workflow would involve: i) digitizing legacy and proprietary data available in brownfield exploration sites; ii) using data science methods to derive data correlations between the historical data and all the mine workings and iii) training machine learning methods to not only understand and derive correlations between deposits and mineralization signatures, but to communicate the correlation in a way that can help in future exploration for similar mineral systems.

The transfer learning workflow can be especially helpful for data acquisition in greenfield exploration environments. Pre-trained models trained on more mature exploration environments can give an estimate of the required data resolution for targeting specific mineral deposit signatures. For example, if a brownfield site requires only a 200-meter line spacing aeromagnetic survey to detect magnetic and conductive bodies associated with magmatic-hydrothermal mineral systems, a geophysical survey in new greenfield exploration sites can use the knowledge gained from transfer learning and collect data at the targeting resolution, this saving time and money.

A study such as this requires multi-disciplinary teams consisting of domain experts in the mineral deposit type being sought and an understanding of the associated mineralization signatures at regional to district and local scales. A team consisting of ore-deposit geologists, geochemists and exploration geophysicists as well as data scientists capable of translating legacy geoscience data into data inputs for machine learning is essential. Exploration geologists and geophysicists can then later determine if the output predictions correlate with expert understanding of deposit models and if the new predictions make geological sense.

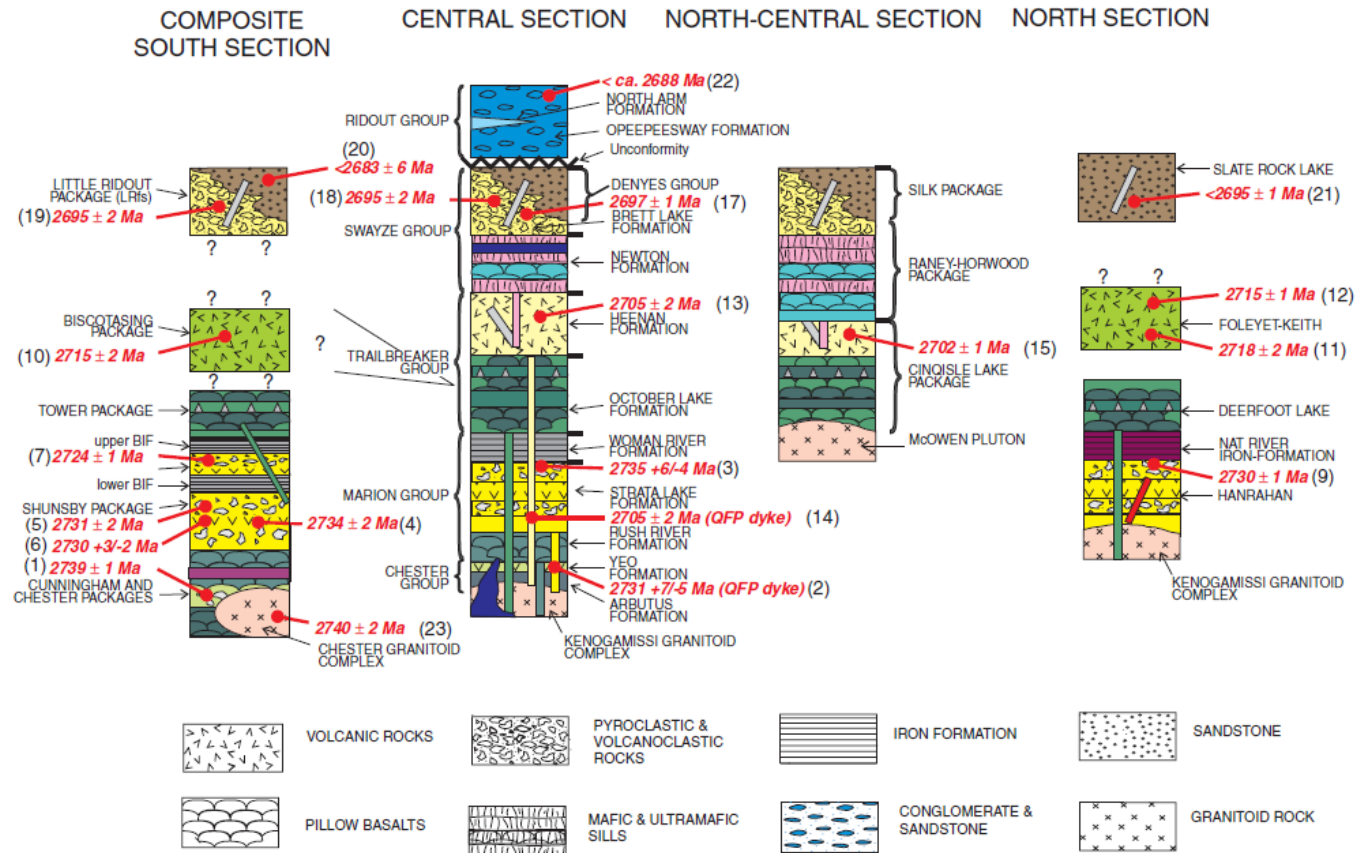
Machine learning approaches are a tool and are vastly dependent on data availability and the data quality. The quality of the geological data collected in an area are the drivers for how well a predictive model will perform. Supervised machine learning methods require that prior knowledge be available in order to make posterior predictions and hence, better data coupled with machine learning can help reform exploration in greenfield and brownfield exploration sites. If models are trained well enough, they should not only be able to rediscover what is already known and do well on new testing sites but they should also be able to communicate new targets that can be investigated further with more data acquisition and subsequent drilling.

Quality assurance and quality control in predictive modelling is needed especially for greenfield to semi-greenfield exploration sites. One critical example, is the classification of deposit types that will be used as the labeled data for training machine learning methods. A lot of the mineral deposit index data is obtained from governmental geological surveys where regional scale geological mapping, sampling and drilling has taken place over many years, during which the names an understanding of deposit types has changed.

As well, the nature of mineral deposits and the ambiguity that exists between mineral deposit types, means that it can be easy to mistake one mineral deposit type for another, especially if they occur in similar tectonic and geological environments. Usually, detailed analysis of mineral deposit types is done at the deposit scale by evaluating the geochemical properties such as fluid inclusions and isotopic data, reviewing structural correlations and geochronology. In areas like the Swayze, the 150 prospects and occurrences of gold have not been studied in detail and hence, care is needed when using information in the mineral deposit index data for mineral prospectivity mapping for mineral deposits and specific mineral-deposit types. This means that a critical assessment of the quality of the information in the mineral deposit index, can significantly improve the quality of any prospectivity mapping exercise that uses this information.

# Appendices

Appendix A: A schematic stratigraphic section for the Swayze greenstone belt obtained from Breemen et al., 2006. The stratigraphic section was derived after Heather (2001) showing the U-Pb zircon ages for the northern, southern and central regions of the Swayze greenstone belt.



Appendix B: A detailed description of the mineral deposit index files from the OGS 2019 file showing each prospect used in the Swayze greenstone belt study data.

Name	Class	Deposit type	Alteration type	Host lithology	Ore min	Gaugue min	Structural ass. Or type	Tectonic Ass.	Geological Age	Geoch Age	Metamorphic grade	Comments	Details (OGS reference)
Woman River-Mallard	Mineral Occurrence	Mesothermal	Sericitization (medium intensity)	brecciated porphyry dyke (host)	Gold	Pyrite, chalcopyrite, tourmaline	Highly sheared	Marion Group	Neoproterozoic	2716 Ma	Regional greenschist	Gold mineralization is associated with quartz-carbonate veins lying within or adjacent to altered and sheared porphyry dikes. Small quantities of sulphides, pyrite and to a lesser extent chalcopyrite, have been reported at some locations. Tourmaline and chlorite occur in fracture surfaces within quartz-carbonate veins.	<a href="http://www.geologyontario.mndm.gov.on.ca/mndmfiles/mdi/data/records/MDI41009NW00006.html">http://www.geologyontario.mndm.gov.on.ca/mndmfiles/mdi/data/records/MDI41009NW00006.html</a>
Mcvittie	Mineral Occurrence	Mesothermal	Metasomatic alteration	quartz vein and intermediate diorite intrusive rock	Gold	pyrite	Diorite is sheared	Horwood Group	Neoproterozoic	2700 Ma	Regional greenschist	Assay by Orofino Mines values from drillhole occurrences gave gold grades of 0.7g/t Au. Mineralization hosted in slightly sheared portion of dioritic rock	<a href="http://www.geologyontario.mndm.gov.on.ca/mndmfiles/mdi/data/records/MDI41016NW00017.html">http://www.geologyontario.mndm.gov.on.ca/mndmfiles/mdi/data/records/MDI41016NW00017.html</a>
Hermiston-Hammerstrom	Mineral Occurrence	Mesothermal	sericite alteration	schist, quartz veins	Gold	pyrite, chalcopyrite	Mineralized shear zone	Marion Group	Neoproterozoic	2716 Ma	Regional greenschist	Mineralization occurs over 4.6m with lenses of quartz and considerable amounts of pyrite. Samples in schist have 0.21 and 0.28 oz/t Au. Grab samples show 0.38 g/t Au and 0.38 g/t Au from shear mafic metavolcanics. Highest grade found at area is 9.6 g/t Au	<a href="http://www.geologyontario.mndm.gov.on.ca/mndmfiles/mdi/data/records/MDI41009NW00007.html">http://www.geologyontario.mndm.gov.on.ca/mndmfiles/mdi/data/records/MDI41009NW00007.html</a>
Berlr-Pez	Mineral Occurrence	Mesothermal	N/A	Quartz-feldspar brecciated porphyry and near a sheared basalt and mylonite/fault Hosted in quartz veins, and intermediate metavolcanic rock. Near a BIF, Diorite.	Gold	Pyrite	Breccia	Marion Group	Neoproterozoic	2705 Ma	Regional greenschist	Unit contains anomalous gold values and is described as quartz-feldspar porphyry. Porphyry is silicified and brecciated with gradational silicification contacts with 9.8 g/t Au. Most gold is found within the brecciated contact of a felsic volcanic and feldspar porphyry.	<a href="http://www.geologyontario.mndm.gov.on.ca/mndmfiles/mdi/data/records/MDI41009NW00018.html">http://www.geologyontario.mndm.gov.on.ca/mndmfiles/mdi/data/records/MDI41009NW00018.html</a>
Orofino	Developed Mineral Prospect with Reserves	Mesothermal	medium carbonatization and chlorite (medium chloritic) alteration	schist, stockwork veins, basalt, feldspar porphyry	Gold, Cu, PB, Zn	Pyrite, chalcopyrite, galena, sphalerite,	Fold, Gold bearing structures within altered diorite.	Horwood Group	Neoproterozoic	2700 Ma	Regional greenschist	Deposit in the nose of regional fold anticline that plunges steeply to the west. At mine scales gold bearing zones are correlated SE striking and shallow dipping structures, and structures that are E striking and dip to the north. Numerous veins with intense shearing	<a href="http://www.geologyontario.mndm.gov.on.ca/mndmfiles/mdi/data/records/MDI41016NW00020.html">http://www.geologyontario.mndm.gov.on.ca/mndmfiles/mdi/data/records/MDI41016NW00020.html</a>
Rundle Mine	Developed Mineral Prospect with Reserves	Mesothermal	carbonatization, pyritic, sericitization, hematization, chloritic	schist, stockwork veins, basalt, feldspar porphyry	Gold	pyrite, chalcopyrite, hematite, magnetite,		Horwood Group	Neoproterozoic	2700 Ma	Regional greenschist	Gold values in the Shaft Zones occur together with quartz-carbonate altered or silicified host rock, or with quartz veinlets. Gold is also associated with 1% to 2% fine grained specular hematite in altered, potassic, silicified feldspar porphyry.	<a href="http://www.geologyontario.mndm.gov.on.ca/mndmfiles/mdi/data/records/MDI41016SW00003.html">http://www.geologyontario.mndm.gov.on.ca/mndmfiles/mdi/data/records/MDI41016SW00003.html</a>
Walker	Discretionary Mineral Occurrence	Possibly porphyry-type	strong chloritic and tourmalinization alteration	quartz-feldspar porphyry, cataclastic, quartz-tourmaline	Gold, Copper	Pyrite, hematite, tourmaline	Dominant fabric is SE trending shear zones	Chester intrusive complex	Neoproterozoic	2740	Regional greenschist	The mineralization is associated with a series of en-echelon 'Black Line' faults and associated shears. The whole collective mineralized zone is about 10m wide but individual zones are less than a meter thick. Adjacent to the shear zones, splay faults and some of the 'Black Line' faults, fine pyrite is disseminated.	<a href="http://www.geologyontario.mndm.gov.on.ca/mndmfiles/mdi/data/records/MDI41P12SW00082.html">http://www.geologyontario.mndm.gov.on.ca/mndmfiles/mdi/data/records/MDI41P12SW00082.html</a>
Crown Minerals Quartz Showing	Discretionary Mineral Occurrence	Possibly porphyry-type	granite containing quartz-pyrite vein	chlorite, epidote, pyrite alteration	Gold	Chalcopyrite, pyrite		Chester intrusive complex	Neoproterozoic	2740 +/- 2 Ma	Regional greenschist	The host rock is a medium-grained, leuco granite typical of the Chester Granitoid Complex. Alteration associated with the faults/shear zones consists of recrystallization and silicification together with some chloritic and pyritic alteration.	<a href="http://www.geologyontario.mndm.gov.on.ca/mndmfiles/mdi/data/records/MDI000000001603.html">http://www.geologyontario.mndm.gov.on.ca/mndmfiles/mdi/data/records/MDI000000001603.html</a>
Burton N-E Zone	Mineral Occurrence	Mesothermal	strong silicification	quartz-vein, gabbro and adjacent a basalt	Gold	arsenopyrite, pyrite	Shear	Halcrow-Swayze	Neoproterozoic	N/A	Regional greenschist	Mineralization occurs as disseminated sulphides in the shear zone and within attenuated quartz veins hosted within the shear zones and orientated parallel to the zones.	<a href="http://www.geologyontario.mndm.gov.on.ca/mndmfiles/mdi/data/records/MDI41009NW00038.html">http://www.geologyontario.mndm.gov.on.ca/mndmfiles/mdi/data/records/MDI41009NW00038.html</a>
Burton Property	Prospect	Mesothermal	iron carbonate alteration	gabbro and near basalt, argillite, adjacent quartz and shear	Gold, Arsenopyrite, chalcopyrite	pyrite, pyrrhotite	Shear	Halcrow-Swayze	Neoproterozoic	N/A	Regional greenschist	Mineralization is confined to a narrow zone near the upper margin of a folded gabbro where arsenopyrite and pyrite are disseminated in high concentrations. This mineralization occurs within a strongly carbonatized and sheared phase of the gabbro and is associated with a number of small quartz veins which parallel the stratigraphy	<a href="http://www.geologyontario.mndm.gov.on.ca/mndmfiles/mdi/data/records/MDI41009NW00023.html">http://www.geologyontario.mndm.gov.on.ca/mndmfiles/mdi/data/records/MDI41009NW00023.html</a>
Jerome Mine	Past Producing Mine with Reserves	possibly intrusion-related gold deposit	biotite, hematite, chlorite, carbonatization, silicification, sericitization	quartz-feldspar porphyry and vein, near arenite	chalcopyrite, molybdenite, tetrahedrite, sphalerite, gold	arsenopyrite, pyrrhotite pyrite	Mineralization is near contacts, shear zones and breccia	Ridout Group	Neoproterozoic	2724 Ma	Regional greenschist	The mineralization is located on the south contact of the 'Jerome Porphyry' and epiclastic 'Timiskaming Type' sediments. Due to alteration the contact between the intrusive and sedimentary rocks is gradational.	<a href="http://www.geologyontario.mndm.gov.on.ca/mndmfiles/mdi/data/records/MDI41009SE00005.html">http://www.geologyontario.mndm.gov.on.ca/mndmfiles/mdi/data/records/MDI41009SE00005.html</a>
Woman River Gold Syndicate Showing	Prospect	Mesothermal	sericitization	brecciated quartz-feldspar and near mafic volcanics and shear zone	Gold	chalcopyrite, tourmaline	Shear zones with vertical dip	Marion Group	Neoproterozoic	2716 Ma	Regional greenschist	The principal host for the gold mineralization are sheared porphyry dikes. These dikes are exhibit various degrees of silicification, carbonatization, sericitization and pyrite alteration and contain, or are adjacent to, quartz-carbonate gold bearing veins. Tourmaline and chlorite are reported to occur on fracture surfaces within quartz-carbonate veins.	<a href="http://www.geologyontario.mndm.gov.on.ca/mndmfiles/mdi/data/records/MDI000000001503.html">http://www.geologyontario.mndm.gov.on.ca/mndmfiles/mdi/data/records/MDI000000001503.html</a>

Cryderman Pit	Mineral Occurrence	Possibly porphyry-type	carbonatization, serpentinization alteration	quartz vein and near a diorite	Gold, silver	Pyrite, chalcopyrite, tourmaline		Ridout Group	Neoproterozoic	2739 +/- Ma	Regional greenschist	The mineralized and altered shear zones are close to and sub-parallel to the irregular contact between highly schistose sediments and the more massive diorite. These shears are up to 4m thick, of variable intensity and alteration, and occur discontinuously along the stripped area. The shear appears to parallel the axial plane of large-scale folds.	<a href="http://www.geologyontario.mndm.gov.on.ca/mndmfiles/mdi/data/records/MDI41P12SW00138.html">http://www.geologyontario.mndm.gov.on.ca/mndmfiles/mdi/data/records/MDI41P12SW00138.html</a>
C.T. Young	Mineral Occurrence	Possibly porphyry-type	sericite, pyritic alteration	Sheared mafic metavolcanic, near granitic porphyry	Gold	pyrite, chalcopyrite, stibnite, arsenopyrite,	shear and contact	Ridout Group	Neoproterozoic	< 2690 Ma	Regional greenschist	The mineralization is located in a carbonatized shear zone up to 2m thick which is parallel to the granite contact.	<a href="http://www.geologyontario.mndm.gov.on.ca/mndmfiles/mdi/data/records/MDI41P12SW00047.html">http://www.geologyontario.mndm.gov.on.ca/mndmfiles/mdi/data/records/MDI41P12SW00047.html</a>
Crown Minerals Area A	Mineral Occurrence	Possibly porphyry-type	chloritic, epidote (saussurization), pyritic alteration	hosted in granite and contains quartz-pyrite vein	Gold	chalcopyrite, pyrite,	N/A	Chester intrusive complex	Neoproterozoic	2740 Ma	Regional greenschist	The host rock is a medium-grained, leuco granite typical of the Chester Granitoid Complex. Alteration associated with the faults/shear zones consists of recrystallization and silicification together with some chloritic and pyritic alteration	<a href="http://www.geologyontario.mndm.gov.on.ca/mndmfiles/mdi/data/records/MDI00000001602.html">http://www.geologyontario.mndm.gov.on.ca/mndmfiles/mdi/data/records/MDI00000001602.html</a>
Quinterra Vein Zone	Mineral Occurrence	Mesothermal	chloritic, carbonatization, pyritic sericitization alteration	quartz vein	Gold	pyrite, tourmaline	Vein ass.	Garnet-tooms?	Neoproterozoic	2730 +/- 3 Ma	Regional greenschist	The intense carbonate alteration is largely restricted to a zone bounded by highly schistose shear zones. The mineralization is hosted in a number of green carbonate horizons within a mafic and ultramafic volcanic sequence. Within these zones, there is locally a well-developed quartz vein stockwork. Individual veins are up to 0.5 m wide. Assays up to 5 g/t Au were obtained from highly carbonatized volcanics, but the average grade was 0.3 g/t Au.	<a href="http://www.geologyontario.mndm.gov.on.ca/mndmfiles/mdi/data/records/MDI41O10NW00042.html">http://www.geologyontario.mndm.gov.on.ca/mndmfiles/mdi/data/records/MDI41O10NW00042.html</a>
Quinterra	Mineral Occurrence	Mesothermal	carbonatization, chloritic, pyritic alteration	carbonatized mafic metavolcanic, ironstone, cataclastic carbonate rock, quartz-carbonate vein	Gold	pyrite, tourmaline, fuschite	Shear, Ridout HSZ	Garnet-tooms?	Neoproterozoic	2730 +/- 3 Ma	Regional greenschist	The best mineralization occurs in quartz/carbonate veins associated with highly carbonatized mafic volcanics. These veins which are typically 2cm thick but up to 7cm, and up to several metres long.	<a href="http://www.geologyontario.mndm.gov.on.ca/mndmfiles/mdi/data/records/MDI41O10NW00013.html">http://www.geologyontario.mndm.gov.on.ca/mndmfiles/mdi/data/records/MDI41O10NW00013.html</a>
Chester 2 Zone	Developed Mineral Prospect with Reserves	Possibly porphyry-type	chloritic, biotitic, carbonatization, pyritic, malachite (supergene) and azurite (supergene) alterations	granodiorite, quartz-chlorite, diorite	chalcop yrite, molybd enite, gold, tellurid e, bornite, covellit e	Pyrrhotite, pyrite, arsenopyrite, sphalerite, tourmaline	shear, breccia	Chester intrusive complex	Neoproterozoic	2740 Ma	Regional greenschist	The mineralization is hosted within a northeast trending shear zone. Within this shear there are a complex set of quartz sulphide veins - veinlets which have reportedly been deformed. The sulphide veins and quartz-sulphide veins also contain rounded fragments (milled) of quartz set in a fine to medium grained matrix	<a href="http://www.geologyontario.mndm.gov.on.ca/mndmfiles/mdi/data/records/MDI41P12SW00049.html">http://www.geologyontario.mndm.gov.on.ca/mndmfiles/mdi/data/records/MDI41P12SW00049.html</a>
Strathy Basin	Developed Mineral Prospect Without Reserves	Possibly porphyry-type	chloritic alteration	quartz vein, chlorite schist, quartz diorite, granodiorite	chalcop yrite, gold	pyrite, pyrrhotite	shear	Chester intrusive complex	Neoproterozoic	2740 Ma	Regional greenschist	The mineralization is located in an altered shear zone that cuts quartz dioritic and granodioritic rocks of the Chester Granitoid Complex.	<a href="http://www.geologyontario.mndm.gov.on.ca/mndmfiles/mdi/data/records/MDI41P12SW00007.html">http://www.geologyontario.mndm.gov.on.ca/mndmfiles/mdi/data/records/MDI41P12SW00007.html</a>
Sheppard #5 & #6	Developed Mineral Prospect Without Reserves	Possibly porphyry-type	chloritic, malachine supergene alteration	diorite, tonalite, quartz-vein	Gold, chalcop yrite	pyrite, galena, hematite, magnetite, pyrrhotite, sphalerite, tourmaline	vein ass. And shear	Chester intrusive complex	Neoproterozoic	2740 Ma	Regional greenschist	The mineralization is hosted in a leucocratic tonalite with roughly equal amounts of quartz and plagioclase. Biotite is the main mafic mineral with minor amounts of clinopyroxene. Magnetite and chlorite occur in minor amounts as an in-situ alteration product of biotite. Chlorite also occurs as fracture and vein fillings. Sericite alteration of the plagioclase is much more widespread.	<a href="http://www.geologyontario.mndm.gov.on.ca/mndmfiles/mdi/data/records/MDI41P12SW00142.html">http://www.geologyontario.mndm.gov.on.ca/mndmfiles/mdi/data/records/MDI41P12SW00142.html</a>
Gogama Resources Area 1	Mineral Occurrence	Possibly porphyry-type	sericite alteration	granodiorite, quartz-vein	Gold	pyrite, hematite, geothite, jarosite	shear	Chester intrusive complex	Neoproterozoic	2740 Ma	Regional greenschist	The host rock is within a granodiorite that is cut by a small shear zone. Alteration in the shear zone consists of sericite. The mineralization occurs in a 3 cm wide quartz vein within the shear zone	<a href="http://www.geologyontario.mndm.gov.on.ca/mndmfiles/mdi/data/records/MDI41P12SW00135.html">http://www.geologyontario.mndm.gov.on.ca/mndmfiles/mdi/data/records/MDI41P12SW00135.html</a>
Coniston DH-1	Mineral Occurrence	Possibly porphyry-type	N/A	granodiorite	Gold, chalcop yrite, copper	pyrite	shear	Chester intrusive complex	Neoproterozoic	2740 Ma	Regional greenschist	Disseminated pyrite with lessor chalcopyrite occur in the host granodiorite where it is sheared and some sulphides are also associated with quartz veining. Minor amounts of native copper have been reported in the drill logs. Emerald Isle Resources Inc drilled holes in the area. Hole 91-2 returned an assay of 0.016 oz/t over 5.1 ft.	<a href="http://www.geologyontario.mndm.gov.on.ca/mndmfiles/mdi/data/records/MDI41P12SW00077.html">http://www.geologyontario.mndm.gov.on.ca/mndmfiles/mdi/data/records/MDI41P12SW00077.html</a>
Sheppard #1 & #2	Mineral Occurrence	Possibly porphyry-type	chloritic alteration	quartz-vein, diorite and tonalite	pyrite, chalcop yrite, covellit e, gold, tellurid e	magnetite, sphalerite, arsenopyrite, tourmaline	shear	Chester intrusive complex	Neoproterozoic	2740 Ma	Regional greenschist	The mineralization is hosted in a leucocratic tonalite with roughly equal amounts of quartz and plagioclase. Biotite is the main mafic mineral with minor amounts of clinopyroxene. Magnetite and chlorite occur in minor amounts as an in-situ alteration product of biotite. Chlorite also occurs as fracture and vein fillings. s.	<a href="http://www.geologyontario.mndm.gov.on.ca/mndmfiles/mdi/data/records/MDI41P12SW00053.html">http://www.geologyontario.mndm.gov.on.ca/mndmfiles/mdi/data/records/MDI41P12SW00053.html</a>
Beaverbridge DDH 67R9	Mineral Occurrence	Possibly porphyry-type	chloritic, pyritic alteration	granodiorite, quartz diorite	chalcop yrite, gold	pyrite, pyrrhotite	shear	Chester intrusive complex	Neoproterozoic	2740 Ma	Regional greenschist	The mineralization occurs in a number of repetitive zones, is centered on a series of closely spaced sheared/fractured zones and consists of disseminated pyrite, pyrrhotite, and chalcopyrite in the granodiorite matrix	<a href="http://www.geologyontario.mndm.gov.on.ca/mndmfiles/mdi/data/records/MDI000000001631.html">http://www.geologyontario.mndm.gov.on.ca/mndmfiles/mdi/data/records/MDI000000001631.html</a>

Cryderma N	Prospect	Possibly porphyry-type	N/A	Quartz-vein, quartz- diorite, brecciated mafic dyke, granodiorite	gold	pyrite, pyrrhotite, chalcopyrite, galena, sphalerite	shear	Chester intrusive complex	Neoproterozoic	2740 Ma	Regional greenschist	The host rock is a massive, coarse grained granodiorite with some quartz diorite phases which have the characteristic blue quartz of the Chester Granitoid Complex and hornblende forms up to 10% of the rock with some disseminated magnetite.	<a href="http://www.geologyontario.mndm.gov.on.ca/mndmfiles/mdi/data/records/MDI41P12SW00054.html">http://www.geologyontario.mndm.gov.on.ca/mndmfiles/mdi/data/records/MDI41P12SW00054.html</a>
P. E. Hopkins	Mineral Occurrence	Possibly porphyry-type	chloritic, sassuritization, pyritic	quartz-pyrite vein, granite	gold	pyrite, chalcopyrite	Fault	Chester intrusive complex	Neoproterozoic	2740 +/- 2 Ma	Regional greenschist	The host rock is a medium-grained, leuco granite typical of the Chester Granitoid Complex. Alteration associated with the faults/shear zones consists of recrystallization and silicification together with some disseminated chloritic and pyritic alteration. Epidote alteration is weak, but pervasive throughout the host granite.	<a href="http://www.geologyontario.mndm.gov.on.ca/mndmfiles/mdi/data/records/MDI41P12SW00141.html">http://www.geologyontario.mndm.gov.on.ca/mndmfiles/mdi/data/records/MDI41P12SW00141.html</a>
Kalbrook	Mineral Occurrence	Mesothermal	chloritic, sericite/potassic, biotitic alteration	quartz vein, cataclastic schist, and near dacite, arenite	Gold, chalcopyrite	pyrite	shear, fold	Muskego-reeves	Neoproterozoic	N/A	Regional greenschist	The general structural setting is that there are a number of parallel bands of intense shearing separated by zones with little or no shearing. The mineralization is hosted in strongly altered schists. The best assays obtained by the OGS from chip sampling of quartz veins were 7.68 g/t Au, 7.5 g/t Au, and 5.17 g/t Au. Diamond drilling by American Barrick returned assays up to 0.31 g/t Au over 1 m	<a href="http://www.geologyontario.mndm.gov.on.ca/mndmfiles/mdi/data/records/MDI42B01NE00010.html">http://www.geologyontario.mndm.gov.on.ca/mndmfiles/mdi/data/records/MDI42B01NE00010.html</a>
Bi-Ore	Mineral Occurrence	Mesothermal	Carbonate alteration	sheared mafic metavolcanic, quartz vein	Gold	pyrite, arsenopyrite	shear	Ridout Group	Neoproterozoic	2724+/-4 Ma	Regional greenschist	Mineralized zone is comprised of a highly sheared and carbonatized rock containing irregular patches and lenses of quartz. Between the masses of silicified rock occur zones of rusty weathered schist.	<a href="http://www.geologyontario.mndm.gov.on.ca/mndmfiles/mdi/data/records/MDI41O09SE00004.html">http://www.geologyontario.mndm.gov.on.ca/mndmfiles/mdi/data/records/MDI41O09SE00004.html</a>
Cyril Knight Occurrence	Mineral Occurrence	Mesothermal	chloritic alteration	quartz vein, schist near pegmatite	Gold	pyrite	shear	Horwood Group	Neoproterozoic	2700 Ma	Regional greenschist	The quartz vein system has a banded appearance or consists of a set of thin parallel quartz veins. Low concentrations of very fine-grained pyrite are disseminated in the quartz veins.	<a href="http://www.geologyontario.mndm.gov.on.ca/mndmfiles/mdi/data/records/MDI41O15SE00030.html">http://www.geologyontario.mndm.gov.on.ca/mndmfiles/mdi/data/records/MDI41O15SE00030.html</a>
Aguara Exploration Occurrence	Mineral Occurrence	Mesothermal	sassuritization, chloritic, hematization	quartz vein, felsic intrusive	Gold	pyrite	shear	Horwood Group	Neoproterozoic	2700 Ma	Regional greenschist	The mineralization is hosted in a massive, coarse grained mafic flow within a sequence of mafic massive flows, pillowed flows, and tuffs. The pillowed flows which are strongly deformed, occur intercalated with mafic and some felsic tuffs in the northern part of the stripped outcrops.	<a href="http://www.geologyontario.mndm.gov.on.ca/mndmfiles/mdi/data/records/MDI41O15SE00002.html">http://www.geologyontario.mndm.gov.on.ca/mndmfiles/mdi/data/records/MDI41O15SE00002.html</a>
Joburke	Past Producing Mine Without Reserves	Mesothermal	chloritic alteration	quartz vein, basalt near argillite, andesite	Pyrite, gold	chalcopyrite	Joburke Deformational zone (local), MacKeith fault (regional), shear, fold drag	Muskego-reeves	Neoproterozoic	N/A	Regional greenschist	Structural controls on the mineralization are dominant. Other than the mineralization being concentrated in two parallel deformation zones trending east - west, an oblique crenulation cleavage striking northeast also appears to be important, together with later generations of quartz veining in 'S' folds and extension quartz veins orientated north - south. In the southern deformation zone are the two main mineralized pods both of which plunge to the west.	<a href="http://www.geologyontario.mndm.gov.on.ca/mndmfiles/mdi/data/records/MDI42B01NW00002.html">http://www.geologyontario.mndm.gov.on.ca/mndmfiles/mdi/data/records/MDI42B01NW00002.html</a>
Sangold	Prospect	Mesothermal	carbonatization, silicification, potassic, chloritic alteration	carbonatined mafic metavolcanic, quartz-carbonate vein	pyrite, chalcopyrite	sphalerite, galena, tourmaline	Vein ass., shears	Muskego-reeves	Neoproterozoic	N/A	Regional greenschist	Mineralization occurs in a south-southeast-trending shear zone within carbonatized mafic metavolcanic rocks cut by abundant intermediate porphyry dikes. The mineralized zone consists of quartz-carbonate veining with disseminated pyrite and rarely chalcopyrite and galena. Erratic gold values as high as 0.528 oz/t over 1.2 m occur over narrow lenses of pyritic quartz-carbonate vein, separated by non-auriferous less-altered rock. The structure consists of a series of anastomosing veins and altered shears subparallel to the regional foliation. Gold tends to be concentrated in the noses of the folded vein stockworks.	<a href="http://www.geologyontario.mndm.gov.on.ca/mndmfiles/mdi/data/records/MDI42B01NE00012.html">http://www.geologyontario.mndm.gov.on.ca/mndmfiles/mdi/data/records/MDI42B01NE00012.html</a>
North Jehann	Mineral Occurrence	Mesothermal	calcite, chlorite, biotite alteration	quartz veins near tholeiitic mafic metavolcanic	gold, arsenopyrite	pyrite, pyrrhotite	Shear	Muskego-reeves	Neoproterozoic	N/A	Regional greenschist	The mineralization consists of fracture-filling quartz veins up to 1 inch wide carrying arsenopyrite and with arsenopyrite disseminated in the adjacent amphibolite. Grab samples taken by the OGS in 1992 returned values of 0.72 g/t Au from a quartz vein.	<a href="http://www.geologyontario.mndm.gov.on.ca/mndmfiles/mdi/data/records/MDI42B01NE00006.html">http://www.geologyontario.mndm.gov.on.ca/mndmfiles/mdi/data/records/MDI42B01NE00006.html</a>
Raney Lake Gold Occurrence	Prospect	Mesothermal	carbonatization, chloritic alteration	quartz vein, near felsic porphyry	molybdenite, gold	pyrite, pyrrhotite, tourmaline, sphalerite, chalcopyrite, galena	shear	Horwood Group	Neoproterozoic	2700 Ma	Regional greenschist	A little native gold occurs together with pyrite and some chalcopyrite, galena, sphalerite and tourmaline in quartz carbonate veins	<a href="http://www.geologyontario.mndm.gov.on.ca/mndmfiles/mdi/data/records/MDI41O15SW00006.html">http://www.geologyontario.mndm.gov.on.ca/mndmfiles/mdi/data/records/MDI41O15SW00006.html</a>
Lyll-Biedelman	Mineral Occurrence	Mesothermal	hematite alteration	quartz vein, syenite	gold,	pyrite, arsenopyrite, chalcopyrite	Shear	Halcrow-Swayze	Neoproterozoic	2700 Ma	Regional greenschist	Quartz veins host the mineralization. In turn the veins occur in a feldspar porphyritic syenite which has intruded a sequence of mafic volcanics and polymictic conglomerates. The syenite is relatively massive and contains between 15 and 50% feldspar phenocrysts in a fine-grained matrix.	<a href="http://www.geologyontario.mndm.gov.on.ca/mndmfiles/mdi/data/records/MDI41O15SW00005.html">http://www.geologyontario.mndm.gov.on.ca/mndmfiles/mdi/data/records/MDI41O15SW00005.html</a>

Miner Kenty	Mineral Occurrence	Mesothermal	chloritic, pyritic, carbonatization alteration	quartz-carbonate vein, basalt, felsic porphyry	gold, pyrite	chalcopyrite,	Shear	Raney-newton	Neoproterozoic	2700 Ma	Regional greenschist	The mineralization is hosted in a sequence of fresh pillowed basalts. In the area of the mineralization these basalts have been intruded by felsic dykes - porphyry dykes. The mineralization is closely associated with quartz vein stockworks and the narrow though strong iron carbonate alteration adjacent to these veins.	<a href="http://www.geologyontario.mndm.gov.on.ca/mndmfiles/mdi/data/records/MDI41015SE00003.html">http://www.geologyontario.mndm.gov.on.ca/mndmfiles/mdi/data/records/MDI41015SE00003.html</a>
Jessop-O'Neill Property	Discretionary Mineral Occurrence	Mesothermal	Carbonate alteration	quartz-vein adjacent conglomerate	molybdenite, gold, chalcopyrite	pyrite, galena, tetrahedrite, specularite	Shear	Ridout Group	Neoproterozoic	2745 +/- Ma	Regional greenschist	The mineralization occurs in blue quartz stringer veins which form a stockwork. Pyrite and lesser amount of molybdenite form up to 20% of these veins. Mariposite has also been reported in the veins. The mode of occurrence of the other reported minerals is not known but may be due to the composite description from several outcrops - drill holes.	<a href="http://www.geologyontario.mndm.gov.on.ca/mndmfiles/mdi/data/records/MDI41009SE00027.html">http://www.geologyontario.mndm.gov.on.ca/mndmfiles/mdi/data/records/MDI41009SE00027.html</a>
J. A. Shannon	Mineral Occurrence	Mesothermal	hematite alteration	quartz-vein, quartz-feldspar porphyry	Gold	pyrite	shear	Ridout Group	Neoproterozoic	2745 +/- Ma	Regional greenschist	The host rock is a pink foliated quartz, feldspar porphyry-granodiorite. Small rounded feldspar phenocrysts are orientated subparallel to the foliation. In addition, there are larger feldspar aggregates up to 5 mm with no preferred orientation. Strong hematite alteration occurs in 5 mm thick zones adjacent to orthogonal fractures within the porphyry.	<a href="http://www.geologyontario.mndm.gov.on.ca/mndmfiles/mdi/data/records/MDI41009SE00044.html">http://www.geologyontario.mndm.gov.on.ca/mndmfiles/mdi/data/records/MDI41009SE00044.html</a>
Flint Rock Island	Mineral Occurrence	Mesothermal	chlorite alteration	quartz-vein, chert	gold	pyrite, chalcopyrite, pyrrhotite	Shear	Halcrow-Swayze	Neoproterozoic	2700 Ma	Regional greenschist	There are a number of small quartz - calcite - epidote veins which locally contain pyrite, pyrrhotite and minor chalcopyrite. These veins are locally associated with the interflow sediments and typically carry anomalous gold values but sub ore grade values.	<a href="http://www.geologyontario.mndm.gov.on.ca/mndmfiles/mdi/data/records/MDI41015SE00017.html">http://www.geologyontario.mndm.gov.on.ca/mndmfiles/mdi/data/records/MDI41015SE00017.html</a>
Halcrow Swayze	Developed Mineral Prospect with Reserves	Mesothermal	chloritic, malachite supergene alteration	quartz-vein, diorite	gold	pyrite, chalcopyrite	Ridout high strain zone (regional), shear, contact	Halcrow-Swayze	Neoproterozoic	2700 Ma	Regional greenschist	The mineralization is hosted in an altered cataclastic zone located on the contact of mafic volcanics and a quartz diorite body. The quartz diorite is weakly foliated and medium to coarse grained. Microbreccias, mylonites and blastomylonites occur, have been folded and are- silicified, carbonatized, chloritized, sericitized, and locally hematized. In the past this unit has been mapped a chert, quartzite or felsic volcanic.	<a href="http://www.geologyontario.mndm.gov.on.ca/mndmfiles/mdi/data/records/MDI41015SW00002.html">http://www.geologyontario.mndm.gov.on.ca/mndmfiles/mdi/data/records/MDI41015SW00002.html</a>
Burtho	Mineral Occurrence	Mesothermal		quartz-vein, basalt	gold	pyrite, chalcopyrite	shear	Muskego-reeves	Neoproterozoic	N/A	Regional greenschist	The host quartz porphyry and the adjacent mafic volcanics are sheared. The reported shearing is in a northwest orientation; however, the location of the mineralization is on the south side of an inferred regional northeast trending shear zone the Hardiman Bay Fault	<a href="http://www.geologyontario.mndm.gov.on.ca/mndmfiles/mdi/data/records/MDI42B01SE00012.html">http://www.geologyontario.mndm.gov.on.ca/mndmfiles/mdi/data/records/MDI42B01SE00012.html</a>
Buffalo Canadian	Mineral Occurrence	Mesothermal	serpentinization, pyritic	quartz-vein near peridotite and basalt	Gold	pyrite, pyrrhotite	shear	Muskego-reeves	Neoproterozoic	2700 Ma	Regional greenschist	The mineralization occurs in a series of quartz veins which roughly parallel the regional volcanic stratigraphy. However, the quartz veins are hosted in an elongated subvolcanic ultramafic intrusive which parallels the stratigraphy. Diamond drilling indicated that there are a number of interflow chert horizons associated with the mineralized vein.	<a href="http://www.geologyontario.mndm.gov.on.ca/mndmfiles/mdi/data/records/MDI41015SE00013.html">http://www.geologyontario.mndm.gov.on.ca/mndmfiles/mdi/data/records/MDI41015SE00013.html</a>
Kerr – Adison (Main showing)	Mineral Occurrence	Mesothermal	strong carbonate alteration	quartz-carbonate vein, diorite, basalt, gabbro	Pyrrhotite, gold, silver		fault	Horwood Group	Neoproterozoic	2700 Ma	Regional greenschist	Mineralization occurs as disseminated sulphides in a number of parallel quartz carbonate veins. These veins pinch and swell and are known to be up to 50cm thick but normally are up to 10 - 15cm thick. The veins have been traced laterally up to 60m. Typically the gold values are low but a section in one vein has consistently returned values between 14 and 18 g/t.	<a href="http://www.geologyontario.mndm.gov.on.ca/mndmfiles/mdi/data/records/MDI42B01SW00014.html">http://www.geologyontario.mndm.gov.on.ca/mndmfiles/mdi/data/records/MDI42B01SW00014.html</a>

Jacobs	Discretionary Mineral Occurrence	Mesothermal	Chloritic alteration	quartz-vein, basalt, amphibolite gneiss	Gold	pyrite, chalcopyrite, pyrrhotite, galena	contact and joint	Horwood Group	Neoproterozoic	2700 Ma	Regional greenschist	The vein consists of a series of a number of elliptical pods orientated to the northwest and the pods are connected by a stockwork of thin quartz - calcite - ankerite(?) veinlets. To the southeast on the same lineament (100m) there are a series of closely spaced, oblique, en-echelon quartz veins with local pods aligned on the same lineament as at the original trenches. The controlling lineament is parallel to a series of joints with epidote alteration which are roughly perpendicular to the pluton contact.	<a href="http://www.geologyontario.mndm.gov.on.ca/mndmfiles/mdi/data/records/MDI41O16NW00029.html">http://www.geologyontario.mndm.gov.on.ca/mndmfiles/mdi/data/records/MDI41O16NW00029.html</a>
Thorne	Mineral Occurrence	Mesothermal	potassic alteration	quartz carbonate vein	Gold	pyrite, pyrrhotite, chalcopyrite	Shear	Horwood Group	Neoproterozoic	2700 Ma	Regional greenschist	The mineralization is hosted in a narrow shear zone with contacts with the adjacent undeformed rocks (<10 cm). Unlike the adjacent pillows, the shared material is rusty and contains carbonate and sericite alteration.	<a href="http://www.geologyontario.mndm.gov.on.ca/mndmfiles/mdi/data/records/MDI41O16NW00035.html">http://www.geologyontario.mndm.gov.on.ca/mndmfiles/mdi/data/records/MDI41O16NW00035.html</a>
Patrie #2 Vein Zone	Mineral Occurrence	Mesothermal	sericitization, carbonatization, chloritic alteration	quartz-carbonate vein, green-carbonate composition in ultramafic,	Gold	pyrite, chalcopyrite, galena, arsenopyrite, fuschite	Ridout high strain zone (regional), shear	Horwood Group	Neoproterozoic	2700 Ma	Regional greenschist	The mineralization is hosted in quartz veins within a highly carbonatized sequence of intercalated basaltic and komatiitic flows. Locally in the sequence there is a horizon of polymictic conglomerates. Compositionally, these rocks range from komatiite through basaltic komatiite to Mg tholeiitic basalt. At the prospect the rocks are strongly carbonatized and sericitized, and have some fuchsite alteration. T	<a href="http://www.geologyontario.mndm.gov.on.ca/mndmfiles/mdi/data/records/MDI41O15SW00009.html">http://www.geologyontario.mndm.gov.on.ca/mndmfiles/mdi/data/records/MDI41O15SW00009.html</a>
Cote, C.	Mineral Occurrence	Possibly porphyry-type		Granodiorite, quartz-sulphide vein	Gold, Copper	pyrite, pyrrhotite		Chester intrusive complex	Neoproterozoic	2740 Ma	Regional greenschist	Samples collected at the time of discovery reportedly returned values of 171 g/t Au in a 5 cm vein. The best assays to come from the channel sampling completed in 1936 was 12 g/t Au and the best assay from the diamond drilling was 14 g/t Au across 0.75 m. Grab samples from a vein in 1979 averaged 3-9% Cu and 8.5 g/t Au.	<a href="http://www.geologyontario.mndm.gov.on.ca/mndmfiles/mdi/data/records/MDI41P12SW00062.html">http://www.geologyontario.mndm.gov.on.ca/mndmfiles/mdi/data/records/MDI41P12SW00062.html</a>
Beaver Bethnal #2	Mineral Occurrence	Mesothermal	chloritic alteration	greuwacke, schist	gold, copper, zinc, silver	pyrite, pyrrhotite	shear	Chester intrusive complex	Neoproterozoic	2690 Ma	Regional greenschist	Sulphides are generally disseminated within the shear zone but also occur as thin seams along the shear planes and in uncommon veins up to 10cm thick. 03/14/2000 (A Wilson) - Assay values up to 13 g/t Au were obtained by prospectors in 1931-33.	<a href="http://www.geologyontario.mndm.gov.on.ca/mndmfiles/mdi/data/records/MDI41P12SW00071.html">http://www.geologyontario.mndm.gov.on.ca/mndmfiles/mdi/data/records/MDI41P12SW00071.html</a>
Eccles-Holmes	Mineral Occurrence	Possibly porphyry-type	chloritic alteration	quartz-vein, granodiorite	chalcopyrite, molybdenite, gold	pyrite, arsenopyrite	shear	Chester intrusive complex	Neoproterozoic	2740 Ma	Regional greenschist	The mineralization is hosted in and adjacent to several discontinuous quartz and quartz - carbonate veins that pinch and swell. Veins vary in size between 10 and 50cm across and are at least 5m in length and follow a series of fractures. Adjacent to the veins and locally adjacent to the controlling fractures are disseminated sulphides up to half a meter from the vein / fracture.	<a href="http://www.geologyontario.mndm.gov.on.ca/mndmfiles/mdi/data/records/MDI41P12SW00061.html">http://www.geologyontario.mndm.gov.on.ca/mndmfiles/mdi/data/records/MDI41P12SW00061.html</a>
Dome West Zone	Mineral Occurrence	Mesothermal	Carbonate alteration	quartz-carbonate, Fe tholeiitic, calc-alkalic	Gold	pyrite	Newton high strainzone (local scale)	Chester intrusive complex	Neoproterozoic	2700 Ma	Regional greenschist	The carbonate alteration apparently is associated with one set of quartz veins which are part of the largest vein set at the occurrence. Gold values are known to be associated with the larger quartz veins and with the intensely carbonatized material adjacent to small quartz feldspar porphyry intrusions or the larger quartz veins.	<a href="http://www.geologyontario.mndm.gov.on.ca/mndmfiles/mdi/data/records/MDI41O16NW00034.html">http://www.geologyontario.mndm.gov.on.ca/mndmfiles/mdi/data/records/MDI41O16NW00034.html</a>
Shaft Veins	Developed Mineral Prospect Without Reserves	Mesothermal	carbonate, pyrite, albite, hematization, silicification	quartz-carbonate vein, tholeiitic, quartz-feldspar porphyry rocks	gold, pyrite	chalcopyrite, galena, sphalerite, molybdenite, tourmaline		Raney-newton	Neoproterozoic	2700 Ma	Regional greenschist	Mineralization occurs in hairline fractures in the altered wall rocks filled with euhedral to subhedral pyrite. The best gold grades occur where the vein cuts through metavolcanics. The vein is a coarse-grained, glassy white to clear quartz which is cut by secondary veins (<2mm) of fine-grained sulphides.	<a href="http://www.geologyontario.mndm.gov.on.ca/mndmfiles/mdi/data/records/MDI41O15SE00055.html">http://www.geologyontario.mndm.gov.on.ca/mndmfiles/mdi/data/records/MDI41O15SE00055.html</a>
Jess-Mac Gold Mines	Mineral Occurrence	Mesothermal	cuprite supergene alteration	quartz-feldspar,	gold, cuprite, copper	pyrite, galena, sphalerite	Shear	Ridout Group	Neoproterozoic	2700 Ma	Regional greenschist	The host porphyry tends to be sheared in a number of directions, 100°, 070° and 160°. The mineralization is hosted in a porphyry with variable zones of silicification and red alteration. This alteration tends to be stronger where the shearing and fracturing tends to be greater.	<a href="http://www.geologyontario.mndm.gov.on.ca/mndmfiles/mdi/data/records/MDI41O09SE00017.html">http://www.geologyontario.mndm.gov.on.ca/mndmfiles/mdi/data/records/MDI41O09SE00017.html</a>

Gaffney-West	Mineral Occurrence	Mesothermal	sericite alteration	quartz-feldspar porphyry, conglomerate	galena, sphalerite	pyrite, chalcopyrite, molybdenite	contact, shear	Ridout Group	Neoarchean	2724+/- 4 Ma	Regional greenschist	Disseminated sparse pyrite and chalcopyrite occur in the matrix of the host porphyry - schist and form up to 2% of the rock. These sulphides have been remobilized locally and are associated with quartz veins. It is presumed that the galena - sphalerite occurrences are associated with such veins.	<a href="http://www.geologyontario.mndm.gov.on.ca/mndmfiles/mdi/data/records/MDI41009SE00009.html">http://www.geologyontario.mndm.gov.on.ca/mndmfiles/mdi/data/records/MDI41009SE00009.html</a>
Osway DDH 83-31	Mineral Occurrence	Magmatic and Mesothermal (possibly intrusion-related)	malachite supergene alteration	quartz-feldspar	chalcop yrite	pyrite, galena, sphalerite	joint	Ridout Group	Neoarchean	2745+/- 4Ma	Regional greenschist	The host rock is a strongly foliated green to pink chlorite quartz porphyry. There are two types of mineralization present, sparsely disseminate sulphides in the porphyry matrix and the massive to semi-massive sulphides associated with the quartz veins and joints.	<a href="http://www.geologyontario.mndm.gov.on.ca/mndmfiles/mdi/data/records/MDI41009SE00047.html">http://www.geologyontario.mndm.gov.on.ca/mndmfiles/mdi/data/records/MDI41009SE00047.html</a>
Osway DDH 82-15	Mineral Occurrence	Magmatic and Mesothermal (possibly intrusion-related)	sericite alteration	quartz-feldspar, quartz-carbonate veins	galena, sphalerite	pyrite, chalcopyrite, molybdenite, tourmaline	shear	Ridout Group	Neoarchean	2745+/- Ma	Regional greenschist	Three types of mineralization occur in the area: 1) disseminated sulphides in the porphyry matrix, 2) sulphide smears along shear planes, 3) vein hosted mineralization. The disseminated sulphide mineralization is variable with sparse grains of pyrite, galena and chalcopyrite.	<a href="http://www.geologyontario.mndm.gov.on.ca/mndmfiles/mdi/data/records/MDI41009SE00042.html">http://www.geologyontario.mndm.gov.on.ca/mndmfiles/mdi/data/records/MDI41009SE00042.html</a>
SILAMS, P.H.	Mineral Occurrence	Mesothermal	carbonatization, potassic, chloritic alteration	quartz-vein, basalt, schist	gold	N/A	shear	Horwood Group	Neoarchean	2700 Ma	Regional greenschist	The supracrustal rocks in the area consist of massive and pillowed Mg tholeiitic basalt with some intercalated pyroclastic calc alkaline metavolcanics and argillaceous plus arenaceous horizons. Close to the plotted location there is a shear zone with intense carbonate - sericite alteration. This schist has numerous cavities where pyrite has been eroded and could be termed a carbonate - sericite - chlorite schist.	<a href="http://www.geologyontario.mndm.gov.on.ca/mndmfiles/mdi/data/records/MDI41016NW00008.html">http://www.geologyontario.mndm.gov.on.ca/mndmfiles/mdi/data/records/MDI41016NW00008.html</a>
CORBETT-MCCAMBLY	Mineral Occurrence	Mesothermal	strong carbonate alteration	quartz, arkose,		pyrite		Ridout Group	Neoarchean	2690 Ma	Regional greenschist	The mineralized quartz vein is hosted in sheared arkoses which have been intruded by a quartz porphyry. The arkoses are now sericite schists with local patches of carbonate and hematite. Some disseminated pyrite is reported in both the quartz-carbonate veins found in the area and the sheared metasediments	<a href="http://www.geologyontario.mndm.gov.on.ca/mndmfiles/mdi/data/records/MDI41P12SW00018.html">http://www.geologyontario.mndm.gov.on.ca/mndmfiles/mdi/data/records/MDI41P12SW00018.html</a>
Osway DDH 82-13	Mineral Occurrence	Mesothermal	sericitization, carbonatization	quartz vein, conglomerate	gold	pyrite, molybdenite, galena, arsenopyrite, tourmaline, tetrahedrite	shear	Ridout Group	Neoarchean	2745+/-4 Ma	Regional greenschist	A strongly sheared pebble conglomerate is cut by a number of large multi-phase quartz veins and shear zones. Adjacent to the shears are broad alteration/ mineralization zones. Alteration is to sericite, pyrite, silica, iron carbonate and locally to anhydrite.	<a href="http://www.geologyontario.mndm.gov.on.ca/mndmfiles/mdi/data/records/MDI41009SE00043.html">http://www.geologyontario.mndm.gov.on.ca/mndmfiles/mdi/data/records/MDI41009SE00043.html</a>
Chesbar	Developed Mineral Prospect with Reserves	Possibly porphyry-type	chloritic, saussuritization	quartz-carbonate, hornblende diorite, granodiorite quartz vein, basalt, porphyry, diorite	chalcop yrite, gold	pyrite, pyrrhotite,	shear	Chester intrusive complex	Neoarchean	2740 Ma	Regional greenschist	The mineralization is hosted in a number of closely spaced veins in a set of shears. Individual shears can be as small as 2cm surrounded by alteration and form a stockwork or be thicker simpler shears. The shears form a zone about 60m thick.	<a href="http://www.geologyontario.mndm.gov.on.ca/mndmfiles/mdi/data/records/MDI41P12SW00073.html">http://www.geologyontario.mndm.gov.on.ca/mndmfiles/mdi/data/records/MDI41P12SW00073.html</a>
Landry, H.	Mineral Occurrence	Mesothermal	Carbonate alteration	quartz vein, basalt, porphyry, diorite	Gold	pyrite, chalcopyrite	shear	Horwood Group	Neoarchean	2700 Ma	Regional greenschist	A network of quartz stringer is hosted in metavolcanics at surface and diamond drilling indicated that these stringers are larger at depth and associated with feldspar porphyry dyke contacts.	<a href="http://www.geologyontario.mndm.gov.on.ca/mndmfiles/mdi/data/records/MDI41016NW00005.html">http://www.geologyontario.mndm.gov.on.ca/mndmfiles/mdi/data/records/MDI41016NW00005.html</a>
Donalda	Mineral Occurrence	Mesothermal	sericite, chlorite alteration	quartz vein, schist, basalt	chalcop yrite,	pyrite, pyrrhotite	shear	Horwood Group	Neoarchean	2700 Ma	Regional greenschist	Mineralization occurs along a number of closely spaced altered shear zones parallel to the general trend of the surrounding metavolcanic sequence. These shear zones are not very thick (<2m).	<a href="http://www.geologyontario.mndm.gov.on.ca/mndmfiles/mdi/data/records/MDI41016NW00023.html">http://www.geologyontario.mndm.gov.on.ca/mndmfiles/mdi/data/records/MDI41016NW00023.html</a>
Bromley	Mineral Occurrence	Mesothermal	carbonatization, chloritic, hematization	iron tholeiitic basalt, quartz-feldspar porphyry, quartz vein	pyrite, chalcop yrite	arsenopyrite, sphalerite,	shear	Muskego-reeves	Neoarchean	N/A	Regional greenschist	The mineralization is located in a fault zone trending roughly 110 within a zone of sheared metavolcanics. Minor westerly plunging drag folds occur adjacent to the vein. The regional MacKeith or Keith - Penhorwood shear zone, an east west trending structure occurs in the immediate area and the shearing in the outcrop may be part of this shear zone.	<a href="http://www.geologyontario.mndm.gov.on.ca/mndmfiles/mdi/data/records/MDI42B01NE00033.html">http://www.geologyontario.mndm.gov.on.ca/mndmfiles/mdi/data/records/MDI42B01NE00033.html</a>
McNeely-McColough	Mineral Occurrence	Mesothermal		quartz vein	gold	pyrite	contact	Halcrow-Swayze	Neoarchean	2700 Ma	Regional greenschist	The mineralization occurs in a series of quartz veins / stockworks hosted in mafic metavolcanics. Other quartz veins and various trenches associated with the prospect generally follow a major contact between a felsic intrusive body to the south and the mafic volcanics but are slightly off-set to the north.	<a href="http://www.geologyontario.mndm.gov.on.ca/mndmfiles/mdi/data/records/MDI41O15SE00010.html">http://www.geologyontario.mndm.gov.on.ca/mndmfiles/mdi/data/records/MDI41O15SE00010.html</a>
Gilbert	Discretionary Mineral Occurrence	Mesothermal		quartz vein, basalt, porphyry	gold	pyrite, chalcopyrite	shear	Horwood Group	Neoarchean	2700 Ma	Regional greenschist	Mineralization is confined to a northeast trending shear zone which is parallel to the foliation in the surrounding rocks. This shear is parallel to the shear zone at the Gifford occurrence further south. The mineralization is reportedly restricted to a single large outcrop of mafic metavolcanics.	<a href="http://www.geologyontario.mndm.gov.on.ca/mndmfiles/mdi/data/records/MDI41O16NW00027.html">http://www.geologyontario.mndm.gov.on.ca/mndmfiles/mdi/data/records/MDI41O16NW00027.html</a>

BACHMAN-CAMPBELL-REANY	Mineral Occurrence	Mesothermal	potassic, hematization, tourmalization	basalt, felsic metavolcanic tuff	gold	chalcopyrite, pyrite	shear	Horwood Group	Neoproterozoic	2700 Ma	Regional greenschist	A number of small shear zones are confined to an epiclastic tuffaceous band and gold mineralization is confined to these zones. Alteration zones are mineralized with disseminated pyrite and rare chalcopyrite which are concentrated closer to the quartz stringer veins.	<a href="http://www.geologyontario.mndm.gov.on.ca/mndmfiles/mdi/data/records/MDI41O16NW00009.html">http://www.geologyontario.mndm.gov.on.ca/mndmfiles/mdi/data/records/MDI41O16NW00009.html</a>
Clam Lake	Mineral Occurrence	Possibly porphyry-type	chlorite alteration	granodiorite, quartz-cabornate vein	pyrite, chalcopyrite, gold		shear	Chester intrusive complex	Neoproterozoic	2740 Ma	Regional greenschist	The host rock is a siliceous green, fine-grained granodiorite with smoky grey, irregular quartz grains. The green colouration is probably due to a weak, pervasive chlorite alteration.	<a href="http://www.geologyontario.mndm.gov.on.ca/mndmfiles/mdi/data/records/MDI41P12SW00084.html">http://www.geologyontario.mndm.gov.on.ca/mndmfiles/mdi/data/records/MDI41P12SW00084.html</a>
West Shore Clam Lake	Discretionary Mineral Occurrence	Possibly porphyry-type	biotitic, chloritic, silicification, carbonatization	granodiorite, quartz -vein	pyrite, chalcopyrite, gold		shear	Chester intrusive complex	Neoproterozoic	2740 Ma	Regional greenschist	There are a number of quartz or quartz and iron carbonate veins within a shear zone exposed in the trenches. The veins pinch and swell from 2m to thin stringers. The surrounding shear zone locally contains sparse disseminated pyrite and chalcopyrite. Mineralization within the veins varies from rather lean to pyrite, chalcopyrite and gold intimately associated with biotite near the lamprophyre contacts.	<a href="http://www.geologyontario.mndm.gov.on.ca/mndmfiles/mdi/data/records/MDI41P12SW00123.html">http://www.geologyontario.mndm.gov.on.ca/mndmfiles/mdi/data/records/MDI41P12SW00123.html</a>
WEST SIDE CLAM LAKE	Mineral Occurrence	Possibly porphyry-type	chloritic alteration	granodiorite, quartz-vein	pyrite	specularite	shear	Chester intrusive complex	Neoproterozoic	2740 Ma	Regional greenschist	The host is a strongly chlorite altered granodiorite similar to the surrounding outcrops. The strong alteration is associated with the development of a strong foliation in the granodiorite.	<a href="http://www.geologyontario.mndm.gov.on.ca/mndmfiles/mdi/data/records/MDI41P12SW00089.html">http://www.geologyontario.mndm.gov.on.ca/mndmfiles/mdi/data/records/MDI41P12SW00089.html</a>
Card Lake Copper Property	Mineral Occurrence	Mesothermal	sericite alteration	schist, basalt, quartz-vein	stibnite, arsenopyrite,	chalcopyrite, pyrite, pyrrhotite	shear	Muskego-reeves	Neoproterozoic	N/A	Regional greenschist	The mineralized shear zone is narrow (<2m) and well defined with relatively sharp margins. However, several metres from the shear there are a series of closely spaced parallel fractures that have been cemented with various minerals including carbonate.	<a href="http://www.geologyontario.mndm.gov.on.ca/mndmfiles/mdi/data/records/MDI42B01NE00021.html">http://www.geologyontario.mndm.gov.on.ca/mndmfiles/mdi/data/records/MDI42B01NE00021.html</a>
Labbie #3	Discretionary Mineral Occurrence	Mesothermal	N/A	quartz-vein, basalt, diorite	pyrite	N/A	N/A	Horwood Group	Neoproterozoic	2690 Ma	Regional greenschist	mineralization is confined to a felsic pluton.	<a href="http://www.geologyontario.mndm.gov.on.ca/mndmfiles/mdi/data/records/MDI42B01NE00043.html">http://www.geologyontario.mndm.gov.on.ca/mndmfiles/mdi/data/records/MDI42B01NE00043.html</a>
Hopkins	Mineral Occurrence	Mesothermal	Carbonate alteration	quartz-carbonate	gold	pyrite	Ridout high strain zone	Halcrow-Swayze	Neoproterozoic	2700 Ma	Regional greenschist	The mineralized fault system is discordant to the regional stratigraphy. A narrow zone of carbonate alteration is associated with the fault cutting pillowed mafic volcanics. A narrow set of quartz veins and quartz stockwork occurs in the alteration zone.	<a href="http://www.geologyontario.mndm.gov.on.ca/mndmfiles/mdi/data/records/MDI41O15SE00018.html">http://www.geologyontario.mndm.gov.on.ca/mndmfiles/mdi/data/records/MDI41O15SE00018.html</a>
Tremblay Option	Mineral Occurrence	Mesothermal	chloritic, carbonatization alteration	quartz-vein, basalt, granodiorite	chalcopyrite, galena, gold	tourmaline, pyrite, arsenopyrite	vein		Neoproterozoic		Regional greenschist	Mineralization is hosted in a massive medium to coarse grained flow though there are reports of quartz stockworks in strongly carbonatized material in drill core. This quartz carbonate material may represent altered ultramafic.	<a href="http://www.geologyontario.mndm.gov.on.ca/mndmfiles/mdi/data/records/MDI42A04NW00033.html">http://www.geologyontario.mndm.gov.on.ca/mndmfiles/mdi/data/records/MDI42A04NW00033.html</a>
R. Tremblay Property	Mineral Occurrence	Mesothermal	potassic, tourmalinization, chloritic alteraion	quartz vein,	pyrite, arsenopyrite	tourmaline, albite	shear		Neoproterozoic	N/A	Regional greenschist	The mineralization occurs in a banded zone oblique to the foliation / schistosity. This schistosity has numerous small to moderate sized 'Z' folds, centimeter to meter scale, which are locally highlighted by discontinuous quartz veinlets. The banded mineralized zone also has 'Z' folds and the axial planar cleavage to these folds is 295/70 and the folds in the mineralized zone plunge at 55 towards 307	<a href="http://www.geologyontario.mndm.gov.on.ca/mndmfiles/mdi/data/records/MDI42A04NW00048.html">http://www.geologyontario.mndm.gov.on.ca/mndmfiles/mdi/data/records/MDI42A04NW00048.html</a>
Winross Gold Property	Mineral Occurrence	Mesothermal	chloritic alteration	quartz vein, schist, basalt	pyrite, pyrrhotite, chalcopyrite	tourmaline	Fault		Neoproterozoic	N/A	Regional greenschist	The mineralization is hosted in a fault locally termed the Gosselin Fault. This fault is marked by shearing and alteration though at present it is largely detected with geophysics.	<a href="http://www.geologyontario.mndm.gov.on.ca/mndmfiles/mdi/data/records/MDI42B01NE00022.html">http://www.geologyontario.mndm.gov.on.ca/mndmfiles/mdi/data/records/MDI42B01NE00022.html</a>
Mining Corporation Property	Prospect	Mesothermal	carbonatization, chloritic	syenite dyke, granite, quartz-vein	malachite, pyrite, chalcopyrite		shear	Kenogamissi batholith	Neoproterozoic	N/A	Regional greenschist	The main vein is located in a small shear zone / fault. Branching off this main structure are numerous splay faults at different orientations. These splays and the main structure are marked by a sharp increase in the foliation intensity and the local development of a schistosity close to the faults. Within the foliation / schistosity crenulation folds and lineation's are developed. These minor faults control the shape of the late mafic dykes. 'Z' folds are present in the main quartz vein with long limbs on the ten-meter scale and short limbs on the meter scale.	<a href="http://www.geologyontario.mndm.gov.on.ca/mndmfiles/mdi/data/records/MDI42A04NW00009.html">http://www.geologyontario.mndm.gov.on.ca/mndmfiles/mdi/data/records/MDI42A04NW00009.html</a>
Sylvanite	Mineral Occurrence	Mesothermal	carbonatization, hematite alteration	quartz-carbonate vein,	gold	pyrite	Swayze lake high strain zone (local)	Halcrow-Swayze	Neoproterozoic	2700 Ma	Regional greenschist	The mineralization is hosted in a series of parallel porphyry dikes intruding schistose wackes and tuffs. Both the porphyry and schist contain quartz filled fractures with associated carbonate alteration and pyrite mineralization. The main vein has been exposed by trenching over a length 200' (61m), striking to the northwest with a 60-degree dip. A number of narrow zones with quartz stringers occur east of the main vein.	<a href="http://www.geologyontario.mndm.gov.on.ca/mndmfiles/mdi/data/records/MDI41O15SW00003.html">http://www.geologyontario.mndm.gov.on.ca/mndmfiles/mdi/data/records/MDI41O15SW00003.html</a>

LEFEVER-SILAMS	Mineral Occurrence	Mesothermal	chloritic alteration	quartz-vein, diorite, basalt	gold	pyrite, pyrrhotite	vein ass.	Horwood Group	Neoproterozoic	2700 Ma	Regional greenschist	The mineralization occurs in a number of thin discontinuous quartz veins over a 600 x 200m area. At the north end of the showing these veins trend northwest parallel to the local lithology and the veins are typically situated on various lithological contacts, e.g., porphyry sills - diabase, rhyolite - chert.	<a href="http://www.geologyontario.mndm.gov.on.ca/mndmfiles/mdi/data/records/MDI42B01SW00013.html">http://www.geologyontario.mndm.gov.on.ca/mndmfiles/mdi/data/records/MDI42B01SW00013.html</a>
KENTY #3 SHAFT	Mineral Occurrence	Mesothermal (Possibly intrusion related)	pyritic alteration	quartz-vein, mafic metavolcanic	gold	pyrite, pyrrhotite	vein ass.	Halcrow-Swayze	Neoproterozoic	2700 Ma	Regional greenschist	Very little sulphide mineralization occurs within the quartz veins. Rather, disseminated subhedral pyrite occurs in the altered wallrock. Pyrite grains are up to 2 mm in size and forms up to 5% of the altered material. The trace amounts of pyrite within the quartz veins are concentrated in chloritic seams. Within the unaltered mafic volcanics, fine-grained, disseminated, pyrrhotite occurs concentrated in stringers and along fractures	<a href="http://www.geologyontario.mndm.gov.on.ca/mndmfiles/mdi/data/records/MDI41O15SE00057.html">http://www.geologyontario.mndm.gov.on.ca/mndmfiles/mdi/data/records/MDI41O15SE00057.html</a>
DENROSS	Mineral Occurrence	Mesothermal	chloritic alteration	epiclastic hornblende near syenodiorite	gold	pyrite, pyrrhotite	shear	Horwood Group	Neoproterozoic	2700 Ma	contact amphibolite	There are a number of very thin pyrite veins found where the higher-grade gold assay values have been obtained. Grab samples collected by Noranda in 1993 returned values of 1.12 g/t Au, 11.5 g/t Au, 8.36 g/t Au and 8.22 g/t Au. Samples taken by the OGS in 1993 did not replicate these values. The mineralization is hosted in a coarse-grained, quartz rich leucogranodiorite. Away from the known mineralization, there are a number of large, fine- to coarse-grained diorites which are probably xenoliths from the earlier phases of the Chester Granitoid Complex.	<a href="http://www.geologyontario.mndm.gov.on.ca/mndmfiles/mdi/data/records/MDI42B01SW00017.html">http://www.geologyontario.mndm.gov.on.ca/mndmfiles/mdi/data/records/MDI42B01SW00017.html</a>
MURGOLD #15 VEIN	Mineral Occurrence	Possibly porphyry-type		granodiorite, diorite	chalcop yrite	pyrite	sheared, podiform	Chester intrusive complex	Neoproterozoic	2740 Ma			<a href="http://www.geologyontario.mndm.gov.on.ca/mndmfiles/mdi/data/records/MDI41P12SW00131.html">http://www.geologyontario.mndm.gov.on.ca/mndmfiles/mdi/data/records/MDI41P12SW00131.html</a>
MURGOLD #16 VEIN	Mineral Occurrence	Possibly porphyry-type	chloritic, saussuritization	granodiorite, diorite, quartz-vein	chalcop yrite	pyrite, pyrrhotite	N/A	Chester intrusive complex	Neoproterozoic	2740 Ma		The mineralization is associated with a shear zone that appears to be located on the northern contact of a granodiorite lens which has intruded and narrows eastward into various fine and coarse grained dioritic phases.	<a href="http://www.geologyontario.mndm.gov.on.ca/mndmfiles/mdi/data/records/MDI41P12SW00132.html">http://www.geologyontario.mndm.gov.on.ca/mndmfiles/mdi/data/records/MDI41P12SW00132.html</a>
LABBE #1	Mineral Occurrence	Possibly porphyry-type		granodiorite, quartz-vein, diorite	chalcop yrite, gold	pyrite	Vein	Chester intrusive complex	Neoproterozoic	2740 Ma		Where the host shear zone is well defined, quartz veining may be present. These veins are discontinuous, up to a metre wide, locally fault offset, brecciated, or folded within the shear. Where the quartz veins are brecciated, the voids in the rock are partizlly mineralized with coarse-grained pyrite, chlorite and minor chalcopyrite. Similarly, mineralization disseminated in the sheared granitoids outside of the quartz veining, is also discontinuous along strike.	<a href="http://www.geologyontario.mndm.gov.on.ca/mndmfiles/mdi/data/records/MDI41P12SW00129.html">http://www.geologyontario.mndm.gov.on.ca/mndmfiles/mdi/data/records/MDI41P12SW00129.html</a>
AJAX	Discretionary Mineral Occurrence	Mesothermal		quartz-vein, basalt, arenite	gold	pyrite	contact	Horwood Group	Neoproterozoic	2700	contact greenschist	The vein consists of clear very coarse quartz with some feldspar. Within the vein there is a ribbon texture with semi continuous chloritic seams.	<a href="http://www.geologyontario.mndm.gov.on.ca/mndmfiles/mdi/data/records/MDI41O16SW00039.html">http://www.geologyontario.mndm.gov.on.ca/mndmfiles/mdi/data/records/MDI41O16SW00039.html</a>
Jonsmith Mines Ltd	Mineral Occurrence	Possibly porphyry-type	chloritic alteration	granodiorite, quartz diorite	chalcop yrite	pyrite, sphalerite	shear, fault	Chester intrusive complex	Neoproterozoic	2740+/-2 Ma		Disseminated pyrite and some chalcopyrite occur in the sheared siliceous granodiorite together with some thin sulphide veins. There is very little quartz vein material in the trenches and the semi massive sulphide veins are sparse and less than 2cm thick. The assay results suggest that some sphalerite occurs together with the chalcopyrite.	<a href="http://www.geologyontario.mndm.gov.on.ca/mndmfiles/mdi/data/records/MDI41P12SW00023.html">http://www.geologyontario.mndm.gov.on.ca/mndmfiles/mdi/data/records/MDI41P12SW00023.html</a>
Schist Lake	Mineral Occurrence	Possibly porphyry-type	sericite alteration	conglomerate, quartz-feldspar vein		pyrite, chalcopyrite, arsenopyrite, magnetite, hematite	shear, fault, intersection	Ridout Group	Neoproterozoic	2739+/- 2 Ma	Regional greenschist	The mineralization is hosted in a schistose conglomerate - arenaceous sequence. Within these schists there is a narrow (<30cm) massive unit, probably a quartz feldspar porphyry sill.	<a href="http://www.geologyontario.mndm.gov.on.ca/mndmfiles/mdi/data/records/MDI41O09SE00002.html">http://www.geologyontario.mndm.gov.on.ca/mndmfiles/mdi/data/records/MDI41O09SE00002.html</a>
Moore Lake	Mineral Occurrence	Possibly porphyry-type	carbonatization, saussuritization	quartz-carbonate vein, diorite, carbonate-sericite schist	gold	pyrite, ilmenite	shear, contact	Ridout Group	Neoproterozoic	2739+/-2 Ma	Regional greenschist	The mineralization is hosted in a shear zone located on the contact between a diorite and highly strained epiclastic sediments. There are some small-scale crenulation folds in the shear zone.	<a href="http://www.geologyontario.mndm.gov.on.ca/mndmfiles/mdi/data/records/MDI41O09SE00006.html">http://www.geologyontario.mndm.gov.on.ca/mndmfiles/mdi/data/records/MDI41O09SE00006.html</a>
Consolidated Silver Butte Mines Ltd.	Discretionary Mineral Occurrence	Possibly porphyry-type	carbonatization alteration	diorite, quartz-carbonate	gold	pyrite, tourmaline	shear	Ridout Group	Neoproterozoic	2739+/-2 Ma	Regional greenschist	Discontinuous narrow quartz-carbonate veins and stringers are concentrated in the sheared contact zone. Within these milky veins, there are local seams (<3mm) which contain clear medium-grained quartz together with sericite and tourmaline.	<a href="http://www.geologyontario.mndm.gov.on.ca/mndmfiles/mdi/data/records/MDI41P12SW00139.html">http://www.geologyontario.mndm.gov.on.ca/mndmfiles/mdi/data/records/MDI41P12SW00139.html</a>
DYMENT PROPERTY	Mineral Occurrence	Mesothermal	sericitization	quartz-feldspar vein	gold	pyrite, galena, chalcopyrite, specularite,	shear	Halcrow-Swayze	Neoproterozoic	2700 Ma	Regional greenschist	The mineralization is hosted in a schistose felsic porphyry and associated with a series of oblique quartz lenses forming an almost continuous vein for about 150' (46m)	<a href="http://www.geologyontario.mndm.gov.on.ca/mndmfiles/mdi/data/records/MDI41O15SW00014.html">http://www.geologyontario.mndm.gov.on.ca/mndmfiles/mdi/data/records/MDI41O15SW00014.html</a>
O'NEIL, C.E.	Discretionary Mineral Occurrence	Mesothermal	tourmalinization, potassic alteration	quartz-vein, basalt	gold	pyrite, chalcopyrite	shear	Horwood Group	Neoproterozoic	2700 Ma	Regional greenschist	Pyrite is disseminated throughout the alteration zones whereas the distribution of chalcopyrite is more irregular and tends to be concentrated into bands together with pyrite. Together both sulphides can form up to 5% of the rock but typically form less than 2% of the rock. The best gold values are associated with zones of increased deformation and alteration combined with quartz stringers but even so the gold values are still less than 1 g/tonne.	<a href="http://www.geologyontario.mndm.gov.on.ca/mndmfiles/mdi/data/records/MDI42B01SW00011.html">http://www.geologyontario.mndm.gov.on.ca/mndmfiles/mdi/data/records/MDI42B01SW00011.html</a>
Michelle Zone	Prospect	Mesothermal	carbonitization, chloritic, silicification	quartz-feldspar vein, fe tholeiitic	gold	pyrite	stockwork, brecciated, shear	Horwood Group	Neoproterozoic	2700 Ma	Regional greenschist	Mineralization is hosted in local brittle shears in crystal tuff, altered basalts and porphyry dikes within carbonatized, silicified and pyritized shear envelopes	<a href="http://www.geologyontario.mndm.gov.on.ca/mndmfiles/mdi/data/records/">http://www.geologyontario.mndm.gov.on.ca/mndmfiles/mdi/data/records/</a>



CLAIM S19970	Developed Mineral Prospect Without Reserves	Possibly porphyry-type	chloritic, malachite and azurite supergene alteration	Granodiorite, quartz-sulphide vein	pyrite, chalcop yrite, bornite, gold	N/A	shear	Chester intrusive complex	Neoproterozoic	2740 Ma	Regional greenschist	Mineralization is centred on a quartz/sulphide vein that pinches and swells between 10cm and 40cm in thickness. Adjacent to this main vein there are a number of small subparallel carbonate veins, quartz veins with wall rock fragments, and coarse grained, quartz - iron carbonate veins. The mineralization occurs as fine disseminated sulphide grains in the matrix of the adjacent granodiorite and in a semi massive portion of the vein structure varying between 4 and 10cm thick.	<a href="http://www.geologyontario.mndm.gov.on.ca/mndmfiles/mdi/data/records/MDI41P12SW00033.html">http://www.geologyontario.mndm.gov.on.ca/mndmfiles/mdi/data/records/MDI41P12SW00033.html</a>
ECCLES-HOLMES #4 VEIN	Mineral Occurrence	Possibly porphyry-type	chloritic, sericitization	granodiorite, near diabase	chalcop yrite, gold	pyrite, arsenopyrite, telluride, tourmaline		Chester intrusive complex	Neoproterozoic	2740 Ma	Regional greenschist	The host rock to the mineralization, consists of a complex mixture of the Chester Granitoid complex. The phases present range from the diorite - quartz diorite - granodiorite with some possible mafic volcanic xenoliths. Alteration in the area is associated with the veins and shear zones. The most widespread is strong chlorite alteration up to a half meter from a shear.	<a href="http://www.geologyontario.mndm.gov.on.ca/mndmfiles/mdi/data/records/MDI41P12SW00127.html">http://www.geologyontario.mndm.gov.on.ca/mndmfiles/mdi/data/records/MDI41P12SW00127.html</a>
EMERALD ISLE RESOURCES K3	Mineral Occurrence	Mesothermal	carbonatization, pyritic alteration	quartz vein, mafic metavolcanics	gold	pyrite	vein ass.	Halcrow-Swayze	Neoproterozoic	2700 Ma	Regional greenschist	The mineralization is hosted in a medium to fine-grained, dark green, massive mafic metavolcanic. The alteration is primarily characterized by a <3 m wide zone of replacement iron carbonate, centred on a braided quartz vein system. Less extensive than the carbonate alteration is a zone of disseminated pyrite which extends tens of centimetres from the veins.	<a href="http://www.geologyontario.mndm.gov.on.ca/mndmfiles/mdi/data/records/MDI41O15SE00056.html">http://www.geologyontario.mndm.gov.on.ca/mndmfiles/mdi/data/records/MDI41O15SE00056.html</a>
GOMAK	Developed Mineral Prospect Without Reserves	Possibly porphyry-type	chloritic, carbonatization, malachite supergene alteration	quartz vein, granite, granodiorite, contained in shear zone	gold, chalcop yrite	pyrite, pyrrhotite, molybdenite, sphalerite	sheared, vein ass.	Chester intrusive complex	Neoproterozoic	2740 Ma	Regional greenschist	The mineralization is hosted in various phases of the Chester Granitoid complex. These are mostly coarse grained, hornblende bearing quartz diorites cut by finer grained, more felsic phases. In some of the quartz diorite phases secondary, diffuse feldspar porphyroblasts are developed. Chlorite is the dominant alteration mineral and is associated with shearing. Locally the intensity of the chlorite and biotite alteration in the sheared zones imparts a schistosity to the rocks.	<a href="http://www.geologyontario.mndm.gov.on.ca/mndmfiles/mdi/data/records/MDI41P12SW00015.html">http://www.geologyontario.mndm.gov.on.ca/mndmfiles/mdi/data/records/MDI41P12SW00015.html</a>
BEAVERBRI DGE	Mineral Occurrence	Possibly porphyry-type	biotitic, carbonatization	granodiorite, quartz veins	chalcop yrite, gold	pyrite, magnetite	shears, joint	Chester intrusive complex	Neoproterozoic	2740 Ma	Regional greenschist	The coarse grained, disseminated sulphide mineralization is associated with an alteration zone. This alteration occurs over a thickness of 3m and consists of multiple zones centered on joints and narrow quartz - semi-massive sulphide veins. The individual zones are up to 60cm wide. Away from these alteration zones the grain size and abundance of sulphides is much lower. There are two types of pyrite in the sulphide veins which occur along the joints, a coarse-grained euhedral variety which is set in a fine-grained botryoidal variety.	<a href="http://www.geologyontario.mndm.gov.on.ca/mndmfiles/mdi/data/records/MDI41P12SW00056.html">http://www.geologyontario.mndm.gov.on.ca/mndmfiles/mdi/data/records/MDI41P12SW00056.html</a>
EAST ARM BAGSVERD LAKE	Mineral Occurrence	Possibly porphyry-type	N/A	granodiorite, diabase	chalcop yrite	pyrite, pyrrhotite	shear, joint	Chester intrusive complex	Neoproterozoic	2740 Ma	Regional greenschist	Disseminated pyrite, pyrrhotite, and chalcopyrite occurs associated with the sheared granodiorite. There are also a number of small quartz and semi-massive sulphide veins with pyrite, pyrrhotite and chalcopyrite along fractures. The higher-grade results are associated with these veins which have a core length of up to 30 cm (1').	<a href="http://www.geologyontario.mndm.gov.on.ca/mndmfiles/mdi/data/records/MDI41P12SW00083.html">http://www.geologyontario.mndm.gov.on.ca/mndmfiles/mdi/data/records/MDI41P12SW00083.html</a>
RUNDLE-HANNA VEIN	Discretionary Mineral Occurrence	Possibly intrusion related	Carbonate alteration	quartz-carbonate vein, diorite	Gold	pyrite	vein	Horwood Group	Neoproterozoic	2700 Ma	Regional greenschist	A highly oxidized vein was exposed in two pits 10 and 12 feet deep. Exposure consists of quartz stringers with carbonate cutting fine-grained diorite. Wall rock inclusions are reported as being well mineralized with disseminated pyrite. The footwall is also said to be mineralized for a width of 2 feet from the veining	<a href="http://www.geologyontario.mndm.gov.on.ca/mndmfiles/mdi/data/records/MDI41O16NW00040.html">http://www.geologyontario.mndm.gov.on.ca/mndmfiles/mdi/data/records/MDI41O16NW00040.html</a>
DERRAUGH NO. 1 VEIN	Mineral Occurrence	Mesothermal	sericitization alteration	quartz-vein	Gold	pyrite, chalcopyrite, galena	shear, fault, breccia	Halcrow-Swayze	Neoproterozoic	2700 Ma	Regional greenschist	The mineralized vein is hosted in strongly altered feldspar porphyry - granodiorite which is very strongly altered and sheared. The matrix of the porphyry is fine grained and contain up to 30% subhedral feldspar phenocryst which are up to 4mm in size. The alteration of the porphyry is primarily to an iron carbonate but where the intensity of foliation and shearing is high, sericite alteration is probably more dominant. Closely associated with the mineralized quartz vein is a lamprophyre dyke.	<a href="http://www.geologyontario.mndm.gov.on.ca/mndmfiles/mdi/data/records/MDI41O15SE00028.html">http://www.geologyontario.mndm.gov.on.ca/mndmfiles/mdi/data/records/MDI41O15SE00028.html</a>

Maltby	Mineral Occurrence	Mesothermal	potassic, chloritic, hematization, tourmalinization	quartz vein, cataclastic schist, fe tholeiitic	gold, pyrite, chalcop yrite, galena	tourmaline, fuschite	shear	Halcrow-Swayze	Neoproterozoic	2716 Ma	Regional greenschist	The mineralization is hosted in sheared basalt within a sequence of massive and pillowed iron tholeiitic flows which trend south east. At the showing there is extensive iron carbonate and chlorite alteration which tends to occur in discontinuous bands parallel to the schistosity and are up to 5m thick. This alteration tends to be more pronounced near contacts with slightly discordant feldspar porphyry sills which also have carbonate alteration.	<a href="http://www.geologyontario.mndm.gov.on.ca/mndmfiles/mdi/data/records/MDI41O09NW00012.html">http://www.geologyontario.mndm.gov.on.ca/mndmfiles/mdi/data/records/MDI41O09NW00012.html</a>
Flint Rock Mainland	Mineral Occurrence	Mesothermal	carbonatization alteration	quartz-carbonate vein, andesite	chalcop yrite, galena, gold	pyrite	shear	Halcrow-Swayze	Neoproterozoic	2700 Ma	Regional greenschist	There are a number of small quartz - calcite - epidote veins which locally contain pyrite, pyrrhotite and minor chalcopyrite. These veins are locally associated with the interflow sediments and typically carry anomalous gold values but sub ore grade values. In addition to the small veins similar gold values have also been returned from finely laminated siliceous interflow sediments.	<a href="http://www.geologyontario.mndm.gov.on.ca/mndmfiles/mdi/data/records/MDI41O15SE00008.html">http://www.geologyontario.mndm.gov.on.ca/mndmfiles/mdi/data/records/MDI41O15SE00008.html</a>
HOODOO	Mineral Occurrence	Mesotherma	carbonatization, potassic, chloritic alteration	quartz-carbonate, cataclastic schist, basalt	pyrite, chalcop yrite	pyrrhotite, galena, sphalerite	shear, fold	Muskego-reeves	Neoproterozoic	2700 Ma	Regional greenschist	The outcrop is dominated by a strong foliation / schistosity trending southeast. It is possible that this foliation may represent a splay off the major east west shearing which is associated with the mineralization at the Joburke Mine. Structural deformation is pronounced and primary features are only recognizable along the northeast limit of the stripped area.	<a href="http://www.geologyontario.mndm.gov.on.ca/mndmfiles/mdi/data/records/MDI42B01SW00016.html">http://www.geologyontario.mndm.gov.on.ca/mndmfiles/mdi/data/records/MDI42B01SW00016.html</a>
EMERALD ISLE	Mineral Occurrence	Possibly porphyry-type	chloritic, pyritic, malachite supergene alteration	granodiorite, quartz-vein	chalcop yrite, tellurid e	pyrite, hematite, arsenopyrite	sheared	Chester intrusive complex	Neoproterozoic	2740 Ma	Regional greenschist	Within the shear zone, mineralization is discontinuous along strike. Where mineralization occurs, it is very similar to that at the Emerald Isle occurrence and consists of narrow massive sulphide veinlets and quartz veins. Associated with these veinlets are disseminations of pyrite which extend into the adjacent granodiorite wall rock a short distance.	<a href="http://www.geologyontario.mndm.gov.on.ca/mndmfiles/mdi/data/records/MDI41P12SW00133.html">http://www.geologyontario.mndm.gov.on.ca/mndmfiles/mdi/data/records/MDI41P12SW00133.html</a>
CHESTER-SHANNON	Developed Mineral Prospect Without Reserves	Possibly porphyry-type	biotitic, supergene azurite and malachite alteration	granodiorite, quartz-sulphide vein, near mafic dyke	pyrite, chalcop yrite, gold, tellurid e, bornite, covellit e	tourmaline	shear, fault	Chester intrusive complex	Neoproterozoic	2740 Ma	Regional greenschist	Disseminated fine grained pyrite and minor chalcopyrite occur in the shear zone which cut the host granodiorite and forms the dominant mineralization. Sulphides are also common in the numerous parting planes. In addition to this there are common short, thin, coarse grained quartz carbonate veins which contain coarse grains of pyrite, chalcopyrite plus trace amounts of the other sulphides.	<a href="http://www.geologyontario.mndm.gov.on.ca/mndmfiles/mdi/data/records/MDI41P12SW00064.html">http://www.geologyontario.mndm.gov.on.ca/mndmfiles/mdi/data/records/MDI41P12SW00064.html</a>
KIDD #2 ZONE	Prospect	Possibly porphyry-type	biotitic, silicification, chloritic alteration	granodiorite, diorite	chalcop yrite, gold	pyrite, pyrrhotite,	vein ass.	chester intrusive complex	Neoproterozoic	2740 Ma	Regional greenschist	The discontinuous shear zones are the locus of the mineralization. Some of these shears have an axial quartz-carbonate vein up to 30 cm thick. Pyrite, chalcopyrite, pyrrhotite and pyrolusite form between 1-30% of these veins. In the wall rock, sulphide extend up to 8m from the veins within the biotite altered diorite, where it occurs as fine disseminated veins or in thin stringers	<a href="http://www.geologyontario.mndm.gov.on.ca/mndmfiles/mdi/data/records/MDI41P12SW00058.html">http://www.geologyontario.mndm.gov.on.ca/mndmfiles/mdi/data/records/MDI41P12SW00058.html</a>
LABBE #2	Mineral Occurrence	Possibly porphyry-type	chloritic, saussuritization	granodiorite, diorite	chalcop yrite, gold	pyrite	shear	Chester intrusive complex	Neoproterozoic	2740 Ma	Regional greenschist	Most of the mineralization is fine-grained chalcopyrite and pyrite disseminated in the matrix of the granodiorite and form up to 5% of the rock. The mineralization tends to be stronger where the granodiorite is cut by a shear zone. Some small quartz veins, up to 2 cm wide by 100cm long, occur within the sheared granodiorite. Outside of the granodiorite, some disseminated mineralization occurs as small splashes of iron staining along the strike of a small shear zone.	<a href="http://www.geologyontario.mndm.gov.on.ca/mndmfiles/mdi/data/records/MDI41P12SW00130.html">http://www.geologyontario.mndm.gov.on.ca/mndmfiles/mdi/data/records/MDI41P12SW00130.html</a>
CYRIL YOUNG	Mineral Occurrence	Possibly porphyry-type	saussuritization	granodiorite, diorite, quartz-vein	chalcop yrite	pyrite, hematite, goethite		Chester intrusive complex	Neoproterozoic	2740 Ma	Regional greenschist	The mineralization is located on the contact of a dioritic inclusion within the Chester Granitoid Complex granodiorite. Sericite alteration has been reported within the shear zone that cuts the outcrop.	<a href="http://www.geologyontario.mndm.gov.on.ca/mndmfiles/mdi/data/records/MDI41P12SW00136.html">http://www.geologyontario.mndm.gov.on.ca/mndmfiles/mdi/data/records/MDI41P12SW00136.html</a>
CHARLEBOIS, J.	Mineral Occurrence	Mesothermal	potassic alteration	quartz-carbonate vein, fe tholeiitic basalt	gold	pyrite, chalcopyrite, pyrrhotite	shear	Horwood Group	Neoproterozoic	2700 Ma	Regional greenschist	The mineralization is confined to a single vein system that trends northwest parallel to stratigraphy in the adjacent rocks. The main vein consists of grey quartz with chloritic inclusions and is well mineralized with chalcopyrite, pyrite, and pyrrhotite located within fractures within the vein. Adjacent to the main vein is a narrow zone of bleached volcanics or zones of sheared chloritic material with some quartz stringers.	<a href="http://www.geologyontario.mndm.gov.on.ca/mndmfiles/mdi/data/records/MDI42B01SW00006.html">http://www.geologyontario.mndm.gov.on.ca/mndmfiles/mdi/data/records/MDI42B01SW00006.html</a>

DEBURMAC	Mineral Occurrence	Mesothermal	carbonatization, potassic, chloritic alteration	quartz-vein, cataclastic schist, basalt	gold	pyrite	shear	Horwood Group	Neoproterozoic	2700 Ma	Regional greenschist	The quartz veining is confined to a strongly foliated and schistose metavolcanic shear zone which is parallel to the regional northeast trend and the Hardiman Bay Fault. Away from the shear zone the host basaltic flows are a fine grained light greyish green color and may be Mg tholeiitic. Away from the shear hosted quartz vein there are numerous, thin, undulating strongly foliated zones transecting the metavolcanics.	<a href="http://www.geologyontario.mndm.gov.on.ca/mndmfiles/mdi/data/records/MDI41O16NW00007.html">http://www.geologyontario.mndm.gov.on.ca/mndmfiles/mdi/data/records/MDI41O16NW00007.html</a>
SHEPPARD #10	Mineral Occurrence	Possibly porphyry-type	sericitization, chloritic alteration	quartz vein, granodiorite	pyrite, chalcopyrite, sphalerite	magnetite	shear	Chester intrusive complex	Neoproterozoic	2740 Ma	Regional greenschist	Mineralization is associated with a quartz veins and altered shear zones. This mineralization is predominantly massive and semi massive pyrite with traces of chalcopyrite in quartz veins. Adjacent to the veins there are disseminated fine grains of pyrite and less abundant chalcopyrite.	<a href="http://www.geologyontario.mndm.gov.on.ca/mndmfiles/mdi/data/records/MDI41P12SW00079.html">http://www.geologyontario.mndm.gov.on.ca/mndmfiles/mdi/data/records/MDI41P12SW00079.html</a>
THREE DUCKS	Mineral Occurrence	Possibly porphyry-type		granodiorite, quartz veins	pyrite, chalcopyrite, pyrrhotite, gold, sphalerite, copper		shear	Chester intrusive complex	Neoproterozoic	2740 Ma	Regional greenschist	The quartz veining pinches and swells between 10cm and 50cm. Within the veins concentrated along the contact of the veins and in bands, less than 1cm thick, are disseminated grains or diffuse aggregates of fine to medium pyrite and chalcopyrite. Pyrite and chalcopyrite also occur in a similar mode in the granodiorite adjacent to the quartz veins. Within the granodiorite there are two types of pyrite mineralization.	<a href="http://www.geologyontario.mndm.gov.on.ca/mndmfiles/mdi/data/records/MDI41P12SW00051.html">http://www.geologyontario.mndm.gov.on.ca/mndmfiles/mdi/data/records/MDI41P12SW00051.html</a>
DOMESTIC EAST ZONE	Mineral Occurrence	Mesothermal		Fe tholeiitic basalt, quartz feldspar vein	gold	pyrite	Newton high strainzone (local scale)	Horwood Group	Neoproterozoic	2700 Ma	Regional greenschist	Mineralization is hosted in a pillowed iron tholeiitic basalt sequence, trending northeast which has been intruded by a number of quartz-feldspar porphyries. A hornblende lamprophyre also intrudes the mafic sequence. The porphyry has been emplaced along an east-west shear zone and is disjointed	<a href="http://www.geologyontario.mndm.gov.on.ca/mndmfiles/mdi/data/records/MDI41O16NW00033.html">http://www.geologyontario.mndm.gov.on.ca/mndmfiles/mdi/data/records/MDI41O16NW00033.html</a>
WDOWCZYK	Discretionary Mineral Occurrence	possibly intrusion-related gold deposit	chloritic, carbonatization alteration	quartz vein, basalt	gold	pyrite, chalcopyrite	shear	Horwood Group	Neoproterozoic	2700 Ma	Regional greenschist	At the main showing there are a number of shallow dipping quartz veins forming a stockwork which is thinly and erratically distributed. The quartz veins, with minor iron carbonate, are thin being less than 10cm, very coarse grained, granular and variable in color from white, to pale translucent green, and grey. Pyrite and trace amount of chalcopyrite form up to 10% of the veins in coarse subhedral grains though the distribution is erratic. The sulphides also occur in the adjacent wall rock but the size and percentage decreases away from the veins	<a href="http://www.geologyontario.mndm.gov.on.ca/mndmfiles/mdi/data/records/MDI41O16NW00032.html">http://www.geologyontario.mndm.gov.on.ca/mndmfiles/mdi/data/records/MDI41O16NW00032.html</a>
KERR-ADDISON (STACK VEIN)	Mineral Occurrence	Mesothermal	chloritic alteration	quartz-carbonate vein, diorite, basalt	gold	pyrite, pyrrhotite	shear	Horwood Group	Neoproterozoic	2700 Ma	Regional greenschist	The Stack vein consists of a series of narrow quartz carbonate or fine-grained cherty veins which are hosted in fine grained and medium grained mafic flows.	<a href="http://www.geologyontario.mndm.gov.on.ca/mndmfiles/mdi/data/records/MDI42B01SW00003.html">http://www.geologyontario.mndm.gov.on.ca/mndmfiles/mdi/data/records/MDI42B01SW00003.html</a>
Smith-Thorne	Developed Mineral Prospect Without Reserves	Mesothermal	tourmalinization	quartz vein, basalt,	gold, chalcopyrite	pyrite, galena, sphalerite, stibnite	shear	Horwood Group	Neoproterozoic	2700 Ma	Regional greenschist	Mineralization occurs primarily as visible gold though sparsely disseminated pyrite is more dominant. In addition, chalcopyrite, pyrrhotite, galena, sphalerite and stibnite have been observed	<a href="http://www.geologyontario.mndm.gov.on.ca/mndmfiles/mdi/data/records/MDI41O16NW00004.html">http://www.geologyontario.mndm.gov.on.ca/mndmfiles/mdi/data/records/MDI41O16NW00004.html</a>
Kenty	Developed Mineral Prospect Without Reserves	Mesothermal	chloritic, hematization, sericitization	quartz vein	gold	pyrite, galena, molybdenite, sphalerite, tourmaline	shear	Raney-newton	Neoproterozoic	2695+/-2 Ma	Regional greenschist	The mineralization is hosted in a pillowed Fe tholeiitic basalt intercalated with massive flows and breccia units. Little deformation or alteration is apparent in these rocks away from the mineralized veins and the sequence strikes NW with tops to the SW. Quartz veins which vary from 10 to 20cm occur in zones of strong carbonate alteration up to several meters thick. Parallel to the main veins within the alteration zone there are thin quartz veinlets. Within the main vein there are fractures perpendicular to the vein mineralized with carbonate and more rarely tourmaline.	<a href="http://www.geologyontario.mndm.gov.on.ca/mndmfiles/mdi/data/records/MDI41O15SE00029.html">http://www.geologyontario.mndm.gov.on.ca/mndmfiles/mdi/data/records/MDI41O15SE00029.html</a>

Appendix C: Tonnage and grade data for magmatic-hydrothermal gold deposits and prospects from the Abitibi and Swayze greenstone belt modified from Mathieu (2021).

Deposit/prospect	Gold		
	Tonnage (Mt)	Grade (g/t)	Type (reference)
Central Camp	53.54	1.55	Production (Leclerc et al. 2012)
Côte Au(-Cu)	355.4	0.87	Ressources (Oshust et al. 2018)
Doyon	24.56	5.93	Production (Simard 2001)
Kiena	5.81	4.99	Production (Gosselin and Dubé 2005)
Selbaie	47.43	0.62	Production (Simard 2001)
Troilus (Lac)	23.79	1.19	Production (Simard 2001)
Bourlamaque (Ferderber Mine - Belmoral, Dumont)	2.35	6.4	Production (Gosselin and Dubé 2005)
McIntyre-Hollinger-Coniaurum complex	96.52	10.02	Production (Gosselin and Dubé 2005) Ressource
MOP-II	10.9	0.45	( <a href="https://www.soquem.qc.ca/projets/">https://www.soquem.qc.ca/projets/</a> )
Bachelor	0.87	4.68	Production (Gosselin and Dubé 2005)
Lac Shortt	2.7	4.62	Production (Gosselin and Dubé 2005)
Upper Beaver	0.53	8.3	Production (Gosselin and Dubé 2005)
Beattie	9.71	4.32	Production (Gosselin and Dubé 2005)
Beattie	60.9	1.59	Resources (Williamson et al. 2013)
Douay	8.6	1.52	Ressources (El Rassi 2019)
Kelore	0.76	5.83	Reserve (Gosselin and Dubé 2005)
Lake Shore	15.61	17.1	Production (Ispalotov et al. 2008)
Macassa	14.59	14.06	Production (Pinheiro Harvey et al. 2019)
Matachewan Consolidated	3.29	3.57	Production (Gosselin and Dubé 2005)

Ross	5.04	5.41	Production (Gosselin and Dubé 2005)
Wasamac	4.71	8.85	Production (Gosselin and Dubé 2005)
Young-Davidson	5.64	3.43	Production (Gosselin and Dubé 2005)
Camflo - Malartic Hygrade	9.38	5.89	Production (Gosselin and Dubé 2005)
Canadian Malartic	343.7	0.97	Reserves (Belzile and Gignac 2011)
Kirkland Lake deposit	2.85	12.8	Production (Ispalotov et al. 2008)
Silidor	4.9	6.2	Reserves (Gosselin and Dubé 2005)
Thunder Creek (Lake Shore Gold's Thunder Creek)	2.88	5.64	Ressources (Crick et al. 2011) Reserve (Fumerton and Houle, 1994; Bousquet, 2012) <a href="http://www.geologyontario.mndm.gov.on.ca/mndmfiles/mdi/data/records/MDI41O09SE00005.html">http://www.geologyontario.mndm.gov.on.ca/mndmfiles/mdi/data/records/MDI41O09SE00005.html</a>
Jerome Mine	193.63	5.9	Reserve (Fumerton and Houle, 1994; Draper, 2015) <a href="http://www.geologyontario.mndm.gov.on.ca/mndmfiles/mdi/data/records/MDI41O15SW00002.html">http://www.geologyontario.mndm.gov.on.ca/mndmfiles/mdi/data/records/MDI41O15SW00002.html</a>
Halcrow prospect	115.6	3.8	Reserve (Fumerton and Houle, 1992; Wilson, 2013) <a href="http://www.geologyontario.mndm.gov.on.ca/mndmfiles/mdi/data/records/MDI41O16NW00020.html">http://www.geologyontario.mndm.gov.on.ca/mndmfiles/mdi/data/records/MDI41O16NW00020.html</a>
Orofino (inferred mineral resource)	533	4.95	Reserve (Fumerton and Houle, 1992; Wilson, 2013) <a href="http://www.geologyontario.mndm.gov.on.ca/mndmfiles/mdi/data/records/MDI41O16NW00020.html">http://www.geologyontario.mndm.gov.on.ca/mndmfiles/mdi/data/records/MDI41O16NW00020.html</a>
Orofino (indicated +measured)	371	6.41	Reserve (Fumerton and Houle, 1993; Wilson, 2013)
Rundle Mine (inferred mineral resource)	267	6.68	<a href="http://www.geologyontario.mndm.gov.on.ca/">http://www.geologyontario.mndm.gov.on.ca/</a>

mndmfiles/mdi/data/records/MDI41O16SW0  
0003.html

Reserve (Fumerton and Houle, 1992;  
Bousquet, 2015)  
[http://www.geologyontario.mndm.gov.on.ca/  
mndmfiles/mdi/data/records/MDI42B01NW0  
0002.html](http://www.geologyontario.mndm.gov.on.ca/mndmfiles/mdi/data/records/MDI42B01NW0002.html)

Joburke Mine (recoverable)

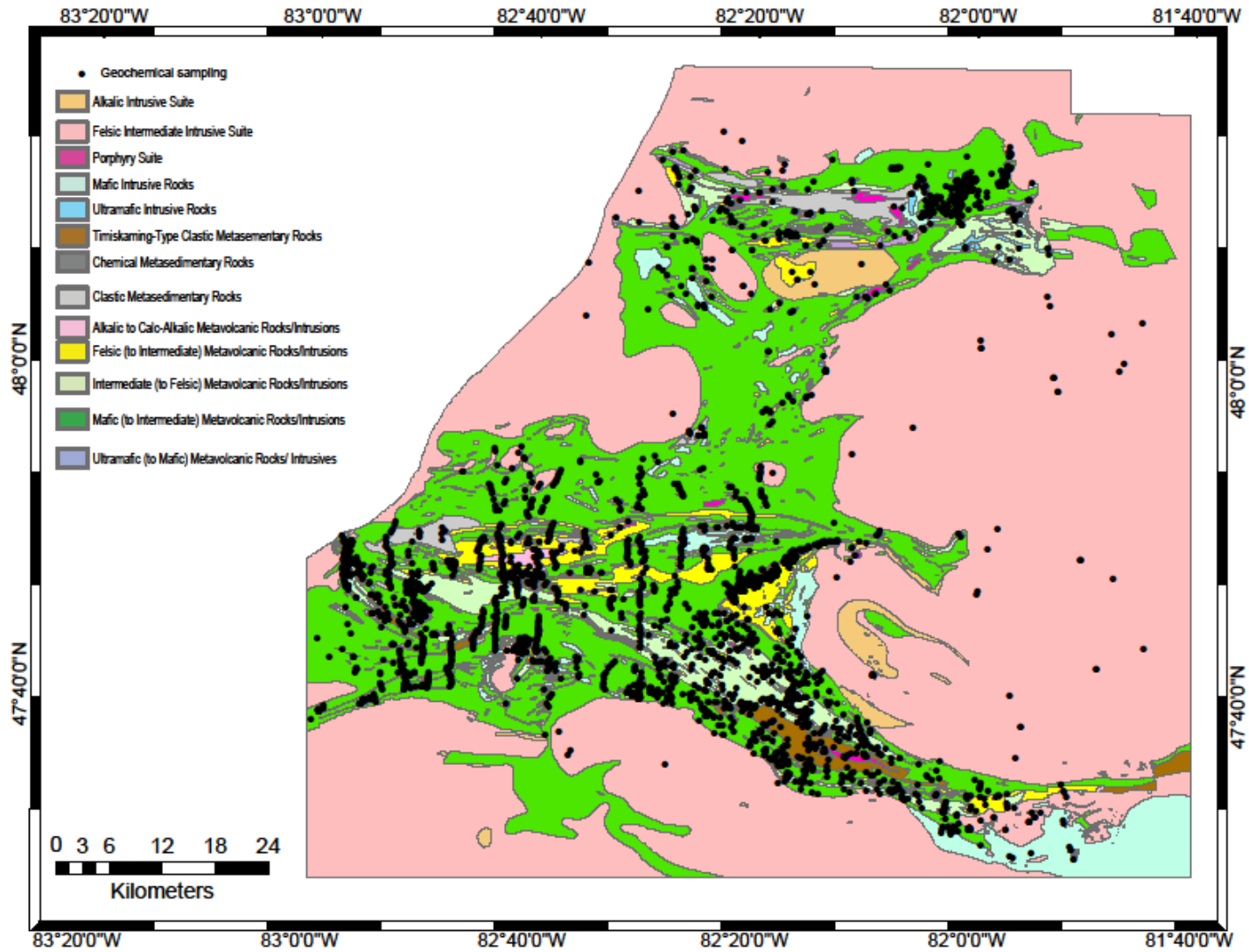
70

2.8

0002.html

---

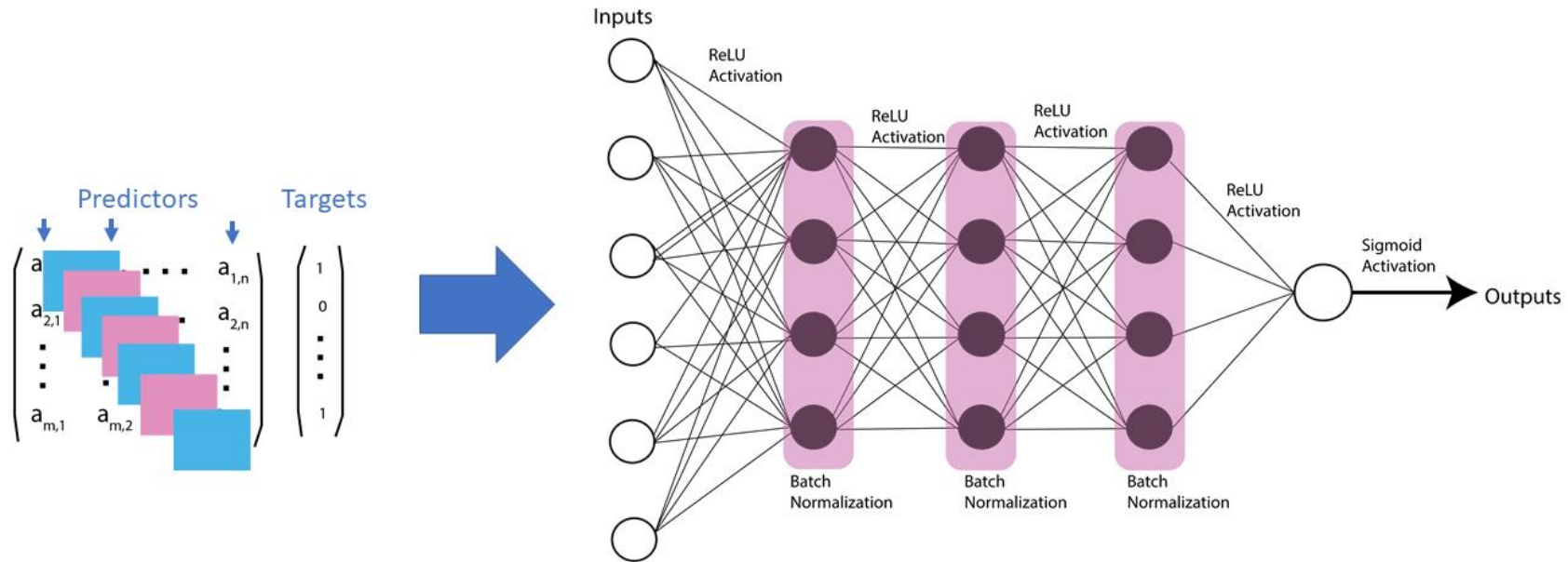
Appendix D: Geological map of the Swayze greenstone belt overlain by geochemical sampling distribution.



## Appendix E: A simplified architecture of a deep neural network

Activation function:

$$f(x) = \max(0, x) = \begin{cases} x, & \text{if } x_i \geq 0 \\ 0, & \text{if } x_i < 0 \end{cases}$$



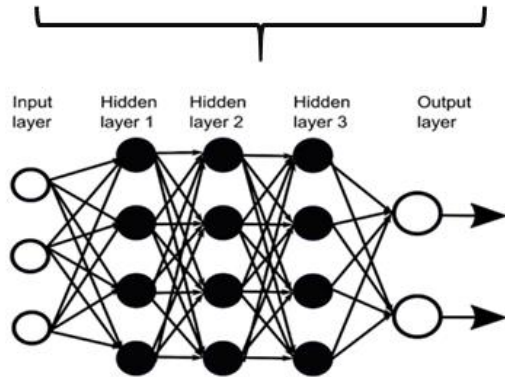
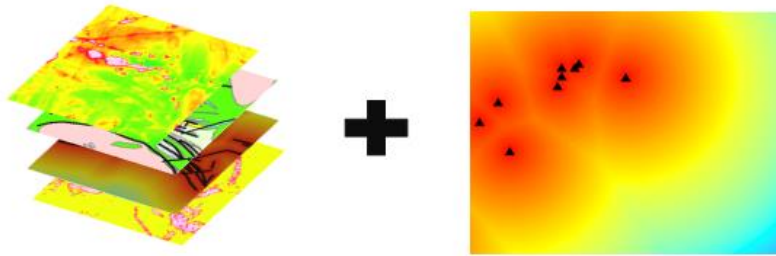
# Transfer learning

## Source Domain

(Brownfield Area)

$$D_s = \{(x_{s_1}, y_{s_1}), \dots, (x_{s_n}, y_{s_n})\}, \text{ where } x_{s_i} \in X_s \text{ and } y_{s_i} \in Y_s$$

Predictors layers      prospect locations



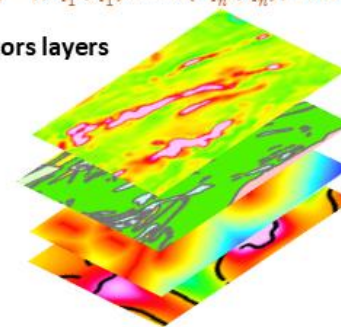
Transferring  
gained  
knowledge  
(weights)

## Target Domain

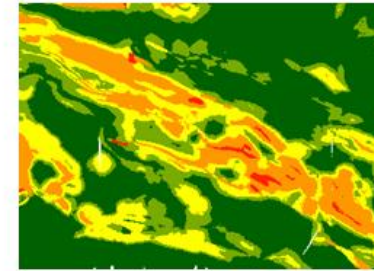
(Greenfield Area)

$$D_T = \{(x_{T_1}, y_{T_1}), \dots, (x_{T_n}, y_{T_n})\} \text{ where } x_{T_i} \in X_T \text{ and } y_{T_i} \in Y_T$$

Predictors layers



No mine or  
prospect data



Deep transfer  
learned  
prospectivity map